Inaugural dissertation

for

obtaining the doctoral degree

of the

Combined Faculty of Mathematics, Engineering and Natural Sciences

of the

Ruprecht - Karls - University

Heidelberg

presented by

M.Sc. Annika Mareike Binder

born in Stuttgart, Germany

Oral examination: 31.03.2025

Microtubule-associated proteins modulate subpellicular microtubule function in the malaria parasite *Plasmodium berghei*

Referees: Prof. Dr. Gislene Pereira

Prof. Dr. Friedrich Frischknecht

Abstract

Malaria, caused by the unicellular eukaryotic parasite *Plasmodium*, is transmitted through the bite of an infected *Anopheles* mosquito. *Plasmodium* has a complex life cycle that involves the development within different tissues and environments, both within the mosquito and the vertebrate host. This lifestyle requires constant adjustment in cell shape to meet the changing demands of the host environments but also fast parasite motility to evade the host immune mechanisms.

In eukaryotic organisms, cell shape is often mediated by microtubules – hollow filamentous structures composed of α- and β-tubulin. Microtubule dynamics and stability are modulated by microtubule-associated proteins (MAPs). MAPs are proteins that bind either externally or internally to the microtubule lattice with the latter named microtubule inner proteins (MIPs). In *Plasmodium*, the dynamic shape changes and the structural stability of the parasite are mediated by subpellicular microtubules (SPMTs) that lie directly underneath the inner membrane complex (IMC) that subtend the plasma membrane of the parasite. SPMTs are characteristic for the invasive stages of the parasite and hence found in merozoites, ookinetes and sporozoites. They also play a pivotal role in the elongated, falciform-shaped gametocytes of *Plasmodium falciparum*, where they facilitate cell elongation and maturation. Disruption of SPMT formation, stability or number affects parasite shape and motility, underscoring their critical functional roles. Unlike the microtubules of model organisms, SPMTs exhibit remarkable stability, a property thought to be conferred by MAPs and potentially MIPs. However, the identities and specific functions of these stabilizing proteins remain largely unknown.

In this study, I investigated the functional roles of several MAPs across the life cycle of the rodent-infecting *Plasmodium berghei*. Individual and combinatorial deletions of two MIPs – previously identified in the related parasite *Toxoplasma gondii* – and one potential outer MAP did not impair parasite development or transmission. Moreover, these deletions did not yield a detectable phenotype under normal conditions. However, cold assays revealed their contribution to SPMT stability under suboptimal environments, which is potentially relevant in natural settings. Exposure of MIP knockout parasites to low temperatures caused SPMT depolymerization and cytosolic dispersion, underscoring their role in maintaining intrinsic microtubule stability under suboptimal temperature conditions.

In addition, I investigated the function of an external MAP, SPM3, unique to *Plasmodium* (and *Cryptosporidium*). SPM3 was previously found to be important for SPMT arrangement in the human-infecting *Plasmodium falciparum*. In *Plasmodium berghei*, *spm3* deletion progressively impaired mosquito-stage development, leading to reduced motility in ookinetes and sporozoites, diminished salivary gland invasion, and defective transmission. Ultrastructure expansion

microscopy and electron microscopy revealed that SPM3 is required for proper tethering of SPMTs to the IMC, which is in particular essential for the mosquito-to-vertebrate transmission stages.

Collectively, these findings illuminate the mechanisms underlying both the intrinsic stability and the IMC tethering of SPMTs, highlighting the indispensable roles of SPMTs in parasite development and infectivity. These findings deepen our understanding of the structural and functional adaptations that enable *Plasmodium* to navigate through its life cycle and ensures a foundation for future investigations into parasite biology.

Zusammenfassung

Malaria wird durch den einzelligen eukaryotischen Parasiten *Plasmodium* verursacht und durch den Stich einer infizierten *Anopheles*-Mücke übertragen. *Plasmodium* hat einen komplexen Lebenszyklus, der die Entwicklung in verschiedenen Geweben und Umgebungen, sowohl in der Mücke als auch im Wirbeltierwirt, umfasst. Diese Lebensweise erfordert eine ständige Anpassung der Zellform, um den wechselnden Anforderungen der Wirtsumgebung gerecht zu werden, aber auch eine schnelle Beweglichkeit des Parasiten, um den Immunmechanismen des Wirts zu entgehen.

In eukaroytischen Organismen wird die Zellform häufig durch Mikrotubuli vermittelt – hohle filamentöse Strukturen, die aus α- und β-Tubulin bestehen. Mikrotubuli-Dynamik und -Stabilität werden durch Mikrotubuli-assoziierte Proteine (MAPs) moduliert. MAPs sind Proteine, die entweder von außen oder von innen an das Mikrotubuli-Gerüst binden, wobei letztere dann Mikrotubuli-innere Proteine (MIPs) genannt werden. Bei *Plasmodium* werden die dynamischen Formveränderungen und die strukturelle Stabilität des Parasiten durch subpellikuläre Mikrotubuli (SPMTs) vermittelt, die direkt unter dem inneren Membrankomplex (IMC) liegen, welcher wiederum direkt unterhalb der Plasmamembran liegt. SPMTs sind charakteristisch für die invasiven Stadien des Parasiten und daher in Merozoiten, Ookineten und Sporozoiten zu finden. Sie spielen auch eine zentrale Rolle in den länglichen, falciformen Gametozyten von *Plasmodium falciparum*, wo sie die Zelldehnung und -reifung erleichtern. Eine Störung der SPMT-Bildung oder -Stabilität wirkt sich auf die Form und Beweglichkeit der Parasiten aus, was ihre kritische funktionelle Rolle unterstreicht. Im Gegensatz zu den Mikrotubuli von Modellorganismen weisen SPMTs eine bemerkenswerte Stabilität auf, eine Eigenschaft, von der man annimmt, dass sie von MAPs und möglicherweise von MIPs verliehen wird. Die Identität und die spezifischen Funktionen dieser stabilisierenden Proteine sind jedoch noch weitgehend unbekannt.

In dieser Studie untersuchte ich die funktionelle Rolle mehrerer MAPs während des Lebenszyklus des Nagetier-infizierenden *Plasmodium berghei*. Einzelne und kombinatorische Deletionen von zwei MIPs - die zuvor in dem verwandten Parasiten *Toxoplasma gondii* identifiziert wurden - und einem potenziellen äußeren MAP beeinträchtigten weder die Entwicklung noch die Übertragung des Parasiten. Außerdem führten diese Deletionen unter normalen Bedingungen zu keinem nachweisbaren Phänotyp. Kältetests zeigten jedoch, dass sie zur SPMT-Stabilität unter suboptimalen Bedingungen beitragen, was unter natürlichen Bedingungen von Bedeutung sein könnte. Die Exposition von MIP-Knockout-Parasiten gegenüber niedrigen Temperaturen führte zu einer Depolymerisation von SPMT und einer Dispersion ins Zytosol, was ihre Rolle bei der

Aufrechterhaltung der intrinsischen Mikrotubuli-Stabilität unter suboptimalen Temperaturbedingungen unterstreicht.

Darüber hinaus untersuchte ich die Funktion eines externen MAP, SPM3, das nur bei *Plasmodium* (und *Cryptosporidium*) vorkommt. SPM3 wurde zuvor als wichtig für die SPMT-Anordnung in den Menschen infizierenden *Plasmodium falciparum* befunden. Bei *Plasmodium berghei* führte die Deletion von *spm3* zu einer fortschreitenden Beeinträchtigung der Entwicklung im Mückenstadium, was sich in einer verminderten Motilität der Ookineten und Sporozoiten, einer verringerten Speicheldrüseninvasion und einer gestörten Übertragung niederschlug. Ultrastrukturelle Expansionsmikroskopie und Elektronenmikroskopie zeigten, dass SPM3 für die ordnungsgemäße Bindung der SPMTs an den IMC erforderlich ist, was insbesondere für die Übertragungsstadien von der Mücke zum Wirbeltier wichtig ist.

Zusammenfassend beleuchten diese Ergebnisse die Mechanismen, die sowohl der intrinsischen Stabilität als auch der IMC-Bindung von SPMTs zugrunde liegen, und unterstreichen die unverzichtbare Rolle von SPMTs bei der Entwicklung und Infektiosität von Parasiten. Diese Erkenntnisse vertiefen unser Verständnis der strukturellen und funktionellen Anpassungen, die es *Plasmodium* ermöglichen, sich durch seinen Lebenszyklus zu bewegen, und bilden eine Grundlage für künftige Untersuchungen der Parasitenbiologie.

Table of Contents

List of Figures

List of Tables

List of supplementary figures

List of Abbreviations

5-FC	5-fluorocytosine
5-FU	5-fluorouracil
α-TAT1	α-tubulin acetyltransferase 1
Å	angstrom
AA	acrylamide
ACT	artemisinin-based combination therapy
amp	ampicillin
ampR	ampicillin resistance
APR	apical polar ring
APR2	apical polar ring associated protein 2
ATP	adenosine triphosphate
Au	arbitrary unit
bioID	proximity-dependent biotin identification
bp	base pair
BIS	N,N'-methylenbisacrylamide
BSA	bovine serum albumin (Fraction V)
°C	degree Celsius
CO_2	carbodioxide
Cryo-EM/ET	cryo-electron microscopy/tomography
CSP	circumsporozoite
ddH_2O	double distilled water
Da	Dalton
DHHC2	enzyme with catalytic signature aspartate-histidine-histidine-cysteine
DNA	deoxyribonucleic acid

dhfr	*dihydrofolate reductase*
dhfs	*dihydrofolate reductase synthase*
dNTP	desoxyribonucleosidtriphosphate
EB1	end-binding protein 1
E. coli	*Escherichia coli*
ef1α	elongation factor 1 alpha
EDTA	ethylenediaminetetraacetic acid
ER	endoplasmatic reticulum
FBS	fetal bovine serum
FIB	focused ion beam
FBT	fresh blood transfer
GAP	glideosome associated protein
GAPM	glideosome associated protein with multiple-membrane spans
gDNA	genomic DNA
GDP	guanosine diphosphate
GFP	green fluorescent protein
GTP	guanosine triphosphate
h	hour/s
hDHFR	*human dihydrofolate reductase*
HEPES	4-(2-hydroxyethyl)-1-piperazineethanesulfonic acid
H_2O	water
Hsp70	heat shock protein 70
IFA	immunofluorescence assay
i. p.	intraperitoneal
iRBC	infected red blood cell

ISP1/2	inner membrane complex sub-compartment protein 1/2
i. v.	intravenous
K40/Q40	lysine 40/ glutamine 40
kb	kilo bases
KO	knockout
L	litre, linker
IFA	Immunofluorescence assay
LB	lysogeny broth
LTD	limiting dilution
M	molar
m	milli
MAP	microtubule-associated protein
min	minute
MIP	microtubule inner protein
µ	micro
MG	midgut
$MgCl_2$	magnesium dichloride
min	minute
MTOC	microtubule organising center
Na_2EDTA	disodium Ethylenediaminetetraacetic acid
NaCl	sodium chloride
NHS	N-hydroxysuccinimide
ns	negatively selected
ORF	open-reading frame
P	primer

PABA	*para*-aminobenzoic acid
PAE	predicted aligned error > e
P. berghei/ Pb	*Plasmodium berghei*
P. falciparum/ Pf	*Plasmodium falciparum*
PBS	phosphate buffered saline
PbDHFR-TS	*Plasmodium berghei* dihydrofolate reductase-thymidine synthase
PCR	polymerase chain reaction
PFA	paraformaldehyde
PhIL1	photosensitized INA-labelled protein 1
PM	plasma membrane
PTM	posttranslational modification
PV	parasitophorus vacuole
PVM	parasitophorus vacuole membrane
RBC	red blood cell
RIPA	radio-immunoprecipitation assay
rpm	revolution per minute
RT	room temperature
s	second
SD	standard deviation
SDS	sodium dodecyl sulphate
SIL6	silent intergenic locus on chromosome 6
SiR	Silicon rhodamine
SG	salivary gland
SMART	Simple Modular Architecture Research Tool
SPM1/SPM2/SPM3	subpellicular microtubule protein 1, 2, 3

SPMT	subpellicular microtubule
spz	sporozoite
TEM	transmission electron microscopy
TEMED	tetramethylethylendiamine
TLAP	thioredoxin-like protein 1-associated protein
Tm	melting temperature
TAE	Tris-acetate-EDTA
tgdhfr	*Toxoplasma gondii dihydrofolate reductase*
T. gondii/ Tg	*Toxoplasma gondii*
Tris/HCl	Tris(hydroxymethyl)aminomethane hydrochloride
TrxL1/2	thioredoxin-like protein 1/2
TTLL	tubulin-tyrosine ligase-like
U	unit
U-ExM	ultrastructure expansion microscopy
UTR	untranslated region
V	volume, volt
WHO	World Health Organization
WT	wild-type
yFCU	yeast cytosine deaminase and uridyl phosphoribosyl transferase
γ-TuRC	γ-tubulin ring complex

1. Introduction

1.1 Malaria

Malaria is a life-threatening disease caused by unicellular eukaryotic parasites of the genus *Plasmodium*. Transmission to humans occurs via the bite of an infected female *Anopheles* mosquito. The disease is characterized by periodic fever episodes and sequestration of parasites within the vasculature (1–3). Cerebral malaria, resulting from parasite sequestration in the brain vasculature, is associated with coma and high mortality rates (4). According to the World Health Organization (WHO), an estimated 263 million cases of malaria were reported globally in 2023, with Africa accounting for 94% of the total cases (5). Although malaria cases declined constantly between 2000 and 2015, recent data indicate a stagnation in this downward trend as 2023 data revealed an increase of 11 million cases compared to the previous year (5). *Plasmodium* infections continue to result in over half a million deaths annually, predominantly affecting children under the age of five (5).

Malaria is derived from the Italian words “mal aria” (“bad air”) as it was initially assumed that the disease is air-transmitted from close-by swamps (6). In 1880, it was Alphonse Laveran that first discovered *Plasmodium* as being the causative agent for malaria, while Ronald Ross demonstrated that mosquitoes are transmitting the parasite and Battista Grassi identified the female *Anopheles* mosquito to be its vector (7–9). To date, more than 200 species of *Plasmodium* have been described, infecting a range of vertebrates including mammals, birds, and reptiles. Six species are known to cause malaria in humans (10). Among these, *P. falciparum* is responsible for the majority of cases in Africa, while *P. vivax* is predominantly found in Asia and South America (11, 12). Additionally, *P. knowlesi*, primarily a parasite of macaques, has been shown to infect humans (13–15). The other human-infecting species include *P. malariae* and *P. ovale*, the latter of which has recently been reclassified into two genetically distinct species: *P. ovale curtisi* and *P. ovale wallikeri* (16).

Despite its identification more than one century ago, fighting this parasite is still challenging. Current control measures include rapid diagnostic tests, insecticide-treated bed nets, and artemisinin-based combination therapies (ACT) (5, 17). ACT comprises a fast-acting artemisinin derivative that eliminates most parasites in conjunction with a slower-acting partner drug to clear residual infections (18). Although malaria vaccine development began in the 1960s, only two vaccines—RTS,S and R21—are currently recommended by the WHO, with R21 receiving approval in October 2023 (5, 17, 19). The RTS,S vaccine exhibits only limited efficacy, achieving only 36% protection in children and 26% in infants even after three doses and a booster (20–22); R21 is

expected to reach similar figures despite initially being more promising with 75% efficacy in a phase III clinical trial following three doses and a booster (15).

The limited success of vaccination efforts, combined with the growing resistance of parasites to antimalarials and mosquitoes to insecticides as well as parasite mutations to avoid detection by rapid diagnostic tests, underscores the urgent need for novel strategies for prevention and treatment (23–25). The complexity of the parasite's life cycle, its immune evasion mechanisms (26, 27)– including antigenic variation and vascular sequestration among others – and its remarkable adaptation to both mosquito and human hosts contribute to the persistence of malaria despite decades of dedicated research.

1.2 *Plasmodium*

1.2.1 The *Plasmodium* life cycle

Plasmodium is an obligate parasite characterized by a complex life cycle. It alternates between a vertebrate host and an insect vector developing within different tissues in both hosts (**Figure 1**). *Plasmodium* is transmitted by an infected female *Anopheles* mosquito, which while probing for a blood vessel, deposits sporozoites into the skin of a vertebrate host (28). Within the dermis, sporozoites exhibit active motility, enabling them to locate and invade blood vessels (29–34). Upon successful entry into the vasculature, sporozoites are transported via the bloodstream to the liver, where they attach to and penetrate the endothelium (35). This invasion occurs through traversal of Kupffer cells or sinusoidal endothelial cells (35–37). Following transmigration of multiple hepatocytes, the sporozoite will terminally invade a hepatocyte and establish an infection (35, 38–40). Upon invasion, the parasite mediates the invagination of the host cell plasma membrane, which will form the parasitophorus vacuole (PV); an enclosed environment that protects the parasite from host cytosol and its defense mechanisms (41). In *P. vivax*, *P. ovale curtisi* and *P. ovale wallikeri*, a subset of liver-stage parasites may differentiate into dormant hypnozoites (16, 42, 43). Inside hepatocytes, the parasite replicates via endopolygeny followed by schizogony (Inês Bento, BioMalParXX). Endopolygeny is characterized by multiple rounds of DNA replication without nuclear division resulting in a polyploid nucleus, while in schizogony nuclei become compartmentalized and daughter cells are separated via a final round of cytokinesis (44). This replication produces thousands of daughter cells, which are subsequently released as membrane-enclosed vesicles, named merosomes, into the bloodstream (45). Merosomes are likely disrupted as they pass through narrow blood vessels, releasing merozoites into circulation (46). Merozoites use short phases of gliding motility to subsequently invade an erythrocyte (47, 48). Inside the erythrocyte, the parasite resides again in a PV, where it acquires nutrients from the host cell cytoplasm and develops from a ring stage to a trophozoite and finally to a mature schizont (49).

Blood-stage schizogony, a process characterized by multiple rounds of asynchronous nuclear division without cytokinesis, gives rise to approximately 20 merozoites, dependent on the *Plasmodium* species (50, 51) (reviewed in (52). To avoid clearance by the spleen, the late-stage parasites establish a protein export system which allows e.g. *P. falciparum* to remodel the surface of their host cell leading to formation of so-called knobs (reviewed in (53, 54). Knobs are membrane protrusions of the erythrocyte on which variant surface antigens are presented that mediate cytoadherence to endothelial cells, enabling sequestration of the parasite to avoid filtration in the spleen (55). Upon maturation, the schizont ruptures, releasing merozoites into the bloodstream. The cyclical release of merozoites is associated with the periodic fewer episodes characteristic of malaria (56).

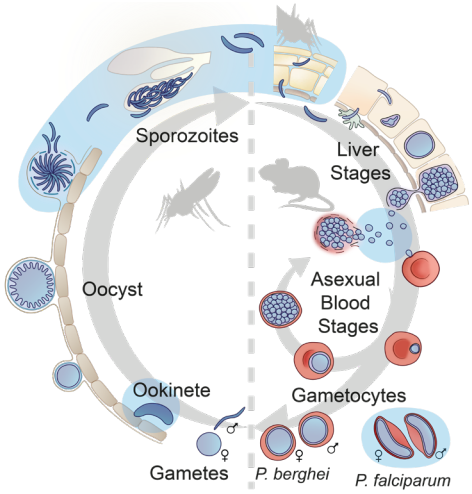

Figure 1 The *Plasmodium* life cycle. During a blood meal of an infected female *Anopheles* mosquito, sporozoites are deposited into the skin of a vertebrate host. From there, mammalian-infecting parasites move in order to find a blood vessel. Within the blood, they travel to the liver and infect hepatocytes and transform into thousands of liver merozoites which are eventually released into the blood stream and infect erythrocytes. Continuous rounds of asexual replication increase the parasite burden in the blood. A proportion of parasites will form into sexual stages (gametocytes). Gametocytes are taken up into the mosquito's blood meal and mature into gametes. Within the mosquito midgut, the microgamete (♂) will fertilize the macrogamete (♀) forming a zygote. The zygote transforms into an ookinete, which traverses the midgut epithelium and develops into an oocyst. High replication within the oocyst gives rise to thousands of sporozoites that are released into the mosquito's hemolymph system. Once having successfully invaded the salivary glands, the life cycle is completed. Stages highlighted in blue possess subpellicular microtubules (SPMTs). This figure was previously published and the figure and legend were adapted for this thesis (57).

Environmental and intrinsic factors eventually trigger a subset of parasites in the blood to commit to sexual development, forming gametocytes (58–61). During gametocytogenesis, male microgametocytes and female macrogametocytes will form. The early gametocyte stages of *P. falciparum* and *P. vivax* sequester in the bone marrow (62–64). Members of the Laveranian clade, including *P. falciparum*, undergo distinct morphological changes (65, 66). Within the bone marrow, *P. falciparum*, immature gametocytes transition through four developmental phases,

transforming from round to the characteristic banana-shaped, falciform morphology with pointed ends (reviewed in (67). By phase V, the ends of the mature gametocyte become blunted, and cells loose rigidity. These shape changes are thought to allow the now mature gametocyte to re-enter the peripheral blood circulation to be transmitted to the mosquito (68, 69). In contrast, rodent-infecting *P. berghei* gametocytes stay round throughout gametocytogenesis and thus do not sequester in the bone marrow but remain in the blood (70).

When another female *Anopheles* mosquito takes a blood meal from an infected vertebrate host, it will take up both asexual and sexual stages. While the asexual stages cannot develop further within the mosquito, gametocytes undergo activation. This activation is triggered by three environmental cues in the mosquito midgut: the presence of xanthurenic acid within the mosquito gut (71, 72), an increase in pH from 7.4 to 8.0-8.2 (73, 74) and a temperature drop from approximately 37 °C to around 20 °C (73, 75). Upon activation, female gametocytes differentiate into mature macrogametes, while male gametocytes undergo rapid transformation into eight haploid, flagellated microgametes (76–79). The latter are formed in a process of only 15 min, which involves three rounds of genome replication, resulting in a polyploid nucleus with eight genome copies, and the formation of eight axonemes in the cytoplasm (80, 81). During a process known as exflagellation, the parasitophorous vacuole membrane (PVM) and the erythrocyte membrane are lysed, releasing motile flagellated microgametes into the mosquito gut lumen (82). These microgametes actively swim in search for a macrogamete. Fertilization occurs when a microgamete successfully fuses with a macrogamete, forming a diploid zygote (78, 83, 84). Within the mosquito midgut, the round zygote elongates, initially forming into a retort and then maturing into a banana-shaped ookinete (85–87). This process, which takes approximately 21 hours, includes meiotic DNA-replication giving rise to a tetraploid ookinete (88) (reviewed in (89)). The motile ookinete traverses the single-cell-layered midgut epithelium and forms a sessile and encapsulated oocyst between the midgut epithelium and the basal lamina (reviewed in (90).

Within the oocysts, the parasite genomes are replicated thousands of times by endopolygeny, resulting in a multi-nucleated oocyst (91, 92). Depending on the *Plasmodium* species, sporogony takes approximately two weeks. During sporozoite budding, the parasite's plasma membrane invaginates, the nuclei align, and subsequently haploid sporozoites elongate from the sporoblast (93–95). The motile sporozoites are then released into the mosquito's haemolymph, where they are passively transported (96). Eventually, sporozoites reach and invade the mosquito's salivary glands (97–99) (reviewed in (40)). From there, the sporozoites are primed for transmission to a new vertebrate host when the infected mosquito takes its next blood meal.

1.2.2 The cytoskeleton of *Plasmodium* and gliding motility

Plasmodium spp. belong to the alveolate family, which is characterized by the presence of a pellicle – a specialized structural feature surrounding the parasite (100). The pellicle comprises flattened vesicles, known as alveoli, and the parasite plasma membrane (PM) (**Figure 2A**) (101). These alveoli, also referred to as the inner membrane complex (IMC), are formed *de novo* during cytokinesis and are present in the invasive stages of the parasite (sporozoites, merozoites and ookinetes), as well as in *P. falciparum* gametocytes (102–104) (**Figure 1**). Depending on the developmental stage, the IMC structure varies: in sporozoites, it consists of a single large flattened vesicle joined by a single suture, whereas in *P. falciparum* gametocytes, it is composed of multiple IMC plates connected by multiple sutures (104–109). The IMC extends along the entire length of the cell, except for small terminal regions at either end of the parasite, called the apical polar ring and the basal polar ring, respectively.

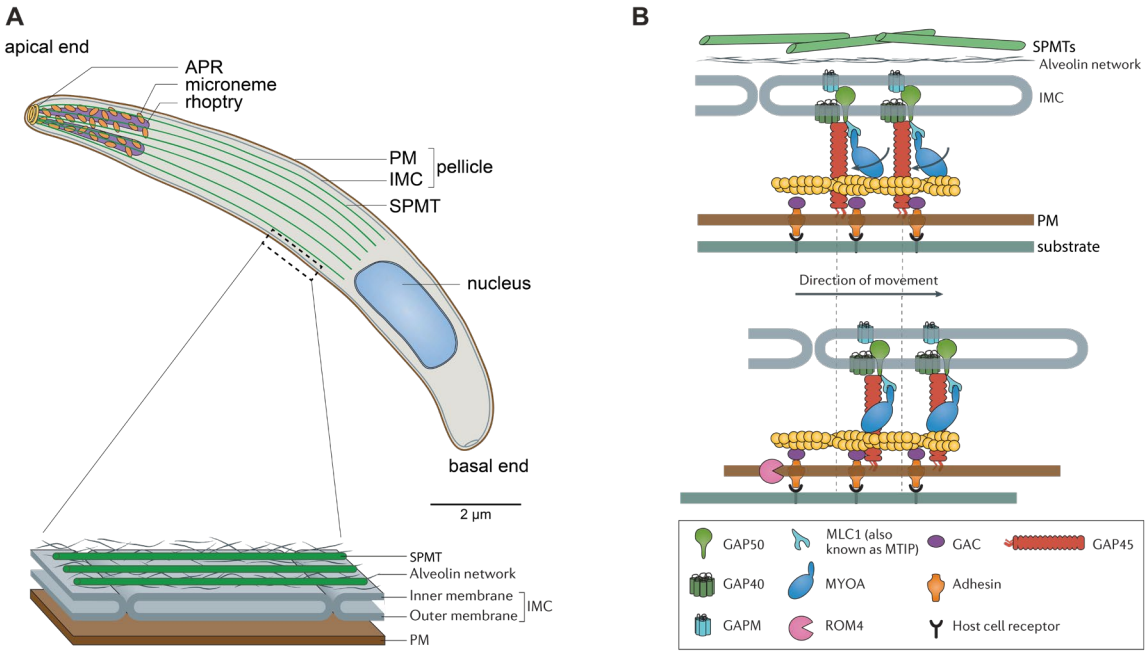

Figure 2 Cytoskeleton and glideosome of *Plasmodium*. *Plasmodium* sporozoite and its organelles. The pellicle, comprising the PM and IMC (highlighted by the dashed box, zoom-in below), is supported by a network of intermediate-filament like proteins, called alveolins, bridge the space between SPMTs and IMC. Note: while the IMC in *P. falciparum* gametocytes consists of several IMC vesicles interspersed by sutures, the IMC in *P. berghei* sporozoites is a continuous membrane-sac, which is not accurately depicted here. Figure modified from (110). **B)** Molecular setup of the glideosome. The glideosome is powered by an actin-myosin complex that consists of myosin (composed of myosin A and myosin-light chain 1) and filamentous actin (yellow). While myosin is anchored via GAPs into the IMC, adhesins span the PM and thereby connect actin to the PM and mediate attachment to the surface necessary for gliding. ATP-hydrolysis triggers the conformational change of myosin whereupon actin is pulled towards the rear-end, which results in the forward movement of the parasite. Figure adapted from (110, 111). APR – apical polar ring, GAC – glideosome-associated connector, GAP – glideosome associated protein, GAPM – glideosome associated protein with multiple membrane spans, IMC – inner membrane complex, MLC1 – myosin light chain 1, PM – plasma membrane, ROM – rhomboid-like protease, SPMT – subpellicular microtubule.

Located underneath the IMC, the subpellicular microtubules (SPMTs) are positioned at a defined distance from the IMC and play a critical role in maintaining cellular stability (112–114). Additionally, the SPMTs anchor secretory organelles, including rhoptries and micronemes, which are hallmarks of Apicomplexan parasites (115). During cell formation, the IMC develops in concert with the alveolin network, a network of proteins forming a fine mesh underneath the cytosolic side of the IMC (101, 116). IMC formation is paralleled by the outgrowth of SPMTs, the latter facilitating cellular elongation (117). Disruption of the IMC-SPMT integrity during this process results in misshaped or underdeveloped parasites (114, 118–120).

Apicomplexans, including *Plasmodium* spp., exhibit a unique form of locomotion known as gliding motility (reviewed in (121)). This substrate-dependent mechanism does not involve cilia or flagella and occurs without changes in cell shape (122, 123). Gliding motility is mediated by the glideosome, a specialized molecular machinery localized within the confined space between the parasite PM and the IMC (**Figure 2B**) (124). The glideosome operates via an actomyosin motor complex composed of four key elements: short actin filaments serving as the core structural element, myosin generating force, adhesins facilitating substrate attachment, and glideosome-associated proteins (GAPs) that anchor the machinery (121) (reviewed in (125)). Myosin is tethered to the inner leaflet of the IMC via GAPs, while filamentous actin connects to the PM through adhesins, the latter mediating attachment to the substrate necessary for gliding motility (126, 127). During gliding, secretory vesicles called micronemes are transported along the SPMTs towards the apical end of the parasite, where their contents, including adhesins, are channelled through the apical polar ring (APR) and released into the extracellular space or onto the plasma membrane (128, 129). The adhesins integrated into the PM, serve as ligands that bind to host cell receptors (130). During gliding, myosin motors drive the retrograde flow of filamentous actin and associated adhesins towards the posterior end of the parasite, resulting in forward movement (131, 132). At the rear end, the actin-adhesin connections are cleaved by rhomboid proteases and adhesins are shed within membrane trails, enabling continuous gliding (133–137). Using gliding motility, sporozoites, one of the invasive stages of *Plasmodium*, achieve the highest gliding speeds among parasite stages, reaching 1–2 µm/s (34, 138, 139). This speed is approximately ten times faster than the speed of a neutrophil chasing it within the human body (140).

1.3 Microtubules

1.3.1 Microtubule structure and dynamics

As described in the previous chapter, SPMTs are of fundamental importance to parasite shape and motility. Microtubules, including SPMTs, are conserved across all eukaryotes (141). Together with actin and intermediate filaments, they are part of the cytoskeleton (141). Microtubules are very versatile and facilitate a wide range of cellular processes. Microtubules provide essential tracks for intracellular cargo transport, establish cell shape and polarity, mediate chromosome segregation during mitosis via spindle microtubules, and drive the motility of cilia and flagella through axonemal microtubules (reviewed in (142)).

Microtubules are composed up of α- and β-tubulin that form into heterodimers that further assemble into linear protofilaments (**Figure 3**) (141). Typically, 13 protofilaments build up the hollow microtubule cylinder that has a diameter of 25 nm (reviewed in (141, 143)). Microtubules are inherently polar: The minus end, at which α -tubulin is exposed, is also called the slow-growing end (reviewed in (144)). *In vivo*, the minus end is anchored into a microtubule organizing center (MTOC), protecting it from depolymerization (reviewed in (145)). Consequently, tubulin heterodimer addition primarily occurs at the plus end, where β-tubulin is exposed (146). *In vitro*, however, incorporation can occur at both ends (145). Tubulin polymerization is driven by GTP hydrolysis. Both α- and β-tubulin can bind GTP, but only β-tubulin can hydrolyse guanosine triphosphate (GTP) to guanosine diphosphate (GDP) and phosphate (147, 148)(reviewed in (149).

Following incorporation of a GTP-bound heterodimer, there is a short delay in GTP hydrolysis which results in the formation of a so-called GTP cap (150). The GTP cap has a stabilizing effect as it promotes continued microtubule growth by accelerating polymerization over depolymerization(142, 150). Microtubule nucleation *in vivo* is facilitated by γ-tubulin, which is a component of the γ-tubulin ring complex (γ-TuRC) located within the MTOC ((151) (reviewed in (152, 153)). Additionally, augmin complexes enhance microtubule nucleation on the lateral surfaces of existing microtubules, thereby enabling microtubule branching (reviewed in (154)).

Microtubules are inherently dynamic polymers that stochastically alternate between phases of growth and shrinkage, a phenomenon termed dynamic instability (150). Since the minus end is anchored within the MTOC, these transitions predominantly occur at the plus end. Two distinct transitions are observed: a shift from growth to shrinkage, known as a catastrophe, and a recovery from shrinkage to growth, termed a rescue event (142). This dynamic turnover, regulated by microtubule-associated proteins (MAPs), allows microtubules to rapidly adapt to environmental changes, thereby playing a critical role in cellular physiology (reviewed in (143, 146, 149, 155)).

Microtubule dynamics are susceptible to modulation by small molecules, many of which are used in cancer chemotherapy due to their effects on spindle microtubules during cell division (reviewed in (156–158). Owing to the inherent flexibility of the microtubule lattice, drugs can interact with microtubules both at the outer surface but also access the microtubule lumen laterally. Microtubule-targeting agents are broadly classified as stabilizers or destabilizers. Microtubule-stabilizing agents, such as taxanes, bind to β-tubulin and stabilize GDP-tubulin within the microtubule lumen, preventing depolymerization and thereby interfering with normal microtubule dynamics (159). In the case of spindle microtubules, this stabilization disrupts cell division, making taxanes widely used in the treatment of various cancers (reviewed in (157)). Among taxanes, paclitaxel (taxol) is the most prominent example, serving as both a therapeutic agent and the basis for the fluorescent microtubule live-imaging dye SiR-tubulin (160). In contrast, microtubule-destabilizing agents inhibit polymerization or promote depolymerization (161). For instance, colchicine and its analogues bind at the interface of tubulin monomers, while vinca-domain ligands interact at the junctions between tubulin heterodimers. Beyond chemical compounds, microtubules are also sensitive to environmental factors, such as temperature, with cold exposure shown to destabilize microtubules (162–164)(reviewed in (143).

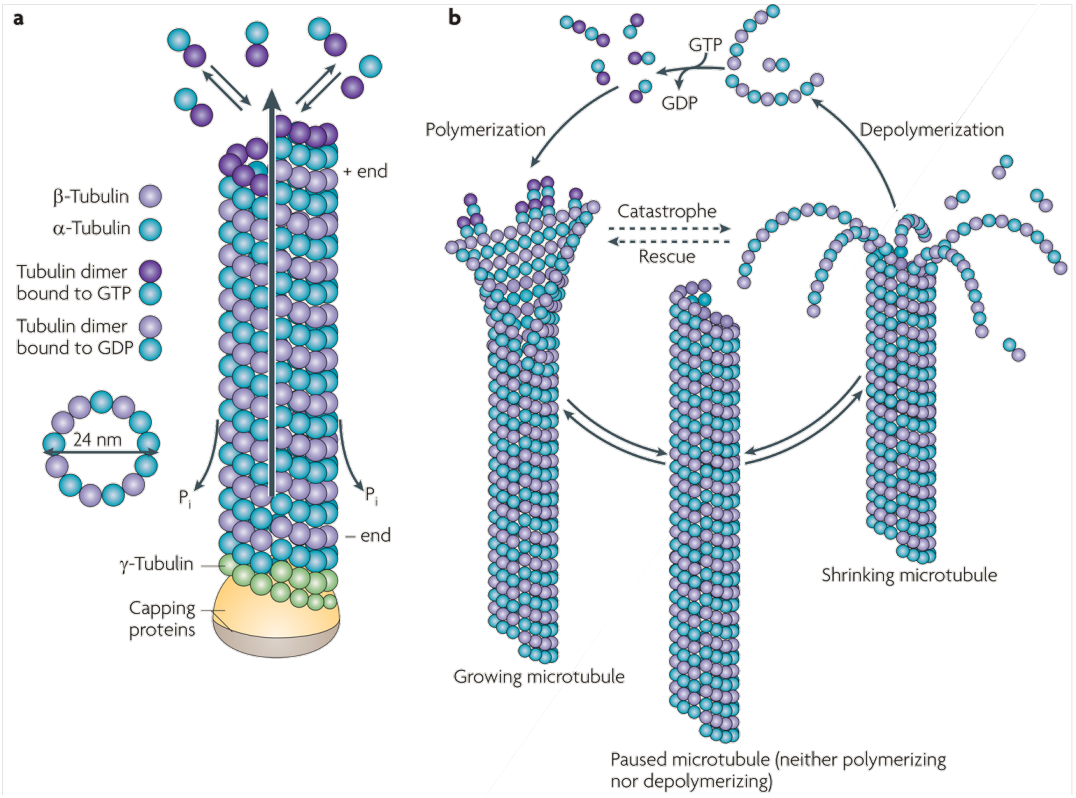

Figure 3 Microtubules are dynamic cytoskeletal structures. Microtubules are made up of α- and β-tubulin that form into heterodimers. GTP-bound heterodimers are added to the plus end, forming a stabilizing GTP-cap. Polymerization (microtubule growth) and depolymerization (microtubule shrinking) constantly happen at the plus end as the minus end is protected by γ-tubulin that is part of the γ-TuRC. Figure from (165).

1.3.2 Microtubule regulation and the tubulin code

Despite being composed of the same fundamental building blocks across nearly all species, microtubules exhibit remarkable functional diversity tailored to specific cellular contexts and organisms. This functional diversity is mediated by the tubulin code, a concept first introduced as the "multi-tubulin hypothesis" in 1976 (166). The tubulin code describes how molecular patterns arise from a combination of tubulin isotypes, post translational modifications (PTMs), and the binding of MAPs that contribute to the unique microtubule functions.

While microtubules are globally composed of α- and β-tubulin heterodimers, the number of tubulin isotypes varies between species. For instance, yeast and *Plasmodium* encode only two α-tubulin and one β-tubulin isotype, whereas humans encode nine α- and nine β-tubulins (167). The isotype composition influences microtubule properties such as dynamic instability, providing an additional layer of functional regulation.

The carboxy-tails of α- and β-tubulin are composed of several acidic residues. As the stick out of the microtubule tube, they render the surface of microtubules negatively charged (reviewed in (168)). These carboxy-tails are subject to various PTMs (reviewed in (169)). PTMs create chemical marks along the microtubule lattice thereby generating distinct patterns that modulate microtubule function and serve as docking sites for MAPs. Common PTMs include phosphorylation, methylation, palmitoylation, ubiquitylation, polyamination, and polyglutamylation, all of which add specific residues to tubulin's carboxy-tails. In contrast, detyrosination removes the carboxy-terminal tyrosine (reviewed in (169)). In addition, a lysine residue within the microtubule lumen is subject to acetylation (reviewed in (170)). Importantly, the type and length of PTMs additionally influence MAP binding. For example, kinesin-2 is recruited by the addition of three or ten glutamate residues, whereas kinesin-1 specifically binds to sites marked by ten glutamates (171). Most enzymes involved in PTM regulation preferentially bind polymerized tubulin, with exceptions like deglutamylase, which can interact with both monomeric and polymerized tubulin, and tubulin-tyrosine ligase, which specifically binds to tubulin dimers for tyrosination (172). PTMs primarily function to recruit MAPs, thereby altering microtubule identity. They can also impact microtubule architecture, such as protofilament number. For instance, in *Caenorhabditis elegans* touch receptor neurons, microtubules are uniquely composed of 15 protofilaments, in contrast to the conventional 13-protofilament structure (173). This specialization is mediated by the acetyltransferase MEC-17, and loss of MEC-17 leads to microtubules with reduced protofilament numbers (174, 175).

A core principle of the tubulin code is the selective recruitment of MAPs to specific microtubules. MAPs are classified based on their activity and localization. Stabilizing MAPs enhance microtubule stability or reduce destabilization, whereas destabilizing MAPs increase the pool of free tubulin

subunits by preventing their incorporation into growing filaments or by actively depolymerizing microtubules via adenosin-triphosphate (ATP)-dependent mechanisms (176–179)(reviewed in (143)). Capping MAPs bind to microtubule ends, modulating the association of tubulin heterodimers. A notable example is the γ-TuRC, a multi-protein complex that caps the minus end, protecting it from depolymerization while also acting as a nucleator to promote microtubule growth (152). Motor proteins like kinesin and dynein use ATP to traverse microtubules and as a result facilitate processes such as organelle transport and spindle dynamics (reviewed in (180, 181)). Additional MAP categories include cytoskeletal integrators, which connect microtubules to actin or intermediate filaments; membrane linkers, which tether microtubules to cellular membranes; and bundlers or cross-linkers, which laterally associate microtubules, as observed in the mitotic spindle (reviewed in (143). MAPs are also classified by their binding sites on microtubules. Lattice-binding MAPs interact along the microtubule lattice but are excluded from the tips, whereas end-targeting MAPs specifically localize to either the plus or minus end (reviewed in (143). A distinct subgroup, microtubule-inner proteins (MIPs), binds to the luminal side of microtubules (182, 183, 192–200, 184–191)(further reviewed in (201)). They have been initially identified by conventional transmission electron microscopy (TEM) of neuronal microtubules of different species and later also found as protein density within axonemal microtubules of *Chlamydomona*s using cryo-electron tomography (183, 202–205). Almost all MIPs have been identified within axonemes of cilia and flagella (183, 184, 193–195, 201, 185–192). While the axoneme of *Chlamydomonas* is filled with 33 MIPs compared to 42 MIPs in *Tetrahymena*; the highest number of MIPs has been observed within axonemes of mammalian sperm with 57 MIPs (194, 195, 198, 206). In the absence of MIPs, flagellar and ciliar beating has been shown to be impaired (184, 194, 195). Among MIPs, α-tubulin acetyltransferase 1 (αTAT1) is well-characterized, catalysing the acetylation of lysine 40 (K40) on α-tubulin and thereby combining two characteristics of the tubulin code (reviewed in (170)). K40 acetylation has been associated with stable microtubules and mechanosensation in *Caenorhabditis elegans* and loss of αTAT1 resulted result in reduced sperm activity and male fertility in mice (174, 207–209).

In summary, the unique functions of microtubules are defined by the interplay of tubulin isotypes, PTMs, and MAP binding, collectively contributing to cellular specialization. Disruption of any component of this system can imbalance cellular homeostasis and, in severe cases, lead to disease.

1.3.3 Microtubule subsets in *Plasmodium*

In *Plasmodium*, three different types of microtubules can be found that serve specialized roles: Spindle microtubules separate chromosomes during replication, axonemal microtubules drive the flagellar motility of male gametes and SPMTs provide structural support and shape to the parasite (reviewed in (125, 210)). Despite being composed of the same tubulin subunits, these microtubule types perform unique functions within the parasite.

Similar to other eukaryotic organisms, *Plasmodium* mitotic spindle microtubules are involved in genome separation during replication. Mitotic spindle microtubules of *Plasmodium* are nucleated from an electron-dense, amorphous protein structure that is embedded in the nuclear envelope (211, 212). This acentriolar MTOC, as the name indicates, does not contain centrioles and thus differs from classical centrosomes (211). Different to many other eukaryotic systems, chromosomes of apicomplexan parasites do not condense prior to separation and parasites divide by closed mitosis, a process in which DNA replication and nuclear division proceeds without nuclear membrane breakdown (52).

Axonemal microtubules are exclusively found in the male gamete, where they drive the flagellar motility of the parasite (81). These structures play a critical role during microgamete formation, a rapid and highly dynamic process of the parasite's life cycle that is completed within 10-15 min only. At this stage, axonemes and spindle microtubules are simultaneously formed from a bipartite MTOC (80): Axonemes are nucleated from the basal body, located in the outer, cytosolic part of the centrosome, in a process indirectly mediated by SAS4 and SAS6 (80, 213). Meanwhile, spindle microtubules are nucleated from the inner part of the acentriolar MTOC. *Plasmodium* axonemes exhibit the classical "9+2" arrangement conserved across eukaryotes, consisting of nine outer doublets and two inner singlets (77, 183, 214). Each axonemal doublets consist of a 13-protofilament A-tubule connected to a 10-protofilament B-tubule, which together surround the two inner singlets. Following their assembly, axonemes begin beating. This movement exerts force on the nuclear membrane through their connection to the centrosome, thereby pulling a genome copy out of the nucleoplasm and eight flagellated gametes exit the parent cell (215) (reviewed in (216). While *Plasmodium* was long thought to lack an actin-related protein 2/3 complex, a recent study has identified its subunits and implicated it in genome segregation during microgamete exflagellation (217).

SPMTs are characteristic for the invasive stages of the parasite and hence found in merozoites, ookinetes and sporozoites (**Figure 3**, stages highlighted in light blue; **Figure 4**). In these stages, SPMTs are nucleated from the apical polar ring (APR) that functions as MTOC and are positioned just underneath the IMC (see 1.2.2) (112, 118, 218). While the number of SPMTs varies among these stages, their arrangement and orientation are fixed within a parasite stage. Merozoites

possess the smallest number of SPMTs, with 3–4 in *P. falciparum* (also termed f-mast, (219)) and up to 9 in *P. berghei* (112, 220, 221). Ookinetes, with 50-60 evenly spaced SPMTs (dependent on the species), have the highest number of SPMTs (220, 222). In *P. berghei* sporozoites, SPMTs are asymmetrically arranged, with one SPMT directly opposing the other 15 (113, 128) (in *P. falciparum* this arrangement is also asymmetric but they usually possess only 14 SPMTs (112)).

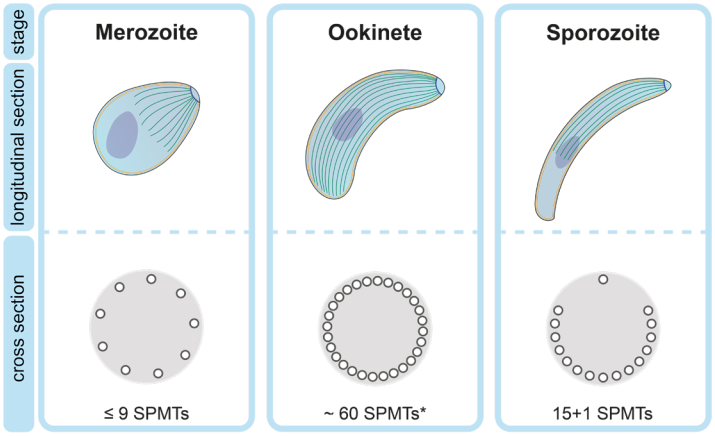

Figure 4 Different stages of *P. berghei* possess different numbers and arrangements of SPMTs. Merozoites possess only 9 SPMTs which cover around half the length of the parasite. Ookinete possess ~ 60 equally spaced SPMTs that cover the full cell length. Sporozoites have 16 SPMTs that cover around 2/3 of the parasite length and are arranged in a 15+1 orientation with one single SPMT being opposite of the other 15. SPMTs are shown in green, nucleus in purple, apical polar ring in blue, IMC in orange. *To allow for better visibility, not all SPMTs in the ookinete are shown. This figure was previously published and adapted for this thesis (57). SPMTs – subpellicular microtubules.

This configuration is thought to establish the dorso-ventral polarity of sporozoites, influencing APR orientation and ensuring directed adhesin secretion during gliding motility (128). SPMTs also play a crucial role in the elongated, falciform gametocytes of *P. falciparum*, where they mediate cell elongation and maturation (67, 103). Similar gametocyte elongation is observed in *P. reichenowi* and *P. gaboni*, other members of the Laveranian clade, though direct evidence for SPMTs in these species remains limited (66, 223). Unlike the invasive stages, SPMTs in *P. falciparum* gametocytes are nucleated from an APR but from the cytosolic part of the bipartite MTOC, which also coordinates IMC development (224). Notably, gametocyte SPMTs exhibit variable protofilament numbers ranging from 13 to 18, whereas invasive-stage SPMTs in *P. berghei* adopt the classical 13-protofilament structure (112). Interestingly, though gametocytes of *P. berghei* stay round during gametocytogenesis and do not possess SPMTs, they still possess a discontinuous IMC (66). SPMTs in both the invasive stages and gametocytes of *P. falciparum* share a common function in driving elongation during parasite development or maturation, contributing to cell shape. Compared to microtubules in other organisms, SPMTs are remarkably stable against drug- or cold-treatment (225–228). Alterations in SPMT number however, caused by modulated α-tubulin expression, or changes in SPMT length, impact parasite viability (113).

The authors showed that sporozoites require at least ten SPMTs to form fully infectious and viable parasites (113). Complete absence of α1-tubulin resulted in developmental arrest and parasites failed to form sporozoites, showing that α1-tubulin is essential for SPMT formation and thus sporozoite development. The α1-tubulin knockout (KO) mutant could be partially complemented with α2-tubulin though SPMTs appeared shorter resulting in a reduced parasite infectivity (113). Furthermore, proper anchorage of SPMTs to the IMC is essential for parasite development. KO studies targeting proteins that link SPMTs to the IMC in the ookinete stage resulted in detachment of SPMTs, severely impairing parasite maturation into banana-shaped ookinetes (114, 118, 119). These findings underscore the critical roles of SPMT number, length, and integrity in parasite viability and infectivity.

1.3.4 Microtubule-associated proteins in Apicomplexa

Spindle microtubules, axonemal microtubules and SPMTs represent highly specialized microtubule subtypes that contribute to the unique cellular architecture and parasitic life cycle. Among the key factors regulating those microtubule subtypes are MAPs. Some MAPs, like kinesins, perform conserved functions similar to those observed in model organisms while others are unique to Apicomplexa.

Kinesins are ATP-dependent microtubule-based motors that drive crucial cellular processes, including cell division, intracellular transport, and motility (180). The *Plasmodium* genome encodes nine kinesins, whose roles have only recently been investigated on a genome-wide scale (229). For instance, kinesin-13, which colocalizes with kinetochores across multiple proliferative stages, is essential for axoneme formation in male gametogenesis, and its disruption prevents parasite transmission. Similarly, kinesin-8B also facilitates male gamete formation, with its absence impairing axoneme formation and nuclear segregation (213, 230, 231). Another conserved MAP is γ-tubulin, which has been long known for its role in microtubule nucleation (152, 153). However, the role of γ-tubulin in apicomplexans has only recently been revealed in *Toxoplasma gondii* (*T. gondii*) and *Cryptosporidium parvum* where it has been shown that it shares conserved functionality with other eukaryotes by nucleating spindle microtubules (232). However, beyond γ-tubulin, the composition of the γ-TuRC in these parasites remains largely uncharacterized. The plus end-binding protein 1 (EB1), another conserved MAP, has diverged functionally in *Plasmodium*. Unlike canonical EB1 in model organisms, which tracks microtubule plus ends, *Plasmodium* EB1 binds along the entire microtubule lattice (233). Despite this difference, it retained an essential role in mediating the connection between kinetochores and spindle microtubules, ensuring proper nuclear segregation during male gametogenesis (233, 234). In *Plasmodium* axonemes, only two MIPs have been identified, which were shown to be functionally conserved compared to other organisms. The combined deletion of flagellar

associated proteins 20 and 52 resulted in partial detachment of the B-tubule from the A-tubule and thus phenocopied the defect observed in similar mutants of *Tetrahymena* and *Chlamydomonas* (185, 186, 195).

SPMTs, which are critical for maintaining cell shape and stability in various life cycle stages, are also decorated with MAPs. Early electron microscopy studies in the 1990s revealed particles that decorated SPMTs in *T. gondii*, suggesting MAP involvement, though the identities of these particles remained elusive for years (225). Later, cryo-tomographic analyses of *Plasmodium* sporozoites identified a protein density at a constant 32 nm periodicity along SPMTs, indicating the presence of one or more MAPs linking SPMTs to the IMC (115). Only recently, several IMC-SPMT linking MAPs were identified, including apical polar ring protein 2 (APR2), which anchors SPMTs to the apical polar ring. Parasites lacking APR2 exhibited structural defects, including straightened rather than crescent-shaped ookinetes, leading to failure in mosquito midgut infection (118). In addition, APR2 (together with Kinesin A) determines apical polarity in *T. gondii* (235). Another MAP, DHHC2 (named based on its catalytic signature of aspartate-histidine-histidine-cysteine) stabilizes distal SPMTs by palmitoylating IMC-subcompartment proteins ISP1 and ISP3, linking SPMTs to the IMC (114).

In *T. gondii*, additional MAPs such as subpellicular microtubule protein 1 (SPM1) and thioredoxin-like proteins (TrxL1 and TrxL2) have been shown to bind the luminal side of SPMTs, contributing to their stability (**Figure 5 A**) (236–239). SPM1 and TrxL1 are classified as MIPs that are exclusively found in apicomplexans (and the closely-related *Chromerida*)(238). TrxL1-associated proteins (TLAPs) further localize to distinct regions of SPMTs (238). Intriguingly, TLAP2 and TLAP3, alongside with SPM1, regulate the parasite's chirality. Parasites lacking these proteins shift from helical to linear motility paths but retain the ability to invade host cells and egress from them (240). Additionally, these proteins appear to protect SPMTs against cold stress, as their absence leads to SPMT depolymerization in *T. gondii* upon cold exposure. Despite these advances in understanding MAP-mediated SPMT stability in *T. gondii*, the molecular mechanisms that confer the remarkable stability of SPMTs in *Plasmodium* remain poorly understood. A recent study demonstrated that two of the three MIPs identified in *T. gondii* – SPM1 and TrxL1 – are conserved in *Plasmodium* and exhibit similar binding patterns to the microtubule lumen (**Figure 5 B**). However, their precise roles for the parasite remains unknown.

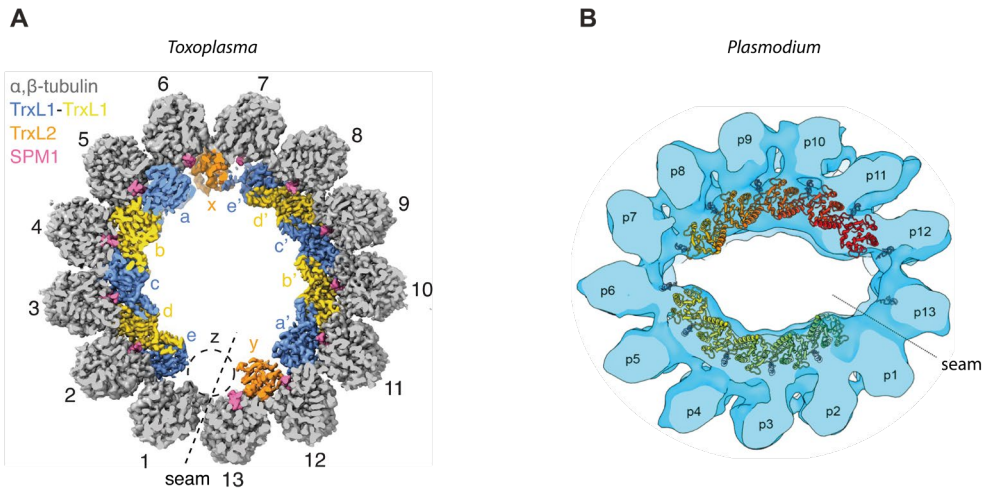

Figure 5 SPMTs are decorated by MIPs that bind to the microtubule lumen. A, B) Cross-view of the cryo-EM structures of A) *Toxoplasma* and B) *Plasmodium* SPMTs. Three MIPs, namely SPM1, TrxL1 and TrxL2 bind to the lumen of SPMT of *Toxoplasma*, from which two are conserved in *Plasmodium* (SPM1, TrxL1). Ten copies each of SPM1 (blue) and TrxL1 (different shades of green, red) form into two-half crescents within the SPMT lumen, while only two copies of TrxL2 bind to opposite sites within the microtubule lumen. Numbers 1-13/p1-p13 indicate protofilaments. Figure modified from (112, 228).

While MAPs in model eukaryotic systems are well-characterized, research on MAPs in apicomplexans is still in its early stages. Nevertheless, recent studies began to unravel their critical roles, particularly in stabilizing the unique SPMT architecture that is essential for parasite survival, motility and transmission.

2. Aim of the thesis

In apicomplexan parasites, SPMTs exhibit a remarkable degree of stability compared to microtubules of other species. These properties are critical for maintaining proper cell morphology, which is essential for successful gliding motility and host cell invasion. Additionally, SPMTs mediate the shape changes that go along with cell formation and maturation, a necessary adaptation to the distinct environments of both the mosquito vector and the mammalian host. Although previous research has demonstrated how tubulin expression levels and slight changes in tubulin isotypes affect the number and length of SPMTs, thereby influencing parasite viability and infectivity (113), the molecular determinants underlying the extraordinary stability of SPMTs in *Plasmodium* remain unresolved.

The objective of my PhD research was to elucidate the role of MAPs contributing to the exceptional stability and functionality of *Plasmodium* SPMTs. Specifically, I focused on characterizing two MIPs, SPM1 and TrxL1, whose roles have been previously studied in the related parasite *T. gondii* but remain uncharacterized in *Plasmodium*. To this end, I aimed to individually and combinatorically delete the genes encoding these proteins and assess their impact on parasite development and infectivity. In parallel, I aimed to study MIP localisation and the hierarchy of MIP binding to MTs by generating GFP-tagged fluorescent lines in both WT and the complementary KO backgrounds. These experiments were designed to investigate the interdependencies of these proteins in the invasive stages of parasite development within mosquitoes. Furthermore, I aimed to combine MIP deletion with the deletion of a potentially outer MAP, SPM2, to investigate the interdependencies between MIPs and outer MAP.

Additionally, I sought to explore the functional role of a putative outer MAP, SPM3, in *P. berghei*. While deletion of *spm3* in *P. falciparum* was shown to disrupt SPMT organization and cause developmental arrest during gametocytogenesis, its role in mosquito stages remained unclear. My aim was to investigate the importance of SPM3 for *P. berghei* development and compare its function to that in *P. falciparum*.

To enable high-throughput ultrastructural analysis of SPMT integrity beyond the current limitations of cryo-tomography, I aimed to establish ultrastructure expansion microscopy (U-ExM) in our laboratory. Using this method, I planned to assess changes in SPMT stability in response to the deletion of MIP or MAP genes, taking into account the parasite's cellular context.

Overall, I aimed to advance our current understanding of the structural integrity of *Plasmodium* SPMTs and the molecular mechanisms underlying their stability. With this, I aimed to shed light on their functional significance in parasite biology.

3. Results

3.1 Characterizing the role of two microtubule inner proteins for parasite development

[The results of part 3.1.1 with the exception of ookinete gliding motility were published in (57). Tagging mutants and the live localization of MIPs in salivary gland sporozoites described in 3.1.2 were published in (112) and their localization was analysed in more depth in this thesis. Figures and tables were adapted and modified when necessary and are indicated in the respective figure legend. Data that was obtained from collaborative work with others is indicated, and the respective people that contributed are mentioned at the end of each respective sub-chapter.]

Microtubule inner proteins (MIPs) are microtubule-associated proteins (MAPs) that bind to the microtubule lumen. Some apicomplexan-specific MIPs have been studied in the related parasite *T. gondii* but their function for *Plasmodium* has been elusive so far. As a first step towards understanding the function of two apicomplexan-specific MIPs in *Plasmodium*, namely SPM1 and TrxL1; I generated depletion mutants and characterized parasite life cycle progression.

3.1.1 Depletion of *spm1* and *trxL1* does not affect parasite life cycle progression.

To investigate the role of SPM1 and TrxL1 for parasite development, I generated the mutant parasite lines *spm1*(-) and *trxL1*(-) that lack the ORF of the respective genes. Both lines were generated via double homologous crossover recombination during which the respective ORF was replaced by a selection cassette (**Figure 6 A**). Following transfection and positive selection with pyrimethamine, I obtained six clones for the *spm1*(-) line and four clones for the *trxL1*(-) line (**Figure 7 A, B, Supplementary Figure 1 A, B**). The inserted selection cassette additionally harbours the gene for the bifunctional protein yeast cytosine deaminase and uridyl phosphoribosyl transferase (yfcu) which renders parasites sensitive to the drug 5-fluorocytosine (5-FC). If 5-FC is administered, yfcu converts 5-FC into its lethal analogue 5-fluorouracil (5-FU). As a result, only parasites that looped out the selection cassette by recombining the two flanking *3'dhfr* regions will survive. Negative selection allows to recycle the selection cassette and hence several gene deletions can be combined in a multi gene KO mutant (**Figure 6 B**) (241). Using this method, I first generated a marker-free line of the *trxL1*(-) mutant followed by knocking out *spm1*, resulting in the double depletion mutant *trxL1*(-)/*spm1*(-). A subsequent negative selection yielded the parasite line *trxL1*(-)/*spm1*(-)ns (**Figure 7 C, D, Supplementary Figure 1 C**). All three parasite lines grew normally in the blood and had asexual growth rates comparable to PbA WT (for simplicity, the PbANKA WT control line will hereafter be abbreviated as WT in the main text) (**Figure 7 E**).

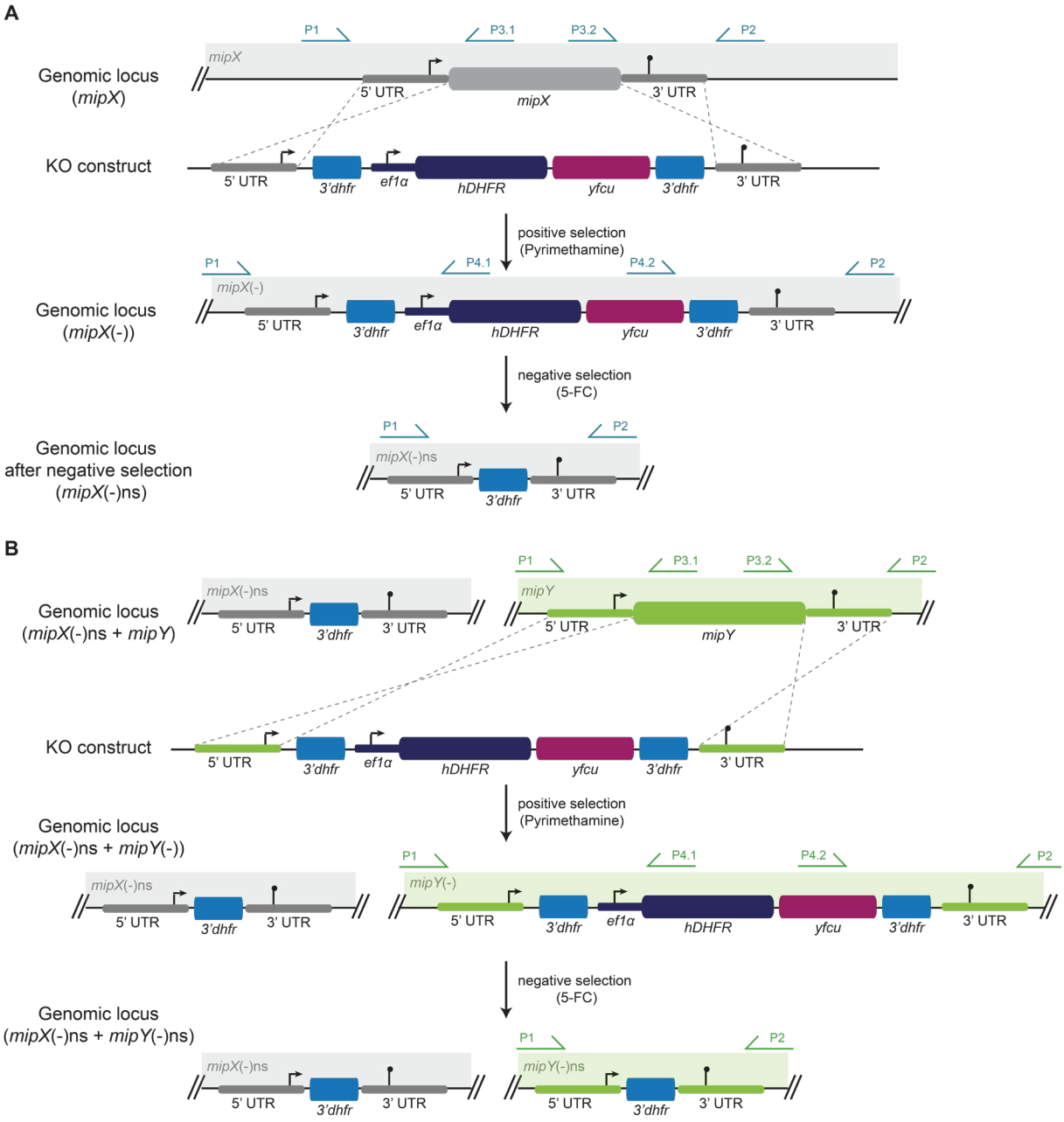

Figure 6 Genetic strategy of generating double KO parasite lines. The original genomic locus is shown on top with dotted lines indicating the double crossover events leading to insertion of the KO construct. This yields the intermediate parasite line that upon negative selection loops out the resistance cassette by excision across the two flanking *3'dhfr* regions (blue). **A)** Scheme of generation of single KO including negative selection. Primers used for genotyping of the initial gene (*mipX*) KO are indicated as blue arrows: whole locus (WL) PCR: P1 x P2, WT PCR: P1 x P3.1 or P3.2 x P2, KO PCR: P1 x P4.1 or P4.2 x P2. **B)** Scheme of generating double KO. Primers used for genotyping PCRs (*mipY*) are indicated as green arrows: WL PCR: P1 x P2, WT PCR: P1 x P3.1 or P3.2 x P2, KO PCR: P1 x P4.1 or P4.2 x P2. ef1α – human elongation factor-1 alpha, *hDHFR – human dihydrofolate reductase*, KO – knockout, *mipX/Y – microtubule inner protein X/Y*, ns – negative selected, UTR – untranslated region, *yfcu – yeast enzyme cytosine deaminase and uridyl phosphoribosyl transferase*. Schemes are not drawn to scale; primer positions are approximate. Figure and legend were previously published (57).

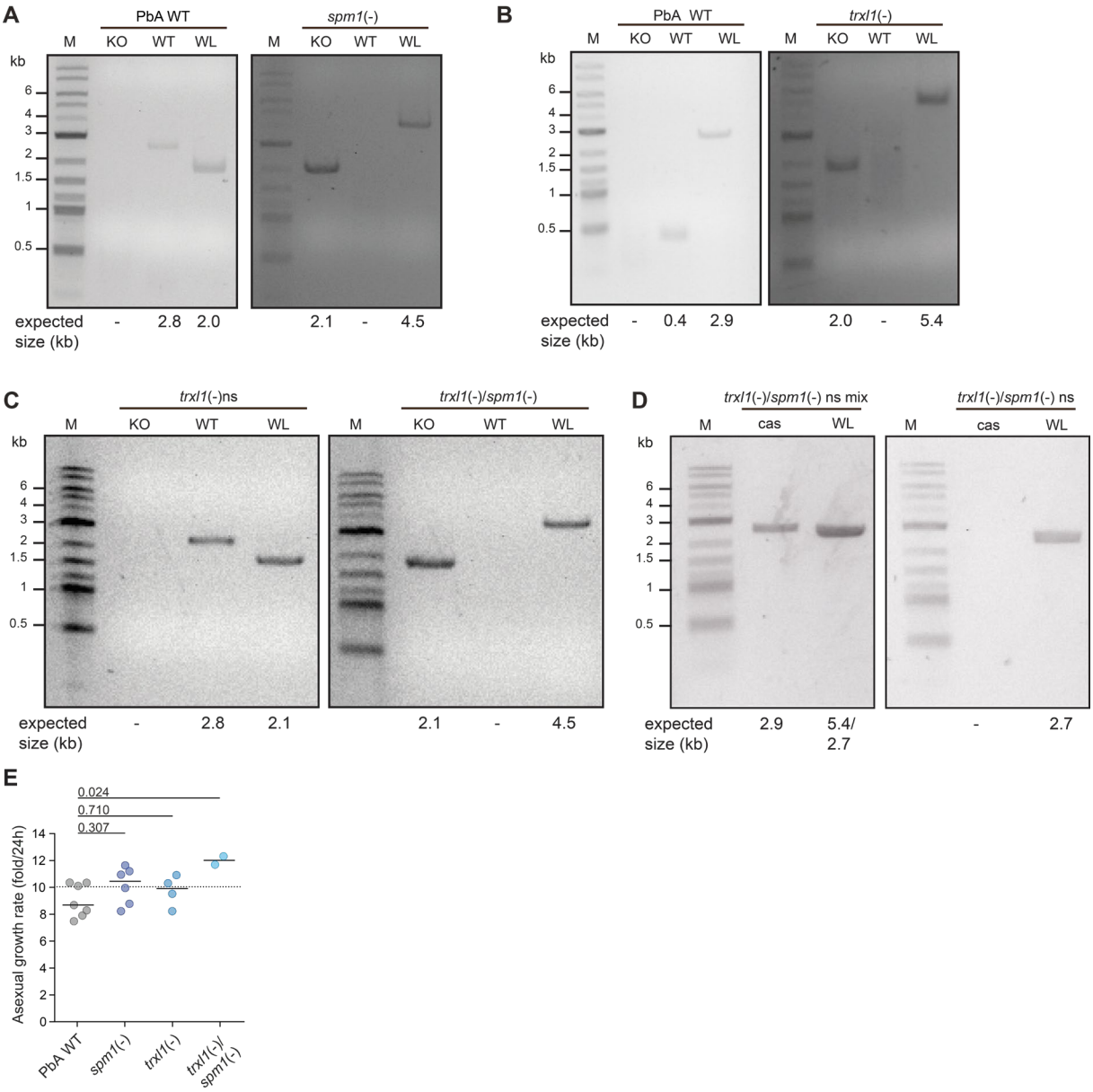

Figure 7 Generation of *spm1* and *trxL1* single and double KO parasite lines. Genotyping PCRs of **A)** *spm1*(-), **B)** *trxL1*(-), **C)** *trxL1*(-)/*spm1*(-) and **D)** *trxL1*(-)/*spm1*(-) ns. Primers used for genotyping PCRs are indicated in (**Figure 6**). Double crossover events leading to the insertion of the KO construct will result in an increased size of the whole locus (WL) PCR fragment. Negative selection loops out the resistance cassette and hence KO primers only result in a PCR fragment in KO parasites which have not yet been negatively selected. **E)** Asexual blood stage growth rate as calculated after injecting mice with one infected red blood cell (iRBC) intravenously. PbANKA WT (PbA WT) growth rates determined and previously published by our laboratory (139, 242, 243) are plotted as reference. Each dot represents growth rate derived from one mouse. Line indicates median. Statistical analysis using Dunnett's multiple comparison test. Kb – kilobase, KO – knockout, M – marker, ns – negatively selected, WL – whole locus, PbA WT – wildtype. Figure and legend were previously published and adapted for this thesis (57).

Next, I assessed whether the single or the combined depletion of both genes would affect ookinete development or SPMT stability and organization in mature ookinetes. Upon developing, SPMTs will start forming within the premature ookinete (also called retort), which subsequently develops into the mature, banana-shaped ookinete (244). Hence, SPMTs during the ookinete stage are required for both the initial ookinete formation and to provide cell rigidity necessary for ookinete motility. To assess ookinete development, *in vitro* ookinete cultures were set up and ookinete motility was examined in 2D performing *in vitro* gliding assays. All three mutant parasite lines developed mature ookinetes and had around 50-60% moving ookinetes in the whole population (**Figure 8 A**). In addition, ookinetes of all mutant lines moved at comparable speeds, indicating no role for these MIPs in ookinete maturation or gliding (**Figure 8 B**). Even though statistical testing resulted in significant differences in gliding proportions between WT and *spm1*(-) and *trxL1*(-)/*spm1*(-)ns ookinetes as well as a significant differences in speed between WT and *spm1*(-) and *trxL1*(-) parasites, they are presumably not of biological relevance as ookinetes from all mutants were fully infective and colonized mosquito midguts (**Figure 9 A**).

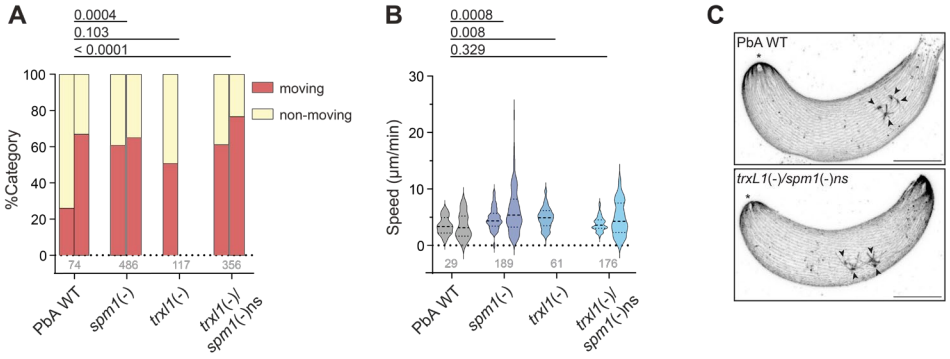

Figure 8 Both *spm1*(-) and *trxL1*(-) form motile ookinetes that possess properly formed SPMTs. A) Gliding motility patterns of mature ookinetes. Each bar represents an independent replicate. Statistics: multiple Fisher's exact tests comparing moving versus non-moving ookinetes, adjusted for multiple testing according to Bonferroni-Holm. Grey numbers show total number of ookinetes analysed per parasite line, individual ookinetes per replicate: PbA WT: 46/28, *spm1*(-): 256/230, *trxL1*(-): 117/0, *trxL1*(-)/*spm1*(-)ns: 243/113. **B)** Median speed of moving ookinetes. Kruskal-Wallis with Dunn's multiple comparisons test. Grey numbers indicate total number of ookinetes analysed per parasite line, individual numbers per replicate: PbA WT: 12/17, *spm1*(-): 90/99, *trxL1*(-): 61/0, *trxL1*(-)/*spm1*(-)ns: 90/86. **C)** U-ExM of ookinetes stained for tubulin. Note that the anti-tubulin staining stains for both subpellicular and spindle microtubules (highlighted with black arrowheads). The apical end is indicated with an asterisk. Scale bar: 10 µm. Figure panel C was previously published in (57).

To determine whether the two MIPs play a role in ensuring SPMT integrity, ultrastructure expansion microscopy (U-ExM) was employed. In this technique, cells are embedded in a swellable gel that expands along with the cells when salt-free water is added. After expansion, an antibody staining is carried out, similar to a standard IFA. Expanded ookinetes were stained with an anti-tubulin antibody that allowed to visualize both SPMTs and spindle microtubules. Ookinetes possess around 60 SPMTs which are evenly spaced towards each other and run from

the apical end all the way to the distal end of the cell (**Figure 4**). As depicted in **Figure 8 C**, SPMTs in both WT and mutant ookinetes were evenly distributed and covered the full cell length.

To check whether the mutant parasite lines can infect *Anopheles stephensi* mosquitos and develop into the different stages, naïve mosquitos were allowed to bite on infected mice. Following infection, the infection rate and the presence of oocysts in mosquito midguts were determined on two separate days between day 10 and day 12 post infection. While infection rates of all four lines were comparable to WT, the three mutants had even slightly higher oocyst counts per infected midgut than WT (**Figure 9 A**). Sporozoites develop within maturing oocysts and eventually emerge to invade the salivary glands. To assess the ability of MIP mutants to form sporozoites, the numbers of sporozoites in both tissues were determined on two separate days and compared to each other. All three mutants developed into sporozoites, which successfully invaded salivary glands, as indicated by a WT-like salivary/midgut sporozoite ratio between 0.4 to 0.6 (**Figure 9B**).

To invade salivary glands and later also hepatocytes, sporozoites need to be motile. Interference with the cytoskeleton often impairs sporozoite movement. Sporozoite gliding (in 2D) can be investigated by allowing sporozoites to settle and glide on a glass substrate.

From this assay, the differential sporozoite motility patterns and the gliding speed can be determined. Sporozoite motility can be differentiated into the following patterns: productive movers show the typical circular motility and move for at least half the length of a movie during which they stay continuously attached; while partial movers move less than half the movie length. Not motile sporozoites are considered those that move less than half a parasite length and also stay attached throughout imaging. Lastly, floating sporozoites are unable to attach to the substrate. In all four parasite lines, the percentage of productive movers ranged between 20-60% with *spm1*(-) and *trxL1*(-)/*spm1*(-)ns sporozoites having significantly less productive movers (**Figure 9 C**). Both *spm1*(-) and *trxL1*(-)/*spm1*(-)ns sporozoite reached speeds similar to WT, whereas *trxL1*(-) sporozoites moved slightly but significantly slower than WT sporozoites (**Figure 9D**).

To check whether the MIP mutants are capable of transmitting from mosquitos back to mice, sporozoites can be either directly injected intravenously (i.v.), thereby bypassing the skin phase, or naturally transmitted by the bite of an infected mosquito. For each transmission setup, parasitemia was quantified daily starting three days post infection. In all mice of both transmission setups, mice became blood stage-positive as early as on day 3-4 (prepatency times after bite-back challenge: WT: 4, *spm1*(-): 4, *trxL1*(-): 3.4, *trxL1*(-)/*spm1*(-)ns: 3.3; prepatency times after i. v. challenge: WT: 3.7, *spm1*(-): 3.8, *trxL1*(-): 3.4, *trxL1*(-)/*spm1*(-)ns: 3.5). Parasites from all parasite lines grew equally fast to WT as can be deduced by the slope of the parasitemia curve during the exponential growth phase (**Figure 9 E, F**).

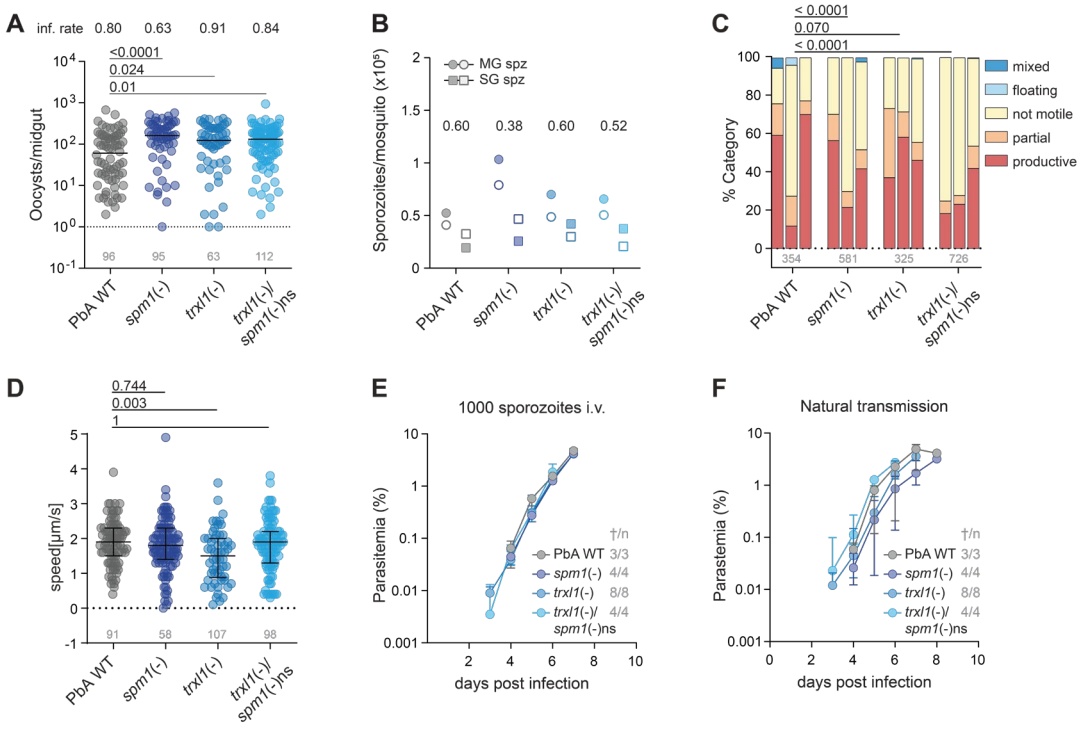

Figure 9 *Spm1*(-) and *trxL1*(-) parasites develop normally within mosquitos and are transmissive. A) Oocyst counts per infected midgut. Pooled data from two cage feeds, each dot representing one midgut. Black line indicates median. Mean infection rates are indicated above the graph. Grey numbers indicate total number of midguts analysed per line, individual midguts per replicate: PbA WT: 32/64, *spm1*(-): 40/55, *trxL1*(-): 30/33, *trxL1*(-)/*spm1*(-)ns: 53/59. Kruskal-Wallis with Dunn's multiple comparisons test. **B)** Salivary gland (SG) and midgut (MG) sporozoite (spz) counts and ratio. Average ratios of salivary gland/midgut sporozoites are depicted at the top. Corresponding counts from one infection are indicated by same symbol filling. **C)** Gliding motility patterns of salivary gland sporozoites. Each bar represents an independent replicate. Statistics: multiple Fisher's exact tests comparing absolute counts of moving (productive, partial movers and mixed) versus non-moving (not motile and floating) sporozoites (numbers pooled over all replicates), adjusted for multiple testing according to Bonferroni-Holm. Grey numbers show total numbers of sporozoites analysed per line, individual replicates for replicate 1-3: PbA WT: 91/51/212, *spm1*(-): 145/204/232, *trxL1*(-): 60/105/160, *trxL1*(-)/*spm1*(-)ns: 185/241/300. **D)** Speed of productively moving salivary gland sporozoites. Kruskal-Wallis with Dunn's multiple comparisons test. Grey numbers indicate total number of sporozoites analysed per line, individual numbers per replicate: PbA WT: 6/36/49, *spm1*(-): 21/20/66, *trxL1*(-): 10/21/27, *trxL1*(-)/*spm1*(-)ns: 22/21/55 **E, F)** Parasitemia after infection with E) 1000 sporozoites intravenously or F) natural transmission by bite. Numbers (†/n) indicate blood-stage positive mice vs total mice. Figure was previously published and adapted for this thesis (57).

To summarize, *spm1* and *trxL1* are alone and in combination dispensable for parasite development within the mouse and the mosquito host, and for the transmission from mosquitos to mice. In addition, *spm1* and *trxL1* are not necessary for gliding motility of ookinetes or sporozoites.

[The *trxL1*(-) mutant and one biological replication from WT was characterized by Lea Herzel during her lab rotation in 2021 under my supervision. In addition, Katharina Röver helped me during her lab rotation in 2023 to analyse the parasitemia of the *trxL1*(-)/*spm1*(-)ns mutant following i.v. and bite-back transmission.]

3.1.2 TrxL1 and SPM1 localize to SPMTs but affect SPMT staining

Single-cell transcriptome analysis in *P. berghei* predicted *trxL1* and *spm1* were to be expressed in ookinetes (*spm1*, *trxL1*) and female gametocytes (*spm1*) (245). To check whether the transcriptome profiles correlate with protein expression and to test whether TrxL1 and SPM1 actually localize to SPMTs, I tagged both *spm1* and *trxL1* C-terminally with GFP using a single cross-over strategy (**Figure 10**). Wang *et al.* showed that, in *T. gondii* parasites, SPM1 links TrxL1 to the microtubule lattice (228). To test whether the binding hierarchy described in *Toxoplasma* is conserved in *Plasmodium*, I generated *spm1-gfp* and *trxL1-gfp* lines in either WT or in the respective complementary KO background (*trxL1*(-) or *spm1*(-) (**Figure 11 A-D**).

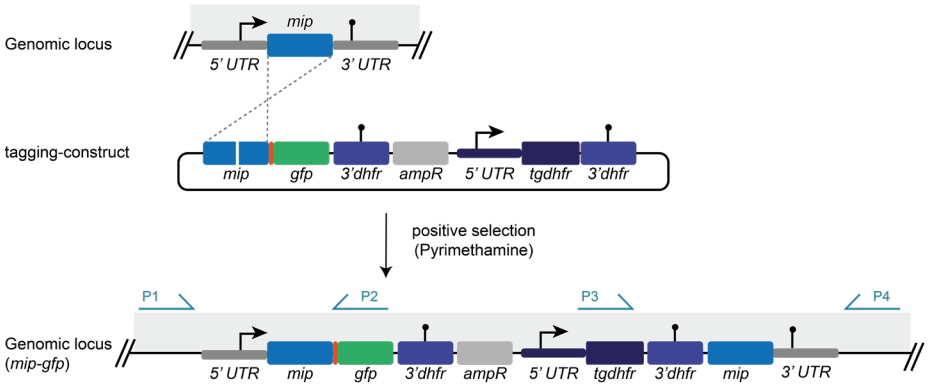

Figure 10 Generation of *P. berghei gfp*-tagged parasite lines. Schematic representation of the single-crossover strategy used to generate tagged parasite lines. Primers (P) used for genotyping PCR are indicated (can be found in **Table 21**). *3'dhfr – 3'UTR of dihydrofolate reductase*, *ampR – ampicillin resistance*, *gfp* – green fluorescent protein, *mip – microtubule inner protein*, *tgdhfr – Toxoplasma gondii dihydrofolate reductase*, UTR – untranslated region. This figure and legend were previously published and adapted for this thesis (112).

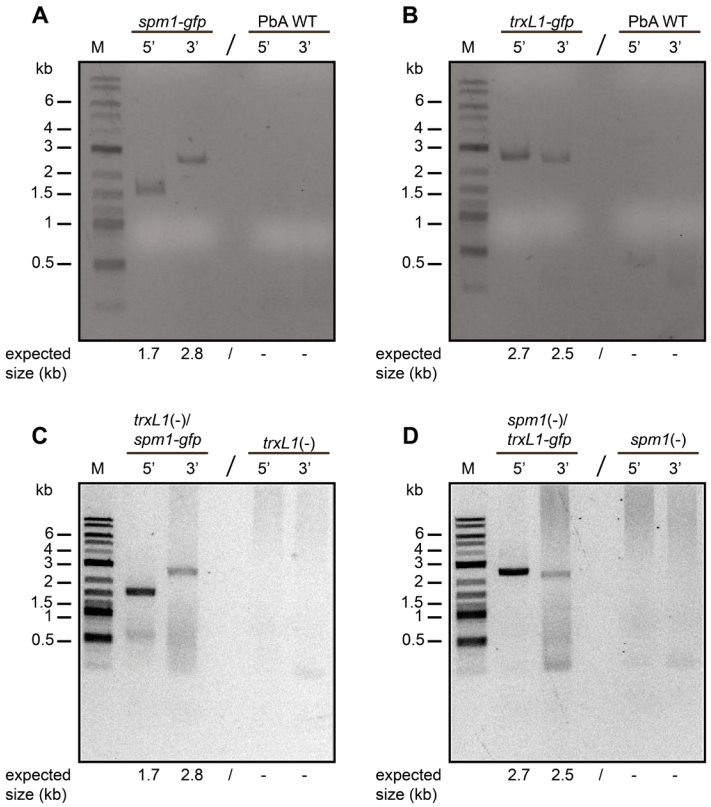

Figure 11 Generation of *spm1-gfp* and *trxL1-gfp* in either wildtype or *spm1*(-) versus *trxL1*(-) background. Genotyping PCRs of **A)** *spm1-gfp*, **B)** *trxL1-gfp*, **C)** *trxL1*(-)/*spm1-gfp* and **D)** *spm1*(-)/ *trxL1-gfp*. Primers used for testing 5' and 3' integration are indicated in **Figure 10**. Single crossover events will lead to the addition of a *gfp*-tag together with the insertion of the selection cassette. Generated tagging lines represent mixed populations. Expected amplicon sizes are indicated at the bottom of the gel images. Int – integration, kb – kilobase, M – marker. Panels A and B of this figure were previously published and adapted for this thesis (112).

First, to investigate whether the *gfp*-tagging affects parasite life cycle progression oocysts, midgut and salivary gland sporozoites and transmission were assessed. Both *spm1-gfp* and *trxL1-gfp* progressed normally through the life cycle and developed midgut oocysts (**Figure 12 A**) and formed into sporozoites (**Figure 12 B**). In live sporozoites, SPM1-GFP localized along the SPMTs whereas TrxL1-GFP localized more strongly to the parasite's apical tip and at a nuclear region (**Figure 12 C, D**) Both mutant lines transmitted normally to the mice as mice readily became blood-stage positive after infectious mosquito bites (data not shown).

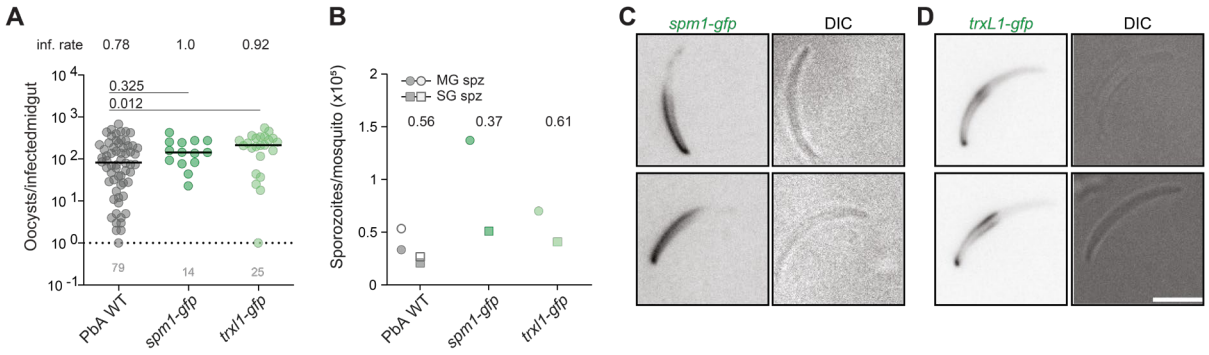

Figure 12 *gfp*-tagging of *spm1* and *trxL1* does not impact parasite life cycle progression. A) Oocyst counts per infected midgut. Each dot represents one infected midgut. Black line indicates median. Mean infection rates are indicated above the graph. Grey number indicate total number of midguts analysed per line. Two cage feeds for PbA WT and one cage feed each for *spm1-gfp*, *trxL1-gfp*. Statistical analysis via Kruskal-Wallis with Dunn's multiple comparison test. **B)** Salivary gland and midgut sporozoite counts and ratios. Average ratios of salivary gland/midgut sporozoites depicted at the top. Corresponding counts from one infection are indicated by same symbol filling. A, B) PbA WT data are the same as in **Figure 23** and were depicted here for comparison. **C, D*)*** Localization of C) SPM1-GFP and D) TrxL1 GFP as determined by live cell imaging of salivary gland sporozoites. Scale bars: 5 µm. Images depicted in panel C and D have been previously published and were adapted for this thesis (112).

Next, the focus was to determine the stages during which SPM1 and TrxL1 are expressed and whether they localize to SPMTs. Therefore, parasites were stained with a tubulin marker and Hoechst for nuclear staining (**Figure 13, Figure 14, Figure 15, Figure 16**). In WT, SPMTs lay underneath the parasite surface (**Figure 4**). Quantifying tubulin signal by creating an intensity profile apically across the parasite thus results in intensity peaks of SPMTs at the cell borders.

In ookinetes, SPM1 localized along the length of SPMTs with an increased signal intensity at the apical end of the parasite (**Figure 13**). Creating an intensity profile across the parasite in 2 µm distance to the apical end resulted in a signal intensity pattern of SPM1-GFP that followed the one of the SPMTs. SPM1 showed SPMT-like localization in both WT and *trxL1*(-) background and hence binds SPMTs independently of TrxL1.

Unlike SPM1, TrxL1 predominantly localized to the apical end and a region near the nucleus, resulting in only partial colocalization with SPMTs in the WT genomic background (**Figure 14**). Upon depletion of *spm1*, TrxL1 was dispersed in the cytosol with a slightly stronger localization close to the nucleus. While the intensity profile of TrxL1-GFP peaked at the cell borders and the center in the WT background, it appeared completely flat and did not follow any expected tubulin intensity profile in the *spm1*(-) background.

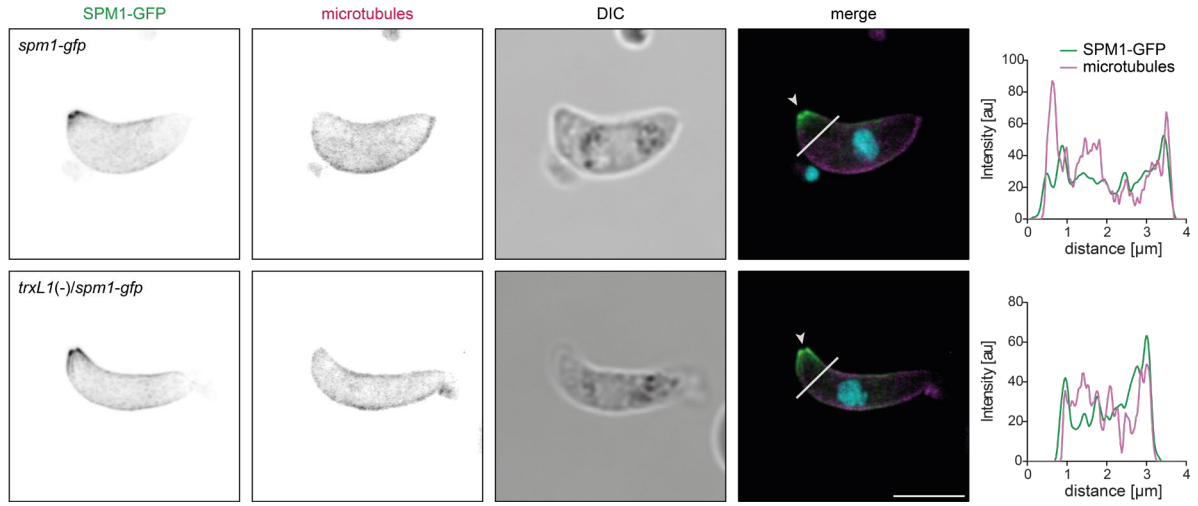

Figure 13 SPM1 localizes to SPMTs independently of TrxL1 in mature ookinetes. SPM1-GFP localization in mature ookinetes in either WT- or *trxL1*(-)-background. Shown is the endogenous SPM1-GFP signal (no antibody staining) while microtubules were stained with an anti-tubulin antibody. Merge images of MIP-GFP (green), microtubules (magenta), and nucleus (cyan). Arrowheads point to the parasite's apical end. Same contrast settings for all images. Shown are maximum Z-projections of fluorescent channels; for the DIC channel the mid slice is shown. Representative of at least 10 images taken. Scale bar: 5 µm. Intensity profiles based on lines of corresponding row image.

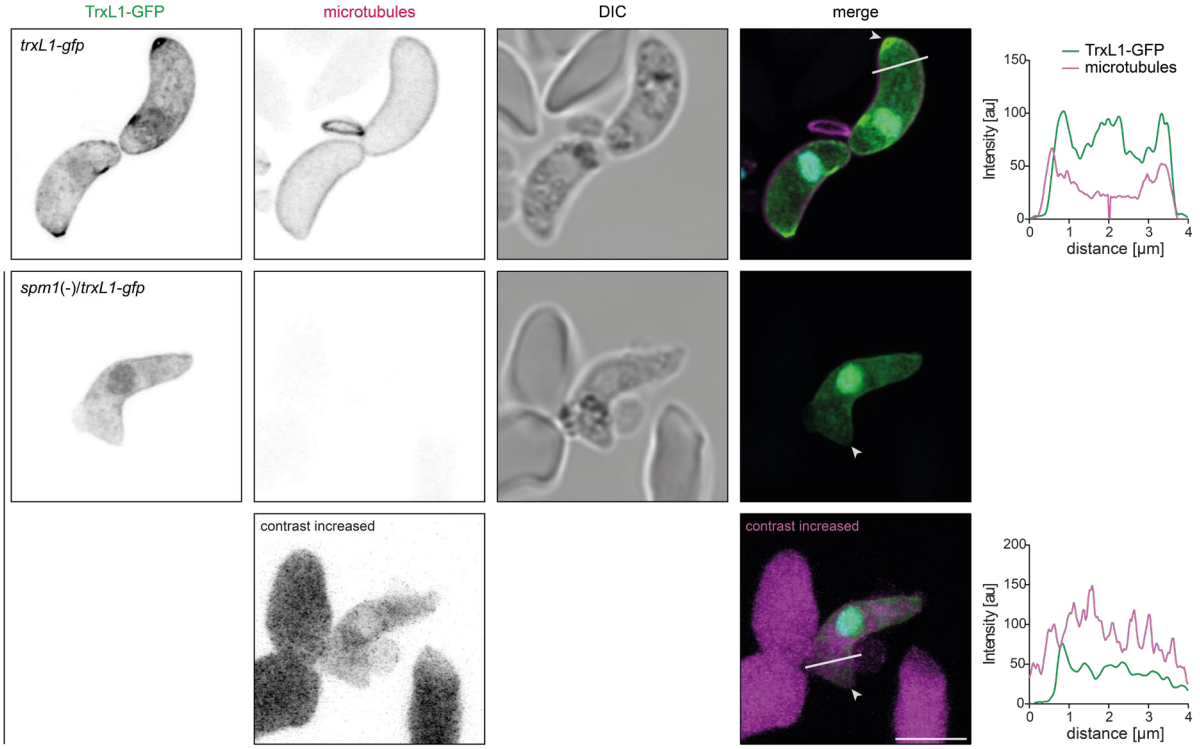

Figure 14 TrxL1 requires SPM1 for SPMT association. TrxL1-GFP localization in mature ookinetes in either WT- or *spm1*(-)-background. Shown is the endogenous TrxL1-GFP signal while microtubules were stained with an anti-tubulin antibody. Merge images of TrxL1-GFP (green), microtubules (magenta), and nucleus (cyan). Arrowheads point to the parasite's apical end. Same contrast settings for all images (if not stated otherwise). Shown are maximum Z-projections of fluorescent channels; for the DIC channel the mid slice is shown. Representative of at least 10 images taken. Scale bar: 5 µm. Intensity profiles based on lines of corresponding merge image of same row.

Similarly to its localization in ookinetes, SPM1 showed a microtubule-following localization pattern in both midgut and salivary gland sporozoites independently of the genomic background (**Figure 15**). Thereby, SPM1 signal largely followed the microtubule signal, with the exception of the single SPMT that extends beyond the nucleus and was devoid of SPM1.

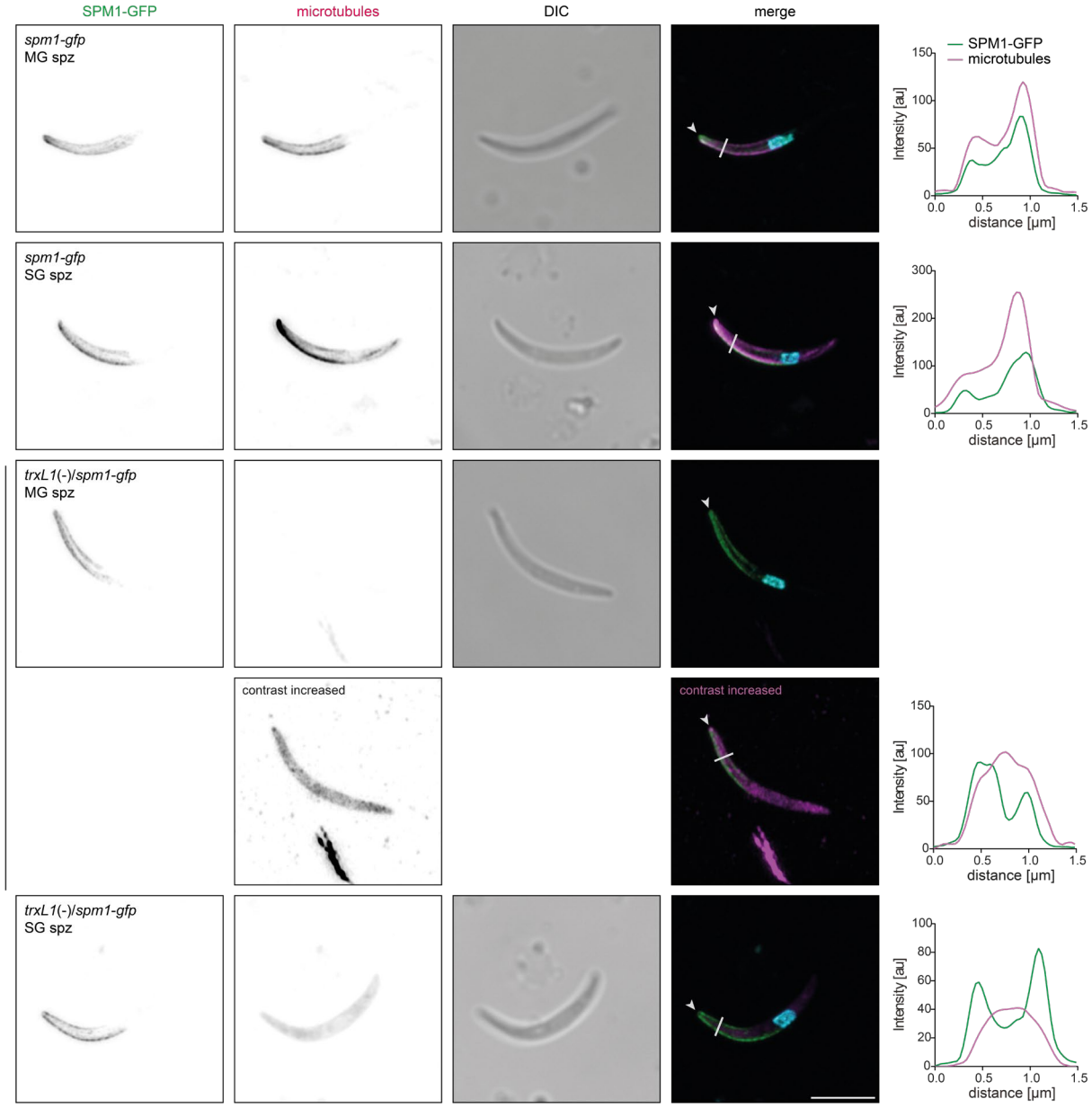

Figure 15 SPM1 localizes to SPMTs in sporozoites independent of *trxL1*. SPM1-GFP localization in midgut and salivary glands sporozoites at day 18-d22 post infection. Shown is the endogenous SPM1-GFP signal while microtubules were SiR-tubulin stained prior to cell fixation. Merge images of SPM1-GFP (green), microtubules (magenta), nucleus (cyan). Arrowheads point to the parasite's apical end. Same contrast settings for all images (if not indicated otherwise). Maximum Z-projections of fluorescent channels; for the DIC channel the mid slice is shown. Representative of at least 10 images taken. Scale bar: 5 µm. Intensity profiles based on lines of corresponding merge image of same row. MG – midgut, SG – salivary gland, spz – sporozoite.

Investigating the localization of TrxL1 in sporozoites, a strong TrxL1 signal was observable at the apical end and additionally around the nucleus in both midgut and salivary gland sporozoites in

the WT background (**Figure 16**). Despite the anti-tubulin antibody and TrxL1 being of similar sizes, the anti-tubulin antibody did not stain the very apical end marked by TrxL1-GFP. The apical end could however be stained with SiR-tubulin. If *spm1* was lacking, TrxL1 completely lost its microtubule-like localization pattern and appeared dispersed in the cytosol as can be also seen in the intensity profiles where the peaks levelled off (**Figure 16).**

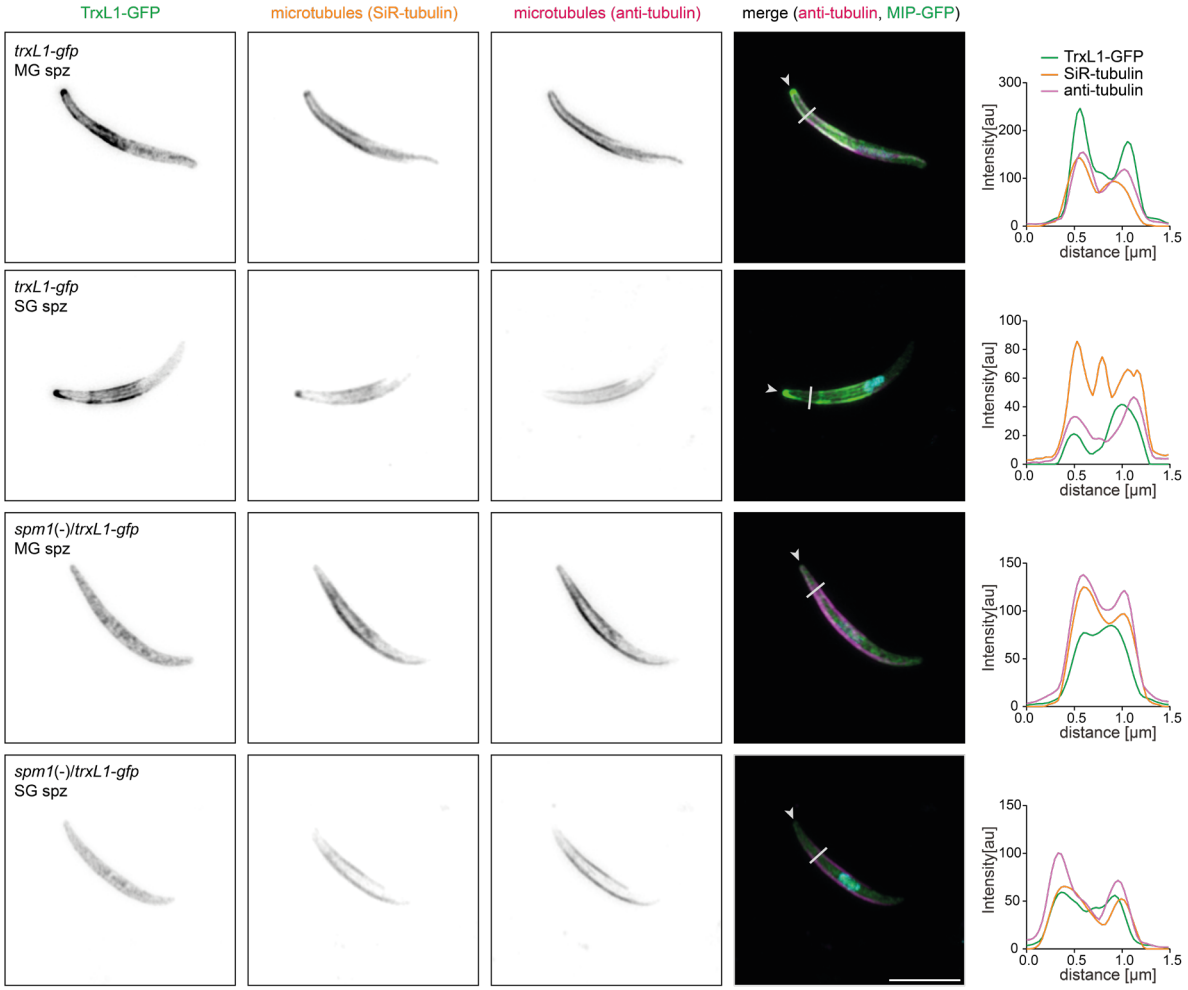

Figure 16 TrxL1 localization to SPMTs in sporozoites is dependent on *spm1*. TrxL1-GFP localization in midgut and salivary glands sporozoites at day 18-d22 post infection. Shown is the endogenous TrxL1-GFP signal while microtubules were both SiR-tubulin stained (prior to cell fixation) and anti-tubulin stained (post fixation). Merge images of TrxL1-GFP (green), microtubules (anti-tubulin signal, magenta), nucleus (cyan). Arrowheads point to the parasite's apical end. Same contrast settings for all images. Shown are maximum Z-projections of fluorescent channels; for the DIC channel the mid slice is shown. Representative of at least 10 images taken. Scale bar: 5 µm. Intensity profiles based on lines of corresponding merge image of same row. MG – midgut, SG – salivary gland, spz – sporozoite.

Naturally, SiR-tubulin would have been the preferred choice of labelling microtubules. SiR-tubulin is based on the microtubule-binding drug Docetaxel and allows for fast and highly specific staining (160, 246). Surprisingly, SiR-tubulin staining often appeared disrupted in the *trxL1*(-) background but remained unaffected in the *spm1*(-) background (**Figure 15, Supplementary Figure 6**). This suggests that the genetic modification caused by the *trxL1* deletion may influence SiR-tubulin

binding, potentially through subtle alterations in tubulin structure or changes to the binding pocket. Consequently, SiR-tubulin proved to be unsuitable as a stain, leading to the use of a complementary approach using an anti-tubulin antibody that successfully revealed the expected tubulin localization in parasites.

To conclude this part, both SPM1 and TrxL1 localize to the SPMTs in ookinetes and sporozoites. While SPM1 follows the SPMTs throughout the cell, TrxL1 localizes more strongly to the apical and near the nucleus. SPM1 colocalises with the SPMTs independent of the presence of TrxL1, while TrxL1 disseminates in the cytoplasm when *spm1* is depleted. This data suggests a binding hierarchy in which SPM1 links TrxL1 to the SPMTs.

[While I generated the tagged parasite lines, Katharina Röver, a Master student supervised by me, performed the genotyping PCRs of the *spm1*(-)/*trxL1-gfp* and the *trxL1*(-)/*spm1-gfp* lines.]

3.1.3 SPM1 and TrxL1 protect SPMTs from depolymerization upon cold treatment

Compared to other eukaryotic microtubules that are highly dynamic, SPMTs of apicomplexans were shown to be extremely stable. While vertebrate microtubules readily depolymerize upon drug or cold treatment, apicomplexan SPMTs showed to be resistant to these treatments (182, 225, 236, 238). The factors that contribute to the extraordinary stability of apicomplexan SPMTs are still not fully understood. Data from collaborators suggested that SPM1 and TrxL1 could contribute to this SPMT stability. Gil Henkin from the laboratory of Simone Reber (MPI Berlin) investigated microtubule dynamics *in vitro*: Using porcine brain tubulin, he investigated microtubule polymerization upon addition of purified *P. falciparum* SPM1 and TrxL1 (*Pf*SPM1, *Pf*TrxL1). Preliminary data revealed that PfSPM1 and PfTrxL1 collaboratively increased microtubule polymerization (personal communication, Gil Henkin). Even more, *Pf*SPM1 and *Pf*TrxL1 appeared to have a stabilizing effect as both proteins together protected already formed microtubules from depolymerizing when incubated on ice (personal communication, Gil Henkin). I thus aimed to test their findings in an *in vivo* setting.

To investigate SPMTs of the different MIP-KO mutants under different temperature conditions, salivary sporozoites were isolated between day 17 and 22 post infection and incubated either at warm (21 °C) or cold (on ice). Since SiR-tubulin only labels microtubules, while the anti-tubulin antibody can bind to both monomeric and polymerized tubulin; parasites were stained with both SiR-tubulin and anti-tubulin to be able to differentiate between the two tubulin states.

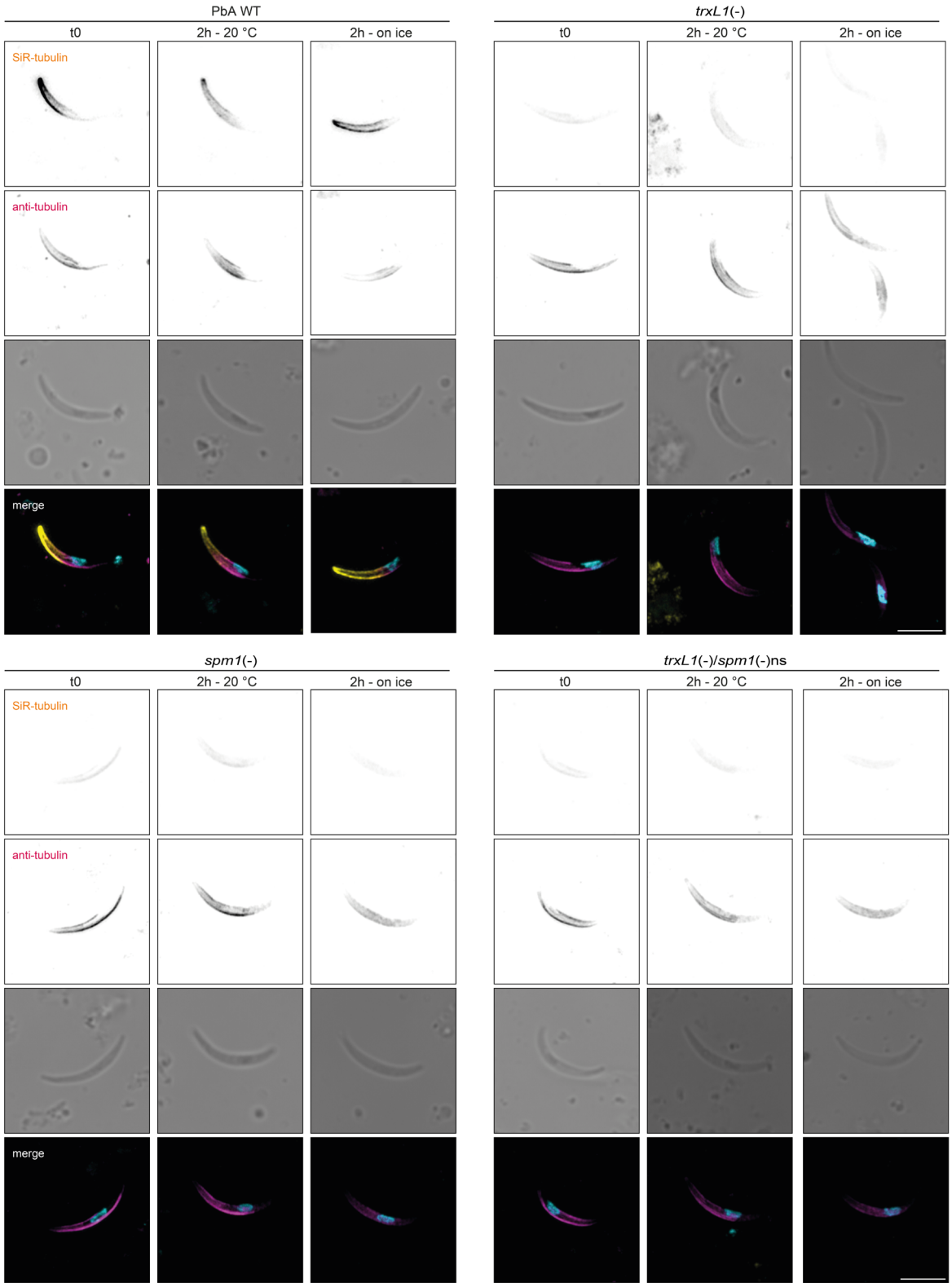

Figure 17 *spm1*(-) and *trxL1*(-)/*spm1*(-)ns, but not *trxL1*(-) appear sensitive to cold treatment. Salivary gland sporozoites (day 18-d20 post infection) were incubated at 20 °C or on ice. Microtubules were stained with SiR-tubulin and anti-tubulin antibodies. Merge images: SiR-tubulin (orange), anti-tubulin (magenta), nucleus (cyan). Images taken with same contrast settings. Maximum Z-projections of fluorescent channels; mid-slice for DIC. Representative of at least 14 images taken. Scale bars: 5 µm. t0 – timepoint 0, fixation immediately after SiR-tubulin staining.

Both SiR-tubulin and anti-tubulin-stained WT sporozoites at both temperatures (**Figure 17**). SiR-tubulin showed a higher staining efficacy at the apical end of WT parasites, while anti-tubulin stained SPMTs more strongly around the nucleus. Staining patterns of the anti-tubulin antibody could be recapitulated in all three MIP-KO mutants when sporozoites had been incubated at 20 °C. However, when MIP-KO sporozoites had been incubated on ice, anti-tubulin signals appeared slightly dispersed in the cytosol in *trxL1*(-) parasites and to a stronger degree in *spm1*(-) and *trxL1*(-)/*spm1*(-)ns sporozoites. As I observed already previously, SiR-tubulin signals were consistently lower in all three MIP-KO mutants compared to WT (**Supplementary Figure 7**).

To determine the extent of microtubule depolymerization/dispersion in MIP-KO mutants dependent on the temperature, I initially quantified SPMT signals along the longitudinal axis of the parasite (**Figure 18 A**). For this, I created an intensity profile along the parasite length and set it to a width that covered the sporozoite thickness. Using both staining approaches, I aimed to investigate whether SiR-tubulin and anti-tubulin would result in different staining patterns and hence would allow me to differentiate between fully polymerized microtubules (SiR-tubulin$^+$/anti-tubulin$^+$) and monomeric tubulin (SiR-tubulin$^-$/anti-tubulin$^+$). In WT sporozoites, the SiR-tubulin signal was highest at the apical end and decreased towards the distal end of the parasite. In contrast, anti-tubulin staining followed a bell-curve that had its maximum at the center of the sporozoite (**Figure 18 A**). There was no difference in neither SiR-tubulin signal nor in the anti-tubulin pattern whether WT sporozoites had been incubated at 20 °C or on ice. In comparison, SiR-tubulin staining in all three MIP-KO mutants followed a bell-curve similar to the one observed for the anti-tubulin staining in WT cells. Also here, temperature treatment did not change the overall shape or signal intensity. As Sir-Tubulin staining efficacies were however drastically reduced (**Figure 17, Supplementary Figure 7 A**), these results have to be evaluated with caution. The bell-curves of the anti-tubulin staining had a similar shape independent of the temperature for all three mutants. As the anti-tubulin antibody generally seems to be unable to access the SPMTs at the parasite's apical end, it was not possible to deduce any information about the distribution of polymerized/unpolymerized SPMTs in different lines or treatments.

To be still able to evaluate whether SPMTs are sensitive to cold treatment upon *mip* depletion, SPMTs were additionally quantified along the lateral axis. Anti-tubulin signals were measured by generating the intensity profile across the sporozoite at a position 2.5 µm from the center of the nucleus towards the apical end (**Figure 18 B**). In the WT scenario, SPMTs are all in close distance to the parasite surface and hence the intensity plots of the anti-tubulin signal along the sporozoite cross sections are M-shaped at both temperatures. In the *trxL1*(-) mutant, this M-shape pattern was similar, independent of the temperature. In *spm1*(-) sporozoites, the M-shape was already not as easily discernible when cells were incubated for 2 hours at 20 °C. Upon incubation on ice, the microtubule signal curves appeared even more flattened. Intensity profiles of *trxL1*(-)/*spm1*(-)ns

incubated at 20 °C peaked at the cell borders, and similarly to the *spm1*(-) mutant these microtubule signal curves of the *trxL1*(-)/*spm1*(-)ns mutant were more flat upon incubation on ice.

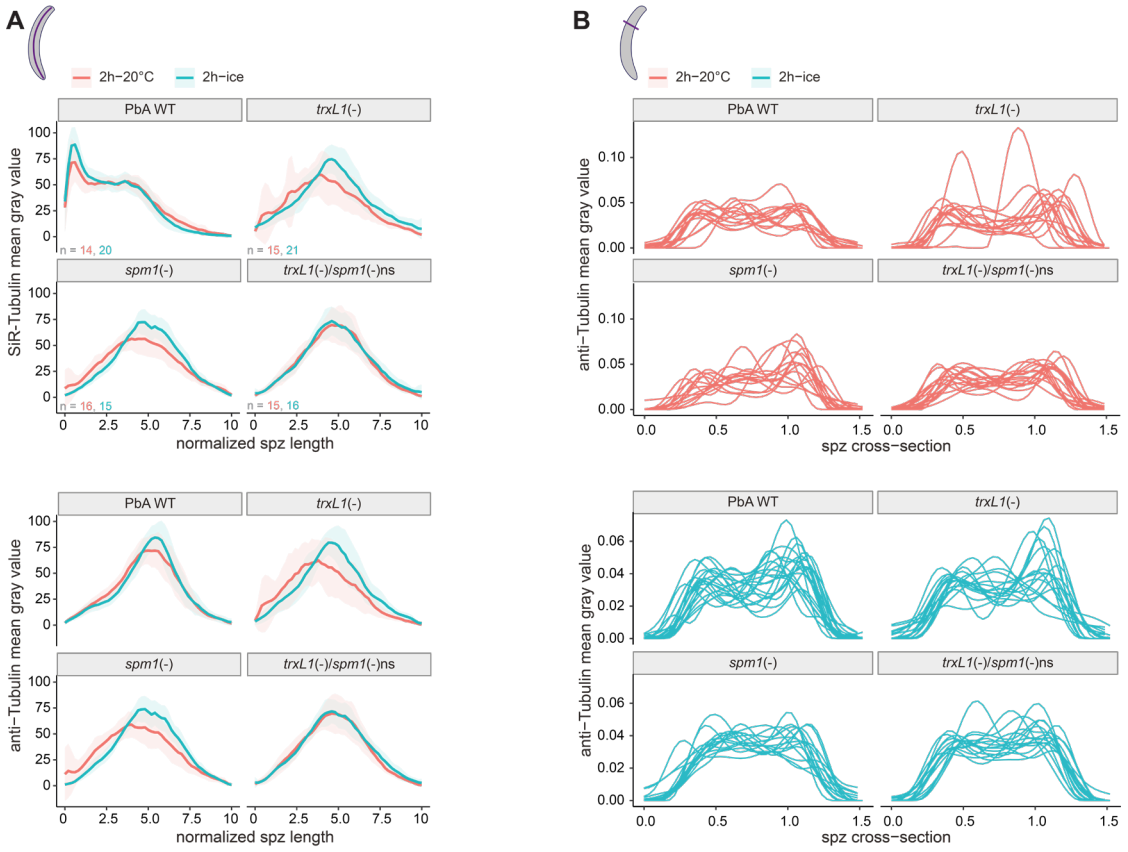

Figure 18 SPMTs appear dispersed in the cytosol in *spm1*(-) and *trxL1*(-)/*spm1*(-) mutants upon cold treatment. **A)** Microtubule signal determined by SiR-tubulin staining (top) and anti-tubulin staining (bottom) along the longitudinal axis of the sporozoite. Mean grey values were normalized to the total signal per sporozoite from maximum Z-projections. Shown is the normalized mean value with SD. **B)** Microtubule signal determined based on anti-tubulin staining along the lateral axis apical from the nucleus after incubation at 20 °C (coral) or on ice (turquoise). Mean grey values were normalized to the total signal per sporozoite from the center Z-slice. N indicates pooled numbers from two biological replicates. Spz – sporozoite.

Taken together, while SPMTs of the *trxL1*(-) mutant appear equally stable as SPMTs from WT, SPMTs of both the *spm1*(-) and the *trxL1*(-)/*spm1*(-)ns mutant seem sensitive to cold treatment and appear dispersed into the cytosol. SiR-tubulin signal in MIP-KO mutants was consistently lower compared to WT, making an analysis comparing SiR-tubulin versus anti-tubulin staining patterns non feasible. Preliminary data revealed that incubation of sporozoites for an extended period of time (> 24 h) at cold results in an almost complete depolymerization of SPMTs in the *trxL1*(-)/*spm1*(-)ns compared to full length SPMTs in WT parasites (**Supplementary Figure 8**) (Josie Ferreira, University College London).

3.2 Combining MIPs and MAPs in a multi depletion mutant

[The results of part 3.2 have not yet been published. However, WT characterization data depicted in 3.1.1 was previously published in (57) and is shown again in **Figure 20** as control line.]

Besides *spm1* and *trxL1*, a third gene called subpellicular protein 2 (*spm2*) was defined as an apicomplexan-specific MAP (238). In *T. gondii*, SPM2 localized to a central region at the SPMTs and, in contrast to SPM1, showed to be dispensable for microtubule stability and parasite fitness (236). While Wang *et al.* showed in their cryo-tomographic analysis that SPM1 and TrxL1 represent MIPs and localize (together with the *T. gondii* specific TrxL2) in a highly regular fashion to the microtubule lumen, SPM2 was not uncovered in this analysis (239). This suggests that compared to SPM1 and TrxL1, SPM2 might actually represent an outer MAP. In the following chapter, I aimed to investigate the function of SPM2 and combine the deletion of this putative outer MAP with deletion of the inner MAPs first in a double and then in a triple KO mutant.

3.2.1 *Spm2*(-) and *spm1*(-)/*spm2*(-)-*gfp* depletion mutants develop normally in both the murine and mosquito host

To investigate the role of *spm2* alone and in combination with the KO of MIPs, the mutant parasite lines *spm2*(-) and *spm1*(-)/*spm2*(-)-*gfp* were generated via double homologous crossover recombination. Generating the *spm1*(-)/*spm2*(-)-*gfp* line, a GFP expression cassette as part of the selection cassette was introduce which allowed to directly identify double KO mutants by their GFP signal. Transfection and generation of a clonal KO parasite lines were successful and a single clone for the *spm2*(-) mutant was readily obtained (**Figure 19 A**). In contrast, the generation of the double depletion mutant revealed to be more difficult. The initial negative selection of the *spm1*(-) mutant required two negative selection attempts (**Supplementary Figure 2**), which might have simply been just bad luck. Also, the introduction of the second mutant was unsuccessful after a first transfection as the three obtained clones from two separate limiting dilutions all represented WT parasites (**Supplementary Figure 3 A, B**). Hence, the transfection was repeated and two transfections were set up in parallel from which a single double KO clone was successfully obtained (**Figure 19 B, Supplementary Figure 3 C**).

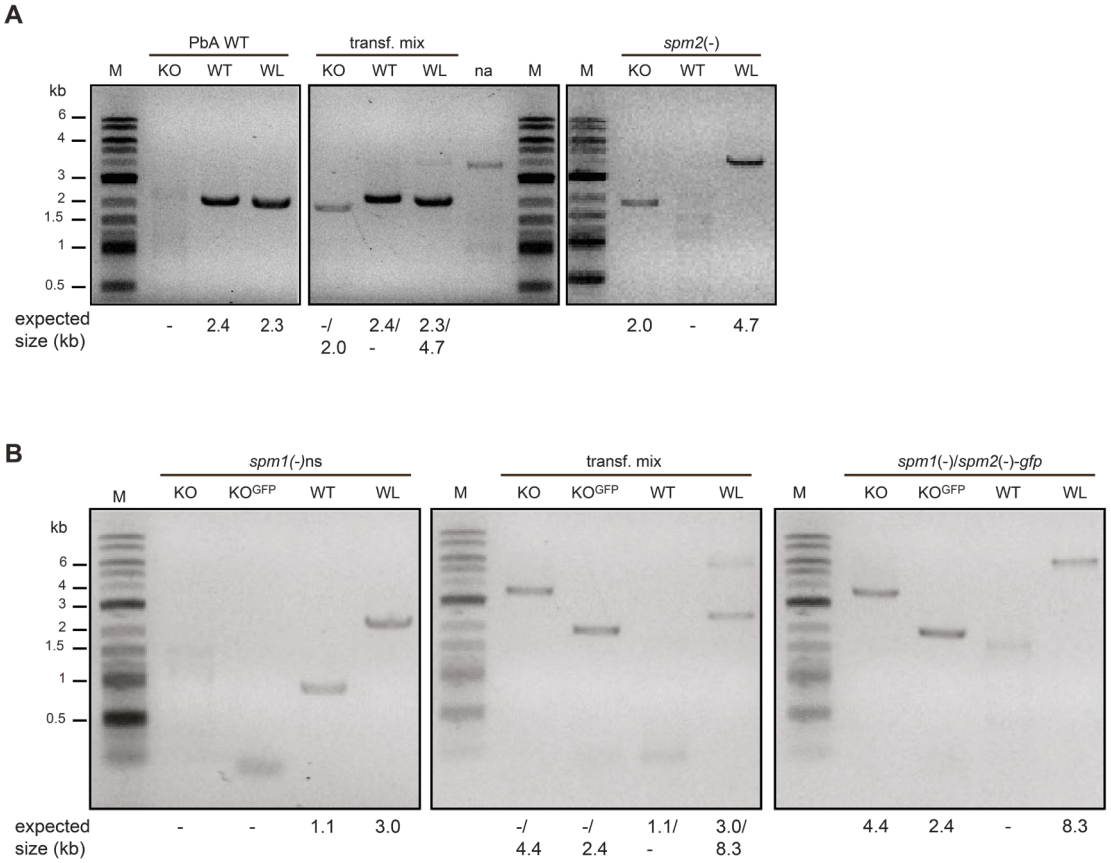

Figure 19 Generation of the *spm2*(-) single and *spm1*(-)/*spm2*(-)-*gfp* double KO parasite lines. Genotyping PCRs of **A)** *spm2*(-) and **B)** *spm1*(-)/*spm2*(-)-*gfp*. Primers used for genotyping PCRs are indicated in **Figure 6 A, B**. Double crossover events leading to the insertion of the KO construct will result in an increased size of the WL PCR fragment. Two PCR mixes (KO, KO^{GFP}) were used to confirm integration of the selection cassette. Kb – kilobase, KO – knockout, M – marker, na – not applicable, ns – negatively selected, WL – whole locus, WT – wildtype.

Mosquitos were then infected with the two obtained single and double KO parasite lines and parasite development was observed as described before. While infection of mosquitos with the *spm2*(-) mutant line resulted in an infection rate of 0.77 similar to the one in WT, infection rates of the *spm1*(-)/*spm2*(-)-*gfp* line were repeatedly lower than WT (**Figure 20 A**). This might represent a phenotype, however as the WT-data was not obtained in parallel to the characterization of the *spm1*(-)/*spm2*(-)-*gfp* mutant this needs to be further evaluated. Nevertheless, both mutants formed oocysts with the *spm2*(-) line having slightly higher oocyst numbers/infected midgut compared to WT while the *spm1*(-)/*spm2*(-)-*gfp* line showed to have significantly reduced oocyst counts (**Figure 20 A**). In both mutants, sporozoites formed within oocysts and were able to invade the salivary glands (**Figure 20 B**). As expected, the lower midgut infection rates resulted in less sporozoites in the *spm1*(-)/*spm2*(-)-*gfp* line in both tissues. Despite the lower sporozoite counts, both tissues were colonized efficiently by the mutant as can be deduced from a salivary gland/midgut sporozoite ratio of 0.62 that is comparable to WT. Similarly, also the *spm2*(-) mutant had a normal salivary gland invasion resulting in a salivary gland/midgut sporozoite ratio of 0.34. I then checked whether the sporozoites from the two mutants were

infectious to mice. In both transmission setups, all mice became positive and developed parasitemias similar to WT (**Figure 20 C, D**). The *spm1*(-)/*spm2*(-)-*gfp* mutant grew slightly slower in the blood than the *spm2*(-) and WT lines as indicated by a lower slope of the parasitemia curve.

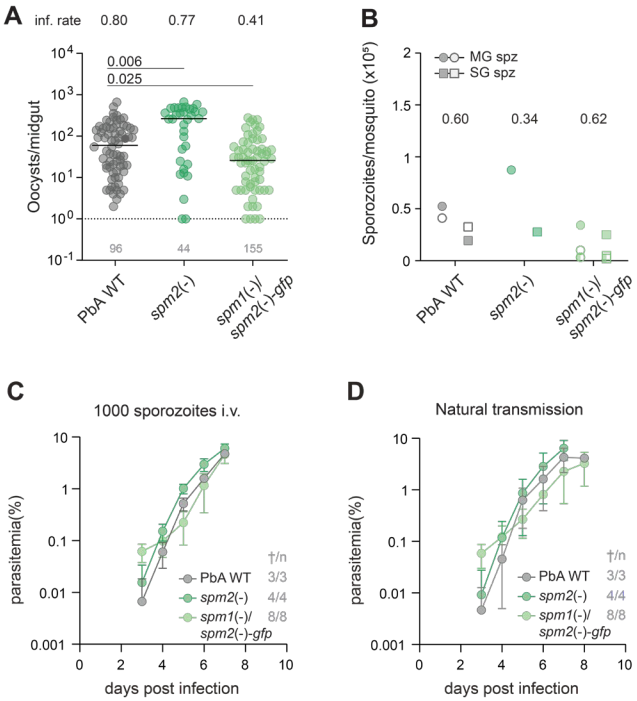

Figure 20 Depletion of neither *spm2* nor *spm1* and *spm2* together affect parasite life cycle progression. Numbers of oocysts per infected midgut. Shown is the pooled data from several cage feeds with each dot representing an infected midgut. Grey numbers at the bottom indicate the total number of midguts analysed per line; single replicate numbers were as following: PbA WT: 32/64, *spm2*(-): 44, *spm1*(-)/*spm2*(-)-*gfp*: 54/53/48. Statistical analysis via Kruskal-Wallis with Dunn's multiple comparison test. **B)** Numbers of midgut (circles) versus salivary gland (squares) sporozoites determined on two separate days between day 17 to day 22. Corresponding replicate numbers are shown by same symbol fillings. Numbers at the top show ratios of salivary gland/midgut sporozoites. **C, D)** Transmission either via intravenous injection of 10000 sporozoites (C) or naturally via mosquito bite (D). Numbers (†/n) indicate blood-stage positive mice vs total mice. PbA WT data is depicted as comparison but was previously shown in **Figure 9** and published as part of (57). Shown is the pooled data from either one (*spm2*(-)) or multiple (PbA WT, n=2, spm*1*(-)/*spm2*(-)-*gfp*, n = 3) cage feeds. MG – midgut, SG – salivary gland.

3.2.2 Attempts to generate a triple MAP KO mutant

To study the function of MAPs in *P. berghei*, I previously generated first single KO mutant parasite lines by double homologous cross over recombination. This yielded isogenic clones for *spm1*(-) and *trxL1*(-) as well as for *spm2*(-), the latter presumably binding outside of the microtubule and hence representing a MAP. Single deletion of these genes did not reveal any phenotype in neither the murine host nor the mosquito vector during standard life cycle characterisation. Consequently, the aim was to combine the KOs into a multi-deletion mutant to ultimately generate a triple KO of all three MAPs. Based on the findings of Wang *et al.* that showed that SPM1 links TrxL1 to the microtubule lattice (239), I reasoned that this hierarchy might be true for *Plasmodium* as well. Investigating the localization patterns of SPM1 and TrxL1, TrxL1 indeed loses its SPMT-localization upon *spm1* depletion (3.1.2).

This led me to hypothesize that the existing *spm1*(-) depletion mutant might actually already represent a double depletion mutant as in the absence of *spm1*, TrxL1 is no longer capable of SPMT binding and hence should not be able to execute its function at the SPMTs. As a consequence, the decision was initially to add the *spm2* depletion onto the pre-existing *spm1*(-) mutant. Thereby, the transfection plasmid was designed in a way that the *spm2* ORF is not only replaced by a selection cassette but at the same time GFP is introduced as a fluorescent marker that allows to directly identify transfected parasites. However, initial attempts to generate this double depletion failed. Therefore, an alternative approach was pursued in parallel, aiming to negatively select the *trxL1*(-) mutant in order to combine it consecutively with the other two MAP KOs. This strategy began by adding the *spm2*(-) onto the *trxL1*(-)ns line to introduce the fluorescent marker, which should then be further combined with the *spm1* depletion (**Figure 21 B**). In the meantime, an isogenic *spm1*(-)/*spm2*(-)-*gfp* line was successfully obtained (**Figure 19 B**) to which then the *trxL1* deletion was introduced. However, attempts to negatively select the mutant to enable the introduction of *trxL1*(-) were unsuccessful (**Figure 21 A**). From 10 mice used in a limiting dilution, only three mice became positive and the isolated parasites all still harboured the selection cassette (data not shown). This was surprising, as negative selection is generally a robust and straightforward method for recycling the selection cassette. Unlike gene targeting via positive selection, negative selection should not interfere with the expression of essential genes. One possibility of the reoccurring failures of negative selection could be a mutation in the *yfcu* gene which could confer resistance to 5-FC treatment. To rule this out, the selection cassette of the three obtained clones was sequenced which revealed no mutation in the *yfcu* gene (data not shown). In line with the negative selection of the *spm1*(-)/*spm2*(-)-*gfp* mutant, the *trxL1*(-)/*spm2*(-)-*gfp* depletion mutation could be successfully generated but negative selection approaches failed (**Figure 21 B, Supplementary Figure 4**).

Ultimately, the aim was to negatively select the third MAP depletion combination, namely the *trxL1*(-)/*spm1*(-) mutant. Unlike earlier approaches, this attempt successfully recycled the selection cassette, resulting in the *trxL1*(-)/*spm1*(-)ns mutant line (**Figure 7, Figure 21 C**). A first transfection aiming to deplete *spm2* while introducing *gfp* via gene out/marker resulted in only a low transfection efficacy as observed by the number of GFP-positive parasites within the total transfection mix of parasites (data not shown). A second transfection attempt resulted in a decent number of transfected parasites, but two independent limiting dilutions with eight mice each did not produce a clonal line.

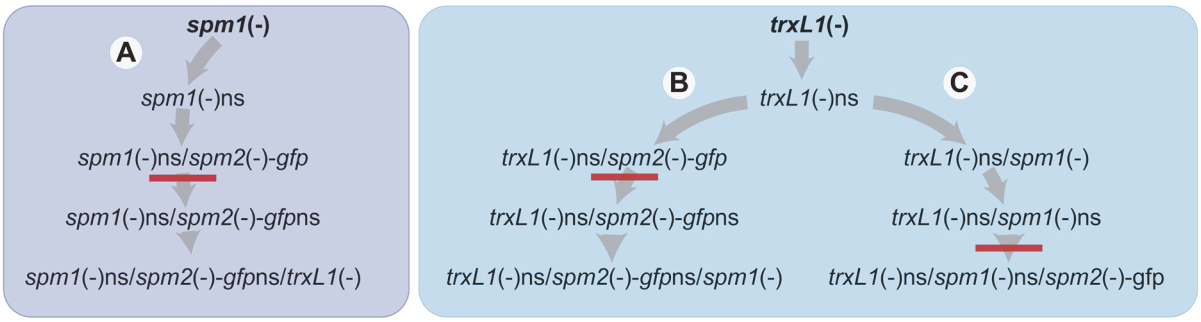

Figure 21 Attempts to generate a triple KO mutant failed so far. Red lines indicate blocks in generating a triple KO line with letters indicating different approaches to generate a triple KO mutant. Ns – negatively selected.

In summary, all attempts to combine *spm1*, *spm2* and *trxL1* in a triple depletion mutant so far failed. Negative selection aiming to recycle the selection cassette was in two attempts not successful (**Figure 21 A, B**). While I was able to obtain a marker-free *trxL1*(-)/*spm1*(-) mutant parasite line and transfection with the *spm2*(-)-*gfp* construct yielded decent numbers of transgenic, GFP-positive parasites, the generation of a clonal *trxL1*(-)/*spm1*(-)/*spm2*(-)-*gfp* line was unsuccessful. This is generally surprising but altogether highlights two general findings: First, *Plasmodium* SPMTs and their associated proteins form a highly robust SPMT system in which depletion of a single MAP does not impact overall parasite development and transmission. Secondly, neither the *trxL1*(-)/*spm1*(-)ns nor the *spm1*(-)/*spm2*(-)-*gfp* line showed any strong developmental defect, suggesting a high degree of protein redundancy. However, the combined presence of all three proteins appears to be essential for the parasite.

3.3 Characterizing the role of an outer MAP, SPM3, for parasite life cycle progression

[The results of part 3.2.1 and 3.2.2 were previously published in mbio (Wichers-Misterek, Binder and Mesén-Ramírez *et al.*, 2023). Figures and tables were adapted and modified when necessary and are indicated in the respective figure legend. Data that was obtained from collaborative work with others is indicated, and the respective people that contributed are mentioned at the end of each respective sub-chapter.]

SPMTs provide cell rigidity and shape to the invasive stages of the parasite. For this, they have to be well-tethered to the IMC. Work by our collaborators in Hamburg identified the subpellicular microtubule protein 3 (SPM3) as a potential interaction partner of the IMC-residing protein PhIL1 in *P. falciparum* (247). To test its putative localization to the IMC, they tagged *spm3* with *gfp* and investigated SPM3-localization in asexual and sexual stages. Surprisingly, PfSPM3 did not colocalize with any of the tested IMC marker proteins but had an SPMT-like localization pattern and was hence named SPM3 (248). To extend the investigation of SPM3 function to the mosquito stages, I first generated a *Pb*SPM3 KO mutant parasite line and investigated life cycle progression.

3.3.1 SPM3 is critical for sporozoite motility, salivary gland invasion and transmission to the mammalian host

To investigate the role of SPM3, the mutant parasite line *spm3*(-) was generated. According to the MIP KO generation, also the *spm3*(-) line was generated via double homologous crossover recombination during which the *spm3* ORF was replaced by a selection cassette (**Figure 6 A**). Following transfection and selection, I obtained four isogenic clones from a limiting dilution (**Figure 22 A**) that all grew slightly faster than WT parasites in the blood resulting in a mean asexual growth rate of 10.8-fold/24h (**Figure 22 B**).

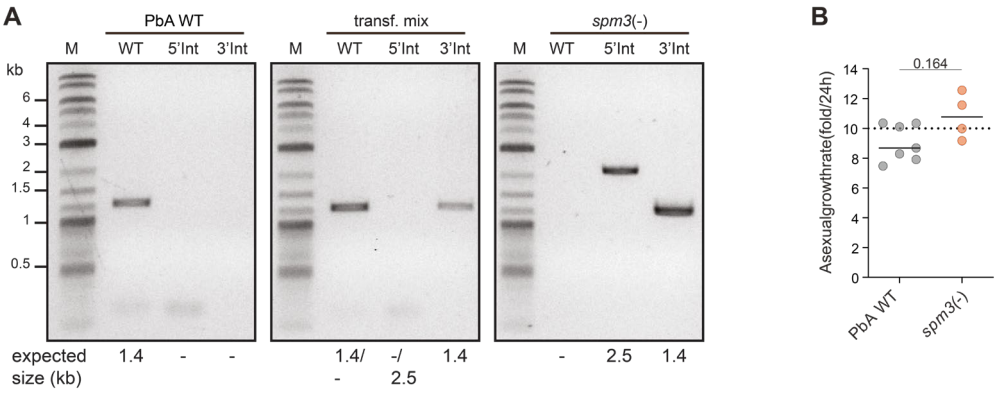

Figure 22 Deletion of *spm3* does not affect asexual blood stage growth rate. **A)** Genotyping PCRs of *spm3*(-). Primers used for genotyping PCRs are indicated in **Figure 6A**. Double crossover events leading to the insertion of the KO construct. **B)** Asexual growth rate shown as mean fold change with a single parasite replication cycle (24 h for *P. berghei*). Mice were injected with a single iRBC intravenously and parasitemia value determined at day 8 was used to calculate the asexual growth rate. PbANKA WT growth rates were plotted as a reference and were determined and previously published by our laboratory (139, 242, 243). Line indicates median. Statistical analysis using unpaired t-test. Int – integration, Kb – kilobase, M – marker, PbA WT – wildtype. Figure and legend were previously published and adapted for this thesis (248).

To check whether parasites can infect mosquitoes, naïve mosquitoes were allowed to bite on *spm3*(-)-infected mice and mosquito midgut infection was determined ten to eleven days later. *Spm3*(-) parasites colonized midguts normally as indicated by both similar infection rates of 88% compared to 78% for WT parasites and median count of 116 oocysts/infected midgut (**Figure 23 A**). This means, that *spm3*(-) parasites are infectious to mosquitoes, as neither gametocyte development and activation, nor ookinete development or midgut traversal were affected.

To investigate whether the *spm3*(-) mutant can then form sporozoites that subsequently invade salivary glands, the number of sporozoites in both midgut oocysts and salivary glands were determined on two separate days and compared to each other. While the *spm3*(-) had high oocyst sporozoites counts comparable to WT, barely any sporozoites in the salivary glands could be detected (median WT: 21 000 salivary gland sporozoites versus median *spm3*(-): 300 salivary gland sporozoites) and hence resulted in a much-reduced average ratio of salivary/midgut sporozoites (**Figure 23 B**). At this point, it is unclear whether *spm3*(-) sporozoites are unable to exit oocysts or whether the invasion of salivary glands is impacted. To find this out, the number of sporozoites in the hemolymph were determined. As WT and *spm3*(-) had hemolymph sporozoites at comparable numbers this points to an invasion defect (**Figure 23 B**).

To assess whether the few sporozoites formed by the *spm3*(-) mutant are motile, 2D *in vitro* gliding assays were performed as previously described. While 81% of WT sporozoites attached to the glass substrate and moved from which 48% showed continuous gliding motility, most of the *spm3*(-) sporozoites were unable to attach and floated in the medium. Only 14% of *spm3*(-) sporozoites moved continuously (**Figure 23 C**). Interestingly, a novel gliding motility phenotype

was observed in the *spm3*(-) mutant, characterized by a helical-like motility behaviour, which was termed "helical" motility. Helically moving parasites were unable to attach completely, but rather changed between short phases of gliding and detachment/ flipping over (**Figure 23 D**, motility movies see (248)). Nevertheless, the few *spm3*(-) sporozoites that showed continuous and circular gliding behaviour reached speeds comparable to WT as determined by the number of frames required to complete one cycle (**Figure 23 E**).

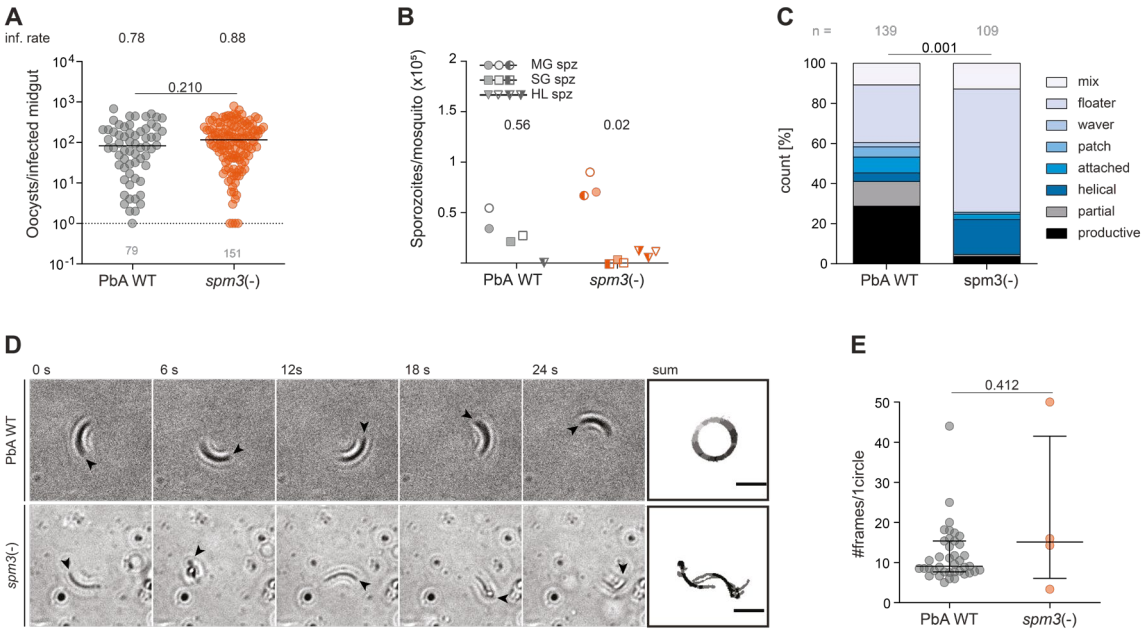

Figure 23 SPM3 is critical for sporozoite motility. **A)** Oocyst counts per infected midgut. Pooled data from two (PbA WT) and three (*spm3*(-)) independent cage feeds, each dot representing one midgut. Black line indicates median. For statistical analysis comparing oocyst numbers in infected MGs, Mann-Whitney test was performed. Grey numbers indicate total number of MGs analysed per line, individual midguts per replicate: PbA WT: 37/42, *spm3*(-): 55/51/45. **B)** Numbers of SG and MG sporozoites isolated from the same mosquito with the average ratio (SG/MG sporozoites) shown at the top of the graph. HL sporozoites dissected on a separate day are indicated by triangles. Corresponding counts from one infection are indicated by same symbol filling. **C)** Different types of movement patterns observed in sporozoites. Pooled data from two (PbA WT) and three (*spm3*(-)) independent cage feeds with two technical replicates per cage infection. Grey numbers on top represent total numbers of sporozoites analysed. Statistics: multiple Fisher's exact tests comparing absolute counts of moving (productive, partial mover, mixed, helical) versus non-moving (waver, patch, attached, floating) sporozoites (numbers pooled over all replicates). **D)** WT-like circular (top) and helical (bottom) movement patterns. Black arrow heads point to the parasite's apical end. Scale bar: 10 µm. **E)** Sporozoite speeds of productively gliding WT- and *spm3*(-) sporozoites shown in panel C. Only four productively moving *spm3*(-) sporozoites were observed across replicates, compared to 40 for PbA WT. P value determined by Mann-Whitney test. Black line indicates median with interquartile range. HL – hemolymph, MG – midgut, SG – salivary gland. Figure and legend were previously published and adapted for this thesis (248).

To assess them mutant's transmissibility to mice, either 1000 sporozoites were injected intravenously into the tail veins of mice, or ten mosquitos were allowed to feed on a single naïve C57/BL6 mouse. For each transmission setup, 3-4 mice per biological replicate were used, and parasitemia was monitored daily starting three days post infection (**Figure 24 A, B**). Due to strong variations across biological replicates for the natural transmission setup, all parasitemia curves are presented separately for each replicate. Intravenous injection of either WT or *spm3*(-) sporozoites resulted in all mice becoming positive (**Figure 24 A**). However, *spm3*(-) parasites exhibited a delayed prepatency time of 4.6 days compared to 3.6 days in WT-infected mice (**Table 1**). Following natural transmission by mosquito bite, only mice from the first biological replicate became positive with the *spm3*(-) mutant, whereas mice from biological replicate two and three remained negative for up to 22 days post infection (**Figure 24 B**). This discrepancy is likely due to the much higher salivary gland sporozoite loads observed in biological replicate one compared to two and three. Even more, mice that got infected by mosquito bite with *spm3*(-) had a delay in prepatency time of two days resulting in a much lower parasitemia at day six post infection compared to WT (**Table 1**). In both transmission setups, *spm3*(-) parasites developed equally fast to WT as soon as parasites had entered the blood stream as can be deduced from the slope of the parasitemia curves.

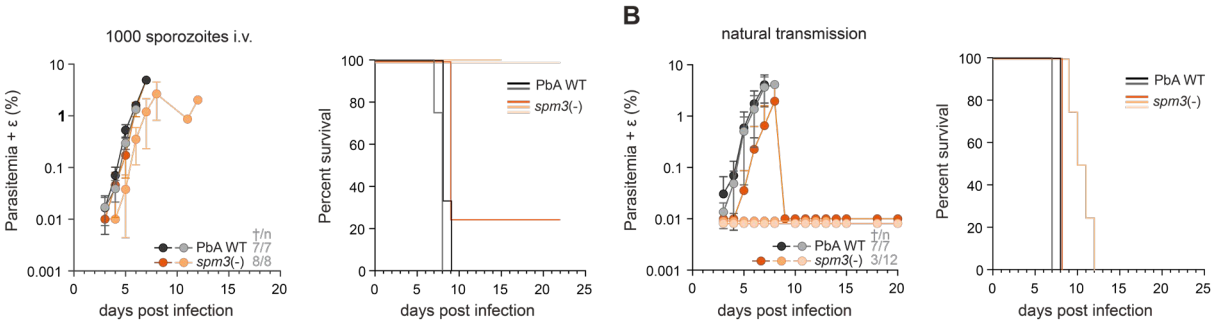

Figure 24 Depletion of *spm3*(-) impairs natural transmission. A, B) Parasitemia and mouse survival after A) intravenous infection with 1000 sporozoites or B) natural transmission by mosquito bite or. Two to three independent infections were performed for PbA WT and *spm3*(-), using 3 to 4 mice per experiment (see **Table 1**). Note that mice from two replicates following natural transmission remained negative over the course of parasitemia monitoring, and would thus not be visible on a logarithmic scale. To show all values, a factor ε (+0.01) was added to each parasitemia value. Further, parasitemia curve of replicate 2 was slightly nudged for better visibility. Figure and legend were previously published and adapted for this thesis (248).

Table 1 Numbers and infectivity of *spm3*(-) sporozoites compared to PbA WT. Per transmission setup, 3-4 C57/BL6 mice were used. Several biological replicates per transmission setup were performed: n = 2 for PbA WT, n = 3 for *spm3*(-) transmitted by bite, and n = 2 for *spm3*(-) transmitted by i.v. injection. Mean parasitemia values from all mice that became positive within 20 days. Table and legend were previously published and adapted for this thesis (248).

	# sporozoites/ mosquito (Mean ±SD (replicates)		**Infection with 1000 spz i.v.**		**natural infection (by bite)**	
Line	Midgut	Salivary gland	Prepatency time (days) (#infected/ #total)	Parasitemia at day 6 (infected only)	Prepatency time (#infected/ #total)	Parasitemia at day 6 (infected only)
PbA WT	34 000 ± 6 000 55 000 ± 16 000	21 000 ± 1000 27 000 ± 10 000	3.6 (7/7)	1.4%	3.7 (7/7)	1.5%
***spm3*(-)**	70 000 ± 22 000 90 000 ± 9000 67 000 ± 18 000	3 000 ± 1000 200 ± 40 300 ± 50	4.6 (8/8)	0.8%	5.7 (3/12)	0.3%

Together these results show that while the *spm3*(-) mutant is infectious to mosquitoes and capable of developing midgut stages, the mutant has a strong defect in salivary gland invasion. *Spm3*(-) salivary gland sporozoites are mostly incapable of continuous gliding motility and show a so far undescribed helical motility. In addition, *spm3*(-) parasites have a prolonged liver stage development phase but as soon as they have appeared in the blood stream, they develop similarly fast to WT parasites.

3.3.2 SPMTs dissociate from the IMC in *spm3*(-) sporozoites

To investigate the defect that led to reduced salivary gland invasion and altered motility, which ultimately impacted transmission efficacy, SPMT organization in *spm3*(-) was analysed in detail using TEM. For this, I fixed *spm3*(-)-infected midguts at day 11 to day 15 post infection. My colleague Buyuan He and Stefanie Gold from the EMCF then processed my samples into thin sections of 70 nm thickness allowing to investigate SPMTs in cross-sections of midgut sporozoites and Lilian Dorner, a research assistant of our laboratory, acquired the TEM images.

While SPMTs of WT largely showed the classical 15+1 arrangement with all SPMTs being closely associated to the IMC (**Figure 4**); various degrees of SPMT displacement could be observed in the *spm3*(-) mutant (**Figure 25 A, B, Supplementary Figure 9**). At the apical end of the parasite, as discernible by a small sporozoite diameter, SPMTs largely showed an SPMT arrangement as described for WT parasites (**Figure 25 A**, first *spm3*(-) panel). As the distance from the apical end

increases (as evident by a larger sporozoite diameter, the presence of apical organelles such as micronemes and rhoptries, and a wider inter-SPMT spacing), the SPMTs were often no longer IMC-associated but located deeper within the cytoplasm (**Figure 25 A**, second to fourth *spm3*(-) panels). The distance between SPMTs and IMC was quantified by measuring from the center of the SPMT to the inner side of the IMC. A threshold of 40 nm, based on previously reported SPMT-IMC distances in sporozoites (112), was used to classify SPMTs as either IMC-associated (≤40 nm) or dissociated (> 40 nm). In WT sporozoites, only 1.2% of SPMTs analysed were dissociated compared to 18.7% of *spm3*(-) sporozoites (**Figure 25 C**).

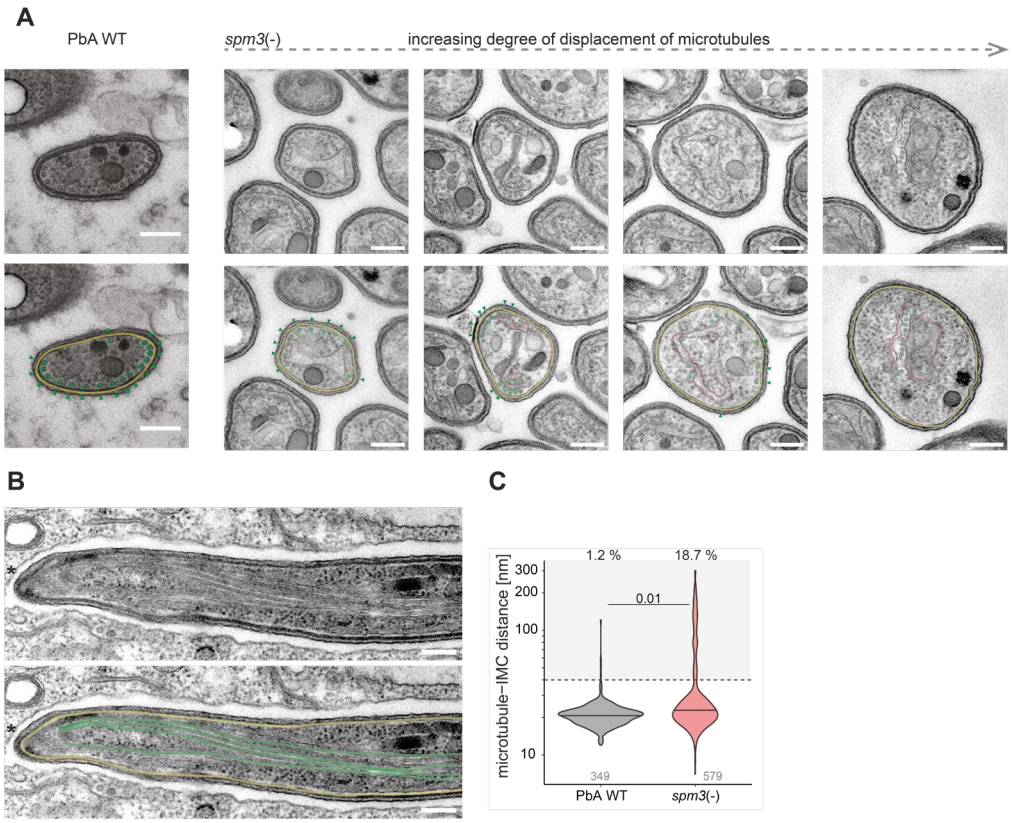

Figure 25 SPMTs dissociate from the IMC in *spm3*(-) sporozoites. TEM cross-images from PbA WT (left) and *spm3*(-) (right) sporozoites within oocysts at day 15 after mosquito infection. Single images are ordered according to increasing degree of SPMT displacement. Scale bars: 200 nm. Green, SPMTs; yellow, IMC; magenta, membrane of unknown origin. **B)** Longitudinal section through a *spm3*(-) midgut sporozoite. Note the dissociation of the SPMTs from the IMC with increasing distance from the apical end (marked by an asterisk). **C)** Distance between SPMTs and IMC, with the black line indicating the median. The dashed line indicates the preset cutoff value of 40 nm; distances of 40 nm or less were defined as IMC-associated SPMTs based on reported SPMT-IMC distances by Ferreira *et al.* (112). Grey background highlights all values considered dissociated, with the corresponding percentages above. Grey numbers at the bottom indicate total numbers of SPMTs analysed in 31 PbA WT and 54 *spm3*(-) sporozoites, respectively. Spread of SPMT-IMC distance was statistically analysed using a linear mixed model. Figure and legend were previously published and adapted for this thesis (248).

Additionally, SPMTs were frequently found associated with non-IMC membranes, whose origin still remains unclear (**Figure 25 A**, magenta-coloured). Yet, there was no difference between WT and *spm3*(-) considering both the distance of SPMTs towards these non-IMC membranes nor the number of SPMTs associated with them (**Figure 26 A-C**).

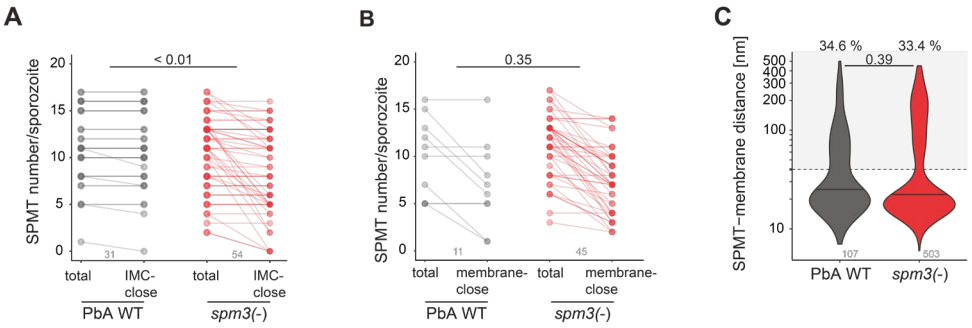

Figure 26 *Spm3* deletion results in less SPMTs associated to the IMC but unchanged association to membrane. A, B) Absolute numbers of SPMTs close to the IMC (A) or close to membranes (B) (≤40 nm) compared to total SPMT numbers. Opacity reflects the number of sporozoites observed with the given SPMT count, with higher opacity indicating more values. Grey numbers below represent the total number of sporozoites analysed per line. Statistical differences in IMC-close versus total SPMT numbers between parasite lines were determined using two-sided *t* test. **C)** SPMT-membrane distances, with median shown as black line and the 40 nm cutoff as dashed line. Values > 40 nm (grey background) were considered dissociated, with corresponding percentages indicated on top. Grey numbers below indicate total number of SPMTs analysed from 11 PbA WT and 45 *spm3*(-) sporozoites, respectively. Statistical analysis using a linear mixed model. Figure and legend were previously published and adapted for this thesis (248).

Taken together, SPMTs in *spm3*(-) sporozoites are disorganized with increasing distance from the apical end. Not only do SPMTs at the distal end dissociate away from the IMC, but the inter-SPMT distances are also altered in the *spm3*(-) mutant. This points to a role of SPM3 in tethering the SPMTs to the IMC and potentially also connecting the SPMTs with each other.

[For the TEM analysis, I infected *Anopheles* mosquitoes and isolated and fixed infected midguts. My colleague Buyuan He and Stefanie Gold from the EMCF then processed the samples and Lilian Dorner, a research assistant of our laboratory, acquired the TEM images. Annotations of TEM images and TEM analysis were done by me.]

3.3.3 SPM3 depletion causes dissociation of SPMTs at the distal end and impaired ookinete gliding motility

It is quite surprising that despite both sporozoites and ookinetes possessing SPMTs, a defect was only observed in sporozoites, with no apparent effect on ookinetes, as indicated by the normal oocyst counts. Furthermore, *spm3* is predicted to be expressed throughout mosquito stage development with expression peaking at ookinete and sporozoite level, as well as in schizonts and female gametocytes (245). This led me decide to take a closer look at ookinetes in the *spm3*(-) mutant.

First, *in vitro* ookinete cultures were set up to assess whether the *spm3*(-) mutant can actually form ookinetes and if so, whether *spm3*(-) ookinetes are motile. The *spm3*(-) mutant was able to develop into mature ookinetes. Performing *in vitro* ookinete gliding assays revealed only 19% of *spm3*(-) mutants being motile compared to 53% of WT ookinetes (**Figure 27 A**). Despite a reduced proportion of motile ookinetes, motile *spm3*(-) ookinetes reached speeds comparable to WT (**Figure 27 B**).

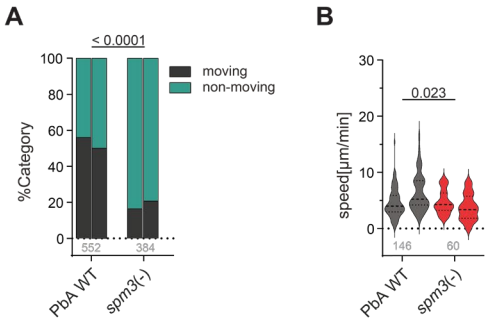

Figure 27 *Spm3*(-) ookinetes are less motile but reach comparable speeds to PbA WT. A) *In vitro* ookinete gliding assay of two biological replicates per parasite line. Grey numbers show total number of ookinetes analysed per line, individual replicates for replicate 1-2: PbA WT: 200/352, *spm3*(-): 207/177. For statistical analysis, Fisher's exact test was used. **B)** Median speed of moving ookinetes. Grey numbers show total number of ookinetes analysed per line, individual replicates for replicate 1-2: PbA WT: 99/47, *spm3*(-): 44/16. Shown is the median as dashed line with the quartiles shown as dotted lines. For statistical analysis, unpaired t-test (Mann-Whitney test) was performed.

In both sporozoites and ookinetes, SPMTs provide cell stability and rigidity required for both cell motility and host cell invasion or traversal. While SPMTs in sporozoites show the 15+1 arrangement as described before, ookinetes possess up to 60 equally spaced SPMTs (**Figure 4**) (114, 220). In addition, SPMTs in sporozoites run from the apical end until approximately the nucleus with the single SPMT being slightly longer than the other 15 and hence covering around 2/3 of the sporozoite length (113). In contrast, all 60 SPMTs in ookinetes occupy the entire length of the cell (220). Performing TEM on oocyst sporozoites allowed me to uncover the dissociation phenotype of SPMTs from the IMC in cross-sections. Despite being a powerful tool for visualizing subcellular structures without the need for an antibody staining, TEM is limited in its ability to

examine SPMTs across the entire cell. In order to visualize SPMTs and assess their organization on the whole-cell level, either cryotomography or whole-cell U-ExM is required. As U-ExM allows assessment of cellular structures in higher throughput than is possible with cryotomography and the direct observation on a whole-cell level rather than the reconstruction from single-slices obtained from tilt-series, I decided to use U-ExM for my purposes. U-ExM has been well-established in *Plasmodium* research, however only for asexual blood stages and ookinetes and not yet for sporozoites. I hence decided to establish U-ExM in our laboratory and investigate SPMT organization in *spm3*(-) ookinetes first.

During U-ExM, *spm3*(-) and WT ookinetes were labelled with an anti-tubulin antibody to stain both SPMTs and spindle microtubules, an anti-polyglutamylation antibody that selectively stained subpellicular but not spindle microtubules, and Hoechst. Beyond target-specific antibody staining, the entire cell can be visualized using pan (N- hydroxysuccinimide) NHS ester staining, which provides a cellular context. Thus, ookinetes were additionally stained with NHS-ester.

Performing U-ExM, an expansion factor between 4.2-4.5 could be typically achieved resulting in approximately 40 µm long ookinetes (**Figure 28 A**). Both the anti-tubulin and anti-polyglutamylation labelling visualized SPMTs on single-microtubule resolution and even allowed to visualize the apical polar ring as a separate structure, which cannot be resolved with classical IFA. In WT or WT-like (*spm3-gfp*) ookinetes, SPMTs were located close to the IMC. While they initially appear as rafts of several SPMTs at the apical end as has been previously observed (117, 249), shortly thereafter they were equally spaced towards each other and extended from the apical end towards the distal end of the parasite. In contrast, U-ExM revealed that *spm3* depletion also affects SPMT organization in ookinetes. While SPMTs showed WT-like arrangement at the apical end of the cell, single SPMTs detached from the IMC and extended into the cytosolic space towards the distal end of the parasite. Similarly to the detachment phenotype observed in sporozoites, different degrees of SPMT disorganization could be observed with the most extreme phenotypes having seemingly curled up SPMTs. Regardless of the degree of detachment (except for very extreme, curled up SPMTs), SPMTs in *spm3*(-) ookinetes had normal lengths and were evenly polyglutamylated.

To quantify the extend of SPMT dissociation, I designed an analysis pipeline using Fiji (see 5.3.21). In this analysis, I aimed to determine the SPMT arrangement at three positions along the longitudinal axis. Based on the whole parasite length, an apical, nuclear and distal position were set automatically by Fiji to exclude any bias. SPMT organization was then semi-automatically analysed (using the anti-polyglutamylation signal to exclude any cross-signal from the spindle microtubules) at an inner/cytosolic area and an outer/IMC-close ring. Taking the two signals, an outer/inner signal ratio can be calculated. Based on the phenotype observed in the 3D-projected images, a ratio larger than one was expected for both WT and *spm3*(-) ookinetes at the apical end,

and a smaller ratio less or equal to one at the nuclear and distal position for the mutant (**Figure 28 B).** As expected, ratios in WT parasites were above one at all three longitudinal positions (**Figure 28 C**). In comparison, ratios determined of the *spm3*(-) mutant differed significantly at all three positions from the WT and were all close to one.

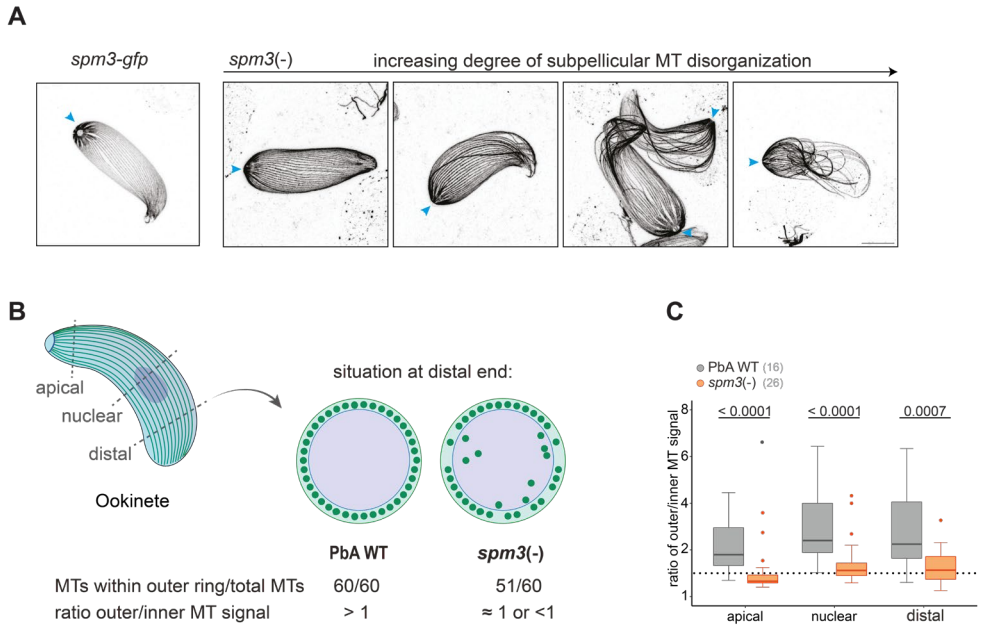

Figure 28 *Spm3* depletion causes dissociation of SPMTs at the distal end. A) U-ExM of ookinetes stained for SPMTs (poly-glutamylation staining). The apical end of the parasite is indicated by a light-blue arrowhead. Shown are representative 3D-interpolated images. Scale bar, 10 µm (expansion factor: ~4.2-4.5). **B, C)** Analysis of SPMT arrangement at an apical, nuclear and distal position along the parasite's longitudinal axis. At each longitudinal position, the microtubule signal intensity was measured within an outer ring and an inner ring and the ratio between outer and inner signal intensities is plotted (median with interquartile range). For statistical analysis, unpaired t-test (Mann-Whitney test) was performed. A total of 16 PbA WT and 26 *spm3*(-) ookinetes were investigated.

In summary, while the SPMT dissociation phenotype was initially only observed in *spm3*(-) midgut sporozoites, also ookinetes show a partial detachment phenotype. From the total 60 SPMTs present in ookinetes, only a small fraction exhibited detachment from the IMC, resulting in a reduced ratio of IMC-associated to dispersed SPMTs. Despised this, the majority of ookinetes remained viable and capable of penetrating the midgut epithelium to establish an infection.

3.3.4 SPM3 localizes along the SPMTs but is absent from the apical end

Upon *spm3* deletion, SPMTs in both ookinetes and sporozoites dissociated from the IMC towards the distal end of the parasite but remain tightly connected to the IMC at the apical end. This implies that the regulation of SPMTs might differ between the apical and distal end, either due to the varying expression and localization of linker proteins connecting SPMTs to the IMC along the longitudinal axis, or as a result of protein redundancy at the apical end but not the distal end. To test whether the observed phenotype in the *spm3*(-) mutant correlates with the localization pattern of SPM3, *spm3* was C-terminally with GPF (**Figure 10**). Based on previous work by our collaborators Jan Stephan Wichers-Misterek and Paolo Mesén-Ramírez from Hamburg, who at the time worked on *P. falciparum spm3*, and data published by Birnbaum *et al.* (250), the same 19-amino acids-long linker (primarily encoding for arginine, alanine and glycine) was inserted between the *spm3*-ORF and *gfp* accordingly.

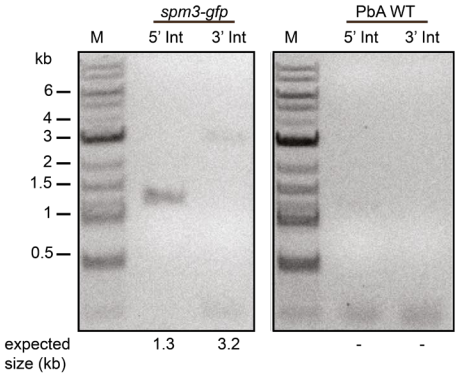

Figure 29 Generation of *spm3-gfp*. Genotyping PCRs of *spm3-gfp* compared to PbA WT (control). Primers used for verify 5' and 3' integration are indicated in **Figure 10**. Single crossover event will lead to the addition of a *gfp*-tag together with the insertion of the selection cassette. Generated tagging lines represent mixed populations. Expected amplicon sizes are indicated at the bottom of the gel images. Int – integration, kb – kilobase, M – marker, WT – wildtype. Figure was previously published and adapted for this thesis (248).

To determine the stages at which *spm3* is expressed, the *spm3-gfp* (**Figure 29**) line was monitored throughout its life cycle. SPM3-GFP was detected in oocysts as well as in midgut and salivary gland sporozoites (**Figure 30 A**). Thereby, SPM3-GFP was highly expressed, allowing its visualization without the need of any signal-amplifying antibody. The GFP-tag did not affect SPM3 function as parasites developed normally (**Figure 30 B, C**).

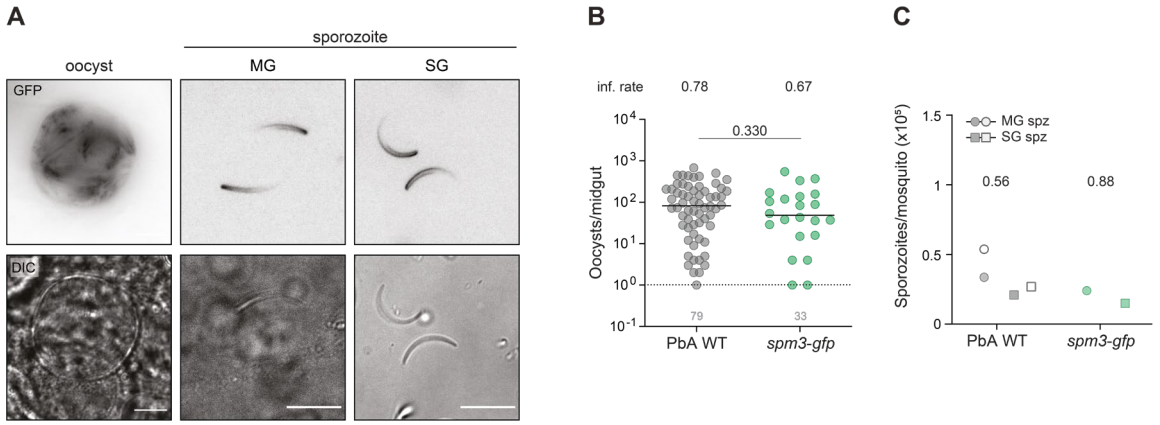

Figure 30 *Spm3-gfp* tagged parasites progress normally through the life cycle. A) Live-cell imaging of endogenously tagged *spm3-gfp* at the oocyst stage and free midgut (MG) and salivary gland (SG) sporozoites. Scale bars: 10 µm. **B)** Oocyst numbers per midgut with each dot representing one midgut. Median shown as black line. Mean infection rates on top of the graph; total midguts analysed per line as grey numbers at the bottom. Statistical analysis of oocyst numbers using Mann-Whitney test; of infection rates using Fisher's exact test. **C)** Sporozoite counts of salivary glands and midguts, with corresponding numbers of same infection indicated by same symbol filling. Average ratios of salivary gland/midgut sporozoites shown on top of the graph. Note that WT data in panels B and C were used for comparison only and represent the PbA WT data set shown in **Figure 23**. Mosquitoes from two (PbA WT) and one (*spm3-gfp*) independent cage infection were analysed. Figure and legend were previously published adapted for this thesis (248).

Performing an IFA using SiR-tubulin to stain for microtubules, we observed that SPM3 localizes to SPMTs in both sporozoites and ookinetes (**Figure 31 A).** However, a clear SPM3-free region at the apical end was noticeable. To quantify the dimensions of this SPM3-free region, both the GPF and SiR-tubulin intensity along the longitudinal axis of SPM3-GFP ookinetes were measured showing a reduced GFP-intensity at the first ~ 7% length of the ookinete (**Figure 31 B**). Contrary to ookinetes, SPM3-GFP occupied the whole length of SPMTs in sporozoites, suggesting that there might be slightly different functional requirements of SPM3 across stages.

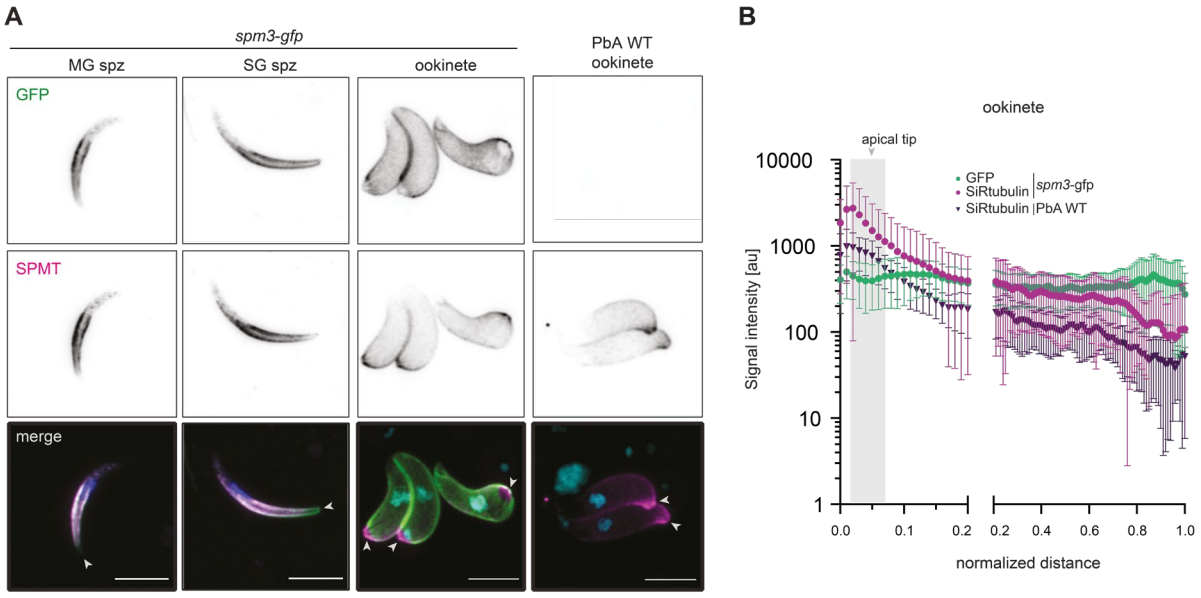

Figure 31 SPM3 localizes along the SPMTs but is absent from the ookinete's apical end. A) Images of ookinetes and sporozoites stained with SiR-tubulin (microtubules) and Hoechst (nucleus) prior to fixation. Same contrast settings for all images. Shown are maximum Z-projections. Representative of at least 7 images taken. Arrowheads point to the apical end of the parasite. Scale: 5 µm. **B)** Line-plots of ookinetes from A along apical-distal axis. Grey bar highlights region at the apical end that shows reduced SPM3-GFP signal in *spm3-gfp* ookinetes. A total of 11 WT ookinetes and 19 SPM3-GFP ookinetes were measured. Spz – sporozoite.

To summarize, SPM3-GFP is highly expressed in both ookinetes and sporozoites. While SPM3 follows the SPMT pattern from the apical end to the distal end of the sporozoite, an apical region that is free from SPM3 was detected in ookinetes.

[While I generated the *spm3-gfp* line, the master thesis student Katharina Röver, under my supervision, prepared and imaged the *spm3-gfp* ookinetes and I performed the GFP intensity analysis.]

4. Discussion

4.1 MIPs are dispensable for parasite development under natural conditions but contribute to high SPMT stability under cold stress

Microtubule function and identity are regulated by multiple factors collectively referred to as the tubulin code, which includes MAPs that interact with the microtubule lattice. MIPs bind to the microtubule lumen and are broadly recognized to be critical for maintaining microtubule stability across various organisms (reviewed in (201)). However, in *P. berghei*, the deletion of *spm1* or *trxL1*, individually or in combination, had no detectable effect on parasite life cycle progression. This indicates that MIPs are not essential for parasite development including transmission to and from the mosquito.

4.1.1 SPM1 and TrxL1 are dispensable for parasite life cycle progression

MIP single KO deletion lines could be easily generated revealing no phenotype during blood stage development (**Figure 7**). Furthermore, MIP deletion mutants demonstrated normal development within the mosquito vector (**Figure 8**). Although sporozoite gliding behaviour was significantly different between *trxL1*(-) and WT, this was considered not to be biologically relevant as all three mutant parasite lines transmitted normally from the mosquito to the mouse (**Figure 9**). This suggests that the complex 3D host tissue environment may compensate for the motility defects observed in 2D *in vitro*.

Initial studies in *T. gondii* identified three MIPs—SPM1, TrxL1, and TrxL2—organized within the microtubule lumen (228). Similarly to the work presented here, the deletion of all MIPs in *T. gondii* under normal conditions resulted in no discernible phenotype. Only under stress conditions, such as chemical treatment with cholic acid, did some of the MIP KO mutants have shorter or absent SPMTs (228). Similarly, a separate study in *T. gondii* showed that SPMTs from *spm1*(-) mutants completely collapsed upon deoxycholate treatment; a common method used to extract microtubules from cells including SPMTs from *T. gondii* (236). SPMTs could be recovered upon complementation with *spm1*, strongly suggesting that SPM1 contributes to the high stability of SPMTs under stress conditions.

Structural modelling of *Plasmodium* SPMTs positioned SPM1 and TrxL1 as two half-crescent structures within the microtubule lumen, separated by a small gap as TrxL2 is not present in *Plasmodium* (112). Despite this gap, its impact on microtubule stability appears to be minimal, as SPMTs remained functional even in the absence of both SPM1 and TrxL1. This observation is supported by studies in *T. gondii*, where *trxL2* deletion alone did not affect parasite viability, even under chemical stress (228). Given the spatial constrains within the microtubule lumen, it is quite

unlikely that several additional proteins besides TrxL1 and SPM1 would fit into the microtubule lumen.

Alternatively, structural stability of SPMTs might be ensured through MAPs that bind to the outer surface of SPMTs. Co-immunoprecipitation studies in *T. gondii* using TrxL1 as bait identified four additional proteins, termed TrxL1-associated proteins 1–4 (TLAP1–4), that localized to SPMTs (237). Among them, TLAP 1-3 have orthologues in *Plasmodium,* though *Tg*TLAP3 shares only very low homology to its *Plasmodium* counterpart (237, 238). Combining *spm1* and *tlap2-3* in a triple KO in *T. gondii* led to significantly shorter SPMTs (240). Interestingly, triple KO parasites moved in more linear rather than the characteristic helical motility tracks found in *T. gondii* parasites, without actually affecting motility speed or invasion efficiency (240). Hence, it might be possible that TLAP function in apicomplexans is conserved and similarly to *T. gondii* TLAPs might ensure sufficient SPMT stability in *Plasmodium*, even in the absence of SPM1 and TrxL1.

In addition to MAPs, PTMs contribute to the tubulin code and play a role in microtubule functionality. One notable PTM is the acetylation of α-tubulin at position 40 (K40) by the αTAT as it represents the only known PTM that faces the microtubule lumen (251, 252). In *T. gondii*, acetylation of K40 was shown to contribute to microtubule stability, and ablation of K40 acetylation resulted in severe nuclear division and parasite segregation defects (253). Intriguingly, all rodent-infecting *Plasmodium* species including *P. berghei* lack the αTAT and code for a glutamine instead of a lysine at position 40 (Q40). This glutamine could act as an acetyl-mimic and hence was initially thought to confer inherent microtubule stability. However, in line with the MIP deletion mutants, substituting glutamine with lysine (Q40K) in *P. berghei* did not result in any phenotypic difference compared to WT (MSc thesis Katharina Röver). These findings suggest that the two factors, MIPs and Q40, might compensate for each other and a combined KO/mutation might compromise microtubule stability.

To test whether SPMT stability is ensured by both MIPs and outer MAPs, deletion of *spm1* and *trxL1* could be combined with the additional KO of TLAPs as described in *T. gondii*. Similarly, the double deletion mutant could be combined with the removal of PTMs and their potential mimics, either by the above described Q40K point mutation However, with the reoccurring issues in combining multiple gene KOs (further discussed in 4.1.2), this might be challenging.

The lack of a phenotype in MIP-deletion mutants suggests functional redundancy among proteins stabilizing the SPMTs. SPM1 and TrxL1 form part of the interrupted luminal helix in SPMTs, which was first characterized in *T. gondii* and recently identified in the SPMTs of *Plasmodium* (112, 228). While the interrupted luminal helix is present in the SPMTs of ookinetes and sporozoites, it is notably absent in merozoites, explaining why deletion of *spm1* and *trxL1* did not impact blood-stage development. But why do ookinetes and sporozoites, but not merozoites require highly

stable SPMTs with SPMT stability possibly ensured by multiple compensatory pathways? Compared to merozoites that only exist extracellularly for a very short time frame before invading the next erythrocyte (48), ookinetes move within the midgut to then traverse the midgut epithelium within approximately 1.5 min (254), while sporozoites circulate with the hemolymph for up to two weeks. Besides invasion/traversal time, also the temperature, to which different parasite stages are exposed to, differ (further discussed in 4.1.7). Hence, a high SPMT stability might simply not be necessary for merozoites but important for ookinete and sporozoite gliding and midgut traversal or salivary gland invasion, respectively. Taken together, the high stability of SPMTs in apicomplexan parasites is very likely conferred by a multitude of MAPs that bind both inside and outside of the SPMTs combined with glutamine at position 40 in α-tubulin, which together with SPM1 and TrxL1 presumably ensures a stable microtubule state. Together these factors ensure that potential lack of stability by deletion of MIPs individually or in combination is compensated sufficiently.

4.1.2 Combinational deletion of *spm1*, *spm2* and *trxL1* might be essential for parasite development

One of the possible factors compensating for deletion of both *trxL1* and *spm1* could be a MAP such as the TLAPs or *spm2*. However, deletion of *spm2*, whether independently or in combination with *spm1*, did not reveal any phenotypic differences compared to WT parasites (**Figure 19**), highlighting the remarkable robustness of SPMTs in *Plasmodium*. Building on this robustness, I attempted to further assess the stability of SPMTs and potential MAP redundancy by generating a triple KO (*spm1*, *trxL1*, and *spm2*), combining two MIPs (*spm1* and *trxL1*) with one putative outer MAP (*spm2*). Despite employing various strategies, these attempts were unsuccessful. While single and double KOs were generated relatively efficiently, creating the triple KO proved significantly more challenging due to issues with negative selection, low transfection efficiency, and difficulties in obtaining isogenic clones.

Negative selection of *spm1*(-)/*spm2*(-)-*gfp* and *trxL1*(-)/*spm2*(-)-*gfp*, a necessary step to recycle the selection cassette before introducing *trxL1(-)* or *spm1(-)*, consistently failed. For example, a limiting dilution of *spm1*(-)/*spm2*(-)-*gfp* negative selection using ten mice resulted in only three parasite-positive mice, all of which retained the selection cassette. This was unexpected, as negative selection is typically a reliable method as it does not disrupt potentially essential genes. Further, other mutant parasite lines generated with the SIL6 plasmid were successfully subjected to negative selection, ruling out the plasmid as source of the issue (255). While parasitemia of the *trxL1*(-)/*spm2*(-)-*gfp* donor mouse as expected initially declined upon negative selection, this behaviour was not observed in the *spm1*(-)/*spm2*(-)-*gfp* donor mouse; potentially explaining the observed issues. Additionally, a mutation in the *yfcu* gene, which could confer resistance to 5-FC

treatment, could explain the observed failures. However, sequencing of the selection cassette from the three *spm1*(-)/*spm2*(-)-*gfp* clones revealed no mutations in *yfcu*, ruling out this hypothesis.

Interestingly, both *spm1*(-)/*spm2*(-)-*gfp* and *trxL1*(-)/*spm2*(-)-*gfp* involved *spm2*(-) as a secondary KO and both encountered negative selection failures. Unlike *spm1* and *trxL1*, which are separated from neighbouring ORFs by at least 1000 base pairs (256), the 3' end of *spm2* lies only 489 base pairs away from the adjacent gene *PBANKA_1444900 (***Figure 32***)*.

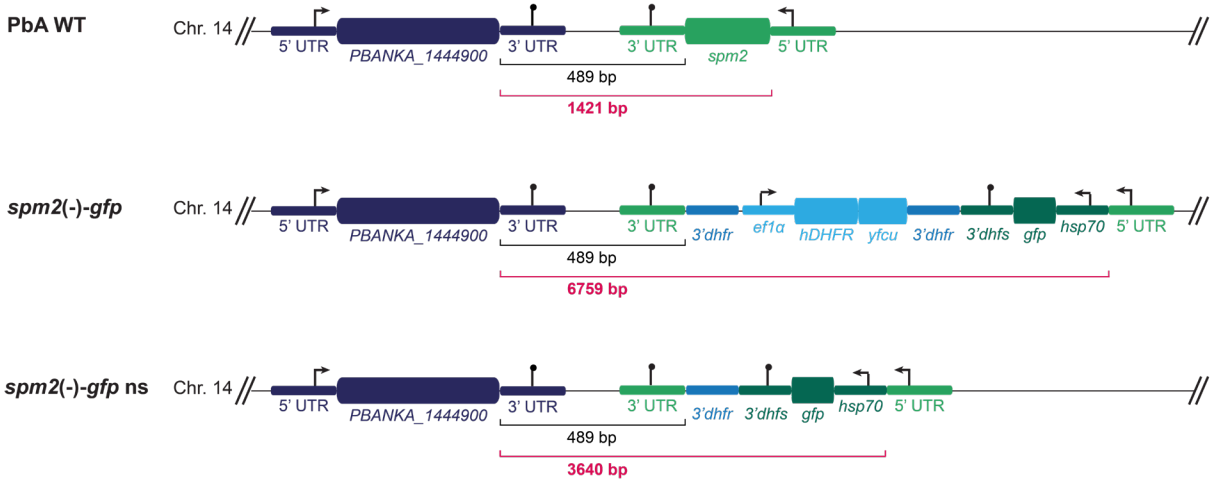

Figure 32 *spm2* and its genomic environment. The 5' UTR is only separated by 489 bp from the 3' UTR of PBANKA_1444900. Bp – base pair, Chr. – chromosome, *dhfr – dihydrofolate reductase, dhfs – dihydro-folate reductase synthase, hsp70 – heat shock protein 70,* UTR – untranslated region.

KO constructs typically include 600–800 base pairs of homology regions for recombination (see 5.2.1). The proximity of *PBANKA_1444900* necessitated the use of a shorter 3' homology region (400 base pairs) to avoid disrupting this neighbouring gene. Despite these precautions, it is possible that the 3' homology region of *spm2* contains regulatory elements critical for *PBANKA_1444900* expression, which may have been disrupted during the introduction of *spm2*(-). Alternatively, the insertion of both a selection cassette and *gfp* could have resulted in excessive separation between *PBANKA_1444900* and its regulatory elements. The latter hypothesis could be tested by introducing the *spm2*(-) only with the selection cassette without the *gfp* maker; however, this approach would require the generation of a new parasite line. Alternatively, regulatory elements within the hsp70 promoter, which is part of the selection cassette and drives GFP expression, may have come in proximity to the *PBANKA_1444900* gene and disrupted its expression upon negative selection. *PBANKA_1444900* is annotated as a vacuolar transport chaperone (256). While it is predicted to be dispensable for parasite survival (257), its function remains unexplored. Interestingly, *PBANKA_1444900* was identified as being part of the sporozoite secretome (258). Chaperones are crucial for maintaining protein homeostasis, and vacuolar transport chaperones are suggested to play a role in trafficking proteins to and from the parasitophorous vacuole (PV) (reviewed in (259)). During red blood cell invasion, the parasite

forms a PV, an enclosed space where asexual replication occurs. Although impaired PV function may not completely prevent replication, it could impair nutrient acquisition or protein export, as chaperones are potentially involved in forming channels within the PV membrane.

In addition to the difficulties with negative selection, subsequent transfections were largely unsuccessful, with transfection efficiencies dropping below 20%. Though most combinational KOs in *P. berghei* represent double KOs, the successful generation of a triple KO has been reported, demonstrating that the combined deletion of three genes is possible (260). Transfection involves exposing parasites to brief electric shocks to facilitate entry of foreign DNA. Repeated transfections to generate the triple KO may have introduced off-target mutations. Accumulation of such mutations over multiple transfections could be lethal to the parasites and thus would prevent the establishment of the triple KO. While whole-genome sequencing could identify potential off-target mutations, this was beyond the scope of this project. To minimize off-target effects, fewer consecutive transfections could be performed by simultaneously deleting multiple genes located in close proximity on the same chromosome. From the three MAPs, only *trxL1* and *spm1* are located on the same chromosome However, *trxL1* and *spm1* are still separated by over 300 000 base pairs, making this strategy impractical (256). Alternatively, CRISPR/Cas9 deletion of the three genes could be attempted or of two genes in a negatively selected deletion line (261–263). However, this would necessitate an entire new cloning and gene deletion strategy.

In summary, the generation of two distinct double KO combinations (*trxL1*(-)/*spm1*(-) and *spm1*(-)*/spm2*(-)-*gfp,* the *trxL1*(-)/*spm2*(-)-*gfp* was not yet characterized) that all lack a clear phenotype demonstrated the high degree of redundancy and robustness of SPMTs. Similarly, in *T. gondii*, the combined deletion of *tlap2* and *spm1* did not yield a phenotype under native conditions. Only the *tlap2*(-)/*tlap3*(-)/*spm1*(-) triple KO exhibited much shorter SPMTs compared to WT parasites (238, 240). This suggest, that a successfully generated triple KO mutant in *P. berghei* might also reveal a phenotype similar to the one observed in *T. gondii*, but the current data is unfortunately inconclusive at this point. It might well be possible that a triple KO couldn't be obtained as a lack of all three proteins at the same time does have a phenotype in blood stages. If this was the case, using an inducible knockout system that allows for MAP expression during blood stage development could be beneficial.

4.1.3 MIP binding hierarchy to microtubule lumen is conserved across stages and species

To investigate the localization of SPM1 and TrxL1, I tagged each gene with GFP at its C-terminus. Both SPM1-GFP and TrxL1-GFP progressed normally through the life cycle (**Figure 12**). To further explore whether the binding hierarchy described in *T. gondii*—where SPM1 anchors TrxL1 to the microtubule lattice (228)—is conserved in *Plasmodium*, I generated *spm1-gfp* and *trxL1-gfp* lines in both WT and the respective complementary KO backgrounds (*trxL1*(-) or *spm1*(-)) (**Figure 11**).

Both SPM1 and TrxL1 were highly expressed during the mosquito stages, requiring no antibody staining to enhance the signal, and both localized along SPMTs. SPM1 consistently followed the SPMT localization pattern in ookinetes and sporozoites (**Figure 13**, **Figure 15**). This was regardless of the genetic background, indicating that its localization is independent of TrxL1. Conversely, TrxL1 only partially colocalized with SPMTs in both stages, showing to be enriched at the apical end and around the nucleus. These finding are in contrast to prior observations in *T. gondii*, where both SPM1 and TrxL1 showed identical localization along SPMTs (236, 237). It is therefore reasonable to hypothesize that GFP tagging enables visualization of TrxL1 within its cellular context but may interfere with its native localization (discussed further in section 4.1.5). Notably, TrxL1 lost its SPMT-like localization in the absence of SPM1 (**Figure 14**, **Figure 16**), strongly suggesting that SPM1 is required to anchor TrxL1 to the microtubule lattice. *In vitro* assays performed by Gil Henkin from the laboratory of Simone Reber (MPI Berlin) further validated the presumed hierarchy between SPM1 and TrxL1. In this assay, Gil Henkin used porcine brain tubulin and investigated microtubule polymerization in response to the addition of purified *P. falciparum* SPM1 and TrxL1. Preliminary data of this experiment revealed that *Pf*TrxL1 is incapable of independently binding to microtubule and indeed requires *Pf*SPM1 for recruitment to the microtubule lattice (personal communication Gil Henkin). Taken together, both *in vitro* and *in vivo* data demonstrated that the binding hierarchy in which SPM1 links TrxL1 to the SPMT lattice is conserved between *T. gondii* and *P. berghei* (228, 237) *(***Figure 33**).

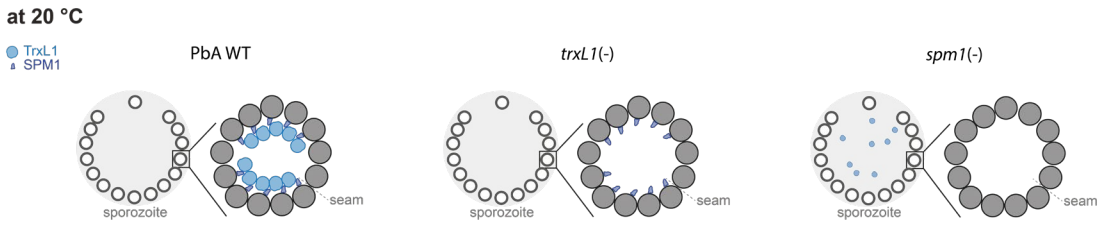

Figure 33 Hierarchy of MIP binding to the microtubule lumen. Localization of SPM1 and TrxL1 within the microtubule lumen. SPM1 links TrxL1 to the microtubule lattice and hence TrxL1 dissociates into the cytosol upon *spm1* deletion. Shown is the sporozoite cross-section.

4.1.4 How and when do MIPs enter the microtubule lumen?

While the binding hierarchy of SPM1 and TrxL1 was shown to be conserved between *T. gondii* and *P. berghei*, the precise timing of SPM1 and TrxL1 recruitment to SPMTs remains to be elucidated. It is unclear whether MIPs are incorporated into the growing SPMTs during their formation, or if they access the SPMT lumen via diffusion either through the plus end or by lateral entry, as demonstrated for αTAT, a protein localized to the microtubule lumen in most organisms but absent in *P. berghei* (207, 264). However, forced expression of αTAT-GFP localizes to *P. berghei* sporozoite microtubules (Master thesis, Madlen Konert (265)). Interestingly, in *T. gondii* it has been shown that SPM1 disperses into the cytoplasm upon knockdown of γ-tubulin. In *T. gondii*, γ-tubulin colocalizes with the nascent conoid and SPMTs during cell division, suggesting its role in the nucleation of these structures. Conditional knockdown of γ-tubulin in *T. gondii* resulted in disorganized and abnormally elongated SPMTs and dispersion of SPM1 into the cytosol (232), supporting the hypothesis that MIP loading occurs during microtubule growth. Given that γ-tubulin is a conserved component of the γ-TuRC, which is involved in microtubule nucleation across eukaryotes (153, 266–268), it is likely that γ-tubulin plays a similar role in *P. berghei*. Though γ-tubulin is also conserved in *Plasmodium*, its function in the parasite remains to be explored (269).

In addition, initial studies investigating dynamics of *Pf*SPM1 and *Pf*Trxl1 suggest that both proteins constitutively bind to the growing microtubule *in vitro* (personal communication Gil Henkin), further supporting the hypothesis of parallel MIP loading into the growing microtubule.

Together, these observations point to a coordinated mechanism of MIP incorporation during microtubule assembly. Further investigations into the interplay between γ-tubulin and MIPs, and generally the role of γ-tubulin in *Plasmodium*, will allow to understand this processes in more detail.

4.1.5 Tagging of TrxL1 appears to cause protein mislocalization

While SPM1-GFP exhibited complete localization along SPMTs, TrxL1-GFP displayed only partial colocalization, showing enrichment at the cell's apical end and around the nucleus (**Figure 13**, **Figure *14***, **Figure 15**, **Figure 16**). As discussed in the previous chapter, these finding are unexpected since the interrupted luminal helix, composed of SPM1 and TrxL1, forms a continuous structure according to focus ion beam (FIB)-milling data (112). This continuity suggests that TrxL1 and SPM1 localization should overlap entirely along the full length of the SPMTs.

To investigate TrxL1 localization, the gene was tagged with *gfp* at its C-terminus. The GFP-tag (~27 kDa) is comparable in size to SPM1 (~38 kDa) and TrxL1 (~23 kDa)(256). In confined environments such as the microtubule lumen, the addition of a tag similar in size to the native

protein could potentially interfere with its function. The choice of fluorescent tag and tagging site was based on previous studies in *T. gondii*. Wang *et al.* used a minimally invasive C-terminal HA-tag for TrxL1, while Liu *et al.* inserted an N-terminal mEmerald- tag, an improved GFP-based fluorescent tag of similar size (~27 kDa) (228, 237). Both publications demonstrated an evenly distributed microtubule-like localization pattern for TrxL1, indicating that the chosen tags did not interfere with protein function in this organism. Here, a C-terminal GFP-tag was selected because N-terminal tagging may lead to phenotypic alterations due to interference with protein folding of the tagged protein or potential masking of signal peptides present in the N-terminus (270). Additionally, the C-terminal tagging process is much quicker to perform with our standard toolbox.

The observed partial localization of TrxL1-GFP around the nucleus raises the possibility that it might have been misdirected to the endoplasmic reticulum (ER). The ER is a critical organelle involved in protein folding and processing and acts as a quality control through the ER-associated degradation pathway (271). Misfolded proteins can either be retained within the ER or misdirected to it, which might explain the atypical localization of TrxL1-GFP. Further experiments comparing the localization of C-terminal- versus N-terminal tagged TrxL1 with respect to the ER using ER-makers are needed.

To address the above discussed potential limitations, alternative strategies for C-terminal tagging could include using an HA-tag or the recently described alfa-tag (272). Both tags are minimally invasive but require secondary detection methods, such as antibodies for the HA-tag or nanobodies for the ALFA-tag, making them unsuitable for live-cell imaging. Wang *et al.* tagged SPM1 and TrxL1 with an HA-tag and could visualize SPM1 and TrxL1 localization in *T. gondii*, indicating that the HA-tagged protein can also access the microtubule lumen (228). Alternatively, the length of the linker between the protein of interest and the tag is a critical factor influencing protein flexibility. A longer linker provides greater flexibility for interactions with other proteins but may reduce the precision of localization. In this study, TrxL1 was separated from GFP by a six-alanine linker, comparable to the five-amino-acid linker used by Liu *et al.* to tag *Tg*TrxL1 with mEmerald (237). Future studies, optimizing the choice and the site of the protein tag could provide more accurate insights into TrxL1 localization without compromising TrxL1 functionality. This may help to distinguish whether the observed partial colocalization of SPM1 and TrxL1 reflects a real biological observation or rather an artefact caused by the tagging strategy. Importantly, adding a small non-fluorescent tag might allow the investigation of localization with U-ExM, where we and others failed to get anti-GFP antibodies to work.

4.1.6 The lack of TrxL1 might change the SiR-tubulin binding site

To investigate the role of SPM1 and TrxL1 as proposed MIPs of SPMTs in *Plasmodium*, parasites were stained with SiR-tubulin and/or anti-tubulin and fixed before proceeding to imaging. While WT parasites displayed robust SPMT staining with SiR-tubulin under standard conditions, all *trxL1* deficient mutants (*trxL1*(-), *spm1*(-) and *trxL1*(-)/*spm1*(-)ns) consistently showed reduced SiR-tubulin staining (**Figure 17**, **Supplementary Figure 7**). Similarly, all tagging mutants in which *trxL1* was deleted, showed inefficient SiR-tubulin staining, regardless whether ookinetes or sporozoites were stained (**Figure 15**, **Supplementary Figure 6**). In contrast, if SPMTs were stained with an anti-tubulin antibody, SPMTs in all parasite lines, including those that lack *trxL1,* were well visualized (**Figure 13**, **Figure 17**). The antibody staining pattern was consistent with data in *T. gondii*, in which *trxL1* deletion did not affect staining SPMTs using different anti-tubulin antibodies (236–238, 240). However, in one setup examining TrxL1-GFP localization in the *spm1*(-) background, TrxL1 mislocalized as expected, but surprisingly, SiR-tubulin staining appeared normal (**Figure 16**). This somehow contradicts the hypothesis that *trxL1* depletion generally disturbs SiR-tubulin binding side and ask for further investigation; especially as a WT control was missing in this particular dataset. With the exception of this particular dataset, the observed differences in SiR-tubulin versus anti-tubulin antibody staining raises the question whether *trxL1* deletion induces subtle conformational changes in the microtubule lattice, thereby impairing SiR-tubulin binding.

SiR-tubulin represents a docetaxol-derived live dye (160). Taxol-derivatives including docetaxol bind at the β-tubulin monomer located at the interior surface of the microtubule near the M-loop (159). This is distinct to MIP binding, as both TrxL1 and SPM1 bind at the α-/β-tubulin interface (228). Hence, how can the lack of TrxL1 reduces SiR-tubulin staining efficacy? There are two possible reasons why less efficient SiR-tubulin stainings were observed under some experimental conditions: 1) Fixation of cells differentially affects microtubule stability or 2) Increased flexibility of microtubules in the absence of TrxL1 reduces binding affinity of SiR-tubulin.

Fixation can generally alter microtubule configuration, with the extend of alteration depending on the specific fixation protocol and the cellular context (273). SiR-tubulin is a live dye and cannot be used to stain microtubules after fixation of cells. However, pre-staining microtubules with SiR-tubulin followed by fixation can preserve the microtubule state and thus the staining status. This approach has been successfully used to analyse SPMT length and number in *Plasmodium* tubulin mutants (113). It is plausible that microtubule fixation that would usually only lead to a minor alteration in microtubule configuration, is reinforced by *trxL1* deletion and results in suboptimal SiR-tubulin binding. One possibility to reduce destabilization of SPMTs simply by fixation would be to either reduce the concentration of the fixative or the length of fixation. Alternatively, gentler

fixatives such as methanol, successfully applied in U-ExM of *P. berghei* ookinetes, could be considered (220). Importantly, changes in fixation protocols require careful optimization, as they could impact staining outcomes (274).

For *T. gondii*, it is hypothesized that TrxL1 (together with SPM1) stabilizes SPMTs internally, and their absence might reduce microtubule rigidity (228). A reduced microtubule rigidity might either reduce SiR-tubulin incorporation into the microtubule lattice or increase dye dissociation rates due to the non-covalent binding nature of SiR-tubulin to microtubules. Notably, incubation of polymerized microtubules with taxol has been shown to increase microtubule flexibility (275); suggesting that both *trxL1* deletion and SiR-tubulin staining combined might result in highly flexible microtubules in which the SiR-tubulin dye cannot be retained. To test whether TrxL1 and SPM1 contribute to the rigidity of SPMTs, one could determine the flexural rigidity of SPMTs in the absence or presence of TrxL1. The flexural rigidity, also called bending resistance, describes how far the microtubule can be bend without significant deformation (276). The more rigid a microtubule is, i.e. the higher the flexural rigidity is, the more pressure can be applied without resulting in microtubule bending. To evaluate TrxL1's role in SPMT rigidity, flexural rigidity can be measured via optical tweezers or atomic force microscopy (275). Alternatively, computational modelling to simulate bending of microtubules under different conditions, hence in the absence/presence of TrxL1, could help to get an initial idea of SPMT stability. However, in a first experiment, one would probably want to test *in vitro* if SiR- tubulin binds to *Plasmodium* microtubules only in the presence of TrxL1.

Intriguingly, Cryo-ET studies in *T. gondii* identified MIPs, including TrxL1, as well as an unknown density on the interior surface of β-tubulin located at the taxol-binding site (228). While this density did not match any known protein densities, the authors speculated it might be originated from a small molecule that is specifically produced by the parasite to stabilize its own SPMTs (228). Hence it might even be that the lack of TrxL1 subsequently leads to dissociation of this potentially small molecule and both factors combined result in a loss in SPMT stability. It would be interesting to see whether cryo-ET of *Plasmodium* SPMTs would detect this small density as well. In case that also *Plasmodium* possesses such a small density, this would strongly indicate that apicomplexan share conserved mechanisms to ensure high SPMT stability.

In summary, the KO of *trxL1* appears to reduce SPMT stability, either directly or indirectly. The weakened ability of SiR-tubulin to stain SPMTs raises the question whether MIP deletions broadly compromise SPMT integrity. Although this reduced stability does not lead to observable phenotypic differences compared to WT parasites, it could increase the vulnerability of SPMTs to microtubule-targeting drugs, which are typically ineffective against apicomplexan SPMTs (277–280). To test this hypothesis *in vitro*, microtubules incubated with SPM1 and TrxL1 could be

exposed to varying concentrations of microtubule inhibitors to assess their protective role. Alternatively, MIP KO lines could be treated with these drugs, and SPMT integrity could be either directly analysed using microscopy or indirectly by force measurements using optical tweezers. It would be especially intriguing to test the effect of taxol or other taxane drugs in WT versus MIP KOs. If recruitment of the hypothesized small molecule to the taxol-binding site is MIP dependent, MIP KO mutants might become sensitive to taxol-treatment.

4.1.7 MIPs contribute to high SPMT stability and protect SPMTs from cold stress

Microtubules are ubiquitous in all eukaryotic organisms. However, different organisms live in different habitats and are exposed to different environmental conditions, including varying temperature ranges. Adaptation to these environments necessitates modifications in microtubule dynamics and stability. Studies in different *Xenopus* species adapted to distinct thermal habitats demonstrated that, despite a high degree of sequence similarity in their tubulins, tubulins from cold-adapted species exhibited lower activation energy, facilitating faster incorporation into growing microtubules (281). Structural analyses further revealed that the microtubule lattices formed by cold-adapted tubulins exhibited increased flexibility in lateral contacts (281). These findings highlight how microtubule dynamics can be fine-tuned to support cellular functions under specific environmental conditions.

MAPs have been proposed to contribute to the extraordinary stability and organization of SPMTs in apicomplexans (282). Although single and double MIP KO mutants displayed no discernible phenotypic differences compared to WT, their conservation across almost all apicomplexan species (238) suggests a conserved and important function. Given the parasite's exposure to fluctuating temperatures during its development, MAPs may play an important role in ensuring SPMT functionality under suboptimal thermal conditions. This raises the intriguing possibility that MAPs are essential for maintaining the stability and adaptability of SPMTs, particularly when the parasite encounters suboptimal conditions.

To test this hypothesis, our collaborator Gil Henkin in the Reber lab (MPI Berlin) examined microtubule stability under cold stress in the presence or absence of MIPs. Incubating microtubules on ice for 5-10 min *in vitro* typically results in complete depolymerization. While microtubules co-incubated with purified *Pf*SPM1 depolymerized under these conditions, the presence of both *Pf*SPM1 and *Pf*TrxL1 preserved a high proportion of polymerized microtubules (preliminary data, personal communication Gil Henkin). Furthermore, studies by Tengganu *et al.* demonstrated that two outer MAPs (Tlap2, Tlap3) along with one MIP (SPM1) are critical for maintaining SPMT integrity in *T. gondii*. In the absence of these proteins, the triple KO mutant possessed only short SPMTs, which completely depolymerized upon cold exposure (238, 240).

To assess whether these observations from previous studies could be replicated in *Plasmodium* in an *in vivo* context, and to investigate the protective roles of SPM1 and TrxL1, the SPMTs of salivary gland sporozoites from single and double MIP KO mutants were analysed at different temperatures. Cross-analysis of mutant parasites using the anti-tubulin staining revealed a disorganization of SPMTs upon cold-incubation (**Figure 18**). As SPMTs align at the cell border, placing an intensity profile should result in two peaks that resemble a "M"-shape. While WT parasites showed consistently M-shape intensity profiles independent of the temperature, this profile was only present in mutants incubated at 20 °C. Upon cold incubation, peaks of the intensity profiles flattened indicative for a dispersion of SPMTs towards the cytosol. This means, that SPM1 and TrxL1 are needed to protect SPMTs against cold stress.

At this point, it was unclear, whether the observed dispersion of tubulin signal in the MIP KO mutants was due to SPMT fragmentation into smaller pieces or due to SPMT depolymerization. SiR-tubulin and anti-tubulin staining were used in an attempt to differentiate between polymerized and monomeric tubulin along the parasite's longitudinal axis. SiR-tubulin predominantly incorporates into polymerized microtubules, whereas anti-tubulin binds to both monomeric and polymerized tubulin (160). Under normal conditions, such as in WT at RT, the combination of both stainings were expected to produce overlapping signals in regions containing microtubules, with anti-tubulin staining alone identifying regions of monomeric tubulin. Unexpectedly, even in WT parasites, SiR-tubulin and anti-tubulin signals did not colocalize at the apical region where microtubules are present, thus preventing to differentiate between the two tubulin states (**Figure 17**, **Figure 18**). As SPMTs are tightly packed within the parasites apical end, this region might simply not be as well accessible for the antibody. Additionally, SiR-tubulin staining was non-functional in all MIP mutant parasites (**Supplementary Figure 6**) (see 4.1.6). While SiR-tubulin has been successfully used for SPMT studies in *Plasmodium* (113), alternative tubulin dyes such as Tubulin Tracker or ViaFluor® could be considered as they also bind to polymerized tubulin only. However, since these dyes are also taxol-based, similar staining challenges might arise in MIP mutants (283).

To further investigate MIP functionality, sporozoites from MIP KO mutants were prepared for FIB-milling and structural analysis via cryo-tomography, aiming to test for the presumed absence of MIP densities within the microtubule lumen. Infected salivary glands were isolated as a whole in Heidelberg and shipped on ice for further processing. Surprisingly, structural analysis revealed that while WT sporozoites had normal length SPMTs, SPMTs of the *trxL1*(-)/*spm1*(-)ns mutant were mostly completely absent or dramatically shortened (**Supplementary Figure 8 A, B**). As samples had been prepared in parallel, with the WT sample being incubated on ice the longest, this result strongly suggests that indeed in MIP KO mutants SPMTs almost completely depolymerized once being incubated on ice for more than 24 hours. Notably, sporozoites

prepared for structural analysis were exposed to cold temperatures for approximately 30 hours during shipping, in contrast to the two-hour incubation used in the temperature assays. These findings suggest that prolonged cold exposure leads to complete SPMT depolymerization or severe destabilization in MIP KO mutants.

To assess the sensitivity of MIP KO mutants to cold exposure without relying on tubulin-specific dyes, global investigations of SPMT stability could be considered: Sporozoites from MIP KO mutants could be isolated and incubated at either warm or cold temperatures as described before. As SPMT stability is critical for both gliding motility and parasite infectivity (113), post-incubation gliding assays or i.v. injection of cold-exposed sporozoites into mice could serve as indirect measured of SPMT stability. However, results of injection experiments have to be evaluated carefully, as SPMTs might recover rapidly upon entering the warm mammalian host. Alternatively, cold-exposed SPMTs could be stained with a microtubule staining live-dye other than SiR-tubulin and SPMTs could be imaged live. A more definitive strategy would involve freezing the MT state immediately after cold incubation and analysing samples via EM, a technique that doesn't rely on any antibody staining. It would be also interesting to investigate temperature sensitivities of SPMTs in ookinetes, in which SPM1 and TrxL1 are also present. Notably, interrupted luminal helix-containing SPMTs have been shown to be slightly flattened compared to the almost perfectly circular MTs in other organisms (112). Hence, it is intriguing to speculate that the slightly flattened appearance of SPMTs contributes to the stable nature of SPMTs which would be inferred by the presence of SPM1 and TrxL1. Alternatively, MIPs could be ectopically expressed in cells which have intrinsically highly dynamic MTs, such as neurons that constantly explore the environment using their growth cone (284), to see whether they stabilize neuronal microtubules.

In summary, cross-sectional analysis of MIP KO mutants revealed dissociation of SPMTs during cold incubation, although microscopic examination of their polymerization status was not feasible. While additional studies, such as TEM analysis, are needed to confirm whether these dissociated structures may represent fragmented SPMTs; cryo-tomographic analysis indicated almost complete depolymerization of SPMTs after a prolonged cold exposure exceeding 24 hours (**Figure 34**). Further investigations into the temporal and thermal thresholds of this process would help clarifying to which extend MIPs stabilize SPMTs under cold stress. During its development, *Plasmodium* is exposed to a broad range of temperatures, transitioning between the mosquito and vertebrate host. The optimal temperature range for *P. falciparum* development spans 16–35 °C, limiting its ability to develop in cooler, high-altitude regions (285). Lower temperatures lengthen the extrinsic incubation period—the time that is required for *Plasmodium* to develop within the mosquito and become transmissible (286, 287). Throughout its life cycle, the parasite depends on SPMTs and MIPs might be a contributing factor to ensure SPMT stability over different temperature ranges necessary for parasite viability and infectivity.

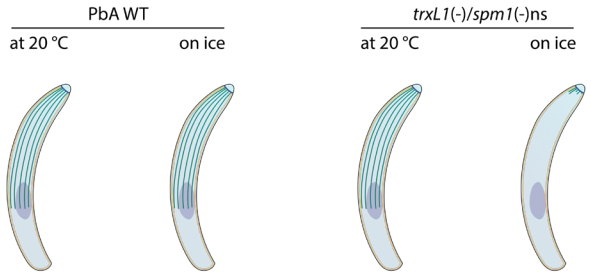

Figure 34 SPMTs depolymerize in the *trxL1*(-)/*spm1*(-)ns mutant upon extended cold incubation. The SPMTs of the *trxL1*(-)/*spm1*(-)ns mutant have a normal length at 20 °C but depolymerize upon extend incubation on ice. Shown is the sporozoite longitudinal section. SPMTs are depicted in green, IMC in yellow.

Interestingly, the interaction between mosquito feeding behaviour and fluctuating environmental temperatures has been shown to influence malaria transmission. Mosquitos feeding in the evening experience cooler temperatures that promote parasite development and enhance transmission potential; whereas excessively low temperatures slow down parasite development and thus potentially limit transmission in cooler environments (287, 288). Although malaria is nowadays primarily prevalent in warmer regions including Africa, South East Asia and South America; it was historically a significant disease across Europe, including Northern Europe, until its eradication in the 20th century in Europe (reviewed in (289)). The colder climates of these regions may have necessitated adaptations in the parasite to protect its SPMTs under suboptimal thermal conditions. Notably, only the SPMTs of ookinetes and sporozoites; stages that develop within the mosquito and that are exposed to broader and more dynamic temperature fluctuations, possess an interrupted luminal helix made off SPM1 and TrxL1. In contrast, merozoites, which develop within the relatively stable and warm environment of mammalian blood (~ 37 °C), lack this structure. These observations suggest that MIPs are critical for maintaining SPMT integrity across the temperature ranges that are naturally encountered by mosquitoes. Their absence likely restricts the thermal tolerance of SPMTs, potentially impairing parasite development and transmission efficacy under colder conditions.

4.2 SPM3 mediates distal SPMT-IMC linkage in ookinetes and sporozoites

The *spm3*(-) deletion line was successfully generated revealing no phenotype during blood stage development (**Figure 22**). *Spm3*(-) parasites developed into transmissive stages and were capable of starting an infection within the mosquito midgut (**Figure 23**). Although mutant parasites formed sporozoites, they exhibited impaired efficiency in colonizing the salivary glands, which subsequently impaired parasite transmission from mosquitoes to mice (**Figure 24**). Gliding motility assays revealed that *spm3*(-) parasites displayed an aberrant helical motility pattern, attributed to a partial dissociation of SPMTs from the IMC at the distal end of the parasite (**Figure**

23, **Figure 25**). Notably, this dissociation phenotype was also observed in ookinetes, the stage preceding oocyst formation, despite the formation of normal numbers of oocysts (**Figure 28**).

4.2.1 SPM3 regulates membrane architecture

In the absence of SPM3, SPMTs detach from the IMC and were found deep within the cytoplasm, often associated with cytoplasmic membranes (**Figure 25**). Although these membranes appeared randomly distributed within the cytoplasm, they often associated with the detached SPMTs. While some WT parasites surprisingly also possessed some cytoplasmic membranes, no significant difference in the number of SPMTs associated with these membranes, nor in their distance from the IMC, was detected between *spm3*(-) and WT parasites (**Figure 26**). Tomographic analysis further revealed that *spm3*(-) budding sporozoites exhibited labyrinthine structures (BSc thesis, Roberta Malamud). These structures are thought to increase the surface area during sporozoite budding but usually disappear after elongation is completed (290). It remains to be explored whether labyrinthine structures are enriched in *spm3*(-) midgut sporozoites compared to WT parasites. Despite the presence of these abnormal membrane structures, *spm3*(-) parasites developed into mature ookinetes and sporozoites with a complete IMC, indicating that the IMC itself assembles correctly. These findings raise questions about the origin of these membranes and their potential role in IMC assembly and SPMT organization.

The additional membranes observed in *spm3*(-) parasites may originate from mis localized IMC precursors or vesicles. While s*pm3*(-) sporozoites still had a double-layered IMC indicative that the IMC is build up correctly, SPM3 may play a role in tethering these membranes to the periphery or regulating vesicle trafficking to ensure proper IMC assembly (291). Interference with this process could lead to uncontrolled membrane production as seen in knockdown of PhIL1 in *P. falciparum* (292) suggesting that SPM3 might play a direct or indirect role in regulating membrane synthesis. Since the IMC forms *de novo* during cytokinesis and is completed once parasites are mature (293), this latter hypothesis is less likely, as *spm3*(-) parasites developed into mature ookinetes and sporozoites containing an IMC.

To test these hypotheses, staining with IMC-specific markers such as ISP1, ISP3, or PhIL1 could be used to identify the origin of the cytoplasmic membranes (294, 295). However, since the IMC is likely derived from the ER and Golgi vesicles (291, 293), these markers might also label these organelles. Colocalization studies of SPM3 with IMC-associated proteins (e.g. DHHC2, ISP1 and ISP3 (114)), could provide insights into whether SPM3 functions within the same pathway, though no additional cytosolic membranes were reported in *dhhc2*(-) and *isp1*/*isp3*(-) parasites (114). Quantifying membrane volume or surface area in *spm3*(-) and examining labyrinthine structures at different stages could provide further insights. Electron tomography of salivary gland sporozoites could clarify whether labyrinthine structures disappear once budding is completed,

(as described for the CSP-mutants (290)), or whether they persist in *spm3*(-) parasites. However, the reduced number of salivary gland sporozoites in the *spm3*(-) mutant might represent a technical challenge.

The abnormalities observed in *spm3*(-) parasites, including detachment of SPMTs, the presence of cytosolic membranes and labyrinthine structures, suggest a critical role for SPM3 in IMC assembly and SPMT tethering. While the precise mechanisms remain unclear, SPM3 likely coordinates membrane organization in addition to SPMT attachment, ensuring proper IMC structure and functionality. Future studies investigating the interactions and pathways in which SPM3 is involved will provide further insights into the role of SPM3 in IMC assembly and membrane organization.

4.2.2 Invasive stage formation is independent of SPM3

SPMTs are thought to polymerize in parallel to the formation of the IMC, thereby facilitating cell elongation (117). SPMT formation is particularly critical for stage-specific morphological changes. For example, the transformation of a round zygote into a the characteristic banana-shaped ookinete is closely associated with SPMT formation (244). In addition, SPMTs are indispensable for sporozoite budding from the sporoblast within oocysts as parasites that completely lack SPMTs fail to complete this process and arrest within the midgut (113). Interestingly, in the *spm3*(-) mutant, mature ookinetes and sporozoites were formed despite detached SPMTs, suggesting that detachment occurs after cell formation or that alternative proteins mediate early-stage SPMT-IMC linkage.

This raises three hypotheses: 1) SPMT-IMC tethering is required only in mature stages, 2) apical SPMT-IMC tethering is sufficient and necessary for cell morphogenesis and 3) initial tethering is mediated by a different protein, which is later replaced by SPM3.

As KO of other SPMT-IMC linkers resulted in maturation/elongation impairment or full developmental arrest (114, 118), a proper SPMT-IMC linkage seems to be already necessary during cell formation, hence making the first hypothesis quite unlikely. To find out whether SPMTs in the *spm3*(-) detach only after the parasite has fully formed or already during cell elongation, the latter indicative that apical SPMT-IMC tethering would be sufficient, live cell imaging of either ookinete maturation or sporozoite formation in *spm3*(-) would be helpful; the latter being presumably technically very challenging. Alternatively, samples could be taken at different time points during *spm3*(-) ookinete development and the SPMT attachment status could be determined via U-ExM or by Cryo-EM. To address the third hypothesis, investigating SPM3 localization to SPMTs during ookinete development would help answering at what time point SPM3 is necessary to ensure SPMT integrity.

In conclusion, the ability of *spm3*(-) parasites to form invasive stages despite SPMT detachment suggests that SPM3 is not essential for initial SPMT-IMC tethering. Further investigations into its temporal function and potential redundancy with other linkers are needed.

4.2.3 Structural demands on SPMT-IMC integrity vary across invasive parasite stages

SPMTs are characteristic of the parasite's invasive stages, including merozoites, ookinetes and sporozoites (**Figure 4**). While they are also present in *P. falciparum* gametocytes, they are absent in *P. berghei* gametocytes (further discussed in 4.2.4). In the invasive stages, the number and arrangement of SPMTs varies (**Figure 4**). For instance, merozoites have fewer SPMTs, less organized SPMTs (also called the f-mast (219)). In all stages, SPMTs function as structural scaffold, supporting morphogenesis and providing the intracellular stability and rigidity essential for cell formation and host cell invasion (113). Loss of SPMT-IMC integrity has been shown to result in misshaped or undeveloped ookinetes (120)

Despite these critical roles, deletion of *spm3* had no apparent effect on the development of asexual stages, as *spm3*(-) parasites displayed growth rates comparable to WT (**Figure 22**). This was consistent with observations from *P. falciparum*, where neither glmS-ribozyme-mediated knockdown nor targeted gene disruption of *Pfspm3* impacted asexual blood stage development (248). Additionally, *spm3*(-) mutants exhibited normal midgut infection rates and oocyst counts despite having disorganized SPMTs in the preceding ookinete stage (**Figure 23, Figure 28**). This suggests that a fully stable SPMT scaffold is not required for ookinete morphogenesis or midgut penetration. Contrary to ookinetes, dissociation of SPMTs severely impacted sporozoites: while sporozoites could still form, they showed an aberrant motility pattern and had an almost complete block in salivary gland invasion (**Figure 23, Figure 25**).

These findings suggest the following: 1) SPM3 might either have different functions across the different parasite stages, 2) that functional redundancy ensures SPMT integrity in some but not all stages, or 3) SPMT integrity is less important in merozoites and ookinetes than in sporozoites.

It seems that SPMTs in merozoites form only a simple scaffold to facilitate a quick entry into erythrocytes. While microtubule inhibition in *P. falciparum* merozoites impaired erythrocyte invasion, the overall cell shape was unchanged (221, 278). In comparison, the SPMT scaffold in ookinetes and sporozoites is more elaborate and critical for maintaining cell shape (113, 114, 118, 119). Consequently, defects in SPMT-IMC interaction are more detrimental in the highly motile, elongated forms than in almost spherical merozoites. It thus might be not too surprising, that the KO of *spm3* did not affect asexual blood stage growth and appears dispensable for merozoites.

Transcriptomic analysis from the Malaria Cell Atlas predicted that *spm3* is expressed in schizonts, ookinetes and sporozoites (245). In addition, *Pf*SPM3 was shown to localize to SPMTs during both early and late schizont stages (296). This suggests that *spm3* disruption would lead to SPMT detachment in merozoites similar to those observed in ookinetes and sporozoites. While I extensively analysed SPMT arrangement in ookinetes and sporozoites, the role of *spm3* in merozoites was assessed only indirectly through determining overall parasite growth in the blood. It is plausible that some merozoites, like ookinetes, may also exhibit SPMT detachment without significantly impairing blood-stage development. Ookinete cultures prepared for U-ExM often contain residual uninfected and infected red blood cells, including schizonts, and in these samples, a few schizonts were observed with apparently normal-looking SPMTs (data not shown). This was however a more qualitative analysis and schizonts present in the ookinete culture were not grown under optimal conditions. Performing U-ExM specifically on schizonts and free merozoites would provide a more quantitative assessment.

SPMT connection to the IMC seems to be less important for ookinete morphogenesis and function than for oocyst and sporozoite formation. While *spm3*(-) ookinetes showed varying degrees of SPMT detachment (**Figure 28**), they were still able to mature and penetrate the MG and to form oocysts, which developed normal numbers of sporozoites (**Figure 23**). It is worth noting, that the laboratory conditions under which mosquito infections take place are optimal if not saturated for mosquito transmission (139). Minor defects, such as those observed in the *spm3*(-) mutant, could likely impair successful midgut infection in natural settings. However, these defects may not be detected in laboratory conditions because sufficient numbers of either unaffected or only slightly impaired ookinetes can still penetrate the midgut. To assess oocyst formation under more natural conditions, the number of transmissive gametocytes could be reduced by transferring less infected red blood cells to the recipient mouse used for mosquito infection, by shortening the actual feeding time of mosquitos or by changing the temperature during transmission. In addition, it would be already quite insightful if the ookinete conversion rate in the *spm3*(-) would be known.

SPMT integrity appears to be most crucial for the invasion of salivary glands. While ookinetes need to traverse only a single cell-layer for midgut invasion, sporozoites need to first cross the basal lamina to then invade the secretory acinar cell for salivary gland invasion, respectively (297–300). It might be possible, that potentially higher forces are necessary for salivary gland invasion and might thus explain why *spm3*(-) ookinetes are still able to initiate a midgut infection while *spm3*(-) sporozoites fail to successfully enter the salivary glands. Besides the SPMT-IMC connection, also the number of SPMTs appeared to be less required for initial sporozoite formation than for salivary gland invasion. Both shorter or fewer SPMTs than found in WT were sufficient for sporozoite formation, but prevented sporozoites from entering the salivary glands (113).

These findings suggest that *spm3* might not be the sole linker between SPMTs and the IMC in merozoites, with protein redundancy likely ensuring the stability of the SPMT network. Alternatively, even if *spm3* deletion or knockdown affects SPMTs, the SPMT scaffold in merozoites may not be as critical for overall parasite infectivity as it is in sporozoites, indicating that the functional demands on SPMTs increase towards later mosquito parasite stages.

4.2.4 *Pf*SPM3 and *Pb*SPM3 only share partial functionality

The deletion of *spm3* in *P. falciparum* and *P. berghei* resulted in different phenotypic outcomes, particularly during gametocytogenesis. In *P. falciparum*, conditional knockdown of *Pf*SPM3 resulted in a complete collapse of SPMTs and a subsequent arrest of gametocytes at early stages (I/II) (248). As a result, the lack of *spm3* prevented their maturation into the characteristic falciform stage V gametocytes. Gametocytemia was also reduced by approximately 50% compared to the control (248). In contrast, *spm3*(-) gametocytes in *P. berghei* were unaffected in terms of gametocytogenesis and transmitted normally to the mosquito vector (**Figure 23**). However, *spm3* deletion in *P. berghei* affected later stages in the mosquito, as SPMTs partially detached in ookinetes and sporozoites. These findings suggest that although *spm3* is conserved across *Plasmodium* species, its role varies. In *P. falciparum*, SPM3 is critical during gametocytogenesis, while in *P. berghei* it is required for maintaining structural integrity of SPMTs in mosquito stages.

The divergent phenotypic outcomes of *spm3* deletion in *P. falciparum* and *P. berghei* align with the differences in gametocyte morphology and developmental requirements. *P. falciparum* gametocytes undergo drastic morphological transformations, progressing from a round stage I to a banana-shaped, falciform stage V gametocyte (67). This transition is driven by the expansion of the IMC and the elongation of SPMTs (292). In *Pf*SPM3 knockdown parasites, the loss of SPMT integrity stops morphogenesis at stage I/II, when SPMTs would usually begin forming. In contrast, *P. berghei* gametocytes maintain a round shape throughout development and lack any SPMTs (66). Interestingly, male *P. berghei* gametocytes still possess a discontinuous IMC and also express PhIL1 (295, 301). While *Pb*SPM3 primarily functions in mature stages, *Pf*SPM3 is necessary for parasite elongation. Testing SPM3 expression and localization during ookinete and sporozoite development could determine if redundancy exists. Expression limited to mature stages would suggest temporal redundancy, while consistent expression during elongation would imply functional redundancy.

A key difference between the two strains lies in the apical anchorage of SPMTs. In *P. falciparum* gametocytes, SPMTs are nucleated from the cytosolic component of a bipartite MTOC and lack an APR and thus apical anchorage (224). This makes SPMTs fully dependent on SPM3 for attachment to the IMC. In *P. berghei*, SPMTs in ookinetes and sporozoites are apically anchored to the APR and

laterally to the IMC. This dual anchorage likely explains the less severe phenotype in mosquito stages, as the apical anchorage provides sufficient structural support in *spm3*(-) parasites. Further differences in SPMT organization include the random polarity of SPMTs in gametocytes, compared to the organized polarity of SPMTs in mosquito stages, in which the minus end is embedded in the APR (112). This further highlights the distinct organization of SPMTs between the different stages.

Interestingly, knockdown of the IMC-associated protein PhIL1 (a potential indirect interactor of SPM3), resulted in a delayed in development (stage III) as gametocytes still managed to form into the "hat-shaped" stage III gametocytes (292). This indicates that SPM3 might function earlier and upstream of PhIL1 by potentially recruiting or stabilizing PhIL1 at the IMC. Investigating PhIL1 localization in PfSPM3 knockdown parasites would help to test this hypothesis. Proximity-dependent biotin identification (Bio-ID) analysis of *Pf*SPM3 identified potential interactors with diverse localizations, including microtubule-like, suture-like patterns and others (personal communication Korbinian Niedermüller, Gilberger lab, BNITM Hamburg). Notably, two of the top interactors lack orthologues in *P. berghei* (256), suggesting species- or stage-specific interaction partners. These findings imply that while *Pf*SPM3 and *Pb*SPM3 share a conserved role in mediating SPMT-IMC connections, their functional importance and interacting partners might differ across species and developmental stages.

These findings highlight a conserved role of SPM3 in stabilizing SPMT-IMC connection, with species- and stage specific differences in its functional importance. The drastic phenotype observed in *P. falciparum* gametocytes likely reflects their full dependency on SPM3 for SPMT attachment, while mosquito stages in *P. berghei* are less affected due to the dual anchorage mechanism. With only a low sequence similarity of 45% (248), they presumably represent orthologues as their importance, temporal activation across stages, and potential interactors might differ between *Plasmodium* species. It would be interesting to see whether *Pf*SPM3 is additionally important during the mosquito stages and thus whether a SPM3 knockdown in *P. falciparum* would result in similar phenotypes as observed for *spm3*(-) in *P. berghei*. It would be also intriguing to complement the *Pf*SPM3 knockdown line with *Pb*SPM3 to examine the extent to which *Pb*SPM3 can fulfil the function of *Pf*SPM3. However, this approach presents challenges, as the *spm3* ORF is 4566 bp long (256), making it nearly impossible to clone into a plasmid backbone using traditional cloning methods. Further studies characterizing SPM3-associated proteins and their temporal roles in parasite development are needed to elucidate these mechanisms.

4.2.5 SPMT-IMC integrity is required for the formation of adhesion sites during gliding motility

Deletion of *spm3* led to impaired motility in both sporozoites and ookinetes (**Figure 23**, **Figure 28**). Most *spm3*(-) sporozoites lacked adhesion entirely and simply floated in the medium without attaching to the surface. Additionally, some *spm3*(-) sporozoites displayed a previously unobserved helical form of motility. These helically moving sporozoites could initiate an adhesion site but struggled to fully attach, resulting in a pattern of brief gliding phases interspersed with flipping movements. The motility defects extended to ookinetes, with significantly fewer *spm3*(-) ookinetes showing continuous movement compared to WT. These findings suggest, that SPM3 function and thus SPMT-IMC integrity is necessary for successful gliding motility.

All three stages—ookinetes, sporozoites, and blood-stage merozoites—use gliding motility, a substrate-dependent form of movement that relies on an intracellular actin-myosin motor, which is coupled to an external substrate through adhesins (121). Adhesins are delivered to the plasma membrane through secretion from micronemes, which themselves are transported to the parasite's apical end along SPMTs (129). The observed adhesion defects in *spm3*(-) parasites may result from three primary issues: 1) Disorganized SPMTs impair efficient microneme transport to the apical end, 2) Microneme secretion is less directed due to disrupted dorso-ventral polarity or 3) Reduced intrinsic cell stability prevents the effective translation of force into movement.

SPMTs act as tracks for facilitating the active transport of micronemes (129, 302). Once the micronemes reach the apical end, their contents are released and adhesins become incorporated into the PM (129). Interference with micronemal transport and release has been shown to impact gliding motility. For example, conditional depletion of the 'claudin-like apicomplexan microneme protein' in *P. berghei*, a microneme-residing protein, completely halted productive sporozoite movement and severely reduced salivary gland invasion. This was accompanied by reduced shedding of 'thrombospondin related anonymous family protein' during sporozoite gliding (303). The integrity of SPMTs is closely linked to efficient microneme transport (118, 249). At the apical end of ookinetes, APR2 stabilizes SPMTs and anchors the APR. KO of *apr2* resulted an impaired anchorage of the APR, resulting in dissociation of SPMTs and a strong reduction in the number of apical micronemes compared to WT parasites (118). Similarly, disorganization of SPMTs in *spm3*(-) likely results in a compromised micronemal transport. This could lead to fewer micronemes reaching the apical end, or to a delayed transport of micronemes, which in turn would reduce the secretion of adhesins available for PM incorporation. Alternatively, microneme secretion may not be well-orchestrated compared to WT. Although micronemes could be observed at the apical end of *spm3*(-) sporozoites (**Figure 25**) and expanded ookinetes (data not shown), a quantitative analysis is needed to test whether *spm3*(-) parasites contain less

micronemes compared to WT. To further explore whether adhesion defects result from impaired microneme transport or an impaired secretion, micronemes could be fluorescently labelled and transport could be imaged live. Microneme secretion could be further investigated by a microneme secretion assay combined with a subsequent immunoblot analysis as has been described before (304).

Upon secretion, micronemes pass through the APR where SPMTs originate and extend towards the distal end of the parasite (305). In sporozoites, the APR appears highly specialized for the directional secretion of micronemes (128). During sporozoite gliding, the APR ring tilts towards the substrate and thus facilitates directed secretion of micronemal content (128). This tilting is thought to result from the uneven distribution of SPMTs, which creates a dorsal-ventral polarity in sporozoites (128). While both ookinetes and sporozoites possess an APR, they likely differ in composition and presumably also in the degree of apical tilting. Cryo-ET studies in ookinetes revealed that compared to sporozoites, the APR of ookinetes consists of two layers of amorphous protein rather than a single ring as observed in sporozoites, suggesting that also tilting of the APR might be differentially regulated (112). Whether the angle of APR tilting in activated *spm3*(-) sporozoites, and thus dorsol-ventral polarity, is altered could be investigated through cryo-ET. An altered dorso-ventral polarity could account for the unusual motility defect of *spm3*(-) sporozoites, while the *spm3*(-) ookinete gliding phenotype might be caused by a different mechanism.

Lastly, disorganized SPMTs likely reduce overall intrinsic cellular stability. If SPMT integrity is lost, the forces generated by myosin may not be fully transmitted into sporozoite gliding. A reduced gliding force would directly affect overall gliding motility and very likely reduce the efficacy of salivary gland invasion. To test whether force transmission is impaired in *spm3*(-) parasite, optical laser tweezers could be used to measure forces in sporozoites and ookinetes (132).

It is surprising that gliding motility remains unaffected in *spm3*(-) merozoites, as indicated by an asexual growth rate that was comparable to WT (**Figure 22**, **Figure 24**). Merozoite gliding features only very short phases of movement lasting less than a minute, which are interrupted by cell rotation (48). This behaviours differs from the circular gliding motility of sporozoites and the snake-like motility pattern of ookinetes, with *P. falciparum* merozoites reaching speeds of 0.6 µm/s (48). Hence, the differences in gliding duration, pattern and speed might explain why merozoites were not affected upon *spm3* KO. Intrinsic cell stability might be only relevant for longer productive gliding phases, and less stable SPMTs may be sufficient for the short duration that is required for merozoite gliding. Microtubule function in merozoites has previously been investigated using global microtubule inhibitors such as colchicine or taxol to disrupt

polymerization and assess invasion efficiency (221, 278). However, the specific role of SPMTs in merozoite gliding remains unclear.

Collectively, SPM3 presumably plays an indirect but crucial role in the formation of adhesion sites required for gliding motility. Although it remains to be determined whether the reduction in gliding motility observed in *spm3(-)* parasites arises from one of the proposed mechanisms or a combination of them, the findings highlight the importance of maintaining a robust stability and coordination among the IMC-glideosome complex, intracellular transport, and SPMTs. These interconnected systems collectively facilitate efficient parasite gliding motility.

4.2.6 Differential regulation of SPMT-IMC linkage along the longitudinal cell axis

TEM on MG sporozoites and U-ExM on ookinetes revealed that SPMTs detach from the IMC in *spm3*(-) parasites (**Figure 25**, **Figure 28**). Notably, SPMT detachment occurred towards the distal end, with SPMTs remaining tightly connected to the IMC at the apical end of the parasite. Interestingly, although SPM3-GFP localized almost along the entire length of the cell (**Figure 31**), the detachment phenotype only occurs at the distal end. This suggests differential regulation of SPMT-IMC linkage along the parasite's longitudinal axis, potentially due to distinct localization of linker proteins or because of protein redundancy.

These observations raise two questions: 1) What ensures apical attachment of SPMTs to the IMC in *spm3*(-) parasites and 2) How is the differential localisation of those putative alternative linker proteins to the SPMTs regulated and might PTMs be involved in this?

The idea of potential linker proteins connecting SPMTs to the IMC was first proposed by Kudryashev *et al.*, who identified a regular density of 32 nm intervals using cryo-EM in sporozoites (115). Recent cryo-tomographic analysis further revealed a uniform SPMT-IMC distance of 18 nm (±10 nm SD) along the cellular axis (112), suggestive for the presence of a single protein linking the two structures. Notably, at the ookinete apex, this distance increases to 50 - 100 nm, likely to accommodate the apical collar as suggested by the authors (112), which may explain the absence of SPM3 in this region.

While SPM3 interacts with PhIL1, a uniformly localized IMC-resident protein in ookinetes and sporozoites and potential interactor of SPM3 (295), deletion of *spm3* only disrupted distal SPMT-IMC linkage. This suggests the presence of an additional apical linker protein, possibly APR2, which is crucial for SPMT tethering at the apical end in ookinetes (118). *Apr2*(-) mutants showed disrupted APR integrity and apical attachment of SPMTs resulting in a severe SPMT disorganization and subsequently developmental arrest in the midgut (118).

In ookinetes, apical and distal SPMT-IMC tethering appear to rely on different mechanisms. SPM3 is absent from the apical region, while several proteins, including APR2 and other apical collar components (118, 306), mediate tethering at the apex. Conversely, in sporozoites, SPM3 localizes uniformly similar to PhIL1 localization (295), yet distal detachment in *spm3(-)* mutants indicates that additional apical linkers maintain SPMT attachment independently of SPM3. As *apr2*(-) mutants arrested in the midgut and were unable to transform into oocysts(118), it remains to be explored whether APR2 also connects SPMTs to the IMC in sporozoites.

SPMT regulation may also involve PTMs that function as chemical marks, also known as the tubulin code, to subsequently attract MAPs to bind (169). SPMTs in merozoites and ookinetes have been shown to be polyglutamylated. With the exception of an apical area of about ~125-250 nm length from the apical tip, ookinete SPMTs are fully decorated with polyglutamylation marks (220). The presence of polyglutamylation marks correlates well with the presence of SPM3 in *P. berghei* ookinetes, as the SPM3-free region has a length of approximately 200 nm (**Figure 31**). Furthermore, *P. falciparum* SPM3 has been shown to localize to the entire length of SPMTs of early gametocyte stages, which are completely polyglutamylated (224, 248). To test whether SPM3 binds specifically to polyglutamylated SPMTs, one could express SPM3 *in vitro* and set up an *in vitro* microtubule-binding assay with polyglutamylated microtubules (by adding a glutamylase enzyme such as tubulin-tyrosine ligase-like to purified tubulin (307)) versus non-polyglutamylated microtubules.

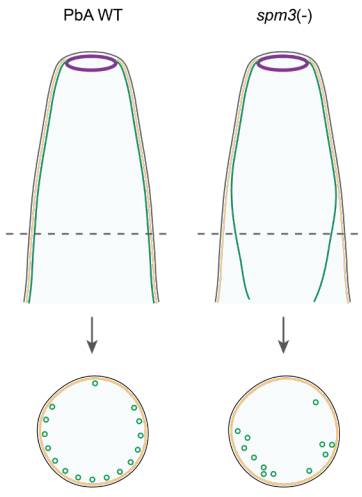

Figure 35 Proposed model of SPM3 function. In PbA WT parasites, SPMTs are closely associated to the IMC along the longitudinal cell axis (top). Thereby, SPMTs follow a stage-specific organization, which is defined as 15+1 in sporozoites (bottom). The dashed line in the longitudinal section shows the position of the cross section below. Conversely, KO of *spm3* resulted in the detachment of SPMTs at the distal end while SPMTs remained tethered to the IMC at the apical end. As a result, the 15+1 organization was lost at the distal end and single SPMTs appeared deep within the cytoplasm. Figure and legend were previously published and adapted for this thesis (248).

In conclusion, SPMTs are subject to differential regulation along the longitudinal axis of the parasite. The localization of SPM3 aligns with distal SPMT detachment in *spm3(-)* mutants (**Figure 35**), while apical tethering likely involves alternative linkers such as APR2. Proteins like DHHC2, ISP1, and ISP3 exhibit region-specific localization during ookinete development (114), further emphasizing the spatially coordinated organization of SPMTs. These findings highlight the complexity of SPMT regulation and underscores the coordinated and spatially regulated organization of SPMTs.

4.2.7 Is SPM3 directly or indirectly linking IMC and SPMTs?

The combined data of SPM3 localization and the observed phenotype in *spm3*(-) parasites strongly suggests that SPM3 connects the IMC and SPMTs. However, it remains uncertain whether SPM3 itself spans between both structures or whether it acts as a hub within a larger protein complex serving as a linker. Any direct interaction of SPM3 with the IMC would require the presence of a transmembrane domain or a site for posttranslational modifications enabling membrane association, while a microtubule-binding domain is necessary for the interaction with microtubules.

To gain preliminary insight into the structural characteristics of SPM3, which might suggest potential functions, I used AlphaFold 3 to predict its structure (308). Unfortunately, AlphaFold 3 was only able to generate a model for SPM3 with low confidence and most regions of the structure scored below 50 on the 'per-atom confidence estimate', indicating limited reliability (**Supplementary Figure 10 A, B**). Co-prediction attempts for SPM3 with PhIL1, α- or β-tubulin, and a triple prediction including SPM3, α- and β-tubulin did not improve the structural confidence for SPM3 and were inconclusive regarding potential interaction sites (**Supplementary Figure 10 C**). Simply from its protein size (172 kDa, corresponding to 1521 amino acids, (256)), SPM3 would be large enough to cover the reported IMC-to-SPMT distance of 18 nm (+/- 10 nm) (112) (an alpha helix of equivalent amino acid length would be 228 nm long).

In addition, i*n silico* domain search using PSIRED ((309–314), **Supplementary Figure 11 A**) predicted a transmembrane domain followed by an extracellular region. It is thus intriguing to speculate that SPM3 contains a transmembrane domain spanning one or both leaflets of the IMC, and potentially the PM as well. To test this hypothesis, two experimental approaches can be considered. First, the predicted transmembrane domain could be attached to an otherwise cytosolic protein to see if it enables membrane binding. Second, one could delete the transmembrane domain in SPM3 and observe any resulting loss in membrane association via fluorescence microscopy. Direct membrane association can also be mediated by post-translational modification, in particular palmitoylation. Four IMC-associated proteins, DHHC2,

ISP1 and ISP3 in *Plasmodium*, as well as the recently identified protein "IMC and SPMT protein1" (IMT1) of *T. gondii*, have been shown to link SPMTs and IMC and contain palmitoylation sites for their incorporation into the IMC (114, 315). Hence, identifying palmitoylation sites within SPM3 would enable to shed light onto the potential direct interaction sites of SPM3 with the IMC.

Furthermore, Simple Modular Architecture Research Tool (SMART) analysis allows to predict structural and functional domains of proteins, generating a network of evolutionary relationship of proteins with similar structural properties and thus potentially similar functions (316, 317). SMART analysis predicted SPM3 to be evolutionary related to kinesin-20 amongst other proteins (**Supplementary Figure 11 B**). Kinesins are well-known microtubule binding proteins. Kinesin-20 is essential for maintaining SPMT organization, and its deletion results in disorganized SPMTs (229), a phenotype resembling the one observed in *spm3(-)* parasites. This raises the possibility that SPM3 may directly associate with SPMTs, although this has not yet been experimentally demonstrated. Direct tests, such as *in vitro* assays incubating SPM3 with polymerized tubulin to assess its binding to polymerized tubulin, or ectopic expression of SPM3 in a system lacking the IMC (such as mammalian cells), could provide clarity on its microtubule-binding capabilities.

Despite these indications of direct interaction, some experimental evidence suggests that SPM3 is more likely part of a larger protein complex that indirectly links the IMC to the SPMTs. Attempts to perform two co-immunoprecipitations with SPM3-GFP as bait were unsuccessful as almost no peptides could be detected. Although SPM3 localization to SPMTs in ookinetes was successfully characterized, it remains uncertain whether the GFP-tag might have been cleaved off during the co-immunoprecipitation process. Fortunately, Bio-ID experiments in *P. falciparum,* performed by our collaborators identified, 16 potential SPM3 interactors, including microtubule-like and suture-like protein, the latter displaying patterns consistent with the IMC plates observed in *P. falciparum* gametocytes (personal communication, Korbinian Niedermüller, Tim Gilberger lab, BNITM Hamburg). Several suture-like candidates localized precisely at the interface between vertically arranged SPMTs and laterally organized IMC sutures, forming a "beads-on-a-string" pattern. This distinct localization implies that SPM3 interacts with these proteins at the IMC-SPMT interface, acting as a hub within a protein network rather than a direct physical linker.

To clarify the molecular mechanisms underlying SPM3's function, further studies are needed. For instance, reverse co-immunoprecipitations using suture-like or microtubule-like proteins identified through Bio-ID could validate SPM3's indirect linkage role. Advanced imaging techniques, such as super-resolution microscopy, could resolve SPM3's precise localization relative to the IMC and SPMTs as has been previously applied (242). Combining these methods

with functional assays, such as domain-specific tagging or targeted mutagenesis, would help identify the specific regions of SPM3 involved in mediating these interactions.

At this point, it remains unclear whether SPM3 binds directly or indirectly via interaction partners to the IMC and SPMTs. It is additionally possible, that a combination of both mechanisms, directly anchoring to one structure while the other connection is mediated by an interaction partner, is true. Regardless of the exact binding mechanism, SPM3 plays a crucial role in maintaining SPMT-IMC linkage and contributes to the overall cell stability, as outlined in the proposed model of SPM3 function.

4.3 Final conclusion

Plasmodium undergoes a complex life cycle during which the parasite's shape continuously adapts to meet the changing demands of its environment. These dynamic shape changes, as well as the parasite's overall cellular stability and rigidity, are mediated by SPMTs that lie directly beneath the pellicle. Unlike the microtubules of model organisms, SPMTs exhibit remarkable stability at different temperature ranges, likely conferred by MAPs that bind either internally or externally to the SPMTs. While deletion of MIPs did not yield a detectable phenotype under normal conditions, cold assays suggest that MIPs contribute to SPMT stability under suboptimal conditions. Ultimately, *Plasmodium* has evolved mechanisms to ensure SPMT stability, enabling the parasite to persist across diverse and challenging environments.

In addition to intrinsic stability, proper tethering of SPMTs to the IMC is crucial. Deletion of *spm3* in both *P. berghei* and *P. falciparum* led to varying degrees of SPMT disorganization and detachment from the IMC. In *P. falciparum*, SPM3 knockdown completely arrested gametocyte development, preventing the formation of transmissive, mature falciform-shaped gametocytes. In contrast, *spm3* KO in *P. berghei* progressively impaired parasite development during mosquito stages: *spm3*(-) parasites exhibited reduced motility in ookinetes and sporozoites, leading to diminished salivary gland invasion and subsequent defects in transmission.

Collectively, these findings illuminate the mechanisms underlying both the intrinsic stability and the IMC tethering of SPMTs, highlighting their indispensable roles in parasite development and infectivity. These findings deepen our understanding of the structural and functional adaptations that enable *Plasmodium* to navigate through its life cycle and ensure a foundation for future investigations into parasite biology. Moreover, these insights expand our knowledge of microtubule organisation and stability beyond that of model organisms.

5. Materials and Methods

5.1 Materials

Table 2 Laboratory equipment.

Equipment	Manufacturer	Location
4k by 4k pixel digital camera TempCam F416	Tietz Video and Image Processing Systems GmbH	Gauting, Germany
Airyscan 2 LSM900	Carl Zeiss	Jena, Germany
Axiostar Plus	Carl Zeiss	Jena, Germany
Axiovert 200M	Carl Zeiss	Jena, Germany
Amaxa Nucleofector II	Lonza	Cologne, Germany
Aquilos2 cryo-FIB-SEM dual beam microscope	Thermo Fisher Scientific	Waltham, MA, USA
Binocular Nikon, SMZ 1500	Nikon	Tokyo, Japan
Binocular Zeiss	Zeiss	Jena, Germany
CCD Camera EASY 400 K	Herolab	Wiesloch, Germany
Centrifuge 5417 R	Eppendorf	Hamburg, Germany
Centrifuge Heraeus Fresco 21	Thermo Fisher Scientific	Waltham, MA, USA
Centrifuge Heraeus Fuge pico 17	Thermo Fisher Scientific	Waltham, MA, USA
Centrifuge Heraeus Multifuge 1 S-R	Kendro	Heidelberg, Germany
Gel electrophoresis system EV231	Consort	Turnhout, Germany
End-over-end rotator, Grant Bio PTR-30	Keison	Chelmsford, United Kingdom
Freezer 1, -80 °C	New Brunswick Scientific	Edison, NJ, USA

Freezer 2, -80 °C, TSX	Thermo Fisher Scientific	Waltham, MA, USA
Freezer -20 °C	Liebherr	Ochsenhausen, Germany
Fridge 4 °C	Liebherr	Ochsenhausen, Germany
Heating block AccuBlock Digital Dry Bath	Labnet	Edison, NJ, USA
Heating block ThermoMixer C	Eppendorf	Hamburg, Germany
Hotplate stirrer CB162	Stuart	Staffordshire, UK
Incubator for parasites (schizonts), CO_2 Ihnova CO-170	New Brunswick Scientific	Edison, NJ, USA
Incubator for parasites (schizonts), CO_2 Lab C201	Labotect	Göttingen, Germany
Incubator for parasites (ookinetes)	New Brunswick Scientific	Edison, NJ, USA
Incubator for bacteria, Multitron 2	Infors Incubator	Bottmingen, Switzerland
Incubator for mosquitos, Sanyo MIR253	LabX	Midland, Canada
Electron microscope, JEOL JEM-1400	Jeol Ltd	Tokyo, Japan
K3 direct electron detector and (Bio)-Quantum energy filter	Gatan	Pleasanton, CA, USA
Liquid Nitrogen Tank, ARPEGE 170	Air Liquide	Düsseldorf, Germany
Microwave oven	Severin	Darmstadt, Germany
NanoPhotometer NP80	Implen	Munich, Germany
Neubauer counting chamber	Paul Marienfeld GmbH & Co. KG	Königshofen, Germany
Orbital shaker, Duomax 1030	Heidolph	Schwabach, German

Orbital shaker, DOS-20S	Neolab Migge GmbH	Heidelberg
Pipettes (P2, P10, P200, P1000)	Gilson	Middleton, WI, USA
Pipetus	Hirschmann Laborgeräte	Eberstadt, Germany
Rotating wheel, Loopstar digital	IKA-Werke	Staufen, Germany
Thermocycler FlexCycler2 PCR machine	AnalytikJena	Jena, Germany
Titan Krios microscope	Thermo Fisher Scientific	Waltham, MA, USA
Tube roller, BRT10P	Ratek	Boronia, Australia
UV-table UVT-28 L	Herolab	Wiesloch, Germany
Ultramicrotome Leica EM UC7	Leica	Wetzlar, Germany
Ultracut UTC ultramicrotome	Leica	Wetzlar, Germany
Ultra-Diamond Knife	DiATOME	Nidau, Switzerland
Vortex-Genie® 2	Scientific Industries, Inc.	Bohemia, NY, USA

Table 3 Consumables.

Name	Description, Ref. no	Manufacturer	Location
96-well optical bottom plate	265300	Thermo Fisher Scientific Inc.	Waltham, MA, USA
Cell Culture flask	Cellstar T75	Greiner bio-one	Frickenhausen, Germany
Cell culture flask	T25	Greiner bio-one	Frickenhausen, Germany
Cover glasses	24x 40 mm, Na.1, 0101192	Paul Marienfeld GmbH & Co. KG	Lauda-Königshofen, Germany
Coverslip	10 mm, round, 0111500	Paul Marienfeld GmbH & Co. KG	Lauda-Königshofen, Germany

Cryotubes	Cryo.s™ with screw cap	Greiner bio-one	Frickenhausen, Germany
Glass slides	AG00000112E01MNZ10	New Erie Scientific LLC	Portsmouth, NH, USA
Imaging dish	µ-slide, 8 well ibiTreat, 80826	ibid GmbH	Gräfelfing, Germany
Imaging dish	µ-slide, 8 well, glass bottom, 80827	ibid GmbH	Gräfelfing, Germany
Needle	BD Microlance™ 3, Ref302200, 27G	Becton, Dickinson and Company Limited	Drogheda, Ireland
Needle	BD Microlance™, 23G x 1, Nr. 16	Becton Dickinson GmbH	Fraga, Spain
Needle	4657705B	B. Braun Melsungen AG	Melsungen, Germany
Pasteur pipette	7095B-5X	Corning Incorporated	Corning, NY, USA
Pipette Tips	10 µl, 200 µl, 1 mL	Gilson	Middleton, WI, USA
Plastic pipettes	5 mL, 10 mL, 25 mL	Greiner bio-one	Frickenhausen, Germany
Stericup Quick Release Millipore	Ø22 µm, SEGPU0538	Merck	Darmstadt, Germany
Syringe Micro-Fine + U-100 Insulin	0.5 mL, 324825	Becton Dickinson GmbH	Heidelberg, Germany
Syringe Insulin2	Omnican®F, 30G x ½", 9161502S	B. Braun Melsungen AG	Melsungen, Germany
Syringe Plastipak	1 mL	Becton Dickinson GmbH	Heidelberg, Germany

Tubes	1.5 mL/ 2 mL	Sarstedt	Nümbrecht, Germany
UltrAufoil EM grid	R1.2/1.3 300 mesh	Quantifoil	Großlöbichau, Germany
Whatman syringe filter	Puradisc FP30, 0.2 µm	Global Life sciences Solutions Operations UK LTd.	Buckinghamshire, UK

Table 4 Chemicals and commercial solutions. HEPES – 4-(2-hydroxyethyl)-1-piperazineethanesulfonic acid

Chemical/ Solution	**Reference number**	**Manufacturer**	**Location**
1 kb plus DNA ladder	N3200	New England Biolabs	Ipswich, MA, USA
2-Mercaptoethanol, 16%	8.05740.0250	Merck Schuchart OHG	Hohenbrunn, Germany
4-Aminobenzoic acid (PABA)	A9878-5G	Sigma-Aldrich	Munich, Germany
5-Fluorocytosine (5-FC)	F7129-5G	Sigma-Aldrich	Munich, Germany
Accudenz	AN7050	Accurate Chemical & Scientific Corp.	Westbury, NY, USA
Acrylamide, 40%	A4058	Sigma-Aldrich	Cream Ridge, USA
Agarose	2267.4	Carl Roth GmbH + Co. KG	Karlsruhe, Germany
Ammonium persulfate (APS)	17874	ThermoFisher Scientific	Waltham, MA, USA
Ampicillin sodium salt	K029	Carl Roth GmbH + Co. KG	Karlsruhe, Germany
Bovine serum albumin Fraction V	9048-46-8	Carl Roth GmbH + Co. KG	Karlsruhe, Germany

Cacodylic acid sodium-salt	15540.02	Serva Electrophoresis GmbH	Heidelberg, Germany
Copper grids, 2 x 1 mm	G2500C	Plano GmbH	Wetzlar, Germany
Dimethylethanolamine	DMAE	Serva Electrophoresis GmbH	Heidelberg, Germany
DMSO (100%)	67-68-5	New England Biolabs	Ipswich, MA, USA
Embedding medium	D.E.R.®736	Serva Electrophoresis GmbH	Heidelberg, Germany
Embedding medium ERL (Epoxycyclohexylmethyl-3,4 epoxycyclohexylcarboxylate)	ERL 4221D	Serva Electrophoresis GmbH	Heidelberg, Germany
ERL-4206 plasticizer	9072-62-2	Serva Electrophoresis GmbH	Heidelberg, Germany
Ethanol (> 99.8%)	E/0650DF/15	Fisher Scientific	Geel, Belgium
FBS Gibco™, 16000 (Origin: US)	26140-079	Invitrogen	Karlsruhe, Germany
Formaldehyde, 16%	28906	ThermoScientific	Rockford, IL, USA
Formaldehyde, 36.5 – 38%	F8775	Sigma-Aldrich	St. Louis, MO, USA
Glutaraldehyde, EM grade	23114.01	Serva Electrophoresis GmbH	Heidelberg, Germany
Glycine, 99+%	220910010	ThermoFisherScientific	Fair Lawn, NJ, USA
Hemacolor® Rapid staining of blood smear Solution 2	1.11956.2500	Merck KGaA	Darmstadt, Germany
Hemacolor® Rapid staining of blood smear Solution 3	1.11957.2500	Merck KGaA	Darmstadt, Germany
Heparin-Sodium 25000 U	-	Leo Pharma A/S	Neu-Isenburg, Germany
Hoechst 33342	-	Sigma-Aldrich	Munich, Germany

Hoechst 33342	62249	ThermoScientific	
Hypoxanthine	H9377-5G	Sigma-Aldrich	Steinheim, Germany
Immersion oil	Immersol W (2010), 444969-0000-000	Carl Zeiss Jena GmbH	Oberkochen, Germany
Immersion oil	Immersol 518N, 6235180	Häberle Labortechnik GmbH & Co. KG	Lonsee-Ettlenschieß, Germany
Ketamine	100 mg/mL, 401650.00.00	Sigma-Aldrich	Munich, Germany
LB Broth (Lennox)	L3022	Sigma Aldrich Chemie AG	Darmstadt, Germany
Lead nitrate	8E 30655	Riedel-de Haën AG	Seelze, Germany
Mercurochrome NF XII (Mercury dibromo-fluorescein disodium salt)	M7011-25G	Sigma-Aldrich	St. Louis, MO, USA
Methanol	32213	Riedel de Haen AG	Seelze, Germany
$MgCl_2$	B0510	Thermo Scientific	Waltham, Ma USA
Midori Green Advance DNA stain	MG04	Nippon Genetics Europe	Düren, Germany
N,N'-methylenbisacrylamide (BIS), 2%	M1533	Sigma-Aldrich	St. Louis, MO, USA
Nonidet P40®	A1594	AppliChem GmbH	Darmstadt, Germany
Nonenylsuccinic anhydride (NSA), hardener	ERL-4206	Serva Electrophoresis GmbH	Heidelberg, Germany

Nycodenz	18003	Serumwerk Bernburg AG	Bernburg, Germany
Osmium tetroxide	19110	Science Services GmbH	Munich, Germany
PBS tablets GibcoTM	18912014	Thermo Fisher Scientific	Waltham, MA, USA
PBS (w/o $CaCl_2$, w/o $MgCl_2$)	14190	Gibco, Invitrogen	New York, NY, USA
Paraformaldehyde (for IFA), 16% stock solution	28906	Thermo Fisher Scientific	Waltham, MA, USA
Paraformaldehyde, EM-grade (for TEM), 16% stock solution	E 15710	Science Services GmbH	Munich, Germany
Penicillin/Streptomycin	100x	PAA Laboratories GmbH	Pasching, Austria
Phenylhydrazine, 97%	P2, 625-2	Sigma-Aldrich	Munich, Germany
PolyD Lysine	A3890401	Gibco	Frederick, MD, USA
Pyrimethamine VETRANAL™	46706-250 MG	Gibco	St. Louis, MO, USA
RPMI-1640 + L-Glutamine – Phenol Red Gibco®	22400089	Thermo Fisher Scientific	Waltham, MA, USA
RPMI-1640 + HEPES + L-Glutamine Gibco®	11835-063	Thermo Fisher Scientific	Waltham, MA, USA
Saccharose	4621.1	Carl Roth GmbH & Co. KG	Karlsruhe, Germany
Saponin Quillaja sp.	S4521-10G	Sigma-Aldrich	Munich, Germany
SiR-tubulin	SC002	Spirochrome	
Sodium acetate	71829-5G	Honeywell GmbH	Seelze, Germany
Sodium hydrogencarbonat, 99.5%	Z12143	Grüssing GmbH	Filsum, Germany

Spy554-tubulin	SC203	Spirochrome	
SOC medium	B9020S	New England Biolabs	Ipswich, MA, USA
Sodium Acrylate, 97-99%	7446-81-3, MDL no. MFCD0006720	AKScience	Union City, CA, USA
Tris-Acetate-EDTA buffer (TAE)	4855.2	Carl Roth GmbH + Co. KG	Karlsruhe, Germany
Tetramethylethylendiamine (TEMED)	17919	Thermo Fisher	Rockford, IL, USA
Tri-sodium citrate dihydrate	A3901, 1000	AppliChem GmbH	Darmstadt, Germany
Tris	4855.2	Carl Roth GmbH + Co. KG	Karlsruhe, Germany
Triton X-100	78787	Sigma-Aldrich	Steinheim, Germany
Tween-20	9127.1	Carl Roth GmbH + Co. KG	Karlsruhe, Germany
Uranyl acetate	77870.01	Serva Electrophoresis GmbH	Heidelberg, Germany
Xanthurenic acid	D120804-1G	Sigma-Aldrich	Steinheim, Germany
Xylazine/Xylavet	20 mg/mL, 401510.00.00	CS-Pharma GmbH	Burgdorf, Germany

Table 5 Buffers and solutions. ddH_2O – double distilled water, Na_2EDTA – disodium Ethylene-diaminetetraacetic acid, NaCl – sodium chloride, V/v – volume per volume, w/v – weight per volume.

Name of buffer or solution	Composition	
5-FC drinking water	1 mg/mL	5-FC In H_2O, kept in the dark, use within 4 days
Accudenz solution	17% (w/v)	Accudenz in ddH_2O
Agarose	0.8% (w/v)	Agarose In TAE buffer Boiled to dissolve
Cross-linking solution (U-ExM)	1.4% 2%	Formaldehyde Acrylamide In PBS Prepare fresh prior to usage
Denaturation buffer (U-ExM)	200 mM 200 mM 50 mM	SDS NaCl Tris In ddH_2O Adjust to pH 9
Fixing solution (TEM)	4% (v/v) 4% (v/v)	PFA GA In 100 mM sodium cacodylate buffer
Fixing solution (IFA, for gametocytes, asexual stages)	4% (v/v) 0.05% (v/v)	Paraformaldehyde (PFA) Glutaraldehyde In PBS Stored at 4 °C
Fixing solution (IFA, ookinetes, sporozoites)	4% (v/v)	Paraformaldehyde (PFA) In PBS Stored at 4 °C
Freezing solution	10% (v/v)	Glycerol in Alsever's solution

Ketamine/Xylazine		
For bite-back	100 mg/kg	Ketamine
	3 mg/kg	Xylazine
		In PBS, kept at 4 °C
For final anaesthesia	120 mg/kg	Ketamine
	16 mg/kg	Xylazine
		In PBS, kept at 4 °C
Laemmli/ 2x SDS-sample buffer	120 mM	Tris/HCl, pH 6.8
	4%	SDS
	1%	β-mercaptoethanol, only add freshly when using
		in ddH_2O
LB medium	10% (w/v)	NaCl
	10% (w/v)	Bacto-Tryptone (Peptone)
	5% (w/v)	Bacto-Yeast extract
LB medium for agarose plates	15% (w/v)	Agarose
		In LB medium
Monomer solution (U-ExM)	19% (v/v)	Sodium acrylate (38% stock)
	10% (v/v)	Acrylamide
	0.1% (v/v)	BIS
	1x	PBS (10x PBS stock)
		Make 90 µl aliquots (sufficient for two gels), store at -20 °C for up to 2 weeks,
		has to be frozen overnight prior to usage
Ookinete medium	5% (w/v)	Hypoxanthine
	0.1% (v/v)	Penicillin/Streptomycin
	0.2% (w/v)	Natriumhydrogencarbonat
	100 µM	Xanthurenic acid
		In RPMI 1640 (Sigma-Aldrich) + HEPES + Glutamine
		pH adjusted to 7.8, stored at -20 °C

Complete ookinete medium	16% (v/v)	FBS in ookinete medium
Nycodenz stock solution (100%)	27. 6%(w/v) 5 mM 2 mM 0.3 mM	Nycodenz Tris Kalium chloride Na_2EDTA In ddH_2O, pH adjusted to 7.5, autoclaved and stored in the dark at 4 °C
Nycodenz working solution (55%/ 63%)	55%/ 63% (v/v)	Nycodenz stock solution In PBS, stored in the dark at 4 °C
Phenylhydrazine working solution	0.6% (v/v)	Phenylhydrazine In PBS, prepare freshly
Pyrimethamine solution	1% (v/v)	Pyrimethamine In H_2O, pH adjusted to 3.5 to 5.5, keep in the dark
Pyrimethamine stock solution		Pyrimethamine In DMSO, pH adjusted to 3.5 to 5.5, keep in the dark
Salt solution for mosquitos	1% (w/v)	NaCl In ddH_2O
Saponin working solution	0.0093% (w/v)	Saponin In PBS Kept at 4 °C
Spurr's resin	23.6% (w/v) 14.2% (w/v) 61.3% (w/v) 0.9% (w/v)	Embedding medium ERL ERL-4206 plasticizer Nonenylsuccinic anhydride Dimethylethanolamine In ddH_2O Stored at -18 °C
Sugar solution for mosquitos	10% (w/v)	Saccharose In dH_2O supplemented with a bit of PABA
TAE buffer		

Transfection medium, complete	20% (v/v) 0.03% (v/v)	FBS (heat inactivated) Gentamycin In RPMI 1640 (Sigma-Aldrich) + HEPES Sterile filtered and aliquots stored at -20 °C

Table 6 Enzymes with corresponding reaction buffers and supplements. HF – high fidelity

Enzyme/ Reagent	Reference number	Manufacturer	Location
AvrII	R0174	New England Biolabs	Ipswich, MA, USA
BamHI-HF	R3136	New England Biolabs	Ipswich, MA, USA
BsmI	R0134	New England Biolabs	Ipswich, MA, USA
CutSmart Buffer (10x)	B7204	New England Biolabs	Ipswich, MA, USA
dNTPs (10 mM)	R0192	Thermo Scientific	Waltham, Ma USA
EcoRI-HF	R3101	New England Biolabs	Ipswich, MA, USA
EcoRV	R0195	New England Biolabs	Ipswich, MA, USA
HindIII-HF	R3104	New England Biolabs	Ipswich, MA, USA
HiFi DNA Assembly Master Mix (2x)	E2621	New England Biolabs	Ipswich, MA, USA
KpnI-HF	R3142	New England Biolabs	Ipswich, MA, USA
MefI	R0589	New England Biolabs	Ipswich, MA, USA
NEB3.1 buffer (10x)	B7203	New England Biolabs	Ipswich, MA, USA
NotI-HF	R3189	New England Biolabs	Ipswich, MA, USA
Phusion GC buffer (5x)	F-519	Thermo Fisher Scientific	Waltham, MA, USA
Phusion HF buffer (5x)	F-518	Thermo Fisher Scientific	Waltham, MA, USA
Phusion Hot Start II polymerase	F-549	Thermo Fisher Scientific	Waltham, MA, USA
PmeI	R0560	New England Biolabs	Ipswich, MA, USA
PvuII-HF	R3151	New England Biolabs	Ipswich, MA, USA
SacII	R0157	New England Biolabs	Ipswich, MA, USA

SwaI	R0604	New England Biolabs	Ipswich, MA, USA
T4 DNA Ligase	M0202S	Fermentas	Burlington, VT, USA
T4 DNA Ligase buffer	B0202S	Fermentas	Burlington, VT, USA
Taq Polymerase	M0273S	New England Biolabs	Ipswich, MA, USA
Taq Standard Buffer (10x)	B9015S	New England Biolabs	Ipswich, MA, USA
XhoI	R0146	New England Biolabs	Ipswich, MA, USA

Table 7 Antibodies and dyes.

Antibody	species	Reference number	Usage/ Dilution		Manufacturer	Location
Primary antibodies						
Anti-tubulin	mouse	Cl B521, T5168	IFA U-ExM	1:1000 1:250	Merck	Darmstadt, Germany
Anti-poly-glutamate chain (polyE)	Rabbit	AG-25B-0030	U-ExM	1:500	AdipoGen AG	Füllinsdorf, Switzerland
Secondary antibodies						
Alexa Fluor™ 488 anti-mouse	Goat	A11029	IFA U-ExM	1:1000 1:200	Thermo Fisher Scientific	Waltham, USA
Alexa Fluor™ 546 anti-mouse	Goat	A11030			Invitrogen	Eugene, OR, USA
Alexa Fluor™ 594 anti-rabbit	Goat	A11010			Thermo Fisher Scientific	Waltham, USA
Alexa Fluor™ 594 anti-mouse	goat	A11005			Thermo Fisher Scientific	Waltham, USA

dyes						
Hoechst33342	-	62249	IFA U-ExM	1:1000 1:100	Thermo Fisher Scientific	Waltham, USA
NHS ester, Atto 594	-	AD594-31	U-ExM	1:200 (10 µg/mL final)	ATTO-TEC GmbH	Siegen, Germany
NHS ester, Atto 647	-	18373-1MG-F	U-ExM	1:200 (10 µg/mL final)	Merck	Darmstadt, Germany
Bodipy™ TR-Ceramide NHS 647	-	D7540	U-ExM	1:500 (2 µm final)	Invitrogen Life Technologies Corporation	Eugene, OR, USA

Table 8 Cloning oligonucleotides used to generate KO- or tagged parasite lines. Bases encoding for linkers are highlighted in red, the bases for restriction sites are highlighted in blue. Overhangs are shown in small letters.

ID	Primer name	Primer sequence (5' → 3')
AB-31	SPM2-fw-SacII-gibson	gaagtacttctcgcgagcgcgccgcggGTAAATACTTACAAATGCATAAACG
AB-32	SPM2-rev-PvuII-gibson	caacaaaatattacttcgaagcagctgATTTCGAGCAAATTATATAATAATGTTC
AB-31_2	SPM3-fw-EcoRI	ccgaGAATTCCTAATAATAATTCCCATTCTGGTG
AB-32_2	SPM3-rev-L1-BamHI	cgcGGATCCCGTACGTCTACCTGCACCTCCAGCACCAGCAGCAGCACCTCTAGCACGCGTCCTAGGAATACAACTACAATAATTCATTGTTG
AB-33	SPM2-fw-AvrII-gibson	gtaagaaaaaacgcgtgggcccctaggTCATATTTTTTGTGATTTGTTTTTTAAAC
AB-34	SPM2-rev-XhoI-gibson	ccatcgataagcttcccgggctcgagCGAAGTTTAAATCGCCTCG
P2229	SPM1-fw-EcoRI	ccgGAATTCATGGAAATAATAGGCGCAAAAC
P2230	SPM1-rev-6Ala-BamHI	cgcGGATCCCGCCGCCGCCGCCGCCGCATACCACGCTTTTTTTACATCATC
P2231	SPM2fw-MfeI	aaaCAATTGATGGAACATTATAATTATGCTGGATTG
P2232	SPM2rev-6Ala-BamHI	cgcGGATCCCGCCGCCGCCGCCGCTCTAATATTTAGGCTATTTTTATGTTCACTTTCA
P2233	*TrxL1*-fw-EcoRI	ccgGAATTCATGTCTTGTGCTAATTTTAATTCCC
P2234	*TrxL1*-rev-6Ala-BamHI	cgcGGATCCCGCCGCCGCCGCCGCCGCTAAACCTTTTTTATTTAAAGAATAAATATTATTTCTG
P2233	*TrxL1*-fw-EcoRI	ccgGAATTCATGTCTTGTGCTAATTTTAATTCCC
P2234	*TrxL1*-rev-6Ala-BamHI	cgcGGATCCCGCCGCCGCCGCCGCCGCTAAACCTTTTTTATTTAAAGAATAAATATTATTTCTG
P2242	SPM2-3UTR-fw_HindIII	cccAAGCTTTCATATTTTTTGTGATTTGTTTTTTAAAC
P2243	SPM2-3UTR-rev_XhoI	ccgCTCGAGCCTTCTTAATTTCTCAAATTTTTATGG
P2244	SPM2-5UTR-fw_EcoRI	ccgGAATTCGTAAATACTTACAAATGCATAAACG

P2245	SPM2-5UTR-rev_EcoRV	aaaGATATCATTTCGAGCAAATTATATAATAATGTTC
P2246	SPM3-5UTR-fw_EcoRI-AB	ccgGAATTCGTATAACATGTGTAGCTAACGG
P2247	SPM3-5UTR-rev_EcoRV-AB	aaaGATATCTACTAGTGTGTTTATTCACTACAAC
P2248	SPM3-3UTR-fw_HindIII-AB	cccAAGCTTACGGGAAAGTGAAAAACG
P2249	SPM3-3UTR-rev_XhoI-AB	ccgCTCGAGGGTTTTAAGTTAAACATACGAGG

Table 9 Oligonucleotides used for genotyping PCR. *Bases encoding* for restriction *sites shown* in blue.

ID	Name	Sequence (5' → 3')
P135	PeFIa_5UTRrev	GTAAACTTAAGCATAAAGAGCTCG
P210	TEstprimerGFPreverse	TTAACATCACCATCTAATTCAACAAG
P650	QCR2_81070	ACGTGCATTTCTTAGCGTTCCT
P862	GFPtestR	TCCAGTGAAAAGTTCTTCTCCT
P960	yFCU_seq_R	TAATTCAAAGGGACGAGG
P962	yFCU_seq_R_2	GAAGAATGATGCTAGCGGAGG
P975	hDHFR R	GATGTCCAGGAGGAGAAAGGC
P1734	Seq10_ef1alpha_for	TGAGGGGTGAGCATTTAAAG
P2019	GFP_rev	ACCATCTAATTCAACAAGAATTGG
P2140	PlasmoGEM KO cassette check	AAGGCGCATAACGATACCAC
P2145	yFCU_seq_R	TAATTCAAAGGGACGAGG
P2219	PBANKA_082020_GT	AGCGCGCATTAGCCAATTCT
P2220	PBANKA_082020_QCR1	GGCCCAAGAAGCGATGTCCCA
P2221	PBANKA_082020_QCR2	ACGTTCTCCACATTGGCAAA
P2222	PBANKA_0810700_GT	TGCCTCTTCCTATGAGACTGA
P2223	PBANKA_0810700_QCR1-AB	GTGTGGCTTTCATAGATGCCC
P2224	PBANKA_0810700_GT2	CACAACACATAAAAAATGCGCACC
P2225	PBANKA_1445000_GT	ACCGCGGCATGGAACTACGA

P2226	PBANKA_1445000_QCR1	TCACTGCTTCTGTGCTTGCGA
P2227	PBANKA_1445000_QCR2	ACAACAGTGCCGAAATCCTACA
P2228	PBANKA_1445000_GT2	CTGGAATTATTATGGCACCTGTTGC
P2239	pL18-tgdhfr-seq-AB	ACTTTAGAGGCCATGAAGAG
P2251	PBANKA_1342500_GT-AB	CCACCCAATAATATTTTTCGTATATACG
P2252	PBANKA_1342500_GT2-AB	TTCACGGGATAATAAAAATTGCTC
P2253	PbANKA_134200_QCR1-AB	CACTTCAATGTATAATGGGCC
P2255	PBANKA_0810700_GT2	GATGATCCGAATGATTTAAGGGCCAG
P2265	PBANKA_1342500_SPM3-QCR	CAGGAGGAGCTAATGCAATGC
P2266	PBANKA_1445000_GT3	TAATGAACTGAATGTGCAGC
P2267	PBANKA_1445000_GT4	AATGGAATGGTAATGGTAAATACC
P2268	PBANKA_1445000_QCR1b	TTCATATCACTGCTTCTGTG
P2269	PBANKA_1445000_QCR1b	TTCATATCACTGCTTCTGTG
P2437	5PbDHFR-TS_AB	ATGAAAAAATGAACGTCCACC
P2439	PBANKA_082020_GT2	CGCGCATTAGCCAATTC
P2440	PBANKA_082020_GT3	AACGTTCTCCACATTGG
P2243	SPM2-3UTR-rev_XhoI	CCGCTCGAGCCTTCTTAATTTCTCAAATTTTTATGG
P2244	SPM2-5UTR-fw_EcoRI	CCGGAATTCGTAAATACTTACAAATGCATAAACG
P2266	PBANKA_1445000_GT3	TAATGAACTGAATGTGCAGC
P2267	PBANKA_1445000_GT4	AATGGAATGGTAATGGTAAATACC
P2268	PBANKA_1445000_QCR1b	TTCATATCACTGCTTCTGTG

Table 10 Plasmids. All plasmids contain an *a*mpicillin resistance and were transformed into C2992 *E.coli* cells.

ID	Plasmid name	Description	insert	Origin
C-0730	pL 18 110530*GFP	Vector to GFP-tag genes in *P. berghei*	-	Jessica Kehrer, (318)
C-0731	Pb262CSmChef1ahDHFRyFCUdeltaHA Mirko	Vector to generate KOs in *P. berghei*	-	Mirko Singer, (260)
C-0732	pL 18 110530*GFP-SPM1	Vector to GFP-tag *spm1* C-terminally in *P. berghei*	SPM1	Annika Binder
C-0733	pL 18 110530*GFP-SPM2	Vector to GFP-tag *spm2* C-terminally in *P. berghei*	SPM2	Annika Binder
C-0734	pL 18 110530*GFP-TrxL1	Vector to GFP-tag *trxL1* C-terminally in *P. berghei*	TrxL1	Annika Binder
C-0737	Pb262-SPM2KO	Vector to delete *spm2* in *P. berghei*	SPM2	Annika Binder
C-0739	Pb262CSmChef1ahDHFRyFCUdeltaHA-SPM3	Vector to delete *spm3* in *P. berghei*	SPM3	Annika Binder
C-0741	pL 18 110530*GFP-SPM3	Vector to GFP-tag *spm3* C-terminally in *P. berghei*	SPM3	Annika Binder
C-0742	pbat-sil6	Vector to generate KOs in *P. berghei*	-	Taco Kojii, (255)
C-0743	pbat-sil6-SPM2KO-GFP-gibson	Vector to delete *spm2* in *P. berghei* and to introduce *gfp* while inserting the KO cassette	SPM2 hom	Annika Binder

Table 11 Commercial molecular biological kits and protocols.

Name of kit	Reference Number	Manufacturer	Location
Amaxa Human T Cell Nucleofactor Kit	VPA-1002	Lonza	Cologne, Germany
DNeasy Blood and Tissue Kit	69504	Qiagen	Hilden, Germany
GenElute™ HP plasmid Miniprep Kit	NA0160-1KT	Sigma-Aldrich	Munich, Germany
Gibson assembly®	E5510	New England Biolabs	Ipswich, MA, USA
High efficiency transformation protocol	C2987H/C2987I	New England Biolabs	Ipswich, MA, USA
High Pure PCR Purification Kit	11732676001	Roche	Basel, Switzerland
NucleoSpin® Gel and PCR Clean-up	740609	MACHERY-NAGEL GmbH & Co. KG	Düren, Germany

Table 12 Bacterial cell lines.

Bacterial cell line	Producer	Location
E. coli, C2992	New England Biolabs	Ipswich, MA, USA

Table 13 Parasite lines.* according to PlasmoDB*(256),* ** according to PlasmoGEM *(257),* *** served as control line (PbA WT). KO – knockout, ns – negatively selected

Parasite line	**Gene-ID***	**PbGEM ID****	**Origin**	**description**
PbANKA*** (PbA)	-	-	Isolated in Antwerp/ Kasapa (ANKA) by Vincke & Lips, 1948	WT line
GFPcon	-	-	(319)	WT-like control line, expresses GFP constitutively
spm1(-)	PBANKA_0810700	PbGEM-090719	Annika Binder	KO line in PbA background
spm2(-)	PBANKA_0820200	-	Annika Binder	KO line in PbA background
spm3(-)	PBANKA_1342500	-	Annika Binder	KO line in PbA background
trxL1(-)	PBANKA_0820200	PbGEM-026142	Annika Binder	KO line in PbA background
trxL1(-) /*spm1*(-)	PBANKA_0820200, PBANKA_0810700	PbGEM-090719	Annika Binder	KO line in *trxL1*(-) background
trxL1(-) /*spm1*(-)ns	PBANKA_0820200, PBANKA_0810700	PbGEM-090719	Annika Binder	KO line in *trxL1*(-) background, completely negatively selected
trxL1(-) /*spm2*(-)-*gfp*	PBANKA_0820200 PBANKA_0820200	PbGEM-090719 -	Annika Binder	KO line in *txL1*(-) background, expresses GFP
spm1(-) /*spm2*(-)	PBANKA_0810700, PBANKA_1445000	PbGEM-090719	Annika Binder	KO line in *spm2*(-) background

spm1(-) /*spm2*(-)-*gfp*	PBANKA_0810700, PBANKA_1445000	PbGEM-090719	Annika Binder	KO line in *spm1*(-) background, expresses GFP
spm1-gfp	PBANKA_0810700	-	Annika Binder	C-terminally *gfp*-tagged under endogenous promoter
spm2-gfp	PBANKA_1445000	-	Annika Binder	C-terminally *gfp*-tagged under endogenous promoter
spm3-gfp	PBANKA_1342500	-	Annika Binder	C-terminally *gfp*-tagged under endogenous promoter
trxL1-GFP	PBANKA_0820200	-	Annika Binder	C-terminally *gfp*-tagged under endogenous promoter

Table 14 Experimental mouse model and mosquito strain.

Mouse model	**Producer**	**Location**
CD1 Swiss	Janvier Labs Charles River Laboratories	Le Genest-Saint-Isle, France Sulzfeld, Germany
C57/BL6	Charles River Laboratories	Sulzfeld, Germany
Anopheles stephensi, strain FDA500	In-house breeding by our laboratory	Heidelberg, Germany

Table 15 Website tools.

Website	Description	Source/ Reference (last date accessed)
AlphaFold3	Structure prediction of proteins	(308) (14.11.2024)
ClustalOmega	Sequence alignment tool	https://www.ebi.ac.uk/Tools/msa/clustalo/ (21.01.2025)
EMBOSS Needle	Pairwise sequence alignment tool	https://www.ebi.ac.uk/jdispatcher/psa/emboss_needle (06.12.2024)
NEBio Calculator	Determine of molar quantities for Gibson assembly	New England Biolabs, Ipswitch, USA https://nebiocalculator.neb.com/#!/ligation (26.10.2024)
NEB Tm calculator	Determination of annealing temperatures in PCRs	New England Biolabs, Ipswitch, USA, https://tmcalculator.neb.com/#!/main (21.01.2025)
PlasmoDB	Genomic, transcriptomic and metabolomic information of *P. berghei* genes	(256)
PlasmoGEM	Gene KO of *P. berghei* genes	(257)

Table 16 List of software tools.

Software, Version	Description	Source/ Reference (last date accessed)
Adobe Illustrator, Version 28.2	Graph and figure design	Adobe Inc., Adobe© 1987-2023, San José, CA, USA https://www.adobe.com/de/products/illustrator.html (21.01.2025)
AreTomo	Tomogram alignment and reconstruction	(320)

AutoTEM	Automated EM sample preparation	Thermo Fisher Scientific
Benchling (2024)	Digital lab book, *in silico* cloning, primer design and sequence analysis	https://benchling. com
Fiji, Version 1.8.0_322	Image analysis	ScriJava Consortium https://imagej.net/Fiji/Downloads (15.11.2024)
GraphPad Prism, version 6.01, 10.4.0	Graph design and statistical analysis of data	GraphPad Software, San Diego, CA, USA
Herolab Easy Win 32	Agarose gel analysis	Herolab, Wiesloch, Germany
IMOD	Tomogram reconstruction	(321)
RStudio, Version 2024.9.0.375	Graph design and statistical analysis of data	Posit team (2024). RStudio: Integrated Development Environment for R. Posit Software, PBC, Boston, MA. URL http://www.posit.co/
SnapGene®, Version 5.0.3	*In silico* cloning, primer design and sequence analysis	GSL Biotech, Chicago, IL, USA https://www.snapgene.com/ (26.11.2019)
Zen 2.6 (blue edition)	Wide-field imaging software	Carl Zeiss, Oberkochen, Germany
Zen 3.1/3.9 (blue edition)	Airyscan imaging/processing software	Carl Zeiss, Oberkochen, Germany

5.2 Molecular biological methods

5.2.1 Knockout strategy

Depletion mutants were generated via double homologous cross-over recombination. Upon double-crossover, the 5' and 3' untranslated region (UTRs) of the respective gene of interest recombined with homologous regions provided by a linearized plasmid and replaced the gene's open reading frame (ORF) with a selection cassette (**Figure 6 A**). The selection cassette harbours the gene for the *human dihydrofolate reductase* (*hDHFR*) which confers resistance to the drug pyrimethamine. Administering pyrimethamine to the drinking water of mice allowed to select for parasites that recombined and hence carry the KO construct. Combination of multiple KOs in a double or triple KO required the subsequent recycling of the selection marker. For this purpose, the selection cassette does not only comprise the *hDHFR* gene for positive selection, but also *yfcu* for negative selection (241). yFCU is a bifunctional protein and consists the two yeast enzymes cytosine deaminase and uridyl phosphoribosyl transferase. Expression of yFCU makes parasites sensitive to 5-fluorocytosine (5-FC) treatment as yFCU metabolizes 5-FC into the lethal thymine-analogue 5-fluorouracile (5-FU). Exposing parasites to 5-FC enables the selection of a small proportion of parasites that had recycled their selection cassette by excision across the two flanking 3' *dhfr* regions (see **Figure 6 A**). Following negative selection, the parasite is once again susceptible to pyrimethamine and an additional KO can be introduced.

5.2.2 Cloning of KO transfection constructs

For gene deletion, a double homologous cross-over recombination was performed. To generate KO mutants of *spm1* and *trxL1*, available PlasmoGEM vectors were used (257)(**Table 13**). For *spm2* and *spm3*, I generated the KO vectors using the Pb262 vector. Both PlasmoGEM and Pb262 vectors contain a selection cassette that encodes both the hDHFR allowing for positive selection using pyrimethamine and yFCU allowing for negative selection, respectively (see 5.2.1).

To generate the *spm2*(-) and *spm3*(-)-plasmids, the respective 3' and 5' homology regions were amplified from PbANKA WT-genomic DNA and inserted into the Pb262 vector. Restriction enzyme cutting sites were added at the 5' end of each amplification primer. I used HindIII and XhoI to introduce the 3' homology region and EcoRI and EcoRV to introduce the 5' homology region into the vector backbone. I used the following oligonucleotides for amplification of the respective homology region: P2244, P2245 (*spm2*, 5'UTR, 610 bp), P2242, P2243 (*spm2*, 3'UTR, 778 bp) and P2246, P2247 (*spm3*, 5'UTR, 768 bp), P2248, P2249 (*spm3*, 3'UTR, 735 bp). The homology regions were amplified using Phusion polymerase. The final PCR mix was composed as depicted in **Table 17** and the thermocycler conditions are shown in **Table 18**.

Table 17 Composition of PCR mix using Phusion polymerase. HF – high fidelity.

Component	Final concentration (1x)
5x Phusion HF buffer	1x
dNTP	200 µM
Forward Primer	0.5 µM
Reverse Primer	0.5 µM
Phusion Hot Start II polymerase	0.02 U/µl
Genomic DNA	~ 50 ng
Total volume	20 µl

Table 18 PCR cycling conditions using Phusion polymerase. Kb – kilobase, s – seconds.

Function	Temperature	Time	Repetition
Polymerase activation/DNA denaturation	98 °C	30 s	
Denaturation	98 °C	10 s	x 30 cycles
Annealing	Tm – 2 °C	30 s	
Extension (15-30 s/kb)	72 (68) °C	1 min	
Final extension	72 °C	5 min	
Slowly cool down to 4 °C	4 °C	hold	

Correct amplification was confirmed via gel electrophoresis using a 0.8% agarose gel. The resulting PCR fragments were purified using the HighPure PCR Purification Kit according to manufacturer's instruction and the DNA was eluted in 35 µl dH_2O. Next, both the amplified fragments and the plasmid backbone were digested with the respective restriction enzymes. For this, 35 µl of eluted and purified PCR fragment was mixed with 4 µl of CutSmart buffer and 1 µl of each restriction enzyme in a total volume of 41 µl. For digest of the backbone, 4 µl of plasmid DNA of purified Pb262 vector was mixed with 2 µl of CutSmart buffer, 0.5 µl of each restriction enzyme and filled to 20 µl with dH_2O. Following digest for 2 hours at 37 °C, the digested DNA was gel-

purified using the NucleoSpin® Gel and PCR Clean-up kit according to manufacturer's instructions and finally eluted in 35 µl of dH_2O. For assembly of the plasmid and ligation, 7 µl of digested insert was mixed with 1 µl of digested backbone, 1 µl of 10x T4 DNA ligase buffer and 1 µl of T4 DNA ligase in a total volume of 10 µl. Ligation was carried out for 1-4 hours at RT. Finally, ligated plasmids were transformed into competent *E. coli* cells (see 5.2.5). The respective 3' and 5' homology regions were consecutively cloned into the Pb262 backbone. The correct plasmid sequence was confirmed via sanger sequencing. The final vector maps are depicted in **Figure 36**.

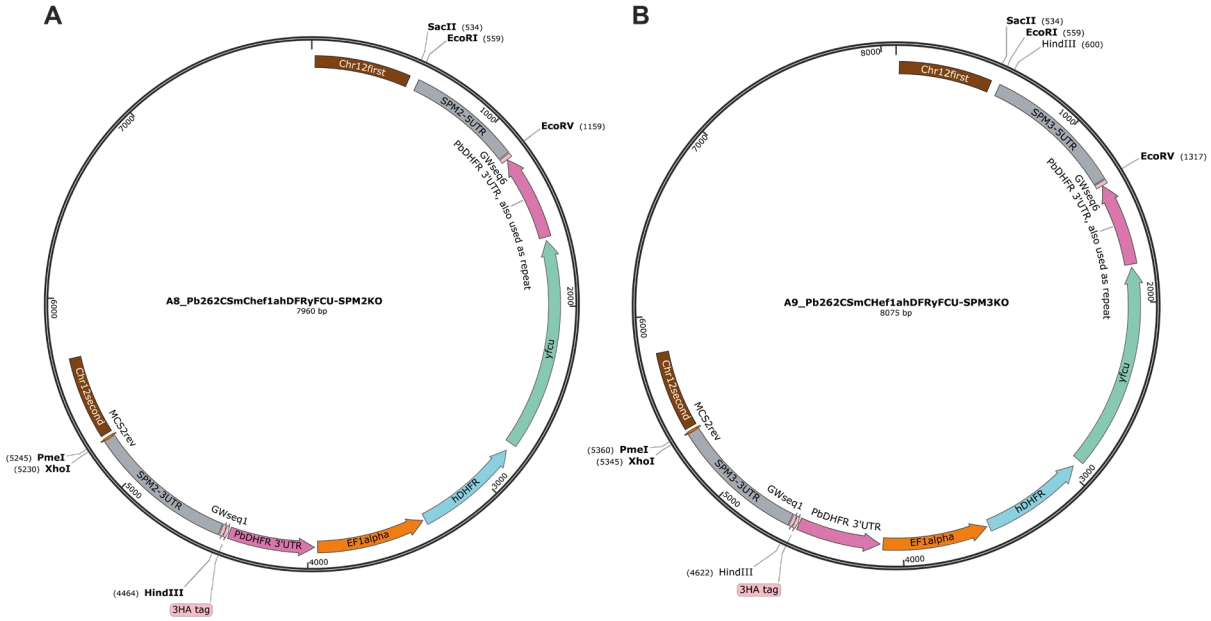

Figure 36 Plasmid maps to generate *spm2*(-) and *spm3*(-) mutant parasite lines. A) *spm2(-),* **B)** *spm3(-).* Enzymes used to insert the respective 3' and 5' untranslated (UTR) regions as well as the enzyme used to linearize the plasmid prior to transfection are highlighted. Chr – chromosome, *Ef1alpha – elongation factor 1 alpha*, *hDHFR – human dihydrofolate reductase*, UTR – untranslated region, *yfcu – yeast cytosine deaminase and uridyl phosphoribosyl transferase*.

Before transfection, vectors were linearized with SacII and PmeI. PlasmoGEM vectors were linearized by NotI digest. In both scenarios, digest was directly followed by purification via ethanol precipitation and proceeded as described in 5.3.4.

5.2.3 Gibson assembly

To insert a GFP-marker upon *spm2* KO, a different vector backbone was used and insertion of fragments was performed via Gibson assembly. For this, the pbatSIL6 vector was used as it already contains *gfp* and thus allows to introduce a fluorescent marker upon successful double crossover recombination. To be able to modify the vector later if needed, I designed the overhangs in a way that the respective cutting sites were kept upon introduction of the 3' and 5' homology regions. I used the following oligonucleotides for amplification of the respective homology region: AB-31,

AB-32 (*spm2*, 5'UTR, 647 bp) and AB-33, AB-34 (*spm2*, 3'UTR, 454 bp). They were amplified using Phusion polymerase. The final PCR mix was composed as depicted in **Table 17** with the adjustment of using GC- instead of HF buffer. The PCR cycling conditions are shown in **Table 18**. To generate the backbone fragments, I digested the pbatSIL6 plasmid with SacII and XhoI (3062 bp) and AvrII and PvuII-HF (6267 bp), respectively. For the assembly of all fragments into one final plasmid using Gibson assembly, the Gibson Assembly® Protocol (E5510) was used. I used 80 ng of backbone (the longest vector fragment) and a 2-fold molar excess of each fragment, as described in the manufacturers protocol. DNA concentrations were measured at the nanophotometer and the required masses were calculated using the NEBioCalculator. 2x Gibson assembly master mix was added to the fragment mix and ddH_2O was used to fill to a total reaction volume of 20 µl. After incubation at 50 °C for 60 min, 5 µl of the assembled plasmid were transformed into competent *E. coli*. The correct plasmid assembly was checked via colony PCR (5.2.6) and confirmed via sanger sequencing. The final vector map is depicted in **Figure 37.**

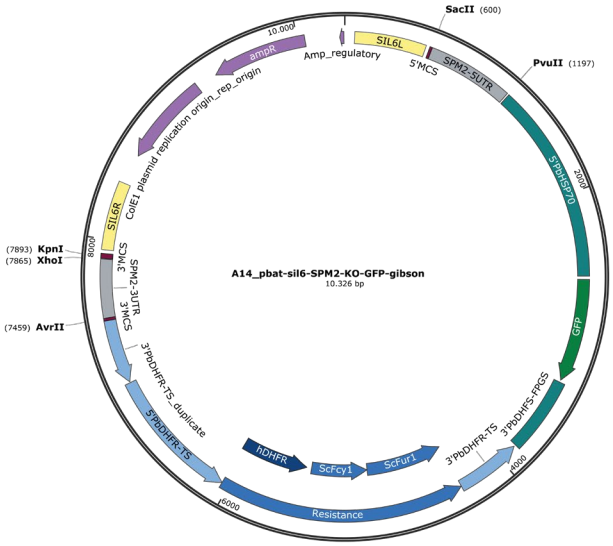

Figure 37 Plasmid map generated via Gibson assembly to generate *spm2*(-)-*gfp* parasite line. Enzymes used to insert the respective 3' and 5' untranslated (UTR) regions as well as the enzyme used to linearize the plasmid prior to transfection are highlighted. AmpR, ampicillin resistance, Chr – chromosome, *Ef1alpha – elongation factor 1 alpha*, *gfp – green fluorescent protein*, *hDHFR/ PbDHFR – human/ P. berghei dihydrofolate reductase*, *hsp70 – heat shock protein 70*, *PbDHFR-TS – P. berghei dihydrofolate reductase-thymidine synthase*, SIL6L/SIL6R – silent intergenic locus left/right, UTR – untranslated region, *yfcu – yeast cytosine deaminase and uridyl phosphoribosyl transferase*.

Before transfection, the plasmid was linearized by KpnI-HF digest followed by purification via ethanol precipitation proceeded as described in 5.3.4.

5.2.4 Generation of *gfp*-tagged parasite lines

Endogenous tagging was performed as previously described using single-crossover integration (248) (**Figure 10**). Using this strategy, an approximately 1 kb long fragment from the C-terminus of the respective gene serves as homology region.

I first amplified the C-terminal fragment from PbANKA WT genomic DNA to be subsequently cloned into the pL18 vector (318) using EcoRI and BamHI restriction sites. The reverse primer included a sequence for six alanines (*spm1*, *spm2*, *trxL1*) or for a mix of 19-amino acids (primarily encoding for arginine, alanine and glycine)(*spm3*) (250) to serve as a linker. As *spm1*, *spm2* and *trxL1* are less than 1 kilobase in length, I amplified the entire open reading using the Phusion HF polymerase (*spm1*, 987 bp; *spm2*, 929 bp; *trxL1*, 918 bp). To integrate the respective fragments into the pL18 vector, I added EcoRI and BamHI restriction cutting sites to the respective primers. I used the following primers for amplification of the respective ORF: P2229, P2230 (*spm1*), P2231, P2242 (*spm2*) and P2233, P2234 (*trxL1*). As the *spm2* ORF contains an EcoRI restriction site, I added an MfeI site to the forward primer P2231 instead. MfeI and EcoRI produce compatible cohesive ends, enabling the PCR fragment digested with MfeI to be integrated into the EcoRI-digested vector backbone. As the *spm3* ORF exceeds 1 kb in length, I amplified only a 1068-bp long 3' homology region at the C-terminus of *spm3* from PbANKA WT-genomic DNA. The primers AB31_2 and AB32_2 were used for amplification of the 3' homology fragment contained restriction cutting sites for EcoRI and BamH as before.

The PCR composition for *spm1*, *spm2* and *trxL1* is shown in **Table 17** with the thermocycling conditions being depicted in **Table 18**. As the Phusion polymerase did not amplify the *spm3* fragment, I used Taq-based amplification alternatively. I supplemented the PCR mix with 0.5 mM $MgCl_2$ (see 5.2.6), used 1 µl gDNA as template and set the extension temperature to 60 °C instead of 68 °C (**Table 19**) The resulting fragments were purified and cloned into the pL18 vector backbone as described in 5.2.2 and correct sequence was confirmed via sanger sequencing. The final vector maps are depicted in **Figure 38 A-D**.

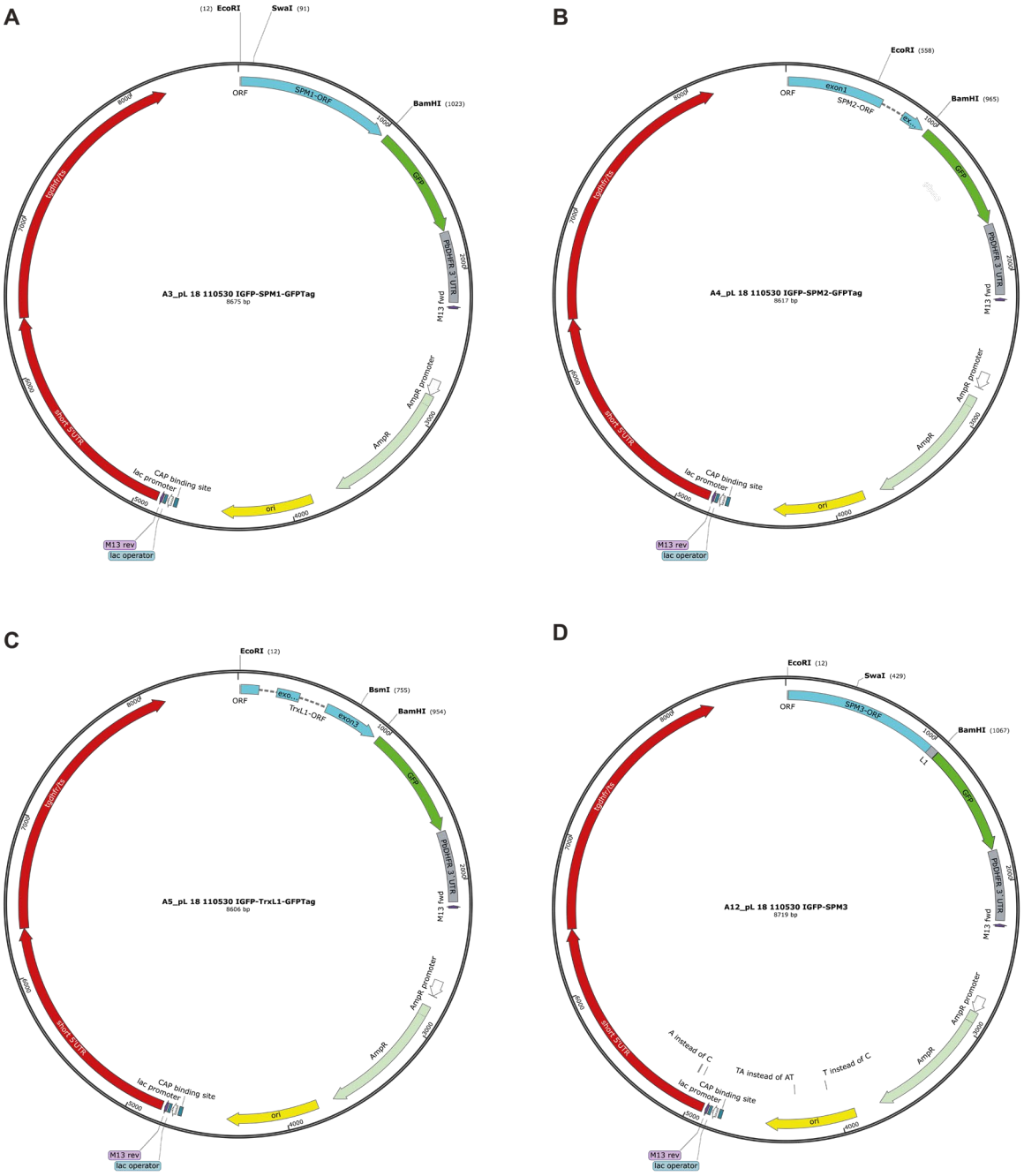

Figure 38 Plasmid maps to generate *gfp*-tagged MAP mutant parasite lines. A) *spm1-gfp*, **B)** *spm2-gfp*, **C)** *trxL1-gfp*, **D)** *spm3-gfp*. Enzymes used to insert complete MIP ORFs (*spm1*, *spm2*, *trxL1*) or a fragment of the C-terminus (*spm3*), respectively, as well as the enzyme used to linearize the plasmid prior to transfection are highlighted. AmpR – ampicillin resistance, L – linker, ORF – open reading frame, Ori – origin of replication, *tgdhfr* – *Toxoplasma gondii* dihydrofolate reductase, UTR – untranslated region.

Before transfection, vectors were linearized with SwaI (*spm1*, *spm3*), EcoRI (*spm2*) and BsmI (*trxL1*), respectively, followed by ethanol precipitation and proceeded as described in 5.3.4.

5.2.5 Transformation of competent *E. coli* and small-scale plasmid purification

For transformation, the high efficiency transformation protocol from NEB was used. For this, 5 µl of plasmid DNA was added to 30 µl of competent *E. coli* (C2992) cells, the tube was carefully flicked, and incubated on ice for 30 min. Heat-shock was carried out exposing bacteria for 30 s to 42 °C before directly placing them back on ice for 5 min. Transformed cells were recovered in 950 µl of SOC medium and incubated at 37 °C and 250 rpm agitation for 1 h. After spinning down, cells were resuspended in remaining 100-200 µl of medium to be directly plated onto LB agar plates containing 0.1 mg/mL ampicillin (LB/Amp). After overnight incubation at 37 °C, 5-10 colonies were picked and analysed via colony PCR. Positive clones were grown in 5 mL of LB medium/ 0.1 mg/mL ampicillin at 37 °C for small-scale plasmid preparation. The next day, plasmid DNA was extracted using the GenElute™ HP plasmid Miniprep Kit from Sigma-Aldrich.

5.2.6 Colony PCR and sequence verification via sequencing

To verify the plasmid sequence prior to sequencing, a colony PCR was performed. For this, 5-8 colonies from overnight transformations were picked, shortly dipped into the prepared PCR mix and spread onto a LB/Amp plate. The PCR mix contained 1x Standard Taq reaction buffer, 200 µM dNTPs, 10 µM of each forward and reverse primer, 2 units of Taq polymerase in a total volume of 25 µl. The PCR cycling conditions are depicted in **Table 19** and included a heat-incubation step of 5 min at 95 °C prior to the actual PCR. Following colony PCR, fragment sizes were checked on a 0.8% agarose gel. Overnight cultures of selected colonies were grown in 5 mL LB/Amp medium overnight at 37 °C for a small-scale overnight bacteria culture. The next day, plasmid DNA was extracted using the GenEluteTM HP plasmid Miniprep Kit from Sigma-Aldrich. To confirm the correct sequence, plasmid DNA was sent to sanger sequencing provided by Eurofins Genomics. The obtained sequence was aligned and analysed with either SnapGene® or Benchling.

Table 19 PCR cycling conditions using Taq polymerase. Kb – kilobase, s – seconds.

Function	Temperature	Time	Repetition
Polymerase activation/DNA denaturation	94 °C	30 s	
Denaturation	94 °C	30 s	x 30 cycles
Annealing (dependent on Tm primer)	Tm – 2°C	30 s	
Extension (1 min/kb)	68 °C	(3 min)	
Final extension	60 °C	10 min	
Slowly cool down to 4 °C	4 °C	hold	

5.3 Experimental Parasitology techniques

5.3.1 Mice infection and anaesthesia

Naïve mice were infected via intraperitoneal (i. p.) injection of either cryopreserved parasites or via fresh blood transfer from a donor mouse. If full blood needed to be collected, the mouse was anesthetized via i. p. injection with 120 mg/mL ketamine and 16 mg/mL xylazine. Following full anaesthesia, blood was harvested via cardiac puncture.

5.3.2 Determination of parasitemia and long-term storage of parasites

Blood-stage parasitemia was determined through thin blood smear. For this, a drop of tail-blood from a mouse was placed onto a glass slide, smeared to a thin layer and air-dried. Following short methanol-fixation, the sample was stained with Hemacolor. The dried slides were then analysed at a Zeiss Axiostar Light microscope at 100x magnification with immersion oil. Parasitemia was determined by counting infected and uninfected erythrocytes in one field of view and uninfected erythrocytes in nine additional fields of view with comparable erythrocyte densities. The total number of erythrocytes in the nine fields was then estimated as the counted number of the first field. The parasitemia was then calculated as the percentage of infected erythrocytes of all erythrocytes.

Generated parasite lines were stored as cryo-stocks in liquid nitrogen. For this, 100 µl of collected blood from an infected mouse with 1-3% parasitemia (see 5.3.1) was mixed with 200 µl of freezing solution and directly placed into liquid nitrogen.

5.3.3 Parasite isolation and genomic DNA extraction

As soon as mice reached parasitemias between 1-3%, mice were bled (see 5.3.1). The collected blood was transferred to a 1.5 mL tube, filled up to 1.5 mL with 1x PBS and supplemented with 0.0093% Saponin/PBS. To facilitate RBC lysis, the tube was vortexed for 15 s. Centrifugation for 1 min at 13 000 rpm pelleted the free parasites, which were subsequently washed three times in 1x PBS. Following parasite isolation, the genomic DNA was isolated using the DNeasy Blood and Tissue kit according to manufacturer's protocol.

5.3.4 Generation of mutant parasite lines

Preparative digest of plasmid DNA and Ethanol precipitation

To either KO or tag a selected gene, plasmid DNA was linearized by restriction enzyme digest. To 50 µl of plasmid DNA obtained from one small-scale overnight culture, 20 µl of CutSmart buffer and 1 µl of the respective restriction enzyme was added and filled up with dH_2O to a total volume of 221 µl. After restriction digest for 2 h at 37 °C, completeness of digest and the correct fragment

size was checked via gel electrophoresis with a 0.8% agarose gel. The remaining digested vector was then ethanol-precipitated. For this, 0.1x of digest volume 3M sodium acetate (pH 5.3) and 2.5x of digest volume 100% ice-cold ethanol were added to the digested plasmid DNA (221 µl). DNA was allowed to precipitate for at least 3 h at -80 °C or alternatively overnight at -20 °C. Subsequently, the precipitated DNA was washed twice with 1 mL of 70% ice-cold ethanol for 10 min at 14800 rpm at 4 °C. The supernatant was removed and the DNA pellet was allowed to air-dry for 10 min under a fume-hood. Finally, DNA was resuspended in 35 µl of dH_2O.

Schizont culture and nycodenz purification

To obtain a sufficient amount of schizonts for transfection, parasites of the desired parental stain were cultured overnight *in vitro* (322). For this, a donor mouse was injected with the parental strain. As soon as it reached a parasitemia between 1-2% it was bled by cardiac puncture, the blood was transferred to prewarmed transfection medium (complete, with FBS) in a T75 culture flask and incubated overnight at 37 °C and 5% CO_2. After 21 to 24 h of incubation, the presence of mature schizonts was checked via blood-smear. If sufficient schizonts were observed, the schizonts were purified via Nycodenz-density centrifugation. For this, the blood culture was transferred to a 50 mL falcon and carefully underlaid with 10 mL of 55% Nycodenz. Centrifugation for 25 min at 1000 rpm and RT (without break) accumulated mature schizonts in a brown interphase between the Nycodenz and the medium phase of the density gradient. The interphase was carefully collected and isolated schizonts were pelleted for 10 min at 1000 rpm. The schizont pellet was taken up into fresh complete T-medium (1 mL per transfection construct).

Transfection and selection

Transfection of linearized constructs was done by electroporating purified schizonts using the Amaxa Nucleofactor II from Lonza. Shortly before transfection, schizonts were spun down. The ethanol-precipitated DNA was first mixed with 100 µl Nucleofactor®, then used to resuspend the schizont pellet and transferred to an electroporation cuvette. Electroporation was carried out using the U-33 program of the electroporator. Directly after successful electroporation, schizonts were allowed to recover by adding 50 µl of incomplete T-medium and directly injected i.v. into the tail vein of a naïve Swiss mouse. The next day, transgenic parasites were positively selected by adding pyrimethamine to the drinking water. Parasitemia was monitored from day 7 post transfection onwards. As soon as mice reached parasitemias between 1-2%, they were bled by cardiac puncture. From the blood, cryostabilates were created and genomic DNA was purified for genotyping PCR (5.3.6).

5.3.5 Limiting dilution to clone out isogenic parasite line

As transfection of parasites are never 100% effective, it will give rise to a mixed parasite population consisting of transgenic and wild-type/non-transgenic parasites. To generate an isogenic parasite line that consists of only transgenic parasites with the genetic change of interest, a limiting dilution (LTD) was performed. For this, the cryostabilate of the transfection mix was injected into a naïve donor mouse which was kept under selective drug pressure (pyrimethamine or 5-FC). As soon as the donor mouse reached a parasitemia between 0.2 – 1% (without multiple infected erythrocytes), it was bled by cardiac puncture. The blood serially diluted in PBS by diluting twice 1:100 before a final dilution step (see below) to reach a statistical concentration of one single parasite (P) in 100 µl of PBS. The formula is shown below:

$$x = \frac{(b \times \frac{P}{100\ \mu l} \times 2000\ \mu l}{\text{Parasitemia} \times 7x10^6\ \text{erythorcytes}/\mu l} \qquad b = \frac{\#\ \text{mice to be injected} - 1}{\#\ \text{mice to be injected}}$$

Parasitemia is given in decimal

In total, six to eight recipient mice per LTD were injected with 100 µl i.v.. Parasitemia was monitored from day7 onwards and mice were kept under normal water supply (no selective drug pressure). As soon as the recipient mice reached parasitemias between 1-2%, they were bled by cardiac puncture. From the blood, cryostabilates were made and parasites were isolated and subjected to genotyping PCR. Mice that did not become positive within 17 days post injection were considered negative.

5.3.6 Genotyping

A genotyping PCR was performed to verify the genotype and isogeneity of a parasite line. The PCR reaction (25 µl) included 1 µl of gDNA, 1x Standard Taq reaction buffer, 200 µM dNTPs, 10 µM for each forward and reverse primer and 2 units of Taq polymerase. The primer combinations used for each parasite line are listed in ***Table* 20**. Thermocycler settings are shown in **Table 19**.

Table 20 Combinations of genotyping oligonucleotides for KO parasite lines. *Primer positions as indicated in **Figure 6** and with their sequences depicted in **Table 9**. The genetic modification tested via genotyping PCR is shown in bold. Cas – cassette, *gfp* – fluorescent protein, KO – knockout, P – primer, WL – whole locus, WT – wildtype.

Genetic modification	PCR	Primer position*	Primer combination
***spm1*(-)**	KO	P4.2 x P2	P962 x P650
trxL1(-)/***spm1*(-)**	WT	P3.2 x P2	P2223 x P2222
	WL	P2 x P1	P650 x P2224
***spm1*(-)ns**	Cas	P4.2 x P2	P962 x P2222
	WL	P1 x P2	P2255 x P2222
***spm2*(-)**	KO	P4.2 x P2	P962 x P2227
	WT	P1 x P3.1	P2225 x P2226
	WL	P1 x P2	P2243 x P2244
spm1(-)ns/***spm2*(-)-*gfp***	KO	P1 x P4.1	P2266 x P960
trxL1(-)ns/***spm2*(-)-*gfp***	KO-GFP	P1 x P4.1	P2266 x P2019
	WT	P1 x P3.1	P2266 x P2268
	WL	P1 x P2	P2266 x P2267
***spm3*(-)**	5'Int	P1 x P4.1	P2251x P962
	3'Int	P4.2 x P2	P135 x P2252
	WT	P1 x P3.1	P2251 x P2253
***trxL1*(-)**	KO	P2 x P4.2	P2221 x P975
	WT	P2 x P3.2	P2221 x P2220
	WL	P2 x P1	P2221 x P2219
***trxL1*(-)ns**	WL	P1 x P2	P2439 x P2440
	Cas	P4.1 x P1	P1734 x P2439
trxL1(-)/***spm1*(-)ns**	KO	P2 x P4.2	P2222 x P2145
	WL	P2 x P1	P2222 x P2140

Table 21 Combinations of genotyping oligonucleotides for tagged genes. Oligonucleotides according to **Figure 10** with 5' Integration: P1 x P2, 3' Integration: P3 x P4. Oligonucleotide sequences are depicted in **Table 9**. *gfp* – green fluorescent protein, P – primer.

	Parasite line			
	spm1-gfp	*spm2-gfp*	*spm3-gfp*	*trxL1-gfp*
5' Integration	P2224 x P210	P2227 x P210	P2265 x P2019	P2219 x P862
3' Integration	P2239 x P650	P2239 x P2228	P2239 x P2252	P2239 x P2221

5.3.7 Determination of asexual blood growth rate

The growth rate of asexual blood stages was determined from mice that had previously been injected with one iRBCs during a LTD. Parasitemia values were determined on day 8 post infection from mice that had been shown to contain isogenic parasites with the correct genotype. The parasitemia was then used to back-calculate the growth rate as shown in the formula below. The asexual growth rate is depicted in fold increase per 24h (323, 324).

$$\frac{\frac{\text{parasitemia (\%)}}{100} \text{ x } 7\text{x}10^6 \text{ RBCs}/\mu\text{l}^6 \text{ x } 2000 \ \mu\text{l}^*}{\text{number of parasites injected}}$$

*the total blood volume of a 6-8 week old Swiss mouse comprises approximately 2000 µl of blood with each µl of blood containing $7\text{x}10^6$ RBCs (325).

5.3.8 Negative selection of isogenic parasite lines

For negative selection (**Figure 6**), a mouse was injected with a cryostabilate of the respective transgenic parasite line and parasitemia was monitored daily. As soon as the parasitemia reached around 1%, 5-FC was added to the drinking water. This results in initial decrease in parasitemia as parasites that kept the selection cassette die off and a following increase in parasitemia due to replication of parasites that successfully excised the selection marker. As negative selection is not 100% accurate, LTD followed to generate isogenic, negatively-selected parasites.

5.3.9 Exflagellation assay

A naïve Swiss mouse was injected with a cryostabilate of the respective parasite line. As soon as the donor mouse reached a parasitemia between 0.5 – 3%, the mouse was bled and 20 x 10^6/10 x 10^6 iRBCs i.p. were transferred into a recipient mouse. Three/Four days later, the presence of gametocytes was checked via exflagellation assay. For this, a drop of tail blood from a mouse was placed onto a glass slide and tightly covered with a cover glass. After 12 min of incubation at 19 °C, the number of exflagellation centers per field of view was determined at a Zeiss Axiostar light microscope at 40x magnification with a phase contrast ring. If at least two exflagellation centers could be observed in multiple fields of view with comparable erythrocyte densities, it was proceeded for mosquito infection or *in vitro* ookinete culture.

5.3.10 Mosquito infection

A naïve Swiss mouse was injected with a cryostabilate of the respective parasite line. As soon as the donor mouse reached a parasitemia between 0.5 – 3%, the mouse was bled and 20 x 10^6/10 x 10^6 iRBCs i.p. were transferred into two recipient mice. Three/Four days later, the presence of gametocytes was checked via exflagellation assay as described before. If exflagellation was sufficient, mice were anaesthetized with 120 Ketamine/ 16 mg Xylazine. Anaesthetized mice were placed onto a mosquito cage containing approximately 200 female *Anopheles stephensi* mosquitoes that had been starved for at least 4 h prior to feed. Mosquitoes were allowed to feed for 20 to 40 min. Infected mosquitoes were kept at 21 °C and 80% humidity and provided with both sugar and salt solution-soaked pads.

5.3.11 Ookinete culture and motility assay

To determine whether parasites can develop into motile ookinetes, an *in vitro* ookinete culture was set up and followed by *in vitro* ookinete gliding assays. From a previously infected donor mouse, either 20 x 10^6 iRBCs (to setup a culture 3 days post infection) or 10 x 10^6 iRBCs (to setup a culture 4 days post infection) were transferred into a recipient mouse. To induce reticulocytosis, the recipient mouse was i.p. injected with 200 µL phenylhydrazine two days prior to the transfer. Three to four days post transfer, the presence of gametocytes was checked as described before. If exflagellation was sufficient, the recipient mouse was bled by cardiac puncture and the blood was transferred into a T25 flask prefilled with 10 mL of complete ookinete media. Ookinetes were allowed to develop for 21 h at 19 °C with 50 rpm shaking. The next day, presence of ookinetes was checked via a thin blood smear. To purify ookinetes, the culture was transferred into a 50 mL falcon and carefully underlaid with 10 mL 63% Nycodenz. Centrifugation for 25min at 1000 rpm and RT (without break) separated ookinetes from iRBCs and RBCs. The ookinete-containing interphase was collected and pelleted for 8 min at 1000 rpm at RT (with break). The ookinete

pellet was reconstitute with 1 mL FBS-free ookinete medium. From the ookinete suspension, 200 µl were taken and concentrated in 20 µl ookinete medium. From this, 2-3 µl of ookinete suspension was put onto a glass slide and tightly covered with a cover glass. Ookinetes were then imaged at a wide-field microscope (Carl Zeiss) at 25x magnification (0.8 NA, water-immersion) in DIC and movies were taken with 15 s/frame for a total of 10 min.

Ookinete motility movies were analysed single-blinded and both the motility pattern and the speed were determined. Ookinetes that moved more than one parasite length were considered continuous movers, whereas all ookinetes that moved less than one parasite length were considered non-movers. Ookinete speed was determined using the manual tracking tool provided in Fiji.

5.3.12 Analysis of oocyst development by mercurochrome staining

To check whether parasites are capable to infect mosquito midguts and develop oocyst, mosquito midguts were dissected on two separate days between day 11 to day 14 post infectious blood meal. Midguts were dissected into 100 µl PBS and kept ice. Midguts were permeabilized for 20 min at RT in 1% Nonidet®P40 followed by staining in 0.1% mercurochrome for 30 min up to 1.5 h at RT. The staining solution was removed and midguts were washed with PBS until the supernatant became colourless. The stained midguts were transferred onto a glass slide, covered with a cover glass and imaged at a Widefield Zeiss microscope at 10x magnification (NA 0.5) with a green filter. Both the infection rate, as in the ratio of infected midguts compared to all midguts, and the number of oocysts per infected midgut were determined.

5.3.13 Analysis of sporozoite formation

Midgut and salivary gland sporozoites

To investigate whether parasites can form into sporozoites and invade the salivary glands, both midguts and salivary glands were dissected on two separate days between day 17 and day 22 post mosquito infection. Both tissues were dissected from the same mosquito and collected into 50 µl PBS each. Crushing tissues for 1 min using a pestle released sporozoites into the suspension from which 10 µl were then loaded onto a Neubauer chamber and allowed to settle for 10 min. The number of sporozoites was determined at a Zeiss Axiostar light microscope at 40x magnification with a phase contrast ring. The ratio was determined as being the number of sporozoites in the salivary glands over the number of sporozoites in the midguts. The collection of two lateral lobes was defined as one salivary gland with each mosquito possessing two salivary glands.

Hemolymph sporozoites

The presence of sporozoites in the mosquito's hemolymph was checked between day 14 to day 16 post infectious blood meal. Mosquitoes were precooled on ice for at least 30 min to immobilize them and dissected dry. The second segment of the abdomen was cut-off. A PBS-preloaded and self-made glass capillary was inserted into the thorax and the hemolymph was subsequently flushed out of the mosquito. At least three drops of hemolymph were collected per mosquito.

5.3.14 *In vitro* sporozoite motility assay

Sporozoite motility was determined performing *in vitro* gliding assays. For this, salivary glands were dissected into 50 µl RPMI and sporozoites were collected on two separate days between day 17 and day 22 post infection as described above. To purify parasite, the sporozoite suspension was filled up to 1 mL with RPMI and transferred into a 15 mL falcon and subsequently underlaid with 3 mL of 17% Accudenz. Centrifugation for 20 min at 2800 rpm at RT (without break) separated sporozoites from cell debris. A total volume of 1.4 mL sporozoite containing interphase was collected and sporozoites were pelleted for 3 min at 13 000 rpm. The supernatant was removed and sporozoites were activated in 100 µl 3% BSA/PBS and transferred to a 96-well optical bottom plate. Prior to imaging, sporozoites were spun down for 3 min at 1000 rpm. Motility was imaged for up to 1 h post activation at a wide-field microscope (Carl Zeiss) using a 25x magnification (0.8 NA, water-immersion). Movies were taken in DIC with 3s/frame for a total of 100 imaging frames.

Sporozoite motility movies were analysed single-blinded and both the motility pattern and the speed were determined. Sporozoites that moved continuously for at least 50 frames without stopping more than 10 frames were classified as productive/continuous movers. All sporozoites that moved less than 50 frames but more than one parasite length were considered partial movers. Not motile sporozoites moved less than one parasite length and stayed attached to the surface with at least one attachment point. Floaters were not attached to the substrate. The speed of continuously moving sporozoites was either determined as the number of circles moved per 100 frames (*spm3*(-) data) or as velocity in µm/s (MIP data). To determine the circle diameter, a Z-projection was created from the movie frames. The Z-projection was processed by subtracting the minimum Z-projection image from the maximum Z-projection image to reduce noise. The speed was then calculated using the outer circle diameter and the total number of circles moved across the frames recorded.

5.3.15 Transmission to mice

To check whether parasites are transmissive and can infect mice either via natural transmission or by avoiding the skin phase, a transmission assay was performed. For natural transmission by

mosquito bite, 10 infected mosquitoes were placed into a cup and allowed to feed on one naïve C57/BL6 mouse for 10-20 min with at least 6 mosquitos having bitten. For transmission while avoiding the skin phase, salivary gland sporozoites were isolated from infected mosquitoes as described before (day 18 to day 22 post infection) and 1000 sporozoites were injected into the teil vein of a C57/BL6 mouse. For each biological replicate, three to four mice for each setup were used. Following infection, parasitemia was determined daily at approximately the same time of the day from day 3 onwards. As soon as mice reached a parasitemia between 1-2%, they were sacrificed by cervical dislocation.

5.3.16 Visualization of microtubules in *Plasmodium* parasites using SiR-tubulin

Localization of MAPs in relation to microtubules in ookinetes and sporozoites was determined by staining microtubules with SiR-tubulin.

Sporozoites were isolated in RPMI (see 5.3.13), resuspended in 3%BSA/PBS containing 1:1000 diluted Hoechst and 1:1000 diluted SiR-tubulin and transferred to an 8-well ibid dish. Centrifugation for 4 min at 800 rpm pelleted sporozoites. Incubating sporozoites for 10 min at RT allowed them to glide and to be stained in parallel. Cells were carefully washed three times with RPMI and then fixed for 1h at RT in 4% PFA/PBS, washed again thrice and immediately imaged.

For ookinete staining, ookinetes were incubated and purified as described before (5.3.11). From the purified ookinetes, 20 µL of resuspended cells were pelleted for 1 min at 13 000 rpm. The pellet was resuspended in incomplete ookinete media containing Hoechst (1:1000) and SiR-tubulin (1:1000) and parasites were stained for 10 min at RT. Cells were washed three times with PBS. For imaging, ookinetes were shortly vortexed and 3 µl of cell suspension was transferred to a glass slide, covered tightly with a cover slip and sealed with wax.

Both sporozoites and ookinetes were imaged at a Zeiss Airyscan 2 LSM900 using a 63x/1.4-NA oil-immersion objective. Imaging stacks with 0.14 µm spacing were acquired and then processed using the internal 3D airyscan processing mode at the Zeiss software, version 3.9. Images were further processed using Fiji. First, a maximum Z-projection was done. To measure the MAP/microtubule intensity signal over the cell width, lines were placed perpendicular to the parasite with 2 µm distance from the cell's apical end and a length of 1.5 µm (sporozoites) or 4 µm (ookinetes) and a width of 2 pixels.

5.3.17 Immunofluorescence assay of *Plasmodium* parasites (anti-tubulin staining)

Localization of MAPs in relation to microtubules in ookinetes and sporozoites was determined by immunofluorescence assay (IFA). Sporozoites were isolated in RPMI as described previously (5.3.13). Sporozoites were then resuspended in 3% BSA/PBS supplemented with 1:1000 Hoechst and 50 000 – 100 000 cells were transferred to an 8-well glass bottom ibid imaging dish.

Centrifugation for 4 min at 800 rpm pelleted sporozoites within the imaging dish. Incubating sporozoites for 10 min at RT allowed them to glide and attach. Ookinetes were stained in solution in a 1.5 mL tube.

Both sporozoites and ookinetes were fixed for 1h at RT in 4% PFA/PBS. Following three washing steps with RPMI, cells were permeabilized in 0.5% Triton X-100/PBS for 1h at RT. Cells were washed again thrice with RPMI and then incubated in primary antibody for 1 h at RT. The primary antibody solution was removed, the cells were washed thrice in PBS and subsequently stained with secondary antibody for 1h at RT. Cells were finally washed thrice in PBS and samples were either directly imaged or kept at 4 °C until further use. For imaging, ookinetes were shortly vortexed and 3 µl of cell suspension was transferred to a glass slide, covered tightly with a cover slip and sealed with wax. Cells were imaged at a Zeiss Airyscan 2 LSM900 using a 63x/1.4-NA oil immersion objective. Imaging stacks with 0.14 µm spacing were acquired and then processed using the internal 3D airyscan processing mode at the Zeiss software, version 3.9. Images were further processed using Fiji. Measurement of MAP/microtubule intensity signal over the cell width was carried out as described before (5.3.16)

5.3.18 Temperature assays in MIP KO mutants

To test whether subpellicular microtubules of MIP-KO mutants are sensitive to cold treatment, a temperature sensitivity assay was performed. For this, salivary gland sporozoites from day 18-d22 post infection were isolated into RPMI as described before, with the difference that collected salivary glands were kept on RT instead on ice (5.3.13). Sporozoites were pelleted for 3 min at 13 000 rpm and activated with 3% BSA/RPMI supplemented with 1:1000 SiR-tubulin and 1:1000 Hoechst. 50 000-100 000 cells (in a volume of 150 µl) were transferred into a well of an 8-well ibid glass bottom imaging dish. Cells were spun down for 4 min at 800 rpm and sporozoites were allowed to settle and glide for 10 min at RT while being stained with SiR-tubulin. The staining solution was removed and cells were washed thrice with RPMI. As initial timepoint T0, sporozoites were immediately fixed in 4% PFA/RPMI. Sporozoites were then incubated either for 2h at 20 °C or on ice. Following incubation at the different temperatures, sporozoites were fixed in 4% PFA/RPMI for 1h at RT. The fixative was removed and the cells were washed thrice with RPMI. Additionally, to SiR-tubulin, microtubules were also stained with an anti-tubulin antibody (see 5.3.17). Sporozoites were imaged at a Zeiss Airyscan 2 LSM900 using a 63x/1.4-NA oil immersion objective. Imaging stacks with 0.14 µm spacing were acquired and then processed using the internal 3D airyscan processing mode at the Zeiss software, version 3.9. Images were analysed in a single-blinded fashion using Fiji.

Using Fiji, I performed a sum Z-projection and determined the microtubule intensities along the longitudinal section of the parasite placing a line along the apical distal axis (line width 30 pixels)

using the segmented line tool from Fiji. I first normalized the sporozoite length and then binned along a set length of 10 µm with bin widths of 0.2 µm. Microtubule intensity values were normalized to the parasite's total Sir-tubulin or anti-tubulin signal, respectively. For the cross-sectional analysis, I took the centre slice of the acquired Z-stack, placed a 1.5 µm long line (line width 10 pixels) perpendicular to the sporozoite (from the inner curvature to the outer edge of the cell) with a distance of 2.5 µm from the centre of the nucleus towards the apical end of the cell. Similar to the longitudinal measurement, I also normalized the cross-sectional values to the parasite's total Sir-tubulin or anti-tubulin signal, respectively.

5.3.19 Cryo-Tomography of salivary gland sporozoites

Sample preparation of infected salivary glands

To investigate SPMTs of MIP-KO sporozoites in high resolution, SPMTs were analysed via cryo-tomography. For this, salivary gland sporozoites from mosquitoes infected with either WT, *spm1*(-), *trxL1*(-) or *trxL1*(-)/*spm1*(-)ns were dissected on day 26 post infection. To preserve the salivary gland tissue and hence sporozoites from degradation, complete salivary glands were dissected into 1 mL 10% human serum/Leibovitz medium in 1.5 mL tubes. Tubes were shipped on ice to our collaborators and around 24-30 hours post dissection, salivary glands were smashed (5.3.13) to releases sporozoites and then processed for plunge-freezing.

Plunge-freezing (performed by Josie Ferreira, University College London)

Samples were processed similarly as previously described (112): First sporozoites were diluted 1:4 in RPMI medium (without phenol red or serum) and 3 µl of parasite suspension was applied onto freshly plasma-cleaned UltrAufoil R1.2/1.3 300 mesh EM grids. Excess liquid was manually back-blotted and grids were plunged into a reservoir of ethane/propane using a manual plunger. Grids were stored in liquid nitrogen.

Cryo-FIB milling, Cryo-EM and tomogram reconstruction

(performed by Jana Lierl, Yuliia Mironova, both University of Hamburg and Vojta Prazak, CSSB Hamburg and Oxford Biochemistry)

After cryo-grid preparation, samples were FIB-milled: The grids were clipped into autogrids modified for FIB preparation (326) and subsequently loaded into a cryo-FIB/SEM dual-beam microscope. A thin layer of platinum was applied to the grids, followed by the deposition of an organometallic platinum layer using a gas-injection system.

The optimal grid side was identified for lamella preparation, after which the AutoTEM system was employed to automatically mill samples resulting in a final lamella thickness of 120-200 nm. Before removing the sample, the grids were coated with a final layer of platinum. Grids were stored in liquid nitrogen.

For tilt-series acquisition, cryo-EM FIB-milled grids were loaded into a Titan Krios microscope equipped with a K3 direct electron detector and a (Bio-) Quantum energy filter. Tomographic data was collected with SerialEM (327) with the energy-selecting slit set to 20 electron volts. Datasets were collected using the dose-symmetric acquisition scheme at a ± 65° tilt range with 3° tilt increments. For each dataset, five to ten frames were collected and aligned dynamically during data collection using SerialEM, maintaining the total fluence to less than 120 $e^{-}/Å^2$. Til series were recorded at defoci ranging from 3-8 µm were. To reconstruct the final tomogram, frames were dynamically aligned in SerialEM; CTF estimation, phase flipping and dose-weighting was performed in IMOD (321). Finally, tilt-series were aligned in IMOD or AreTomo using patch-tracking.

5.3.20 Transmission electron microscopy (TEM) of midgut sporozoites

Localization of SPMTs in comparison to the IMC in the *spm3*(-) was analysed by performing TEM of midgut sporozoites. For this, highly infected midguts were isolated as described before (5.3.12) and fixed over night at 4 °C in 4% PFA/ 4% glutaraldehyde in 100 mM sodium cacodylate buffer. Fixative was removed washing samples thrice in 100 mM sodium cacodylate buffer at RT for 5 min followed by a secondary fixation at RT for 60 min in 1% osmium in 100 mM sodium cacodylate buffer. Secondary fixative was removed by washing samples again twice in 100 mM sodium cacodylate buffer and twice in ddH_2O. The cells were contrasted with 1% uranyl acetate (in ddH_2O) at 4 °C overnight. The samples were then washed twice with ddH_2O for 10 minutes each and dehydrated by sequential incubation in acetone solutions of increasing concentrations (30%, 50%, 70%, and 90%) for 10 minutes each, followed by two 10 min incubations in 100% acetone. The samples were gradually transferred to Spurr's resin mixture by incubating in solutions of increasing concentration (25%, 50%, and 75%) at room temperature for 45 minutes each,

followed by 100% Spurr's resin at 4 °C overnight. Midguts were then embedded in Spurr's resin and polymerized at 60 °C overnight. The embedded midguts were sectioned into 70-nm-thick slices and imaged using a JEOL JEM-1400 transmission electron microscope at 80 kV, equipped with a TempCam F416 camera. The images were processed with the Fiji software, applying a Gaussian blur to enhance contrast.

The numbers and distances of SPMTs towards the IMC were measured in a single-blinded fashion. All sporozoites with clearly identifiable SMTs were selected, and the SPMTs per sporozoite were manually counted. The distances from the SPMTs to either the IMC or a membrane of yet unknown origin were measured from the centre of the microtubule to the inner side of the IMC or to the membrane, respectively. Based on Ferreira *et al.* (112), a threshold distance of 40 nm was defined, with any measurements of 40 nm or less classified as "IMC-close".

5.3.21 Ultrastructure Expansion microscopy (U-ExM) of ookinetes

U-ExM and image acquisition

Sample preparation of ookinetes for U-ExM was carried out as previously described (220, 328) with some modifications highlighted here (**Figure 39**). Ookinetes were incubated and purified as described before (5.3.11). The resulting pellet was resuspended in incomplete ookinete medium and 200 µl of suspended cells were seeded onto polyD-lysine precoated 10 mm coverslips. After allowing them to settle for 10 min at RT, the supernatant was removed and replaced with 200 µl 4% PFA/PBS. Following fixation for 20 min at 37 °C, cells were washed very carefully three times with PBS and kept in PBS at 4 °C until further use. Coverslips were then incubated for 3.5 h (or up to 5 h) at 37 °C in 1.4% formaldehyde/ 2% acrylamide/in PBS solution being agitated at 80 rpm. Afterwards, cells were embedded into a gel consisting of 10%TEMED/10% ammonium persulfate/monomer solution. For this, the gel was polymerized for 5 min on ice followed by incubation for 1 h at 37 °C. Denaturation of the gel for 1.5 h at 95 °C released it from the cover slip. It was then placed for 30 min into ddH_2O at RT to expand. After this initial expansion, the gel was fully expanded in autoclaved ddH_2O overnight at RT. The following day, the expansion factor was determined as the gel diameter/coverslip diameter. Small pieces of gel of approximately 10 x 10 mm were cut out and incubated in PBS at RT. The PBS was replaced and the incubation was repeated. Afterwards, samples were blocked in 3% BSA/PBS (filtered) for at least 1h and stained with primary antibody over night or up to 72h at 4 °C and agitation at approximately 30 rpm. Following five washing steps in 0.5% Tween/PBS, the gel pieces were stained with secondary antibody and Hoechst for 2.5 h at 37 °C with 80 rpm agitation. Residual antibody solution was removed by washing the gel pieces five times in 0.5%Tween/PBS. Thereafter, gel pieces were stained for 1.5 h at RT with NHS ester and washed five times. The shrunken gel pieces were re-expanded twice for 30 min at RT before a final re-expansion overnight at RT in ddH_2O

(supplemented with 0.2% sodium azide). To avoid drifting of the sample during imaging, gel pieces were attached to poly-D lysine precoated 8-well imaging dishes (ibiTreat). Gels were imaged at a Zeiss Airyscan 2 LSM900 using a 63x/1.4-NA oil-immersion objective. Imaging stacks with 0.14 µm spacing were acquired and then processed using the internal 3D airyscan processing mode at the Zeiss software, version 3.9.

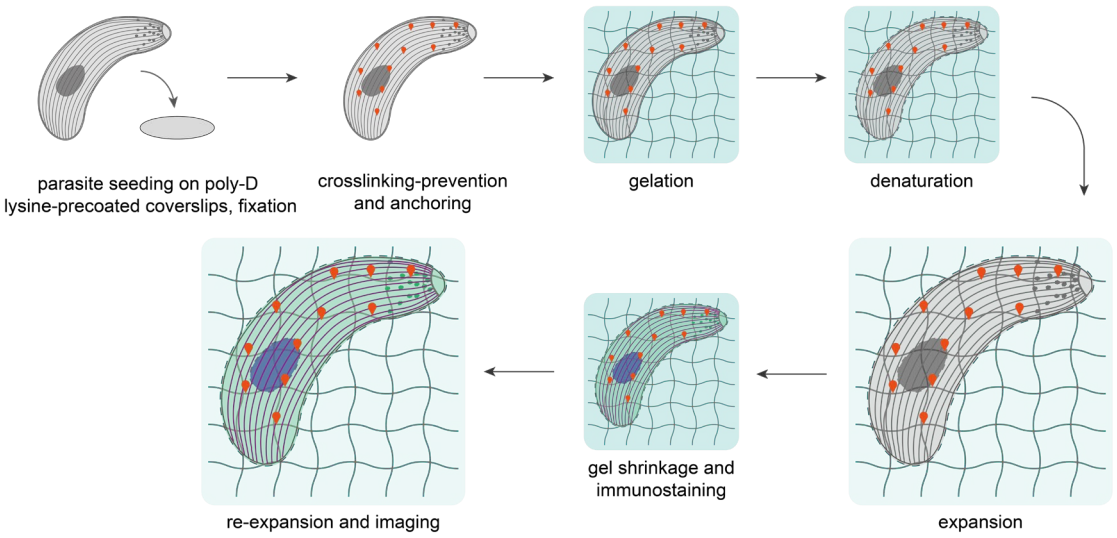

Figure 39 Workflow of U-ExM. Orange icons *indicate* crosslinkers, *w*ave-like lines represent gel meshwork (gel in different shades of turquoise*)*. Cells were stained with *different* antibodies and dyes to visualize SPMTs (magenta), nucleus (blue) and cellular context (green).

Semi-automatic Fiji pipeline for analysing SPMT attachment in U-ExM cross sections

To analyse the extent of SPMT detachment from the IMC, I developed a semi-automated imaging workflow using Fiji. For this, the cell borders were determined using the NHS ester signal as the cellular context. To ensure consistent orientation, the selected region of interest containing the ookinete was first rotated so that the apical end aligned to the left. Next, the image stack was further adjusted by rotating it using the reslice-function in Fiji so that the apical end faced directly towards the viewer (cross-sectional view). Based on the whole parasite length, Fiji then automatically sets positions for an apical (= 10% of parasite length), a nuclear (= 50% of parasite length) and a distal (= 80% of parasite length) location. The NHS ester signal was used to automatically define the outer cell borders by mask detection, which were adjusted manually. This "outer-mask" was sequentially shrunk by applying an erosion operation with 10 iterations resulting in the "inner-mask". Based on the two masks, the SPMT signal (using the anti-polyglutamylation signal to exclude any cross-signal from the spindle microtubules) was measured as raw intensity within the cytosolic (inner mask) and at the periphery (outer mask). The ratio between inner versus outer signal was then calculated for each of the three longitudinal positions.

5.4 Mouse handling and ethics statement

All animal experiments were performed according to the Federation of European Laboratory Animal Science Associations (FELASA) and Society of Laboratory Animal Science (GV-SOLAS) guidelines and approved by the responsible German authorities (Regierungspräsidium Karlsruhe). For all *in vivo* mouse experiments that involved parasite propagation and mosquito infection, 6–8-week-old female Swiss mice were used. For transmission experiments either by mosquito bite or by i.v. injection of sporozoites, 6–8-week-old female C57/ BL6 mice were used. Mice were obtained from Janvier or Charles River Laboratories and kept in the dedicated animal facility at Heidelberg University according to the current guidelines (3 mice per cage, *ad libitum* food and water, 12 h light/dark cycle). Mice were sacrificed by cervical dislocation.

5.5 Mosquito breeding and maintenance

Anopheles stephensi mosquitoes from the strain FDA500 were used for all mosquito work. Mosquitoes were bred according to standard procedures and kept at the mosquito facility of the parasitology department in Heidelberg.

5.6 *In silico* structure prediction using AlphaFold3

For structure predictions, amino acid sequences were obtained from PlasmoDB and structures were predicted using AlphaFold3.

5.7 Statistical analysis

All statistical analysis was using the software GraphPad Prism version 6.01, 10.4.0 or RStudio, Version 2024.9.0.375. The respective statistical tests used is indicated in the respective figure legend.

5.8 Disclosure of usage of artificial-intelligence based tools

ChatGPT (based on the GPT-4 architecture, OpenAI 2023), was used to improve the language style of single sentences or paragraphs in the following chapters: abstract, introduction and discussion. I herewith declare, that I am the sole author of this thesis and take full responsibility for its content and accuracy.

6. Publication list

F. Hentzschel*, **A. M. Binder***, L. P. Dorner, L. Herzel, F. Nuglish, M. Sema, M. C. Aguirre-Botero, M. Cyrklaff, C. Funaya, F. Frischknecht, *Proc. Natl. Acad. Sci.* in press (2025). https://doi.org/10.1073/pnas.2421737122.

(chapter 3.1, 4.1)

J. S. Wichers-Misterek*, **A. M. Binder***, P. Mesén-Ramírez*, L. P. Dorner, S. Safavi, G. Fuchs, T. L. Lenz, A. Bachmann, D. Wilson, F. Frischknecht, T.-W. Gilberger, A Microtubule-Associated Protein Is Essential for Malaria Parasite Transmission. *MBio*. **14**, e03318-22 (2023)

(chapter 3.3, 4.2)

J. L. Ferreira*, V. Pražák*, D. Vasishtan, M. Siggel, F. Hentzschel, **A. M. Binder**, E. Pietsch, J. Kosinski, F. Frischknecht, T. W. Gilberger, K. Grünewald, Variable microtubule architecture in the malaria parasite. *Nat. Commun.* **14**, 1216 (2023)

(chapter 3.1.2, 4.1.3, 4.1.5)

Manuscripts in preparation

F. J. Stortz*, K. Röver*, **A. M. Binder**, M. Konert, B. Spreng, T. Kumar, F. Frischknecht, M. Meissner, E. Jimenez-Ruiz, Luminal acetylation of microtubules is not essential for *Plasmodium* and *Toxoplasma*. In preparation

(chapter 4.1.1)

Other publications

B. Dupouy, L. Cotos, **A. Binder**, L. Slavikova, M. Rottmann, P. Mäser, D. Jacquemin, M. Ganter, E. Davioud-Charvet, M. Elhabiri, Click Coupling of Flavylium Dyes with Plasmodione Analogues: Towards New Redox-Sensitive Pro-Fluorophores. *Chem. – A Eur. J.*, e202403691 (2024)

7. References

1. C. Coban, M. S. J. Lee, K. J. Ishii, Tissue-specific immunopathology during malaria infection. *Nat. Rev. Immunol.* **18**, 266–278 (2018).

2. D. A. Milner, Malaria Pathogenesis. *Cold Spring Harb. Perspect. Med.* **8**, a025569 (2018).

3. S. R. Pavithra, G. Banumathy, O. Joy, V. Singh, U. Tatu, Recurrent Fever Promotes *Plasmodium falciparum* Development in Human Erythrocytes. *J. Biol. Chem.* **279**, 46692–46699 (2004).

4. D. A. Milner, *et al.*, Quantitative Assessment of Multiorgan Sequestration of Parasites in Fatal Pediatric Cerebral Malaria. *J. Infect. Dis.* **212**, 1317–1321 (2015).

5. W. World Health Organization, World malaria report 2024. (2024). Available at: https://www.who.int/teams/global-malaria-programme/reports/world-malaria-report-2024 [Accessed 19 December 2024].

6. F. E. Cox, History of the discovery of the malaria parasites and their vectors. *Parasit. Vectors* **3**, 5 (2010).

7. L. Alphones, Un nouveau parasite trouvé dans le sang des malades atteints de fièvre palustre : origine parasitaire des accidents de l'impaludisme / par A. Laveran. | Wellcome Collection. (1881). Available at: https://wellcomecollection.org/works/fcnztmy5 [Accessed 19 December 2024].

8. Grassi; Battista, *Studio di uno zoologo sulla malaria* (1900).

9. R. Ross, On some Peculiar Pigmented Cells Found in Two Mosquitos Fed on Malarial Blood. *BMJ* **2**, 1786–1788 (1897).

10. S. Sato, *Plasmodium*—a brief introduction to the parasites causing human malaria and their basic biology. *J. Physiol. Anthropol.* **40**, 1 (2021).

11. K. E. Battle, *et al.*, Mapping the global endemicity and clinical burden of *Plasmodium vivax*, 2000–17: a spatial and temporal modelling study. *Lancet* **394**, 332–343 (2019).

12. D. J. Weiss, *et al.*, Mapping the global prevalence, incidence, and mortality of *Plasmodium falciparum*, 2000–17: a spatial and temporal modelling study. *Lancet* **394**, 322–331 (2019).

13. M. Imwong, *et al.*, Asymptomatic Natural Human Infections With the Simian Malaria Parasites *Plasmodium cynomolgi* and *Plasmodium knowlesi*. *J. Infect. Dis.* **219**, 695–702

(2019).

14. B. Singh, *et al.*, A large focus of naturally acquired *Plasmodium knowlesi* infections in human beings. *Lancet* **363**, 1017–1024 (2004).

15. B. Singh, C. Daneshvar, Human Infections and Detection of *Plasmodium knowlesi*. *Clin. Microbiol. Rev.* **26**, 165–184 (2013).

16. G. Snounou, P. M. Sharp, R. Culleton, The two parasite species formerly known as *Plasmodium ovale*. *Trends Parasitol.* **40**, 21–27 (2024).

17. A. A. El-Moamly, M. A. El-Sweify, Malaria vaccines: the 60-year journey of hope and final success—lessons learned and future prospects. *Trop. Med. Health* **51**, 29 (2023).

18. F. Nosten, N. J. White, Artemisinin-based combination treatment of *falciparum* malaria. *Am. J. Trop. Med. Hyg.* **77**, 181–92 (2007).

19. I. Olufadewa, *et al.*, The approval of the first malaria vaccine: The beginning of the end of the malaria epidemic. *J. Glob. Health* **12**, 03087 (2022).

20. M. S. Datoo, *et al.*, Safety and efficacy of malaria vaccine candidate R21/Matrix-M in African children: a multicentre, double-blind, randomised, phase 3 trial. *Lancet* **403**, 533–544 (2024).

21. S. RTS, C. T. Partnership, Efficacy and safety of RTS,S/AS01 malaria vaccine with or without a booster dose in infants and children in Africa: final results of a phase 3, individually randomised, controlled trial. *Lancet* **386**, 31–45 (2015).

22. N. Arora, L. C. Anbalagan, A. K. Pannu, Towards Eradication of Malaria: Is the WHO's RTS,S/AS01 Vaccination Effective Enough? *Risk Manag. Healthc. Policy* **14**, 1033–1039 (2021).

23. A. A. Fola, *et al.*, *Plasmodium falciparum* resistant to artemisinin and diagnostics have emerged in Ethiopia. *Nat. Microbiol.* **8**, 1911–1919 (2023).

24. K. Haldar, S. Bhattacharjee, I. Safeukui, Drug resistance in *Plasmodium*. *Nat. Rev. Microbiol.* **16**, 156–170 (2018).

25. V. A. Ingham, L. Grigoraki, H. Ranson, Pyrethroid resistance mechanisms in the major malaria vector species complex. *Entomol. Gen.* **43**, 515–526 (2023).

26. B. Dinko, G. Pradel, Immune evasion by *Plasmodium falciparum* parasites: converting a host protection mechanism for the parasite's benefit. *Adv. Infect. Dis.* **06**, 82–95 (2016).

27. X. Y. Yam, P. R. Preiser, Host immune evasion strategies of malaria blood stage parasite. *Mol. Biosyst.* **13**, 2498–2508 (2017).

28. H. Matsuoka, S. Yoshida, M. Hirai, A. Ishii, A rodent malaria, *Plasmodium berghei*, is experimentally transmitted to mice by merely probing of infective mosquito, Anopheles stephensi. *Parasitol. Int.* **51**, 17–23 (2002).

29. S. Sidjanski, J. P. Vanderberg, Delayed Migration of *Plasmodium* Sporozoites from the Mosquito Bite Site to the Blood. *Am. J. Trop. Med. Hyg.* **57**, 426–429 (1997).

30. C. S. Hopp, *et al.*, Longitudinal analysis of *Plasmodium* sporozoite motility in the dermis reveals component of blood vessel recognition. *Elife* **4**, e07789 (2015).

31. D. L. Medica, P. Sinnis, Quantitative Dynamics of *Plasmodium yoelii* Sporozoite Transmission by Infected Anopheline Mosquitoes. *Infect. Immun.* **73**, 4363–4369 (2005).

32. J. P. Vanderberg, U. Frevert, Intravital microscopy demonstrating antibody-mediated immobilisation of *Plasmodium berghei* sporozoites injected into skin by mosquitoes. *Int. J. Parasitol.* **34**, 991–996 (2004).

33. F. Frischknecht, *et al.*, Imaging movement of malaria parasites during transmission by Anopheles mosquitoes. *Cell. Microbiol.* **6**, 687–694 (2004).

34. R. Amino, *et al.*, Quantitative imaging of *Plasmodium* transmission from mosquito to mammal. *Nat. Med.* **12**, 220–224 (2006).

35. U. Frevert, *et al.*, Intravital Observation of *Plasmodium berghei* Sporozoite Infection of the Liver. *PLoS Biol.* **3**, e192 (2005).

36. K. Baer, *et al.*, Kupffer cells are obligatory for *Plasmodium yoelii* sporozoite infection of the liver. *Cell. Microbiol.* **9**, 397–412 (2007).

37. J. Tavares, *et al.*, Role of host cell traversal by the malaria sporozoite during liver infection. *J. Exp. Med.* **210**, 905–915 (2013).

38. M. M. Mota, *et al.*, Migration of *Plasmodium* sporozoites through cells before infection. *Science* **291**, 141–144 (2001).

39. V. Risco-Castillo, *et al.*, Malaria Sporozoites Traverse Host Cells within Transient Vacuoles. *Cell Host Microbe* **18**, 593–603 (2015).

40. F. Frischknecht, K. Matuschewski, *Plasmodium* Sporozoite Biology. *Cold Spring Harb. Perspect. Med.* **7**, a025478 (2017).

41. B. Nyboer, K. Heiss, A.-K. Mueller, A. Ingmundson, The *Plasmodium* liver-stage parasitophorous vacuole: A front-line of communication between parasite and host. *Int. J. Med. Microbiol.* **308**, 107–117 (2018).

42. W. A. Krotoski, *et al.*, Demonstration of Hypnozoites in Sporozoite-Transmitted *Plasmodium vivax* Infection. *Am. J. Trop. Med. Hyg.* **31**, 1291–1293 (1982).

43. P. C. C. Garnham, The continuing mystery of relapse in malaria. *Protozool. Abstr.* **1**, 1–12 (1977).

44. J. M. J. Verhoef, M. Meissner, T. W. A. Kooij, Organelle Dynamics in Apicomplexan Parasites. *MBio* **12** (2021).

45. A. Sturm, *et al.*, Manipulation of Host Hepatocytes by the Malaria Parasite for Delivery into Liver Sinusoids. *Science (80-.).* **313**, 1287–1290 (2006).

46. K. Baer, C. Klotz, S. H. I. Kappe, T. Schnieder, U. Frevert, Release of Hepatic *Plasmodium* yoelii Merozoites into the Pulmonary Microvasculature. *PLoS Pathog.* **3**, e171 (2007).

47. I. Tardieux, J. Baum, Reassessing the mechanics of parasite motility and host-cell invasion. *J. Cell Biol.* **214**, 507–515 (2016).

48. K. Yahata, *et al.*, Gliding motility of *Plasmodium* merozoites. *Proc. Natl. Acad. Sci. U. S. A.* **118**, 1–10 (2021).

49. N. A. Counihan, J. K. Modak, T. F. de Koning-Ward, How Malaria Parasites Acquire Nutrients From Their Host. *Front. Cell Dev. Biol.* **9**, 649184 (2021).

50. S. Garg, *et al.*, Visualization and quantification of *Plasmodium falciparum* intraerythrocytic merozoites. *Syst. Synth. Biol.* **9**, 23–26 (2015).

51. Q. Li, L. H. Xie, J. Zhang, B. S. Pybus, Identification and Assessment of *Plasmodium berghei* Merozoites and Cell Cycle by Flow Cytometry. *Mil. Med.* **186**, 108–115 (2021).

52. Y. Voß, S. Klaus, J. Guizetti, M. Ganter, *Plasmodium* schizogony, a chronology of the parasite's cell cycle in the blood stage. *PLOS Pathog.* **19**, e1011157 (2023).

53. A. G. Maier, B. M. Cooke, A. F. Cowman, L. Tilley, Malaria parasite proteins that remodel the host erythrocyte. *Nat. Rev. Microbiol.* **7**, 341–354 (2009).

54. P. R. Gilson, S. A. Chisholm, B. S. Crabb, T. F. de Koning-Ward, Host cell remodelling in malaria parasites: a new pool of potential drug targets. *Int. J. Parasitol.* **47**, 119–127 (2017).

55. B. S. Crabb, *et al.*, Targeted Gene Disruption Shows That Knobs Enable Malaria-Infected Red Cells to Cytoadhere under Physiological Shear Stress. *Cell* **89**, 287–296 (1997).

56. J. M. Crutcher, S. L. Hoffman, *Malaria* (University of Texas Medical Branch at Galveston, 1996).

57. F. Hentzschel, *et al.*, Microtubule inner proteins of *Plasmodium* are essential for transmission of malaria parasites. *Proc. Natl. Acad. Sci.* in press (2025). https://doi.org/10.1073/pnas.2421737122.

58. B. F. C. Kafsack, *et al.*, A transcriptional switch underlies commitment to sexual development in malaria parasites. *Nature* **507**, 248–252 (2014).

59. A. Sinha, *et al.*, A cascade of DNA-binding proteins for sexual commitment and development in *Plasmodium*. *Nature* **507**, 253–257 (2014).

60. A. Buckling, L. C. Ranford-Cartwright, A. Miles, A. F. Read, Chloroquine increases *Plasmodium falciparum* gametocytogenesis *in vitro*. *Parasitology* **118**, 339–346 (1999).

61. N. M. B. Brancucci, *et al.*, Lysophosphatidylcholine Regulates Sexual Stage Differentiation in the Human Malaria Parasite *Plasmodium falciparum*. *Cell* **171**, 1532-1544.e15 (2017).

62. E. Farfour, F. Charlotte, C. Settegrana, M. Miyara, P. Buffet, The extravascular compartment of the bone marrow: a niche for *Plasmodium falciparum* gametocyte maturation? *Malar. J.* **11**, 285 (2012).

63. R. Joice, *et al.*, *Plasmodium falciparum* transmission stages accumulate in the human bone marrow. *Sci. Transl. Med.* **6** (2014).

64. B. Baro, *et al.*, *Plasmodium vivax* gametocytes in the bone marrow of an acute malaria patient and changes in the erythroid miRNA profile. *PLoS Negl. Trop. Dis.* **11**, e0005365 (2017).

65. K. Venugopal, F. Hentzschel, G. Valkiūnas, M. Marti, *Plasmodium* asexual growth and sexual development in the haematopoietic niche of the host. *Nat. Rev. Microbiol.* **18**, 177–189 (2020).

66. P. Ngotho, *et al.*, Revisiting gametocyte biology in malaria parasites. *FEMS Microbiol. Rev.* **43**, 401–414 (2019).

67. M. W. A. Dixon, L. Tilley, *Plasmodium falciparum* goes bananas for sex. *Mol. Biochem. Parasitol.* **244** (2021).

68. M. Aingaran, *et al.*, Host cell deformability is linked to transmission in the human malaria

parasite *Plasmodium falciparum*. *Cell. Microbiol.* **14**, 983–993 (2012).

69. M. Tibúrcio, *et al.*, A switch in infected erythrocyte deformability at the maturation and blood circulation of *Plasmodium falciparum* transmission stages. *Blood* **119**, e172–e180 (2012).

70. F. Hentzschel, *et al.*, Host cell maturation modulates parasite invasion and sexual differentiation in *Plasmodium berghei*. *Sci. Adv.* **8**, 1–14 (2022).

71. O. Billker, *et al.*, Identification of xanthurenic acid as the putative inducer of malaria development in the mosquito. *Nature* **392**, 289–292 (1998).

72. G. E. Garcia, R. A. Wirtz, J. R. Barr, A. Woolfitt, R. Rosenberg, Xanthurenic Acid Induces Gametogenesis in *Plasmodium*, the Malaria Parasite. *J. Biol. Chem.* **273**, 12003–12005 (1998).

73. R. E. Sinden, 'Sexual Development of Malarial Parasites' in *Advances in Parasitology*, (Adv Parasitol, 1983), pp. 153–216.

74. M. M. Nijhout, R. Carter, Gamete development in malaria parasites: bicarbonate-dependent stimulation by pH *in vitro*. *Parasitology* **76**, 39–53 (1978).

75. R. E. Sinden, G. A. Butcher, O. Billker, S. L. Fleck, 'Regulation of Infectivity of *Plasmodium* to the Mosquito Vector' in *Advances in Parasitology*, (Adv Parasitol, 1996), pp. 53–117.

76. R. E. Sinden, N. A. Croll, Cytology and Kinetics of microgametogenesis and fertilization in *Plasmodium yoelii nigeriensis*. *Parasitology* **70**, 53–65 (1975).

77. R. E. Sinden, E. U. Canning, B. Spain, Gametogenesis and fertilization in *Plasmodium yoelii nigeriensis* : a transmission electron microscope study. *Proc. R. Soc. London. Ser. B. Biol. Sci.* **193**, 55–76 (1976).

78. C. J. Janse, P. F. J. van der Klooster, H. J. van der Kaay, M. van der Ploeg, J. Prosper Overdulve, DNA synthesis in *Plasmodium berghei* during asexual and sexual development. *Mol. Biochem. Parasitol.* **20**, 173–182 (1986).

79. C. J. Janse, P. F. J. Van der Klooster, H. J. Van der Kaay, M. Van der Ploeg, J. P. Overdulve, Rapid repeated DNA replication during microgametogenesis and DNA synthesis in young zygotes of *Plasmodium berghei*. *Trans. R. Soc. Trop. Med. Hyg.* **80**, 154–157 (1986).

80. R. Rashpa, M. Brochet, Expansion microscopy of *Plasmodium* gametocytes reveals the molecular architecture of a bipartite microtubule organisation centre coordinating mitosis with axoneme assembly. *PLOS Pathog.* **18**, e1010223 (2022).

81. R. Sinden, A. Talman, S. Marques, M. Wass, M. Sternberg, The flagellum in malarial parasites. *Curr. Opin. Microbiol.* **13**, 491–500 (2010).

82. S. Bennink, M. J. Kiesow, G. Pradel, The development of malaria parasites in the mosquito midgut. *Cell. Microbiol.* **18**, 905–918 (2016).

83. Y. Liu, *et al.*, The conserved plant sterility gene HAP2 functions after attachment of fusogenic membranes in Chlamydomonas and *Plasmodium* gametes. *Genes Dev.* **22**, 1051–1068 (2008).

84. M. R. van Dijk, *et al.*, A Central Role for P48/45 in Malaria Parasite Male Gamete Fertility. *Cell* **104**, 153–164 (2001).

85. H. Patil, *et al.*, Zygote morphogenesis but not the establishment of cell polarity in *Plasmodium berghei* is controlled by the small GTPase, RAB11A. *PLoS Pathog.* **16**, 1–27 (2020).

86. G. Siciliano, *et al.*, Critical Steps of *Plasmodium falciparum* Ookinete Maturation. *Front. Microbiol.* **11**, 1–9 (2020).

87. M. Singer, F. Frischknecht, Still running fast: *Plasmodium* ookinetes and sporozoites 125 years after their discovery. *Trends Parasitol.* **39**, 991–995 (2023).

88. C. J. Janse, *et al.*, *In vitro* formation of ookinetes and functional maturity of *Plasmodium berghei* gametocytes. *Parasitology* **91**, 19–29 (1985).

89. D. S. Guttery, M. Zeeshan, A. A. Holder, E. C. Tromer, R. Tewari, Meiosis in *Plasmodium*: how does it work? *Trends Parasitol.* **39**, 812–821 (2023).

90. M. Singh, *et al.*, *Plasmodium*'s journey through the Anopheles mosquito: A comprehensive review. *Biochimie* **181**, 176–190 (2020).

91. T. Araki, *et al.*, Three-dimensional electron microscopy analysis reveals endopolygeny-like nuclear architecture segregation in *Plasmodium* oocyst development. *Parasitol. Int.* **76**, 102034 (2020).

92. F. Hentzschel, F. Frischknecht, Still enigmatic: *Plasmodium* oocysts 125 years after their discovery. *Trends Parasitol.* **38**, 610–613 (2022).

93. V. Thathy, Levels of circumsporozoite protein in the *Plasmodium* oocyst determine sporozoite morphology. *EMBO J.* **21**, 1586–1596 (2002).

94. P.-C. Burda, *et al.*, A *Plasmodium* plasma membrane reporter reveals membrane dynamics by live-cell microscopy. *Sci. Rep.* **7**, 9740 (2017).

95. B. Spreng, 'The role of microtubules in *Plasmodium berghei* sporozoite development, morphology, motility and infectivity', Ruprecht-Karls-University Heidelberg. (2018).

96. R. G. Douglas, R. Amino, P. Sinnis, F. Frischknecht, Active migration and passive transport of malaria parasites. *Trends Parasitol.* **31**, 357–362 (2015).

97. Sterling, C. R., M. Aikawa, J. P. Vanderberg, The passage of *Plasmodium berghei* sporozoites through the salivary glands of Anopheles stephensi: an electron microscope study. *J. Parasitol.* **59**, 593–605 (1973).

98. P. F. Pimenta, M. Touray, L. Miller, The Journey of Malaria Sporozoites in the Mosquito Salivary Gland. *J. Eukaryot. Microbiol.* **41**, 608–624 (1994).

99. A. K. Ghosh, *et al.*, Malaria Parasite Invasion of the Mosquito Salivary Gland Requires Interaction between the *Plasmodium* TRAP and the Anopheles Saglin Proteins. *PLoS Pathog.* **5**, e1000265 (2009).

100. T. Cavalier-Smith, Kingdom protozoa and its 18 phyla. *Microbiol. Rev.* **57**, 953–994 (1993).

101. T. Mann, B. C., Characterization of the subpellicular network, a filamentous membrane skeletal component in the parasite *Toxoplasma gondii*. *Mol. Biochem. Parasitol.* **115**, 257–268 (2001).

102. J. A. Yeoman, *et al.*, Tracking Glideosome-Associated Protein 50 Reveals the Development and Organization of the Inner Membrane Complex of *Plasmodium falciparum*. *Eukaryot. Cell* **10**, 556–564 (2011).

103. M. K. Dearnley, *et al.*, Origin, composition, organization and function of the inner membrane complex of *Plasmodium falciparum* gametocytes. *J. Cell Sci.* **125**, 2053–2063 (2012).

104. M. Kono, *et al.*, Evolution and Architecture of the Inner Membrane Complex in Asexual and Sexual Stages of the Malaria Parasite. *Mol. Biol. Evol.* **29**, 2113–2132 (2012).

105. C. A. M. Meszoely, E. F. Erbe, R. L. Steere, J. Trosper, R. L. Beaudoin, *Plasmodium falciparum*: Freeze-fracture of the gametocyte pellicular complex. *Exp. Parasitol.* **64**, 300–309 (1987).

106. A. L. Chen, *et al.*, Novel Components of the *Toxoplasma* Inner Membrane Complex Revealed by BioID. *MBio* **6**, e02357-14 (2015).

107. A. L. Chen, *et al.*, Novel insights into the composition and function of the *Toxoplasma* IMC sutures. *Cell. Microbiol.* **19**, e12678 (2017).

108. A. Raibaud, *et al.*, Cryofracture Electron Microscopy of the Ookinete Pellicle of *Plasmodium gallinaceum* Reveals the Existence of Novel Pores in the Alveolar Membranes. *J. Struct. Biol.* **135**, 47–57 (2001).

109. J. F. Dubremetz, G. Torpier, Freeze fracture study of the pellicle of an Eimerian sporozoite (Protozoa, Coccidia). *J. Ultrastruct. Res.* **62**, 94–109 (1978).

110. K. Frénal, J.-F. Dubremetz, M. Lebrun, D. Soldati-Favre, Gliding motility powers invasion and egress in Apicomplexa. *Nat. Rev. Microbiol.* **15**, 645–660 (2017).

111. K. Frénal, D. Soldati-Favre, Un complexe moléculaire unique à l'origine de la motilité et de l'invasion des Apicomplexes. *médecine/sciences* **29**, 515–522 (2013).

112. J. L. Ferreira, *et al.*, Variable microtubule architecture in the malaria parasite. *Nat. Commun.* **14**, 1216 (2023).

113. B. Spreng, *et al.*, Microtubule number and length determine cellular shape and function in *Plasmodium*. *EMBO J.* **38**, e100984 (2019).

114. X. Wang, P. Qian, H. Cui, L. Yao, J. Yuan, A protein palmitoylation cascade regulates microtubule cytoskeleton integrity in *Plasmodium*. *EMBO J.* **39**, 1–22 (2020).

115. M. Kudryashev, *et al.*, Positioning of large organelles by a membrane- associated cytoskeleton in *Plasmodium* sporozoites. *Cell. Microbiol.* **12**, 362–371 (2010).

116. B. R. Anderson-White, *et al.*, A family of intermediate filament-like proteins is sequentially assembled into the cytoskeleton of *Toxoplasma gondii*. *Cell. Microbiol.* **13**, 18–31 (2011).

117. K. Engelberg, C. Bauwens, D. J. P. Ferguson, M.-J. Gubbels, Co-dependent formation of the *Toxoplasma gondii* sub-pellicular microtubules and inner membrane skeleton. *bioRxiv* (2024). Available at: https://www.biorxiv.org/content/10.1101/2024.05.25.595886v1 [Accessed 27 May 2024].

118. P. Qian, *et al.*, Apical anchorage and stabilization of subpellicular microtubules by apical polar ring ensures *Plasmodium* ookinete infection in mosquito. *Nat. Commun.* **13**, 7465 (2022).

119. J. M. Santos, *et al.*, The *Plasmodium* palmitoyl-S-acyl-transferase DHHC2 is essential for ookinete morphogenesis and malaria transmission. *Sci. RepoRts* | **5**, 1–10 (2015).

120. R. Rashpa, N. Klages, D. Schvartz, C. Pasquarello, M. Brochet, The Skp1-Cullin1-FBXO1 complex is a pleiotropic regulator required for the formation of gametes and motile forms in *Plasmodium berghei*. *Nat. Commun.* **14**, 1312 (2023).

121. M. B. Heintzelman, Gliding motility in apicomplexan parasites. *Semin. Cell Dev. Biol.* **46**, 135–142 (2015).

122. A. J. Ridley, Life at the Leading Edge. *Cell* **145**, 1012–1022 (2011).

123. M. Bergert, S. D. Chandradoss, R. A. Desai, E. Paluch, Cell mechanics control rapid transitions between blebs and lamellipodia during migration. *Proc. Natl. Acad. Sci. U. S. A.* **109**, 14434–14439 (2012).

124. C. Opitz, D. Soldati, 'The glideosome': a dynamic complex powering gliding motion and host cell invasion by *Toxoplasma gondii*. *Mol. Microbiol.* **45**, 597–604 (2002).

125. R. G. Douglas, R. W. Moon, F. Frischknecht, Cytoskeleton Organization in Formation and Motility of Apicomplexan Parasites. *Annu. Rev. Microbiol.* **78**, 311–335 (2024).

126. E. Gaskins, *et al.*, Identification of the membrane receptor of a class XIV myosin in *Toxoplasma gondii*. *J. Cell Biol.* **165**, 383–393 (2004).

127. D. Jacot, *et al.*, An Apicomplexan Actin-Binding Protein Serves as a Connector and Lipid Sensor to Coordinate Motility and Invasion. *Cell Host Microbe* **20**, 731–743 (2016).

128. M. Kudryashev, *et al.*, Structural basis for chirality and directional motility of *Plasmodium* sporozoites. *Cell. Microbiol.* **14**, 1757–1768 (2012).

129. L. H. Bannister, *et al.*, *Plasmodium falciparum* apical membrane antigen 1 (PfAMA-1) is translocated within micronemes along subpellicular microtubules during merozoite development. *J. Cell Sci.* **116**, 3825–3834 (2003).

130. M. M. Paing, N. H. Tolia, Multimeric Assembly of Host-Pathogen Adhesion Complexes Involved in Apicomplexan Invasion. *PLoS Pathog.* **10**, e1004120 (2014).

131. S. Münter, *et al.*, *Plasmodium* Sporozoite Motility Is Modulated by the Turnover of Discrete Adhesion Sites. *Cell Host Microbe* **6**, 551–562 (2009).

132. K. A. Quadt, M. Streichfuss, C. A. Moreau, J. P. Spatz, F. Frischknecht, Coupling of Retrograde Flow to Force Production During Malaria Parasite Migration. *ACS Nano* **10**, 2091–2102 (2016).

133. R. A. O'Donnell, *et al.*, Intramembrane proteolysis mediates shedding of a key adhesin during erythrocyte invasion by the malaria parasite. *J. Cell Biol.* **174**, 1023–1033 (2006).

134. R. P. Baker, R. Wijetilaka, S. Urban, Two *Plasmodium* Rhomboid Proteases Preferentially Cleave Different Adhesins Implicated in All Invasive Stages of Malaria. *PLoS Pathog.* **2**, e113 (2006).

135. G. Rugarabamu, J. Marq, A. Guérin, M. Lebrun, D. Soldati-Favre, Distinct contribution of *Toxoplasma gondii* rhomboid proteases 4 and 5 to micronemal protein protease 1 activity during invasion. *Mol. Microbiol.* **97**, 244–262 (2015).

136. M. J. Stewart, J. P. Vanderberg, Malaria sporozoites leave behind trails of circumsporozoite protein during gliding motility. *J. Protozool.* **35**, 389–93 (1988).

137. I. Ejigiri, *et al.*, Shedding of TRAP by a Rhomboid Protease from the Malaria Sporozoite Surface Is Essential for Gliding Motility and Sporozoite Infectivity. *PLoS Pathog.* **8**, e1002725 (2012).

138. J. K. Hellmann, *et al.*, Environmental Constraints Guide Migration of Malaria Parasites during Transmission. *PLoS Pathog.* **7**, e1002080 (2011).

139. J. Ripp, X. Smyrnakou, M. Neuhoff, F. Hentzschel, F. Frischknecht, Phosphorylation of myosin A regulates gliding motility and is essential for *Plasmodium* transmission. *EMBO Rep.* **23**, e54857 (2022).

140. T. Lämmermann, *et al.*, Neutrophil swarms require LTB4 and integrins at sites of cell death in vivo. *Nature* **498**, 371–375 (2013).

141. B. Alberts, *et al.*, *Molecular Biology of the cell*, Matthew Welck, *et al.*, Eds., 7th Ed. (W. W. Norton & Company, 2022).

142. N. B. Gudimchuk, J. R. McIntosh, Regulation of microtubule dynamics, mechanics and function through the growing tip. *Nat. Rev. Mol. Cell Biol.* **22**, 777–795 (2021).

143. H. V Goodson, E. M. Jonasson, Microtubules and Microtubule-Associated Proteins. *Cold Spring Harb. Perspect. Biol.* **10**, a022608 (2018).

144. A. Akhmanova, M. O. Steinmetz, Microtubule minus-end regulation at a glance. *J. Cell Sci.* **132** (2019).

145. C. Vineethakumari, J. Lüders, Microtubule Anchoring: Attaching Dynamic Polymers to Cellular Structures. *Front. Cell Dev. Biol.* **10**, 867870 (2022).

146. A. Akhmanova, M. O. Steinmetz, Control of microtubule organization and dynamics: two ends in the limelight. *Nat. Rev. Mol. Cell Biol. 2015 1612* **16**, 711–726 (2015).

147. G. Margolin, *et al.*, The mechanisms of microtubule catastrophe and rescue: implications from analysis of a dimer-scale computational model. *Mol. Biol. Cell* **23**, 642–656 (2012).

148. R. Melki, S. Fievez, M.-F. Carlier, Continuous Monitoring of P i Release Following Nucleotide Hydrolysis in Actin or Tubulin Assembly Using 2-Amino-6-mercapto-7-

methylpurine Ribonucleoside and Purine-Nucleoside Phosphorylase as an Enzyme-Linked Assay. *Biochemistry* **35**, 12038–12045 (1996).

149. G. J. Brouhard, L. M. Rice, Microtubule dynamics: an interplay of biochemistry and mechanics. *Nat. Rev. Mol. Cell Biol.* **19**, 451–463 (2018).

150. T. Mitchison, M. Kirschner, Dynamic instability of microtubule growth. *Nature* **312**, 237–242 (1984).

151. P. Liu, *et al.*, Insights into the assembly and activation of the microtubule nucleator γ-TuRC. *Nature* **578**, 467–471 (2020).

152. V. Sulimenko, E. Dráberová, P. Dráber, γ-Tubulin in microtubule nucleation and beyond. *Front. Cell Dev. Biol.* **10**, 880761 (2022).

153. C. A. Tovey, P. T. Conduit, Microtubule nucleation by γ-tubulin complexes and beyond. *Essays Biochem.* **62**, 765–780 (2018).

154. C. Sánchez-Huertas, J. Lüders, The Augmin Connection in the Geometry of Microtubule Networks. *Curr. Biol.* **25**, R294–R299 (2015).

155. S. Bodakuntla, A. S. Jijumon, C. Villablanca, C. Gonzalez-Billault, C. Janke, Microtubule-Associated Proteins: Structuring the Cytoskeleton. *Trends Cell Biol.* **29**, 804–819 (2019).

156. L. Wilson, D. Panda, M. Ann Jordan, Modulation of Microtubule Dynamics by Drugs. A Paradigm for the Actions of Cellular Regulators. *Cell Struct. Funct.* **24**, 329–335 (1999).

157. J. Gallego-Jara, G. Lozano-Terol, R. A. Sola-Martínez, M. Cánovas-Díaz, T. de Diego Puente, A Compressive Review about Taxol®: History and Future Challenges. *Molecules* **25**, 5986 (2020).

158. J. Sebastian, K. Rathinasamy, Microtubules and Cell Division: Potential Pharmacological Targets in Cancer Therapy. *Curr. Drug Targets* **24**, 889–918 (2023).

159. E. Nogales, S. G. Wolf, K. H. Downing, Structure of the αβ tubulin dimer by electron crystallography. *Nature* **391**, 199–203 (1998).

160. G. Lukinavičius, *et al.*, Fluorogenic probes for live-cell imaging of the cytoskeleton. *Nat. Methods* **11**, 731–733 (2014).

161. R. Kaur, G. Kaur, R. K. Gill, R. Soni, J. Bariwal, Recent developments in tubulin polymerization inhibitors: An overview. *Eur. J. Med. Chem.* **87**, 89–124 (2014).

162. C. Delphin, *et al.*, MAP6-F Is a Temperature Sensor That Directly Binds to and Protects

Microtubules from Cold-induced Depolymerization. *J. Biol. Chem.* **287**, 35127–35138 (2012).

163. J. C. Lee, S. N. Timasheff, *In vitro* reconstitution of calf brain microtubules: effects of solution variables. *Biochemistry* **16**, 1754–1764 (1977).

164. G. Li, J. K. Moore, Microtubule dynamics at low temperature: evidence that tubulin recycling limits assembly. *Mol. Biol. Cell* **31**, 1154–1166 (2020).

165. C. Conde, A. Cáceres, Microtubule assembly, organization and dynamics in axons and dendrites. *Nat. Rev. Neurosci.* **10**, 319–332 (2009).

166. C. Fulton, P. A. Simpson, *Cell Motility*, R. . Goldman, T. . Pollard, J. L. Rosenbaum, Eds. (Cold Spring Harbor, 1976).

167. R. F. Ludueña, A. Banerjee, 'The Isotypes of Tubulin: Distribution and Functional Significance' in *The Role of Microtubules in Cell Biology, Neurobiology, and Oncology*, T. Fojo, Ed. (Humana Press, 2008), pp. 123–175.

168. A. Roll-Mecak, Intrinsically disordered tubulin tails: complex tuners of microtubule functions? *Semin. Cell Dev. Biol.* **37**, 11–19 (2015).

169. C. Janke, M. M. Magiera, The tubulin code and its role in controlling microtubule properties and functions. *Nat Rev Mol Cell Biol* **21**, 307–326 (2020).

170. C. Janke, G. Montagnac, Causes and Consequences of Microtubule Acetylation. *Curr. Biol.* **27**, R1287–R1292 (2017).

171. M. Sirajuddin, L. M. Rice, R. D. Vale, Regulation of microtubule motors by tubulin isotypes and post-translational modifications. *Nat. Cell Biol.* **16**, 335–344 (2014).

172. S. Audebert, *et al.*, Reversible polyglutamylation of alpha- and beta-tubulin and microtubule dynamics in mouse brain neurons. *Mol. Biol. Cell* **4**, 615–626 (1993).

173. M. Chalfie, J. N. Thomson, Structural and functional diversity in the neuronal microtubules of Caenorhabditis elegans. *J. Cell Biol.* **93**, 15–23 (1982).

174. J. G. Cueva, J. Hsin, K. C. Huang, M. B. Goodman, Posttranslational Acetylation of α-Tubulin Constrains Protofilament Number in Native Microtubules. *Curr. Biol.* **22**, 1066–1074 (2012).

175. I. Topalidou, *et al.*, Genetically Separable Functions of the MEC-17 Tubulin Acetyltransferase Affect Microtubule Organization. *Curr. Biol.* **22**, 1057–1065 (2012).

176. K. M. Burns, M. Wagenbach, L. Wordeman, D. C. Schriemer, Nucleotide Exchange in Dimeric MCAK Induces Longitudinal and Lateral Stress at Microtubule Ends to Support Depolymerization. *Structure* **22**, 1173–1183 (2014).

177. A. B. Asenjo, *et al.*, Structural Model for Tubulin Recognition and Deformation by Kinesin-13 Microtubule Depolymerases. *Cell Rep.* **3**, 759–768 (2013).

178. A. Desai, S. Verma, T. J. Mitchison, C. E. Walczak, Kin I Kinesins Are Microtubule-Destabilizing Enzymes. *Cell* **96**, 69–78 (1999).

179. C. A. Moores, *et al.*, A Mechanism for Microtubule Depolymerization by KinI Kinesins. *Mol. Cell* **9**, 903–909 (2002).

180. N. Hirokawa, Y. Noda, Y. Tanaka, S. Niwa, Kinesin superfamily motor proteins and intracellular transport. *Nat. Rev. Mol. Cell Biol.* **10**, 682–696 (2009).

181. S. L. Reck-Peterson, W. B. Redwine, R. D. Vale, A. P. Carter, The cytoplasmic dynein transport machinery and its many cargoes. *Nat. Rev. Mol. Cell Biol.* **19**, 382–398 (2018).

182. M. Cyrklaff, *et al.*, Cryoelectron tomography reveals periodic material at the inner side of subpellicular microtubules in apicomplexan parasites. *J. Exp. Med.* **204**, 1281–1287 (2007).

183. D. Nicastro, *et al.*, The Molecular Architecture of Axonemes Revealed by Cryoelectron Tomography. *Science (80-.).* **313**, 944–948 (2006).

184. D. Stoddard, *et al.*, Tetrahymena RIB72A and RIB72B are microtubule inner proteins in the ciliary doublet microtubules. *Mol. Biol. Cell* **29**, 2566–2577 (2018).

185. E. E. Dymek, *et al.*, PACRG and FAP20 form the inner junction of axonemal doublet microtubules and regulate ciliary motility. *Mol. Biol. Cell* **30**, 1805–1816 (2019).

186. H. Yanagisawa, *et al.*, FAP20 is an inner junction protein of doublet microtubules essential for both the planar asymmetrical waveform and stability of flagella in Chlamydomonas. *Mol. Biol. Cell* **25**, 1472–1483 (2014).

187. A. S. Fabritius, *et al.*, Proteomic analysis of microtubule inner proteins (MIPs) in Rib72 null Tetrahymena cells reveals functional MIPs. *Mol. Biol. Cell* **32**, br8 (2021).

188. D. Nicastro, *et al.*, Cryo-electron tomography reveals conserved features of doublet microtubules in flagella. *Proc. Natl. Acad. Sci.* **108**, E845-853 (2011).

189. G. Pigino, *et al.*, Comparative structural analysis of eukaryotic flagella and cilia from Chlamydomonas, Tetrahymena, and sea urchins. *J. Struct. Biol.* **178**, 199–206 (2012).

190. M. Ma, *et al.*, Structure of the Decorated Ciliary Doublet Microtubule. *Cell* **179**, 909-922.e12 (2019).

191. M. Gui, *et al.*, SPACA9 is a lumenal protein of human ciliary singlet and doublet microtubules. *Proc. Natl. Acad. Sci.* **119**, e2207605119 (2022).

192. J. Kirima, K. Oiwa, Flagellar-associated Protein FAP85 Is a Microtubule Inner Protein That Stabilizes Microtubules. *Cell Struct. Funct.* **43**, 1–14 (2018).

193. M. M. Shimogawa, *et al.*, FAP106 is an interaction hub for assembling microtubule inner proteins at the cilium inner junction. *Nat. Commun.* **14**, 5225 (2023).

194. M. Owa, *et al.*, Inner lumen proteins stabilize doublet microtubules in cilia and flagella. *Nat. Commun.* **10**, 1143 (2019).

195. S. Kubo, *et al.*, Native doublet microtubules from Tetrahymena thermophila reveal the importance of outer junction proteins. *Nat. Commun.* **14**, 2168 (2023).

196. D. Zabeo, *et al.*, A lumenal interrupted helix in human sperm tail microtubules. *Sci. Rep.* **8**, 2727 (2018).

197. M. R. Leung, *et al.*, The multi-scale architecture of mammalian sperm flagella and implications for ciliary motility. *EMBO J.* **40**, e107410 (2021).

198. M. R. Leung, *et al.*, Structural specializations of the sperm tail. *Cell* **186**, 2880-2896.e17 (2023).

199. J. S. Andersen, *et al.*, Uncovering structural themes across cilia microtubule inner proteins with implications for human cilia function. *Nat. Commun. 2024 151* **15**, 1–17 (2024).

200. M. M. Shimogawa, K. Jonnalagadda, K. L. Hill, FAP20 is required for flagellum assembly in Trypanosoma brucei. *Mol. Biol. Cell* **35**, br22 (2024).

201. M. Ichikawa, K. H. Bui, Microtubule Inner Proteins: A Meshwork of Luminal Proteins Stabilizing the Doublet Microtubule. *BioEssays* **40**, 1700209 (2018).

202. E. L. R. Echandía, R. S. Piezzi, E. M. Rodríguez, Dense-core microtubules in neurons and gliocytes of the toad Bufo arenarum Hensel. *Am. J. Anat.* **122**, 157–167 (1968).

203. A. Peters, C. C. Proskauer, I. R. Kaiserman-Abramof, The small pyramidal neuron of the rat cerebral cortex. *J. Cell Biol.* **39**, 604–619 (1968).

204. P. R. Burton, Luminal material in microtubules of frog olfactory axons: structure and distribution. *J. Cell Biol.* **99**, 520–528 (1984).

205. H. J. Hoops, G. B. Witman, Outer doublet heterogeneity reveals structural polarity related to beat direction in Chlamydomonas flagella. *J. Cell Biol.* **97**, 902–908 (1983).

206. L. Tai, G. Yin, X. Huang, F. Sun, Y. Zhu, In-cell structural insight into the stability of sperm microtubule doublet. *Cell Discov.* **9**, 116 (2023).

207. S. C. Howes, G. M. Alushin, T. Shida, M. V Nachury, E. Nogales, Effects of tubulin acetylation and tubulin acetyltransferase binding on microtubule structure. *Mol. Biol. Cell* **25**, 257–266 (2014).

208. T. Shida, J. G. Cueva, Z. Xu, M. B. Goodman, M. V. Nachury, The major α-tubulin K40 acetyltransferase αTAT1 promotes rapid ciliogenesis and efficient mechanosensation. *Proc. Natl. Acad. Sci.* **107**, 21517–21522 (2010).

209. N. Kalebic, *et al.*, αTAT1 is the major α-tubulin acetyltransferase in mice. *Nat. Commun.* **4**, 1962 (2013).

210. S. Reber, M. Singer, F. Frischknecht, Cytoskeletal dynamics in parasites. *Curr. Opin. Cell Biol.* **86**, 102277 (2024).

211. C. S. Simon, *et al.*, An extended DNA-free intranuclear compartment organizes centrosome microtubules in malaria parasites. *Life Sci. Alliance* **4**, 1–15 (2021).

212. B. Liffner, *et al.*, Atlas of *Plasmodium falciparum* intraerythrocytic development using expansion microscopy. *Elife* **12** (2023).

213. M. Zeeshan, *et al.*, *Plasmodium* SAS4: basal body component of male cell which is dispensable for parasite transmission. *Life Sci. Alliance* **5**, 1–11 (2022).

214. R. E. Sinden, E. U. Canning, R. S. Bray, M. E. Smalley, Gametocyte and gamete development in *Plasmodium falciparum*. *Proc. R. Soc. London. Ser. B. Biol. Sci.* **201**, 375–399 (1978).

215. M. Hair, *et al.*, Atypical flagella assembly and haploid genome coiling during male gamete formation in *Plasmodium*. *Nat. Commun.* **14**, 8263 (2023).

216. D. S. Guttery, M. Zeeshan, D. J. P. Ferguson, A. A. Holder, R. Tewari, Division and Transmission: Malaria Parasite Development in the Mosquito. *Annu. Rev. Microbiol.* **76**, 113–134 (2022).

217. F. Hentzschel, *et al.*, A non-canonical Arp2/3 complex is essential for *Plasmodium* DNA segregation and transmission of malaria. *bioRxiv* 2023.10.25.563799 (2023). https://doi.org/10.1101/2023.10.25.563799.

218. N. Tosetti, *et al.*, Essential function of the alveolin network in the subpellicular

microtubules and conoid assembly in *Toxoplasma gondii*. *Elife* **9**, 1–22 (2020).

219. J. Hopkins, *et al.*, The Plastid in *Plasmodium falciparum* Asexual Blood Stages: a Three-Dimensional Ultrastructural Analysis. *Protist* **150**, 283–295 (1999).

220. E. Bertiaux, *et al.*, Expansion microscopy provides new insights into the cytoskeleton of malaria parasites including the conservation of a conoid. *PLOS Biol.* **19**, e3001020 (2021).

221. R. E. Fowler, R. E. Fookes, F. Lavin, L. H. Bannister, G. H. Mitchell, Microtubules in *Plasmodium falciparum* merozoites and their importance for invasion of erythrocytes. *Parasitology* **117**, 425–433 (1998).

222. P. C. C. Garnham, R. G. Bird, J. R. Baker, Electron microscope studies of motile stages of malaria parasites. *Trans. R. Soc. Trop. Med. Hyg.* **56**, 116–120 (1962).

223. M. W. A. Dixon, M. K. Dearnley, E. Hanssen, T. Gilberger, L. Tilley, Shape-shifting gametocytes: how and why does P. *falciparum* go banana-shaped? *Trends Parasitol.* **28**, 471–478 (2012).

224. J. Li, *et al.*, Repurposing the mitotic machinery to drive cellular elongation and chromatin reorganisation in *Plasmodium falciparum* gametocytes. *Nat. Commun.* **13**, 5054 (2022).

225. N. S. Morrissette, J. M. Murray, D. S. Roos, Subpellicular microtubules associate with an intramembranous particle lattice in the protozoan parasite *Toxoplasma gondii*. *J. Cell Sci.* **110**, 35–42 (1997).

226. B. A. Nichols, M. L. Chiappino, Cytoskeleton of *Toxoplasma gondii*. *J. Protozool.* **34**, 217–26 (1987).

227. N. S. Morrissette, L. D. Sibley, Disruption of microtubules uncouples budding and nuclear division in *Toxoplasma gondii*. *J. Cell Sci.* **115**, 1017–1025 (2002).

228. X. Wang, *et al.*, Cryo-EM structure of cortical microtubules from human parasite *Toxoplasma gondii* identifies their microtubule inner proteins. *Nat. Commun.* **12**, 3065 (2021).

229. M. Zeeshan, *et al.*, Genome-wide functional analysis reveals key roles for kinesins in the mammalian and mosquito stages of the malaria parasite life cycle. *PLOS Biol.* **20**, e3001704 (2022).

230. D. Depoix, *et al.*, Vital role for *Plasmodium berghei* Kinesin8B in axoneme assembly during male gamete formation and mosquito transmission. *Cell. Microbiol.* **22**, e13121 (2020).

231. M. Zeeshan, *et al.*, Kinesin-8B controls basal body function and flagellum formation and is

key to malaria transmission. *Life Sci. Alliance* **2** (2019).

232. R. Haase, A. Puthenpurackal, B. Maco, A. Guérin, D. Soldati-Favre, γ-tubulin complex controls the nucleation of tubulin-based structures in Apicomplexa. *Mol. Biol. Cell* **35** (2024).

233. S. Yang, *et al.*, EB1 decoration of microtubule lattice facilitates spindle-kinetochore lateral attachment in *Plasmodium* male gametogenesis. *Nat. Commun.* **14**, 2864 (2023).

234. S. Mauer, *et al.*, *Plasmodium* microtubule-binding protein EB1 is critical for partitioning of nuclei in male gametogenesis. *MBio* **14**, 1–12 (2023).

235. L. F. Arias Padilla, J. Munera Lopez, A. Shibata, J. M. Murray, K. Hu, The initiation and early development of apical-basal polarity in *Toxoplasma gondii*. *J. Cell Sci.* **137** (2024).

236. J. Q. Tran, C. Li, A. Chyan, L. Chung, N. S. Morrissette, SPM1 stabilizes subpellicular microtubules in *Toxoplasma gondii*. *Eukaryot. Cell* **11**, 206–216 (2012).

237. J. Liu, *et al.*, Novel Thioredoxin-Like Proteins Are Components of a Protein Complex Coating the Cortical Microtubules of *Toxoplasma gondii*. *Eukaryot. Cell* **12**, 1588–1599 (2013).

238. J. Liu, *et al.*, An ensemble of specifically targeted proteins stabilizes cortical microtubules in the human parasite *Toxoplasma gondii*. *Mol. Biol. Cell* **27**, 549–571 (2016).

239. S. Y. Sun, *et al.*, Cryo-ET of *Toxoplasma* parasites gives subnanometer insight into tubulin-based structures. *Proc. Natl. Acad. Sci. U. S. A.* **119**, 1–11 (2022).

240. I. F. Tengganu, *et al.*, The cortical microtubules of *Toxoplasma gondii* underlie the helicity of parasite movement. *J. Cell Sci.* **136** (2023).

241. R. Y. Orr, N. Philip, A. P. Waters, Improved negative selection protocol for *Plasmodium berghei* in the rodent malarial model. *Malar. J.* **11**, 1–6 (2012).

242. J. Kehrer, *et al.*, *Plasmodium* sporozoite disintegration during skin passage limits malaria parasite transmission. *EMBO Rep.* **23**, e54719 (2022).

243. R. G. Douglas, *et al.*, Inter-subunit interactions drive divergent dynamics in mammalian and *Plasmodium* actin filaments. *PLOS Biol.* **16**, e2005345 (2018).

244. N. Kumar, M. Aikawa, C. Grotendorst, *Plasmodium gallinaceum*: Critical role for microtubules in the transformation of zygotes into ookinetes. *Exp. Parasitol.* **59**, 239–247 (1985).

245. V. M. Howick, *et al.*, The Malaria Cell Atlas: Single parasite transcriptomes across the complete *Plasmodium* life cycle. *Science (80-.).* **365**, 1–13 (2019).

246. G. Lukinavičius, *et al.*, A near-infrared fluorophore for live-cell super-resolution microscopy of cellular proteins. *Nat. Chem.* **5**, 132–139 (2013).

247. J. S. Wichers, *et al.*, Identification of novel inner membrane complex and apical annuli proteins of the malaria parasite *Plasmodium falciparum*. *Cell. Microbiol.* **9**, 1–17 (2021).

248. J. S. Wichers-Misterek, *et al.*, A Microtubule-Associated Protein Is Essential for Malaria Parasite Transmission. *MBio* **14**, e03318-22 (2023).

249. B. Liu, *et al.*, A subpellicular microtubule dynein transport machinery regulates ookinete morphogenesis for mosquito transmission of *Plasmodium yoelii*. *Nat. Commun.* **15**, 8590 (2024).

250. J. Birnbaum, *et al.*, A genetic system to study *Plasmodium falciparum* protein function. *Nat. Methods* **14**, 450–456 (2017).

251. V. Soppina, J. F. Herbstman, G. Skiniotis, K. J. Verhey, Luminal Localization of α-tubulin K40 Acetylation by Cryo-EM Analysis of Fab-Labeled Microtubules. *PLoS One* **7**, e48204 (2012).

252. S. K. Yang, *et al.*, Effect of α-tubulin acetylation on the doublet microtubule structure. *Elife* **12** (2024).

253. J. M. Varberg, L. R. Padgett, G. Arrizabalaga, W. J. Sullivan, TgATAT-Mediated α-Tubulin Acetylation Is Required for Division of the Protozoan Parasite *Toxoplasma gondii*. *mSphere* **1**, 10.1128/msphere.00088-15 (2016).

254. N. Trisnadi, C. Barillas-Mury, Live In Vivo Imaging of *Plasmodium* Invasion of the Mosquito Midgut. *mSphere* **5** (2020).

255. T. W. A. Kooij, M. M. Rauch, K. Matuschewski, Expansion of experimental genetics approaches for *Plasmodium berghei* with versatile transfection vectors. *Mol. Biochem. Parasitol.* **185**, 19–26 (2012).

256. J. Alvarez-Jarreta, *et al.*, VEuPathDB: the eukaryotic pathogen, vector and host bioinformatics resource center in 2023. *Nucleic Acids Res.* **52**, D808–D816 (2024).

257. F. Schwach, *et al.*, PlasmoGEM, a database supporting a community resource for large-scale experimental genetics in malaria parasites. *Nucleic Acids Res.* **43**, D1176–D1182 (2015).

258. J. Kehrer, 'Identification and functional characterization of micronemal proteins in *Plasmodium berghei* parasites', Ruprecht - Karls - University Heidelberg. (2024).

259. A. Florentin, D. W. Cobb, H. M. Kudyba, V. Muralidharan, Directing traffic: Chaperone-mediated protein transport in malaria parasites. *Cell. Microbiol.* **22**, e13215 (2020).

260. K. Beyer, *et al.*, Limited *Plasmodium* sporozoite gliding motility in the absence of TRAP family adhesins. *Malar. J.* **20**, 430 (2021).

261. T. K. Jonsdottir, *et al.*, A scalable CRISPR-Cas9 gene editing system facilitates CRISPR screens in the malaria parasite *Plasmodium berghei*. (2024). Available at: https://doi.org/10.1101/2024.04.20.590404 [Accessed 2 May 2024].

262. E. Deligianni, I. S. Kiamos, Gene editing in *Plasmodium berghei* made easy: Development of a CRISPR/Cas9 protocol using linear donor template and ribozymes for sgRNA generation. *Mol. Biochem. Parasitol.* **246**, 111415 (2021).

263. N. Shinzawa, *et al.*, Improvement of CRISPR/Cas9 system by transfecting Cas9-expressing *Plasmodium berghei* with linear donor template. *Commun. Biol.* **3**, 426 (2020).

264. C. Coombes, *et al.*, Mechanism of microtubule lumen entry for the α-tubulin acetyltransferase enzyme αTAT1. *Proc. Natl. Acad. Sci. U. S. A.* **113**, E7176–E7184 (2016).

265. M. Konert, 'K40-acetylation of subpellicular microtubules affects malaria parasite morphogenesis', Ruprecht-Karls-University Heidelberg. (2014).

266. N. Teixidó-Travesa, J. Roig, J. Lüders, The where, when and how of microtubule nucleation – one ring to rule them all. *J. Cell Sci.* **125**, 4445–4456 (2012).

267. J. M. Kollman, A. Merdes, L. Mourey, D. A. Agard, Microtubule nucleation by γ-tubulin complexes. *Nat. Rev. Mol. Cell Biol.* **12**, 709–721 (2011).

268. V. Sulimenko, Z. Hájková, A. Klebanovych, P. Dráber, Regulation of microtubule nucleation mediated by γ-tubulin complexes. *Protoplasma* **254**, 1187–1199 (2017).

269. N. Morrissette, I. Abbaali, C. Ramakrishnan, A. B. Hehl, The Tubulin Superfamily in Apicomplexan Parasites. *Microorganisms* **11**, 706 (2023).

270. E. Palmer, T. Freeman, Investigation into the use of C- and N-terminal GFP fusion proteins for subcellular localization studies using reverse transfection microarrays. *Comp. Funct. Genomics* **5**, 342–353 (2004).

271. L. Krshnan, M. L. van de Weijer, P. Carvalho, Endoplasmic Reticulum–Associated Protein Degradation. *Cold Spring Harb. Perspect. Biol.* **14**, a041247 (2022).

272. H. Götzke, *et al.*, The ALFA-tag is a highly versatile tool for nanobody-based bioscience applications. *Nat. Commun. 2019 101* **10**, 1–12 (2019).

273. A. R. Cross, R. C. Williams Jr., Kinky microtubules: Bending and breaking induced by fixation *in vitro* with glutaraldehyde and formaldehyde. *Cell Motil.* **20**, 272–278 (1991).

274. K. Hua, R. J. Ferland, Fixation methods can differentially affect ciliary protein immunolabeling. *Cilia* **6**, 5 (2017).

275. H. Felgner, R. Frank, M. Schliwa, Flexural rigidity of microtubules measured with the use of optical tweezers. *J. Cell Sci.* **109**, 509–516 (1996).

276. F. Gittes, B. Mickey, J. Nettleton, J. Howard, Flexural rigidity of microtubules and actin filaments measured from thermal fluctuations in shape. *J. Cell Biol.* **120**, 923–934 (1993).

277. N. S. Morrissette, L. D. Sibley, Cytoskeleton of Apicomplexan Parasites. *Microbiol. Mol. Biol. Rev.* (2002). https://doi.org/10.1128/mmbr.66.1.21-38.2002.

278. P. A. Bejon, *et al.*, A role for microtubules in *Plasmodium falciparum* merozoite invasion. *Parasitology* **114**, 1–6 (1997).

279. D. G. Russell, R. E. Sinden, The role of the cytoskeleton in the motility of coccidian sporozoites. *J. Cell Sci.* **50**, 345–359 (1981).

280. A. Bell, Microtubule inhibitors as potential antimalarial agents. *Parasitol. Today* **14**, 234–240 (1998).

281. L. Troman, *et al.*, Mechanistic basis of temperature-adaptation in microtubule dynamics across frog species. (2024). Available at: http://biorxiv.org/lookup/doi/10.1101/2024.07.29.605571 [Accessed 25 November 2024].

282. N. S. Morrissette, L. D. Sibley, Cytoskeleton of Apicomplexan Parasites. *Microbiol. Mol. Biol. Rev.* **66**, 21–38 (2002).

283. G. Logan, B. McCartney, Comparative analysis of taxol-derived fluorescent probes to assess microtubule networks in a complex live three-dimensional tissue. *Cytoskeleton (Hoboken).* **77**, 229 (2020).

284. M. P. Daniels, Colchicine inhibition of nerve fiber formation *in vitro*. *J. Cell Biol.* **53**, 164–176 (1972).

285. F. Mozaffer, G. I. Menon, F. Ishtiaq, Exploring the thermal limits of malaria transmission in the western Himalaya. *Ecol. Evol.* **12** (2022).

286. E. Suh, *et al.*, Estimating the effects of temperature on transmission of the human malaria parasite, *Plasmodium falciparum*. *Nat. Commun.* **15**, 3230 (2024).

287. J. L. Waite, E. Suh, P. A. Lynch, M. B. Thomas, Exploring the lower thermal limits for development of the human malaria parasite, *Plasmodium falciparum*. *Biol. Lett.* **15**, 20190275 (2019).

288. E. Suh, *et al.*, The influence of feeding behaviour and temperature on the capacity of mosquitoes to transmit malaria. *Nat. Ecol. Evol.* **4**, 940–951 (2020).

289. M. A. Boualam, B. Pradines, M. Drancourt, R. Barbieri, Malaria in Europe: A Historical Perspective. *Front. Med.* **8**, 691095 (2021).

290. M. Singer, F. Frischknecht, Fluorescent tagging of *Plasmodium* circumsporozoite protein allows imaging of sporozoite formation but blocks egress from oocysts. *Cell. Microbiol.* **23**, e13321 (2021).

291. C. Agop-Nersesian, *et al.*, Biogenesis of the Inner Membrane Complex Is Dependent on Vesicular Transport by the Alveolate Specific GTPase Rab11B. *PLoS Pathog.* **6**, e1001029 (2010).

292. M. Parkyn Schneider, *et al.*, Disrupting assembly of the inner membrane complex blocks *Plasmodium falciparum* sexual stage development. *PLoS Pathog.* **13** (2017).

293. L. H. Bannister, J. M. Hopkins, R. E. Fowler, S. Krishna, G. H. Mitchell, A brief illustrated guide to the ultrastructure of *Plasmodium falciparum* asexual blood stages. *Parasitol. Today* **16**, 427–433 (2000).

294. B. Poulin, *et al.*, Unique apicomplexan IMC sub-compartment proteins are early markers for apical polarity in the malaria parasite. *Biol. Open* **2**, 1160–1170 (2013).

295. E. Saini, *et al.*, Photosensitized INA-Labelled protein 1 (PhIL1) is novel component of the inner membrane complex and is required for *Plasmodium* parasite development. *Sci. Rep.* **7**, 1–11 (2017).

296. J. S. Wichers, *et al.*, Dissecting the Gene Expression, Localization, Membrane Topology, and Function of the *Plasmodium falciparum* STEVOR Protein Family. *MBio* **10**, e01500-19 (2019).

297. H. Zieler, J. A. Dvorak, Invasion *in vitro* of mosquito midgut cells by the malaria parasite proceeds by a conserved mechanism and results in death of the invaded midgut cells. *Proc. Natl. Acad. Sci. U. S. A.* **97**, 11516 (2000).

298. T. Ishino, Y. Orito, Y. Chinzei, M. Yuda, A calcium-dependent protein kinase regulates *Plasmodium* ookinete access to the midgut epithelial cell. *Mol. Microbiol.* **59**, 1175–1184 (2006).

299. A. K. Ghosh, M. Jacobs-Lorena, *Plasmodium* sporozoite invasion of the mosquito salivary gland. *Curr. Opin. Microbiol.* **12**, 394–400 (2009).

300. A. S. I. Aly, A. M. Vaughan, S. H. I. Kappe, Malaria Parasite Development in the Mosquito and Infection of the Mammalian Host. *Annu. Rev. Microbiol.* **63**, 195–221 (2008).

301. B. Mons, Intra erythrocytic differentiation of *Plasmodium berghei*. *Acta Leiden.* **54**, 1–124 (1986).

302. J. SCHREVEL, *et al.*, Vesicle trafficking during sporozoite development in *Plasmodium berghei* : ultrastructural evidence for a novel trafficking mechanism. *Parasitology* **135**, 1–12 (2007).

303. M. Loubens, *et al.*, The claudin-like apicomplexan microneme protein is required for gliding motility and infectivity of *Plasmodium* sporozoites. *PLOS Pathog.* **19**, e1011261 (2023).

304. N. Philip, H. J. Vaikkinen, L. Tetley, A. P. Waters, A Unique Kelch Domain Phosphatase in *Plasmodium* Regulates Ookinete Morphology, Motility and Invasion. *PLoS One* **7**, e44617 (2012).

305. N. J. Katris, *et al.*, The Apical Complex Provides a Regulated Gateway for Secretion of Invasion Factors in *Toxoplasma*. *PLoS Pathog.* **10**, e1004074 (2014).

306. L. Koreny, *et al.*, Molecular characterization of the conoid complex in *Toxoplasma* reveals its conservation in all apicomplexans, including *Plasmodium* species. *PLOS Biol.* **19**, e3001081 (2021).

307. C. P. Garnham, *et al.*, Multivalent Microtubule Recognition by Tubulin Tyrosine Ligase-like Family Glutamylases. *Cell* **161**, 1112–1123 (2015).

308. J. Abramson, *et al.*, Accurate structure prediction of biomolecular interactions with AlphaFold 3. *Nature* **630**, 493–500 (2024).

309. K. Bryson, D. Cozzetto, D. Jones, Computer-Assisted Protein Domain Boundary Prediction Using the Dom-Pred Server. *Curr. Protein Pept. Sci.* **8**, 181–188 (2007).

310. S. M. Kandathil, J. G. Greener, A. M. Lau, D. T. Jones, Ultrafast end-to-end protein structure prediction enables high-throughput exploration of uncharacterized proteins. *Proc. Natl.*

Acad. Sci. **119**, e2113348119 (2022).

311. L. J. McGuffin, D. T. Jones, Improvement of the GenTHREADER method for genomic fold recognition. *Bioinformatics* **19**, 874–881 (2003).

312. T. Nugent, D. T. Jones, Transmembrane protein topology prediction using support vector machines. *BMC Bioinformatics* **10**, 159 (2009).

313. D. W. A. Buchan, L. Moffat, A. Lau, S. M. Kandathil, D. T. Jones, Deep learning for the PSIPRED Protein Analysis Workbench. *Nucleic Acids Res.* **52**, W287–W293 (2024).

314. D. T. Jones, D. Cozzetto, DISOPRED3: precise disordered region predictions with annotated protein-binding activity. *Bioinformatics* **31**, 857–863 (2015).

315. E. S. Cheng, A. S. Moon, W. D. Barshop, J. A. Wohlschlegel, P. J. Bradley, Function and interactions of a protein bridge between the inner membrane complex and subpellicular microtubules in *Toxoplasma gondii*. (2024). Available at: https://doi.org/10.1101/2024.05.29.595897 [Accessed 14 October 2024].

316. I. Letunic, S. Khedkar, P. Bork, SMART: recent updates, new developments and status in 2020. *Nucleic Acids Res.* **49**, D458–D460 (2021).

317. I. Letunic, P. Bork, 20 years of the SMART protein domain annotation resource. *Nucleic Acids Res.* **46**, D493–D496 (2018).

318. J. Kehrer, *et al.*, APEX-based proximity labeling in *Plasmodium* identifies a membrane protein with dual functions during mosquito infection. *bioRxiv* 2020.09.29.318857 (2020). https://doi.org/10.1101/2020.09.29.318857.

319. B. Franke-Fayard, *et al.*, A *Plasmodium berghei* reference line that constitutively expresses GFP at a high level throughout the complete life cycle. *Mol. Biochem. Parasitol.* **137**, 23–33 (2004).

320. S. Zheng, *et al.*, AreTomo: An integrated software package for automated marker-free, motion-corrected cryo-electron tomographic alignment and reconstruction. *J. Struct. Biol. X* **6**, 100068 (2022).

321. J. R. Kremer, D. N. Mastronarde, J. R. McIntosh, Computer Visualization of Three-Dimensional Image Data Using IMOD. *J. Struct. Biol.* **116**, 71–76 (1996).

322. C. J. Janse, J. Ramesar, A. P. Waters, High-efficiency transfection and drug selection of genetically transformed blood stages of the rodent malaria parasite *Plasmodium berghei*. *Nat. Protoc.* **1**, 346–356 (2006).

323. R. Spaccapelo, *et al.*, Plasmepsin 4-Deficient *Plasmodium berghei* Are Virulence Attenuated and Induce Protective Immunity against Experimental Malaria. *Am. J. Pathol.* **176**, 205–217 (2010).

324. D. Klug, G. R. Mair, F. Frischknecht, R. G. Douglas, A small mitochondrial protein present in myzozoans is essential for malaria transmission. *Open Biol.* **6**, 160034 (2016).

325. D. J. Weiss, K. J. Wardrop, O. W. Schalm, *Schalm's veterinary hematology.*, 6th ed. / (Wiley-Blackwell, 2010).

326. M. Schaffer, *et al.*, Cryo-focused Ion Beam Sample Preparation for Imaging Vitreous Cells by Cryo-electron Tomography. *BIO-PROTOCOL* **5** (2015).

327. D. N. Mastronarde, Dual-Axis Tomography: An Approach with Alignment Methods That Preserve Resolution. *J. Struct. Biol.* **120**, 343–352 (1997).

328. D. Gambarotto, *et al.*, Imaging cellular ultrastructures using expansion microscopy (U-ExM). *Nat. Methods 2018 161* **16**, 71–74 (2018).

8. Acknowledgements

My thesis would not have been possible without the support, guidance and help of many different people and I am grateful to everyone who contributed to this journey.

First of all, I want to thank my PI Prof. Friedrich (Freddy) Frischknecht, for offering me the opportunity to work on this incredible project and for welcoming me back into the lab. I am grateful for our many scientific discussions. But most I want to thank you for creating an environment that allowed me to grow, both scientifically and also personally. Thank you for all the opportunities you gave me during my PhD, allowing me to join the most wonderful BoP-course, for best preparing me for conferences and broadening my horizon beyond the PhD project.

I am grateful to all the other members of my thesis advisory committee, Prof. Gislene Pereira, Prof. Ulrich Schwarz and Dr. Julien Guizetti. Thank you all for the fruitful discussions during my TAC meetings and for your support and input throughout the years. A special thanks to Gislene for your thoughtful career advice and to Prof Gislene Pereira, Prof. Ulrich Schwarz and Dr. Viet Loan Dao Thi for readily accepting to examine my thesis.

My deepest gratitude goes to Dr. Franziska Hentzschel for her continuous support, guidance and all her help throughout my PhD. Franzi, you are the best mentor I could have wished for; I learned so much from you. Your advice, whether on science or figure design have been immensely helpful. Big thanks also for proof-reading my thesis. Besides science, you became one of my best friends in Heidelberg and my best boardgame buddy in building the most beautiful zoos in Arche Nova.

I would also like to thank Dr. Markus Ganter, for his scientific input and engaging discussions together with Franzi during our time that we shared an office.

Doing a PhD is not only working on a scientific project but also being part of a team. I would like to thank the whole Frischknecht lab for the great time I had in the lab, including the EM team for all their support in sample processing. Thanks, Kevin (Walz), for your calm attitude that helped me to cool down when I was just running around like crazy and for our great scientific discussions. Thank you, Julia (Sattler), for being such a great colleague and for Monami (Chowdhury) for reminding us all, that being emotional is human. Big thanks also to the neighbouring labs, the Ganter, Guizetti and Hentzschel lab, for creating such a great and supportive environment. I want to thank the whole parasitology department for being such a great group of people and the fruitful discussions we had in our departmental seminars.

I would like to thank the Heidelberg Biosciences International Graduate School (HBIGS) for just being the best graduate school one could wish for. Thank you, Sandra Martini, Manuela Arlt, Marina Galvan and Dr. Rolf Lutz, for the amazing course and workshop program as well as career guidance.

Furthermore, I am most grateful for all the support I obtained from the core facilities. Big thanks go to the infectious disease imaging platform, IDIP, namely Dr. Vibor Laketa, Dr. Sylvia Olberg and Dr. Severina Klaus for running such a great facility and providing users with excellent microscopy trainings. The generation and processing of all EM data would not have been possible with the kind support of the EMCF, namely Dr. Stefanie Gold, Buyuan He and Lilian Dorner. In addition, I want to thank Dr. Marcin Luzarowski and the staff from the mass spec core facility for processing my data.

I was very lucky to be part of several amazing collaborations that all valuably contributed to my PhD work. While the initial samples were unfortunately not possible to process, I still want to thank Sarah Peter from the Chlanda lab, Bioquant Heidelberg, for her support in plunge-freezing my samples multiple times and especially on very short notice. A big thank goes to Dr. Josie Ferreira, University College London, for plunge-freezing my MIP KO samples even though this meant to fly over from London to Hamburg and arrange everything in a short time frame. Thank you so much for your effort in making this possible. On the same note, I would like to thank Jana Lierl and Yuliia Mironova, both University of Hamburg and Dr. Vojtěch Pražák, Centre for Structural Systems Biology (CSSB) and Oxford Biochemistry, for processing my cryo-EM samples and generating the tomograms. This was a huge effort in coordinating everyone from three different European locations and I really appreciate all your help.

Furthermore, I had a great collaboration with Dr. Jan Stephan Wichers-Misterek and Dr. Paolo Mesén-Ramírez, both from the lab of Prof. Tim Gilberger at the CSSB and the Bernhard-Nocht-Institute for Tropical Medicine (BNITM) in Hamburg, during which we explored the function of SPM3 in both *P. falciparum* and *P. berghei*. The PfSPM3 project is now further investigated by Korbinian Niedermüller, who kindly provided me with the data of his Bio-ID experiment.

Further thanks go to Dr. Gil Henkin and Dominik Fachet, both from the lab of Prof. Simone Reber at the Max-Planck institute of Infection Biology in Berlin, who gave me an *in vitro* perspective on studying MIPs. Thank you, Dominik, for growing flasks over flasks of parasites to purify *P. falciparum* tubulin and Gil for taking this tubulin to run your *in vitro* polymerization assays.

I would also like to thank Felix Mikus and Dr. Caroline Simon, both from EMBL Heidelberg and Dr. Sabrina Absalon (Indiana University School of Medicine, USA) and Dr. Ben Liffner (University of Adelaide, Australia) for all their input and fruitful discussions on U-ExM.

My PhD project involved animal experiments and hence would not have been possible without mice or mosquitos. Thus, I would like deeply thank the animal caretakers of the IBF at Heidelberg that take great care of our mice; and Miriam Reinig and all students involved for taking care of the mosquito rearing.

During my PhD, I had the great pleasure to supervise several talented students: Thanks go to Lea Herzel, Katharina Röver, Roberta Malamud, Lilian Dorner and Ebenezer Taylor, for all contributing to my PhD work. Each of you played a part in this journey, and I learned so much from you working with you.

Further, I had the unique opportunity to join the renowed 'Biology of Parasitism: Modern Approaches'- course (BoP) at the Marine Biological Laboratory. Not only did I learn so much about a diversity of different protozoan parasites but I was lucky to have joined the most awesome group of BoP students there. Thank you all for the most amazing summer, the endless hours in the lab, the laughing and fun in Mervs and for all becoming friends for life. Special thanks also go to Prof. Scott Dawson, University of California, Davis, USA, for inviting Ju and me after the BoP-course to join your lab for two weeks and establish U-ExM in your lab to study *Giardia*; and of course, Ju for being such a great roomie during that time.

Writing a thesis works so much better when having an environment that supports a writing atmosphere. I would like to thank the whole team of the graduate academy, especially Silke (Hoffmann) for taking on this pilot experiment to enable the whole 'Schreibgruppe @Graduiertenzentrum' to extend the opening hours. Your graduate center is a very special co-working space and the best place I could have imagined to write my thesis.

Life is so much more than a PhD. I hence would like to take the opportunity to thank everyone who shares my enthusiasm of looooong and complicated board games. The 'Spieleabend am Berg' (Franzi, Caro, Lukas and Yannik) as well as the 'Pandemic group' (Julia, Pengbo, Alexa, Daniel, Simon, Helge and our smallies Hanna and Liam). Thank you all for being such great friends and sharing the love of going on the adventures of Robin Hood, saving the world from a pandemic or destroying enemies in a dungeon.

Furthermore, I would like to thank my close friends Katharina and Ann-Kathrin for being such wonderful friends. It helps so much to just having a coffee together and to share the ups and downs of (PhD) life. Also, thanks to Severina and Henrik, for just being so nice and thoughtful; picking me up for a coffee or providing me with some snacks to fuel my writing times. Thank you all, for your thoughtful care-packages to survive my writing time!!

Nothing would have been possible without all the support and guidance I received from my family from the very beginning. DANKE Mama und Papa, dass ihr immer an mich geglaubt habt und alles in meinem Leben möglich gemacht habt. Ohne euch würde ich niemals da stehen, wo ich heute bin! Danke für eure Unterstützung in dieser intensiven Zeit und euer Verständnis, wenn am Wochenende mal wieder wenig Zeit war, weil die Doktorarbeit gerufen hat. Danke an mein liebes Schwesterli, Linnea, für all Deine Unterstützung, egal ob während der Promotion oder noch

während dem Studium. Danke, für Dein liebes Care-Paket und Deine unzähligen Anrufe, ob ich denn irgendwo zwischen allen den Thesis-Seiten noch leben würde.

My biggest thanks go to my wonderful husband. Felix, it is impossible to tell you how much I love you and how much I appreciated all your support throughout. Thanks, for just taking me in your arms when PhD life hit hard again, for "simply" taking care of almost all the household throughout my entire writing time, for making me laugh and to take a step back and look at the PhD life from a different angle. I am so happy that I found you and I am looking so much forward what life will bring next to us. I love you.

Thank you all for accompanying me during this exciting time and for each contributing in your own way to making the last four years a wonderful time.

9. Supplementary files

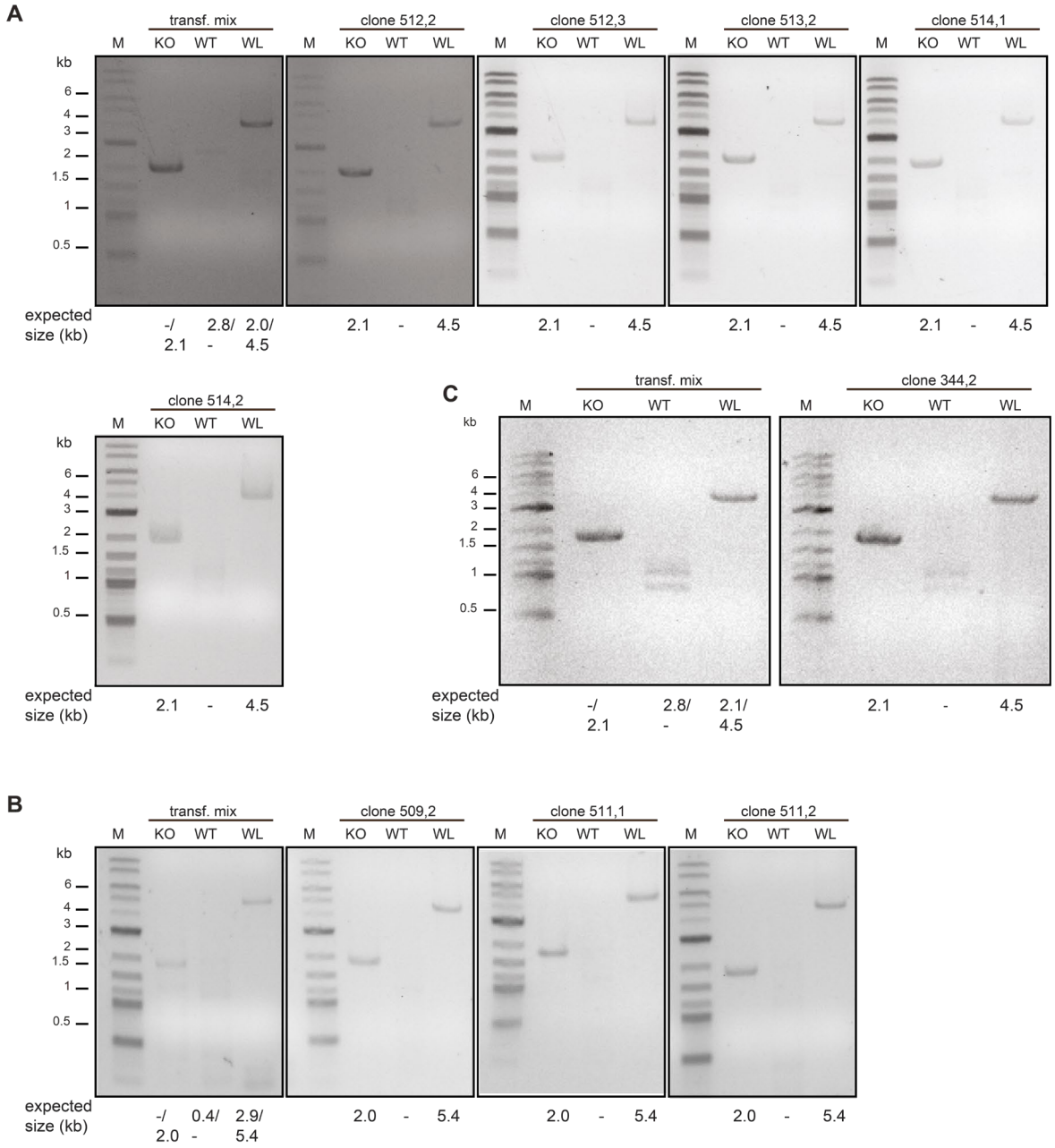

Supplementary Figure 1 Generation of *spm1* and *trxL1* single and double KO parasite lines. Genotyping PCRs of the parental transfection mix and the remaining isogenic clones of **A)** *spm1*(-), **B)** *trxL1*(-) and **C)** *trxL1*(-)/*spm1*(-). Primers used for genotyping PCRs are indicated in **Figure 6**. Double crossover events leading to the insertion of the KO construct will result in an increased size of the whole locus (WL) PCR fragment. Transfection mixes represent a mixed population of the parental line (upper amplicon sizes) and the KO line (bottom amplicon sizes). Kb – kilobase, KO – knockout, M – marker, transf. mix – transfection mix, WL – whole locus, WT – wildtype.

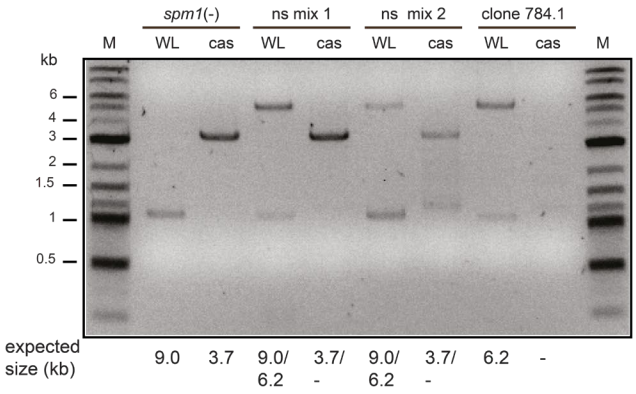

Supplementary Figure 2 Negative selection of the *spm1*(-) KO parasite line. Genotyping PCRs of two independent negative selection (ns mix1, ns mix2). Primers used for genotyping PCRs are indicated in **Figure 6**. Negative selection (ns) mixes represent a mixed population of the parental line (upper amplicon sizes) and the selected line (bottom amplicon sizes). Negative selection loops out the resistance cassette and hence KO primers only result in a PCR fragment in KO parasites which have not yet been negatively selected. Cas – cassette, kb – kilobase, KO – knockout, M – marker, ns – negatively selected, WL – whole locus.

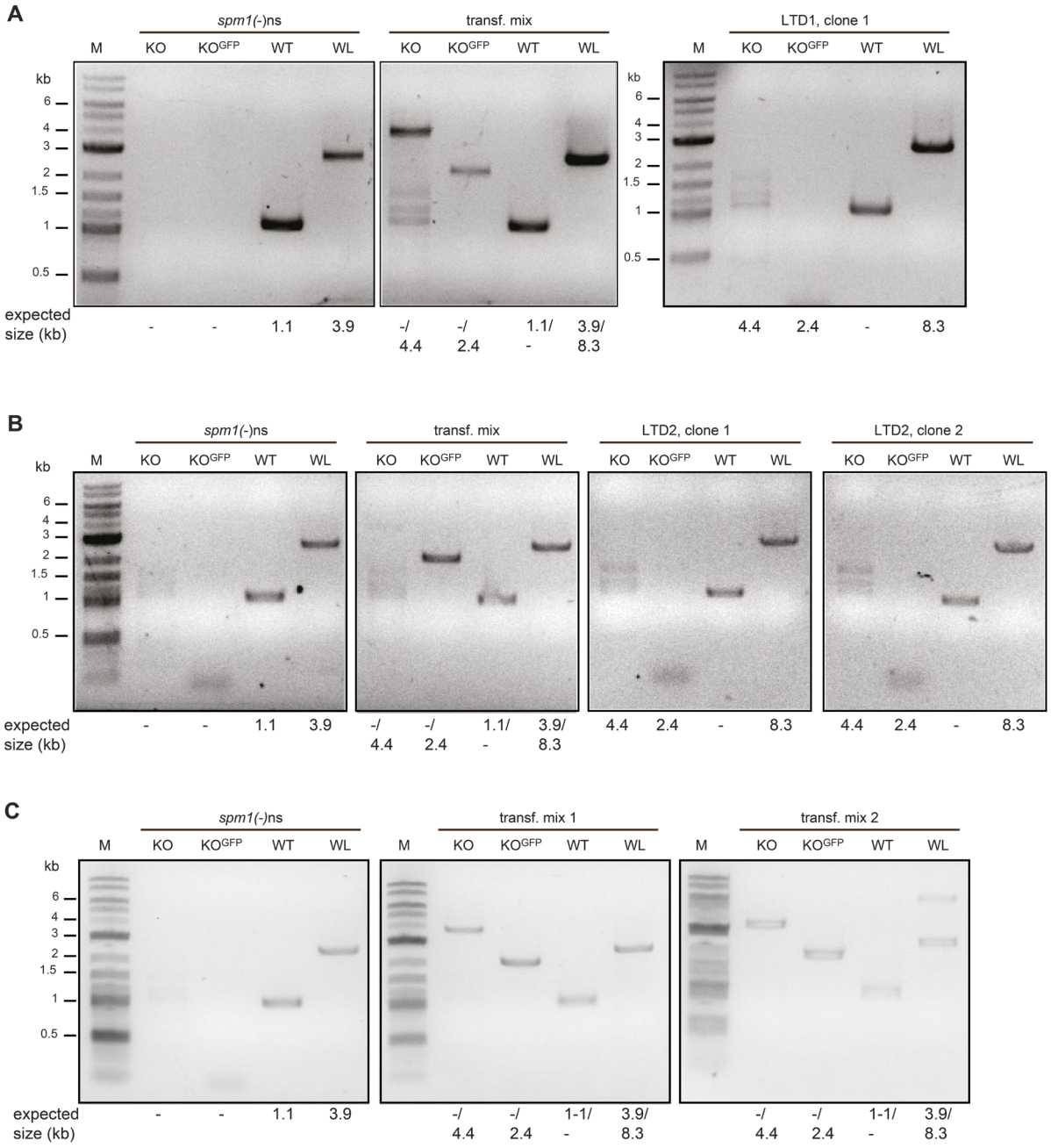

Supplementary Figure 3 Generation of the *spm1*(-)/*spm2*(-)-*gfp* double KO parasite line. Genotyping PCRs of **A)** *spm1*(-)/*spm2*(-)-*gfp***,** transfection 1, limiting dilution 1 (LTD1), **B)** *spm1*(-)/ *spm2*(-)-*gfp*, transfection 1, LTD2. **C)** *spm1*(-)/*spm2*(-)-*gfp***,** transfection 2, LTD1, Primers used for genotyping PCRs are indicated in **Figure 6**. Double crossover events leading to the insertion of the KO construct will result in an increased size of the whole locus (WL) PCR fragment. Transfection mixes represent a mixed population of the parental line (upper amplicon sizes) and the KO line (bottom amplicon sizes). Kb – kilobase, KO – knockout, KO^{GFP} – knockout^{GFP}, LTD – limiting dilution, M – marker, ns – negatively selected, transf. mix – transfection mix, WL – whole locus, WT – wildtype.

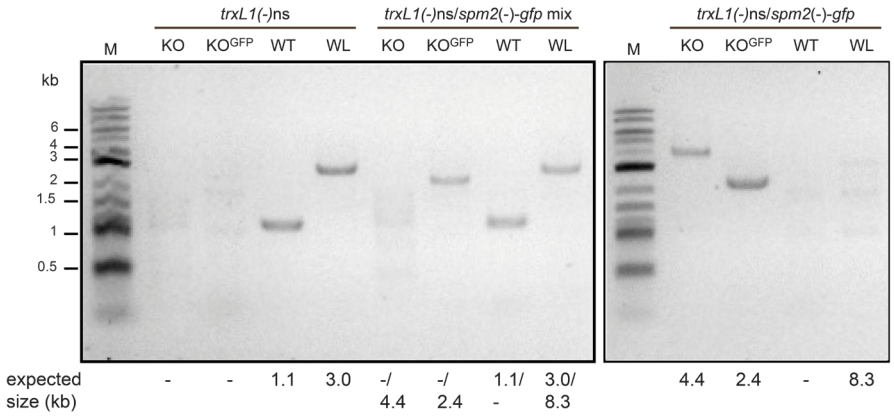

Supplementary Figure 4 Generation of *trxL1*(-)/*spm2*(-)-*gfp* double KO parasite line. Primers used for genotyping PCRs are indicated in **Figure *6* A, B**. Double crossover events leading to the insertion of the KO construct will result in an increased size of the whole locus (WL) PCR fragment. Two PCR mixes (KO, KO^{GFP}) were used to confirm integration of the selection cassette. Kb – kilobase, KO – knockout, M – marker, na – not applicable, ns – negatively selected, WL – whole locus, WT – wildtype.

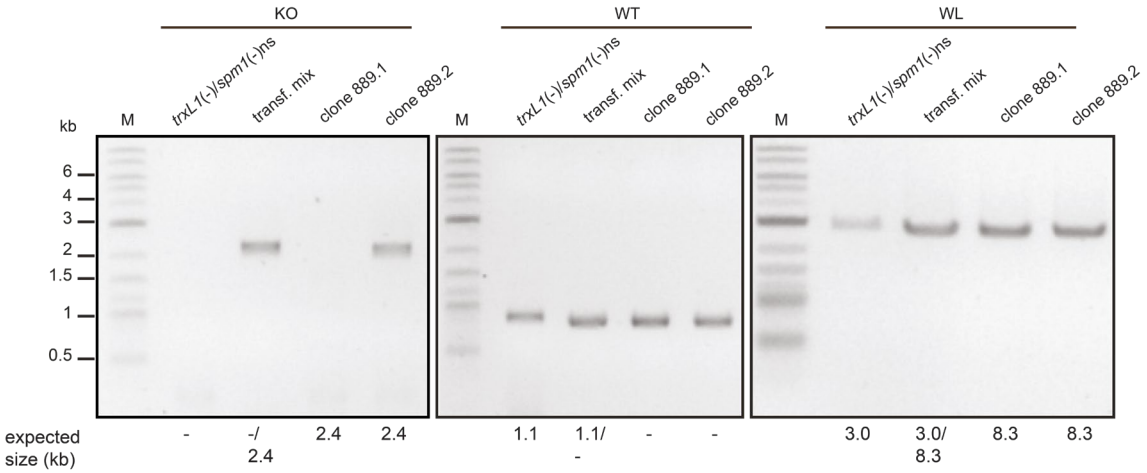

Supplementary Figure 5 Generation of the *trxL1*(-)/*spm1*(-)/*spm2*(-)-*gfp* triple KO parasite line. Genotyping PCRs for KO (left), WT (middle) or WL (right) amplification. Primers used for genotyping PCRs are indicated in **Figure 6**. Double crossover events leading to the insertion of the KO construct will result in an increased size of the whole locus (WL) PCR fragment. Transfection mix represents a mixed population of the parental line (upper amplicon sizes) and the KO line (bottom amplicon sizes). Kb – kilobase, KO – knockout, M – marker, ns – negatively selected, transf. mix – transfection mix, WL – whole locus, WT – wildtype.

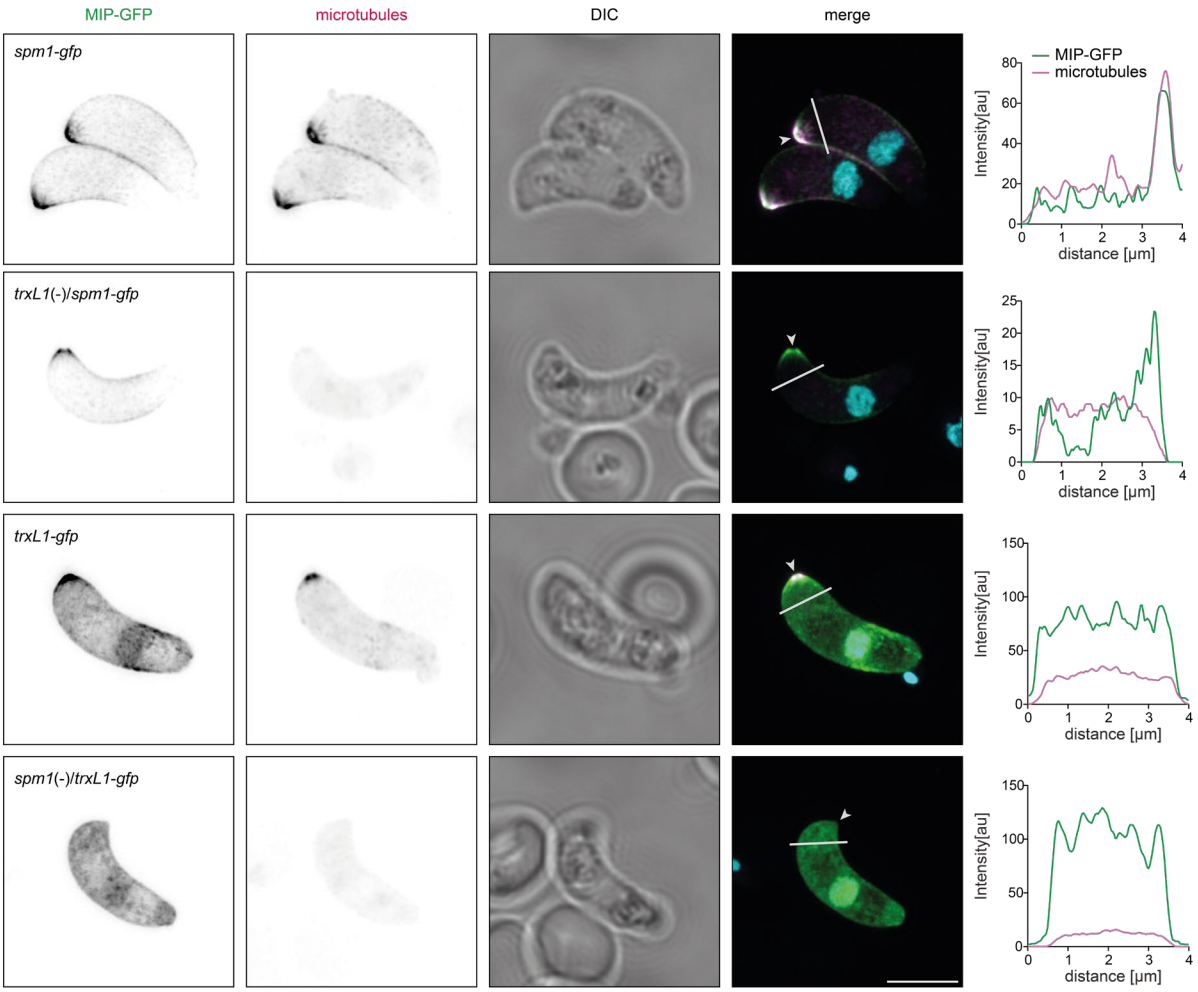

Supplementary Figure 6 SiR-tubulin staining in ookinetes is impaired upon either depletion of *spm1* or tagging of *trxL1*. MIP-GFP localization in mature ookinetes in either WT- / *spm1*(-)- or *trxL1*(-)-background. Shown is the endogenous MIP-GFP signal while microtubules were stained with SiR-tubulin. Merge images of MIP-GFP (green), microtubules (magenta), and nucleus (cyan). Arrowheads point to the parasite's apical end. Same contrast settings for all images. Shown are maximum Z-projections of fluorescent channels; for the DIC channel the mid slice is shown. Representative of at least 10 images taken. Scale bar: 5 µm. Intensity profiles based on lines of corresponding merge image of the same row.

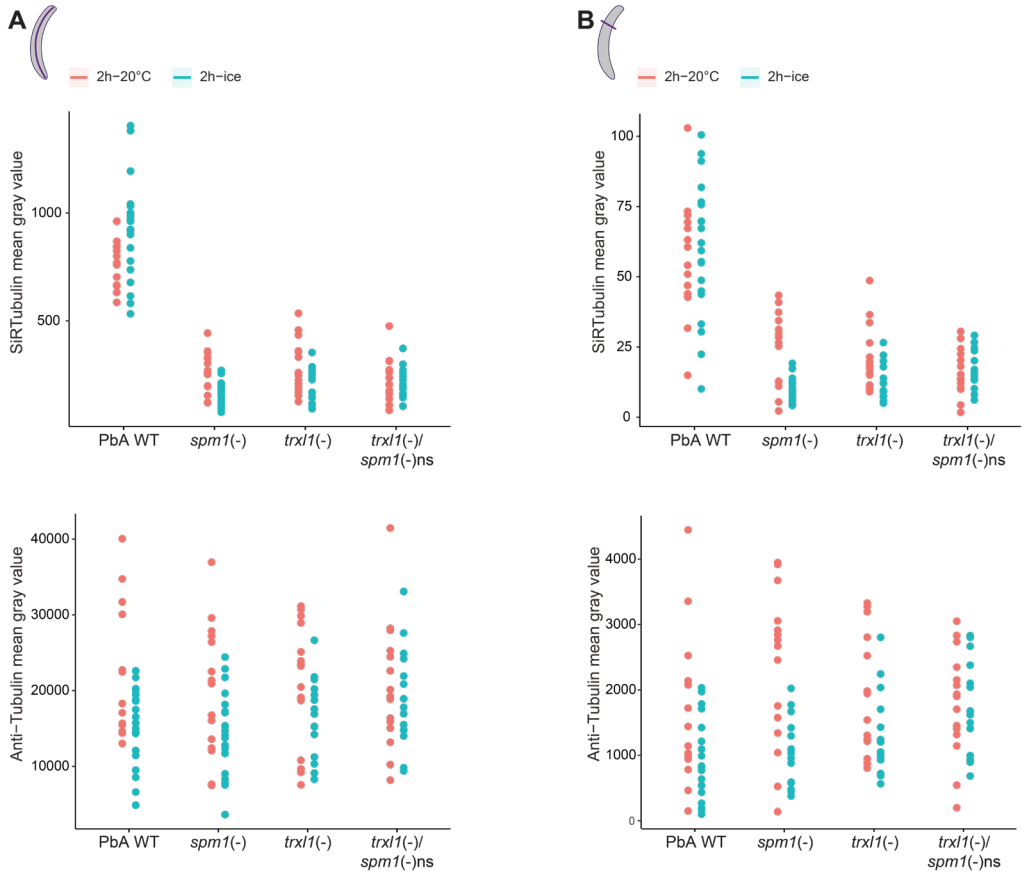

Supplementary Figure 7 SiR-tubulin intensities are drastically decreased in all MIP-KO mutants. **A, B)** Microtubule signal determined by SiR-tubulin staining (top) and anti-tubulin staining (bottom) along the A) longitudinal axis or the B) cross axis of the sporozoite. Spz – sporozoite.

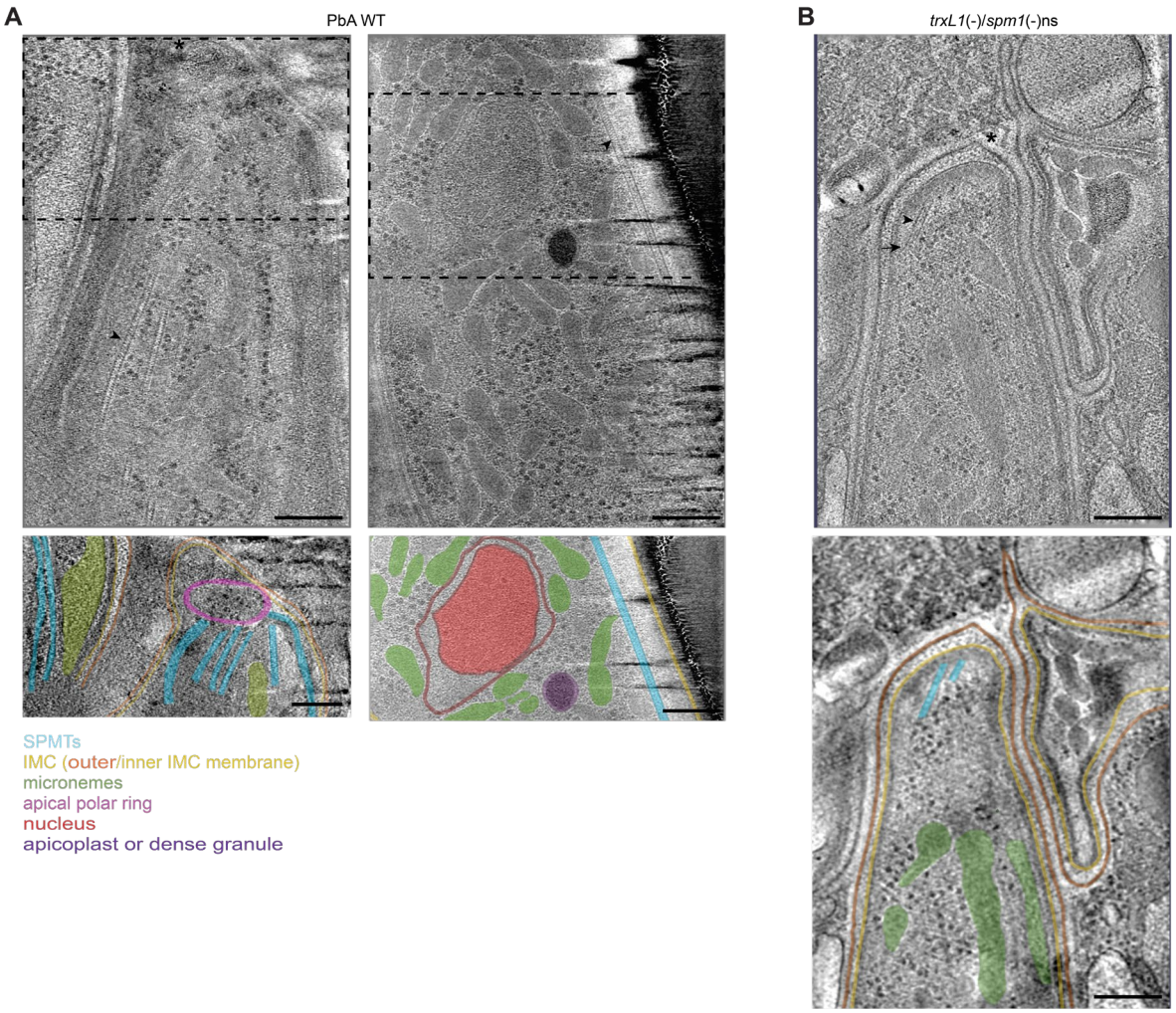

Supplementary Figure 8 In the absence of SPM1 and TrxL1, SPMTs are drastically shortened and destabilized. **A, B)** Cryo-EM of FIB-milled A) PbA WT and B) *trxL1*(-)/*spm1*(-)ns salivary glands sporozoites. Dashed-line boxes indicate coloured images below. Asterisk marks apical end of the parasite, arrowhead points to SPMTs with the black arrow marking the flared ends of a SPMT in the *trxL1*(-)/*spm1*(-)ns mutant.

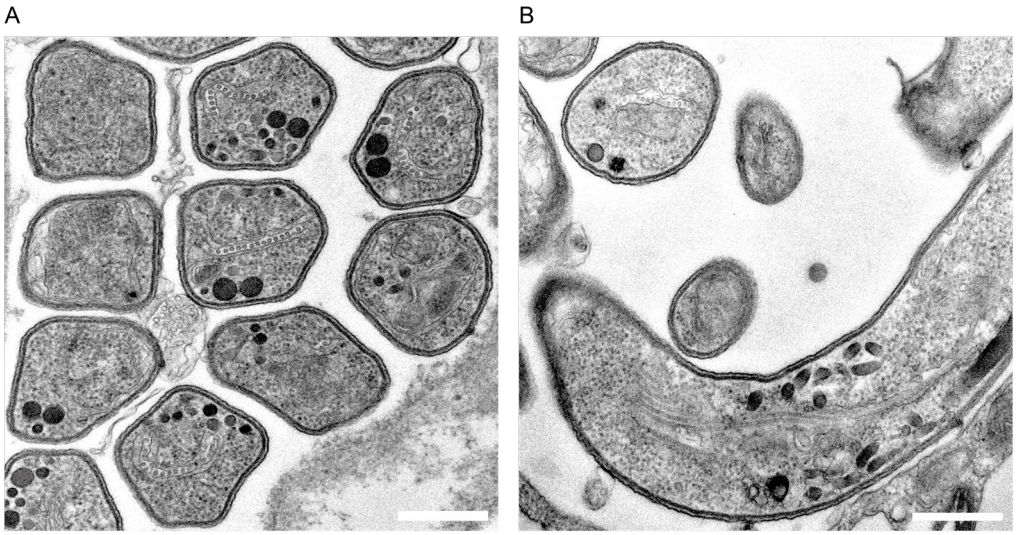

Supplementary Figure 9 Transmission electron micrographs through *spm3*(-) sporozoites. A, B) TEM of A) cross section and B) longitudinal section of oocysts at day 15 days post infection. Note the different phenotypes in individual sporozoites, with some cells displaying a microtubule distribution similar to that of PbA WT sporozoites. Scale bars: 500 nm. Figure and legend were previously published and adapted for this thesis (248).

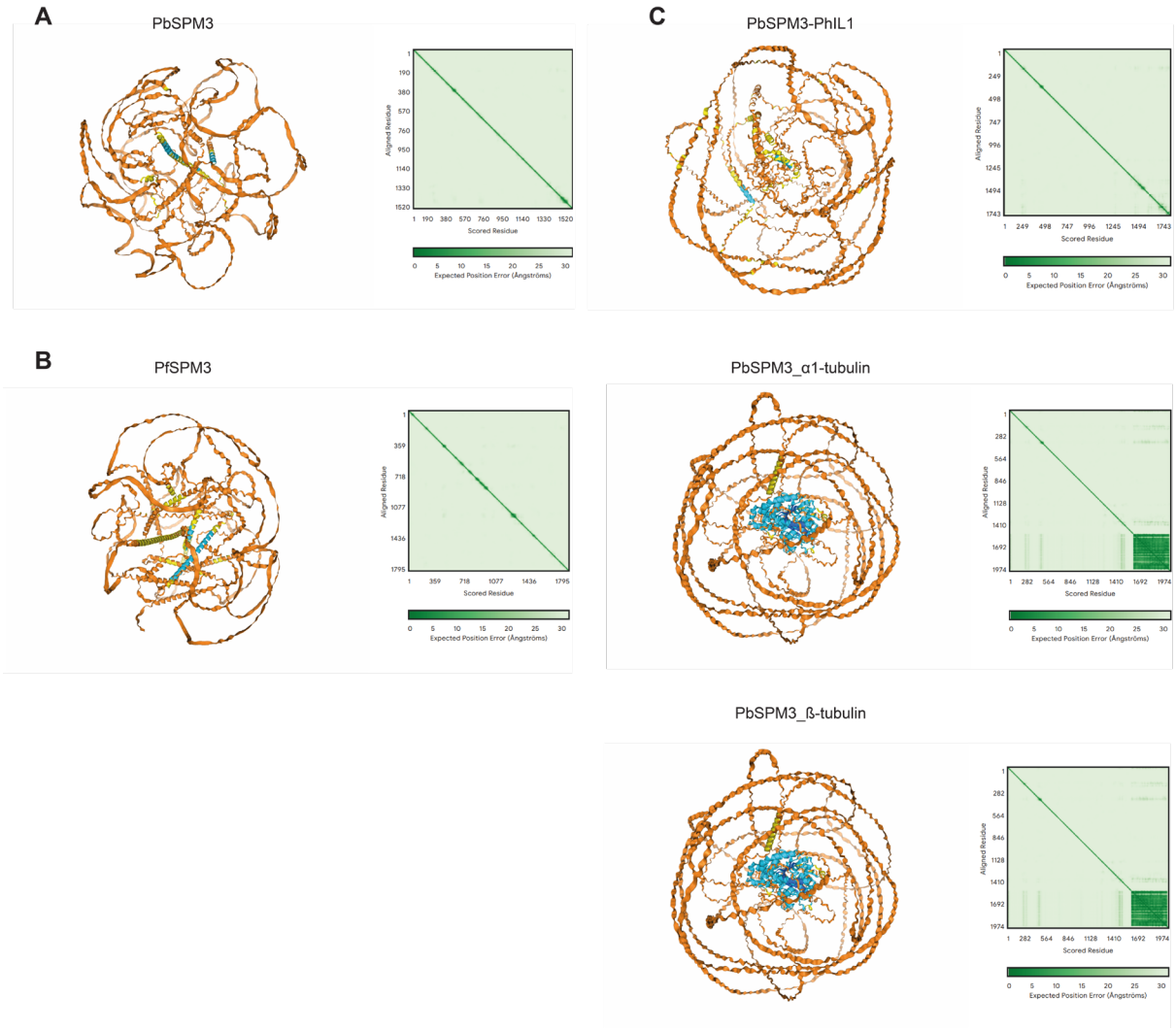

Supplementary Figure 10 Structural predictions of SPM3 are of low confidence. Structural prediction of **A)** *Pb*SPM3, **B)** *Pf*SPM3 or co-predictions of **C)** *Pb*SPM3 with either PhIL1, α1-tubulin or β-tubulin using AlphaFold3 (308). Colour code of structures indicates confidence score with dark blue representing high confidence (pIDDT > 90) and orange representing very low confidence (pIDDT > 50). PAE plot on the right next to each structure prediction indicates the expected distance error in Ångströms for a pair of residues with dark green (= lower PAE score) indicating good prediction. PAE – predicted alignment error, pIDDT - per-atom confidence estimate.

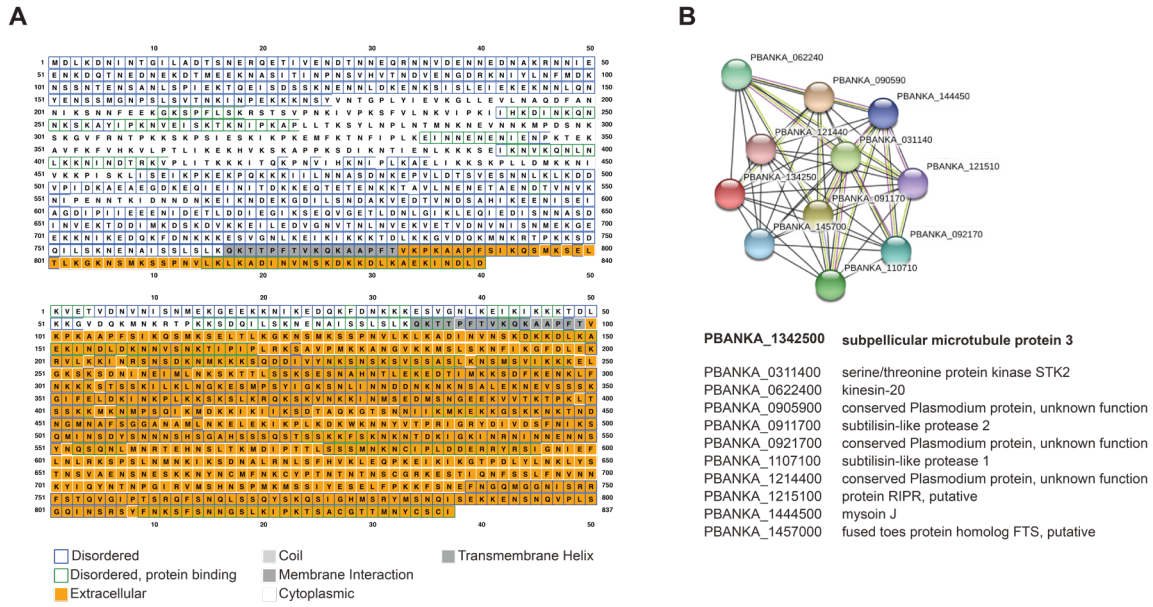

PBANKA_1342500 subpellicular microtubule protein 3

PBANKA_0311400	serine/threonine protein kinase STK2
PBANKA_0622400	kinesin-20
PBANKA_0905900	conserved Plasmodium protein, unknown function
PBANKA_0911700	subtilisin-like protease 2
PBANKA_0921700	conserved Plasmodium protein, unknown function
PBANKA_1107100	subtilisin-like protease 1
PBANKA_1214400	conserved Plasmodium protein, unknown function
PBANKA_1215100	protein RIPR, putative
PBANKA_1444500	mysoin J
PBANKA_1457000	fused toes protein homolog FTS, putative

Supplementary Figure 11 PSIRED predicts membrane- and extracellular domain. A) Domains were predicted using the PSIRED server (309–314). As *Pb*SPM3 exceeds the amino acid length that can be analysed within one attempt, SPM3 was split and an N- (top) and C-terminal (bottom) domain of 840/837 aa in length and with an overlap of 90 aa was analysed separately. B) Simple Modular Architecture Research Tool (SMART) analysis (normal mode) of *Pb*SPM3 shows evolutionary relationships of proteins based on shared protein domains (316, 317).